Multiscale study of a perfusion bioreactor for bone tissue engineering

Morgan Chabanon

ÉCOLE CENTRALE DES ARTS ET MANUFACTURES «ÉCOLE CENTRALE PARIS»

THÈSE

présentée par

Morgan CHABANON

pour l'obtention du

GRADE DE DOCTEUR

Spécialité : Bioingénierie, Biophysique

Laboratoires d'accueil : MSSMat (UMR CNRS 8579), EM2C (UPR CNRS 288)

Multiscale Study of a Perfusion Bioreactor for Bone Tissue Engineering

soutenue le : 12 janvier 2015

devant un jury composé de :

Mme. Cécile LEGALLAIS (DR)	UMR CNRS 7338, BMBI	Rapporteure
Mr. Michel QUINTARD (DR)	UMR CNRS 5502, IMFT	Rapporteur
Mr. Bruno LE PIOUFLE (Prof. ENS Cachan)	UMR CNRS 8029, SATIE	Examinateur
Mr. Didier LASSEUX (CR, HDR)	UMR CNRS 5295, I2M	Examinateur
Mr. Benoît GOYEAU (Prof. ECP)	UPR CNRS 288, EM2C	Directeur de Thèse
Mr. Bertrand DAVID (CR)	UMR CNRS 8579, MSSMat	Co-encadrant

2015ECAP0003

REMERCIEMENTS

Je souhaite remercier particulièrement Benoît Goyeau pour ses conseils, son encadrement et son soutien. J'ai eu énormément plaisir à débattre et échanger aux sujets de prise de moyenne, de dispersion, d'interfaces fluide/poreux, d'Harley-Davidson, de Gong, de politique et bien d'autres.

Je remercie Bertrand David, grâce à qui ce sujet de thèse a vu le jour, et qui m'a fait confiance pour le mener à bien (et parfois à mal).

Mes remerciements s'adressent également à Hachmi Ben Dia, directeur du MSSMat, et Olivier Gicquel, directeur du EM2C, dont les soutiens ont permis l'aboutissement de cette thèse dans de bonnes conditions.

Je remercie Michel Quintard et Cécile Legallais d'avoir accepté d'être les rapporteurs de cette thèse, ainsi que Bruno Le Pioufle et Didier Lasseux qui ont bien voulu endosser les rôles d'examinateurs.

J'adresse mes chaleureux remerciements à Bruno Le Pioufle, Olivier Français et tous les membres du SATIE-BIOMIS, qui m'ont si souvent accueilli au sein de leur équipe, toujours dans la bonne humeur.

Je souhaite remercier également Eric Perrin pour son support et son humour, ainsi que Hervé Duval pour ses conseils et son soutien. Muchas gracias à Francesco Valdes-Parada, qui a affronté tremblements de terre et chaleurs torrides pour m'aider à finaliser quelques calculs de permeabilité en milieu fibreux. Merci aussi à Benjamin dont la participation à l'exploitation des données expérimentales a été précieuse.

Je tiens à exprimer ma profonde gratitude à tous les membres du MSSMat, qui ont participé de près ou de loin au bon déroulement de ma thèse. Merci donc à Natalie, Nadège, Nicolas, Thomas, Sokona, Gilbert, Farida, Francis... Et je ne voudrais pas oublier les filles de l'ED, Catherine et Emmanuelle, qui m'ont sponsorisé en stylos pointeurs et mug.

Et bien sûr, un grand merci à mes collègues thésards, postdoc ou au autres, avec qui l'amitié s'est développée en delà des murs du laboratoire, Ahlem (par qui je dois commencer sous peines de représailles), Diana, Samuel, Julien, Mathieu, Sofi (Wang), Silvana, Fernando, Gilles, Aurélie, Wenlong ...

Enfin, je remercie mes amis et ma famille qui m'ont supporté aussi bien pendant les hauts que pendant les bas de cette passionnante aventure.

ABSTRACT

TISSUE ENGINEERING represents a promising approach for the production of bone substitutes. The use of perfusion bioreactors for the culture of bone-forming cells on a three-dimensional porous scaffold material, resolves mass transport limitations and provides physical stimuli, increasing the overall proliferation and differentiation of cells. Despite the recent and important development of bioreactors for tissue engineering, the underlying mechanisms leading to the production of bone substitutes remain poorly understood.

The aim of this thesis is to gain insight on the influence of transport phenomena, on cell and tissue growth within a perfusion bioreactor. To this purpose, a combined modeling and experimental approach is followed.

To start with, a rigorous theoretical framework is developed in order to study the transport properties of the bioreactor. Given the hierarchical nature of the system, the multiscale aspect of the problem must be taken into account. Based on the volume averaging theory with closure, mass and momentum transport processes are upscaled from the extracellular matrix scale, to the bioreactor scale. The effective properties of the encountered structures are evaluated, and the influence of the interscale dependencies are emphasized. The resulting macroscopic model includes non-conventional terms, which contributions are evaluated in the case of the bioreactor culture conditions.

Then, cell proliferation and tissue growth are studied both, from an experimental and modeling point of view. First, fibroblast cells are cultured on glass beads in a bioreactor, perfused with culture medium at 10mL/min, for up to three weeks. A protocol combining histological techniques and image analysis allows the quantification of cell and tissue growth as a function of space and time. Second, a theoretical tissue production kinetic is introduced in the multiscale transport model previously developed. Finally, the resolution at the bioreactor scale allows to discuss the theoretical and experimental results in regard to the transport phenomena taking place in the perfusion bioreactor.

Key words : Tissue engineering, Perfusion bioreactor, Transports in porous media, Volume averaging, Cell and tissue growth

RÉSUMÉ

L'INGÉNIERIE TISSULAIRE représente une solution prometteuse pour la production de substituts osseux. L'utilisation de bioréacteurs à perfusion pour cultiver des cellules ostéo-compétentes sur des matrices poreuses, permet de résoudre les limitations dues au transfert de masse, et d'apporter des stimuli physiques améliorant la prolifération et la différenciation cellulaire. Malgré les récents et importants développements des bioréacteurs en ingénierie tissulaire, les mécanismes menant à la production de substituts osseux en bioréacteurs restent mal compris.

Le but de cette thèse est d'améliorer la compréhension de l'influence des phénomènes de transport, sur la croissance cellulaire et tissulaire dans un bioréacteur à perfusion. Dans cet objectif, une approche combinant modélisation et expérimentation est proposée.

Dans un premier temps, un cadre théorique rigoureux est développé afin d'étudier les propriétés de transport du bioréacteur. Etant donné la nature hiérarchique du système, l'aspect multi-échelle du problème doit être pris en compte. En se basant sur la méthode de prise de moyenne volumique avec fermeture, les processus de transport d'espèces et de quantité de mouvement sont homogénéisés à partir de l'échelle de la matrice extracellulaire, jusqu'à l'échelle du bioréacteur. Les propriétés effectives des différentes structures rencontrées sont évaluées, et l'influence des dépendances inter-échelles sont mises en valeur. Le modèle macroscopique obtenu inclut des termes non-conventionnels, dont les contributions sont évaluées pour les conditions de fonctionnement du bioréacteur.

Dans un second temps, la prolifération cellulaire et la production de tissu sont étudiées d'un point de vue expérimental et théorique. Premièrement, des cellules de type fibroblaste, sont cultivées jusqu'à trois semaines sur des billes de verre, dans un bioréacteur perfusé à 10mL/min. Un protocole combinant des techniques d'histologie et d'analyse d'image, permet de quantifier la croissance de cellules et de tissu en fonction du temps et de l'espace. Deuxièmement, une cinétique de production de tissu est introduite dans le modèle de transport multiéchelle développé plus tôt. Finalement, la résolution à l'échelle du bioréacteur permet de discuter les résultats expérimentaux et théoriques au regard des phénomènes de transport ayant lieu dans le bioréacteur à perfusion.

Mots clés : Ingénierie tissulaire, Bioréacteur à Perfusion, Transport en milieux poreux, Prise de moyenne volumique, Croissance cellulaire et tissulaire

Contents

INTRODUCTION

LARGE BONE DEFECTS can result from high energy traumatic events, ablation due to a pathology (for instance bone tumor or infection), or non-healing fractures. In these cases, the natural regeneration ability of bone is insufficient, and grafts are required to fill the defects. Presently, more than 2 million bone grafting procedures are conducted annually in the United States, representing an estimated market of $2.5 billion [McCoy & O'Brien, 2010]. The current "gold standard" surgical procedure is autologous graft, where a volume of bone is harvested from a healthy spot of the patient (typically the iliac crest in the hip), to be implanted in the defect. Although healing rates with this procedure have been reported as high as 60-100%, several drawbacks remain [Calori et al., 2011]. Indeed, the harvesting procedure is a heavy surgical intervention implying risks of complications and additional cost. Moreover the harvested volume is limited and may be inadequate for large defects or multiple sites reconstruction. Other acellular treatments such as allografts or filling material, present lower success rate and heterogeneous bone formation. This motivates the research of alternative bone substitutes and treatments for large bone defects.

Tissue engineering aims to answer this need, by providing an interdisciplinary framework to produce tissue and organs *in vitro*. In one of its primary approach, bone tissue engineering combines three-dimensional porous materials with osteocompetent cell culture, in order to produce bone substitutes. Whilst this methodology has shown very promising results [Petite et al., 2000], very few clinical studies have been carried [Quarto et al., 2001]. This is mainly due to long and expensive culture periods as well as low reproducibility and heterogeneous substitute production. These limitations may be addressed by the use of more automated culture devices called bioreactors.

Bioreactors for bone tissue engineering are designed to improve mass transport within the forming bone substitute, and provide biophysical stimuli to enhance cell proliferation, differentiation and extracellular matrix deposition. Despite an extensive literature on bioreactors for bone tissue engineering, the translation of this technology to clinical applications still faces important challenges. Most importantly, great difficulties remain in increasing the quantities of produced bone substitutes to clinically relevant volumes. This can be partly explained by the empiric development of bioreactors, which has led to gaps in the understanding of tissue growth within these environment. Limitations to the design of relevant bioreactor for clinical applications cannot be addressed without a deeper understanding of the biological, biochemical and biophysical phenomena taking place in these systems.

Modeling approaches have been shown to be promising tools to represent and predict mechanisms that are difficult or impossible to observe experimentally. Theoretical and numerical studies related to bioreactors, have mainly focused on the development of mass transport, hydrodynamics, or cell growth models at a specific scale. Yet, in order to propose a relevant model for the prediction of substitute production, it appears necessary to take into account the coupling of the different physics, as well as the multiscale aspect of the problem. Additionally, in the interest of facilitating the use of such model in bioengineering applications, strong interactions between the modeling and experimental approaches should be maintained.

Objectives of the thesis

The aim of the project, is to gain insight in the driving mechanisms leading to cell proliferation and tissue production within a perfusion bioreactor. It has been experimentally observed that mass transport, as well as flow induced mechanical stimuli, have a critical importance in the development of *in vitro* bone substitutes. Yet the relative contribution of these phenomena on tissue growth remains to be assessed. To this purpose, the following objectives have been identified

- Establish a theoretical framework taking into account relevant biophysical parameters at different scales in order to model mass and momentum transport phenomena within a perfusion bioreactor.
- Investigate the effective transport properties for a wide range of culture conditions.
- Develop an experimental methodology able to quantify the time and space evolution of biological tissues within a porous medium.
- Propose a model capable of predicting bone substitute production in a perfusion bioreactor. This necessitates to identify and take into account the relevant phenomena influencing tissue growth.
- Approach experimental and theoretical representations, in order to improve the understanding of the coupling between transport processes and tissue formation within the bioreactor.

In an attempt to answer this challenges, the following approach is proposed. Given the hierarchical nature of biological systems, and the dependency of cell proliferation on its culture environment, a bioreactor experimental model is set up in order to isolate the main features of the original process. Next, a multiscale theoretical model for mass and momentum transport, is developed by multiple upscalings. This allows the computation of the effective transport properties of the bioreactor at different scales. Based on a rigorous theoretical framework, a cell/tissue growth model is then proposed, which parameters are shown to rely on experimentally relevant quantities at the cellular scale. Finally, the coupled resolution of this models at the macroscopic scale, allows the comparison with experimental results of cell growth in the bioreactor.

The present manuscript is organized as follows. A literature review on bioreactors for bone tissue engineering is presented in Part I. This covers the fundamentals of tissue engineering for bone substitutes, as well as the working principles of the most popular bioreactor designs.

After discussing the remaining challenges to translate bioreactor technologies to clinical applications, the main modeling approaches related to bioreactors are reviewed. Finally, it is shown that a multiscale framework combining transport processes and tissue growth is missing. In Part II, the derivation of such a model for mass and momentum transport is presented. Four scales are described (i) the bioreactor scale, (ii) the tissue scale, (iii) the cellular scale and (iv) the interstitial scale. Three successive upscaling steps are operated from scale (iv) to (i) using the volume averaging method. The closure problems at the interstitial and cellular scales are solved for the determination of the associated effective transport properties (permeability, diffusion/dispersion coefficient). The interscale interactions on these effective properties are highlighted. Part III is dedicated to the bioreactor scale (i). First an experimental study of the bioreactor is presented, in order to quantify cell and tissue production kinetic in space and time. Then the bioreactor scale transport properties are evaluated at scale (i), and a cell/tissue growth model is derived based on the theory developed in the second part. Finally a macroscopic resolution of the transport process, coupled with tissue growth is proposed. This work is concluded by a discussion on the comparison between the experimental and modeling results.

PART I

THE PERFUSION BIOREACTOR : FROM TISSUE ENGINEERING TO MULTISCALE MODELS

CHAPTER 1

BONE TISSUE ENGINEERING

AS DEFINED by Langer & Vacanti [1993], the discipline of *"tissue engineering, applies the principles of biology and engineering to the development of functional substitutes for damaged tissue"*. More precisely, this field aims to repair, replace or regenerate specific tissues or organs through the implementation of physical, chemical and biological sciences into materials, devices, systems and clinical strategies. In one of its fundamental approaches, tissue engineering associates cells with a porous scaffold which serves as the structure for three-dimensional tissue development, and which degrades or is resorbed at a defined rate. The cell-scaffold construct is cultured *in vitro*, in controlled conditions in order to support the nutrition of cells, and possibly provide stimuli (e.g. biochemical, biophysical) to direct and/or enhance cellular activity (e.g. proliferation, differentiation, production of biomolecules and extracellular matrix).

The development of bioreactors for tissue engineering has been motivated by the need to simplify, control and optimize culture conditions of the bioengineered constructs. The use and design principles of bioreactors for bone tissue engineering will be discussed in Chap. 2, but first it may be useful to recall the basic concepts of bone biology and tissue engineering.

1.1 Introduction to bone biology

Bones form a complex structure which serves as the mechanical support for the body, protection for vital organs, and attachment sites for the tendons and muscles. In addition to their mechanical role, bones are the place of production of a variety of indispensable cells for the organism. Bone marrow is housed in the head of long bones and in flat bones, and is responsible for the production of red blood cells (hematopoiesis) and lymphocytes. Stem cells are found in bone marrow, mainly in the form of mesenchymal stem cells (MSC) or bone marrow stromal cells (BMSC), and hematopoietic stem cells (HSC). Additionally, bone is the mineral reservoir of the organism and is implied in the regulation of the blood calcium level [Kneser et al., 2006].

Bone tissue is a special type of connective tissue. In its mature form, two types of bones

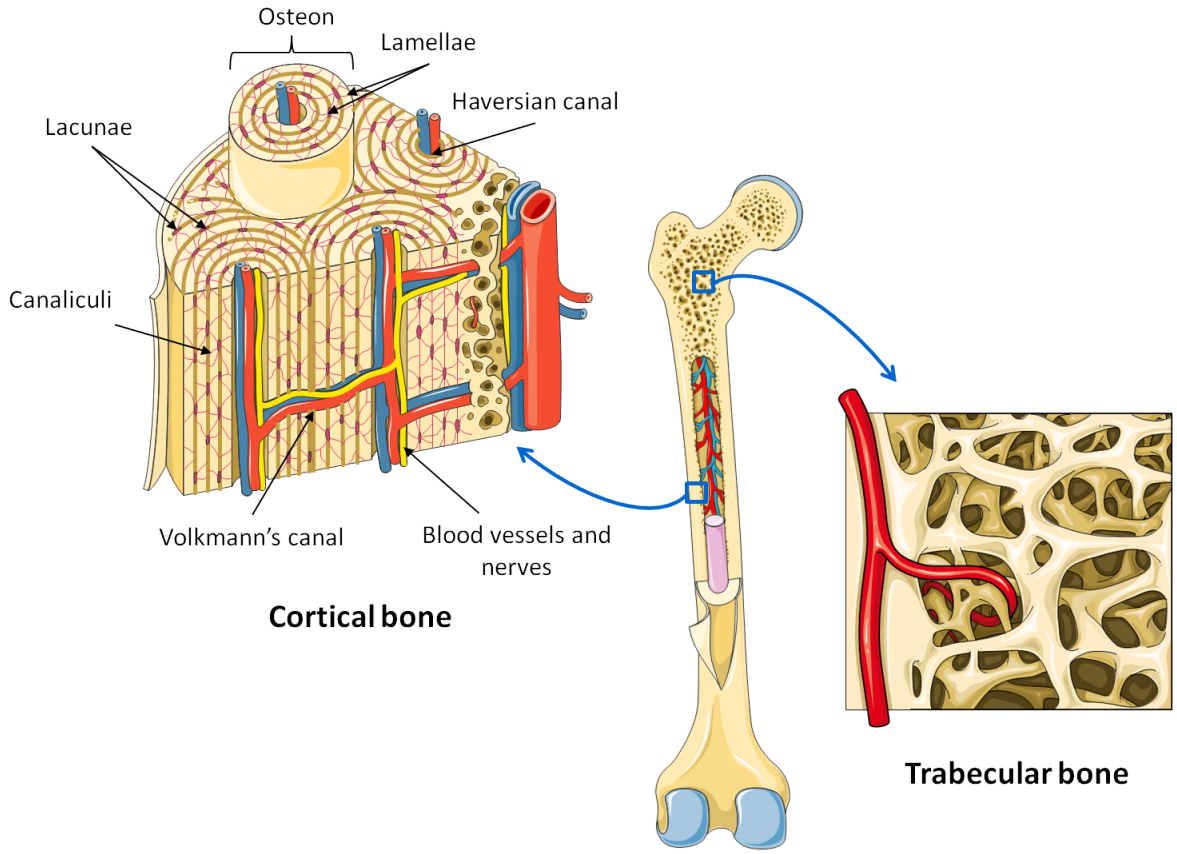

Figure 1.1 – Illustration of cortical and trabelcular bone structure[1]

exist : the cortical bone (also named compact bone), and the trabecular bone (also called cancellous or spongy bone). Although they differ greatly in their microstructure, functions and location, both are made of the same basic mineral (hydroxyapatite crystals) and organic (type I collagen, glycosaminoglycans, osteocalcin, osteonectin, bone sialoprotein) materials [Buckwalter et al., 1995a].

Cortical bone is the strongest part of the bone, having a porosity of less than 0.1 it supports most of the stress of the skeleton. It is located in the diaphysis (central part) of long bones and on the exterior part of short and flat bones. Its characteristic structure is the Harvesian system which is composed of concentric lamellae constituting osteons of around 200µm diameter (Fig. 1.1). The canals present at the center of the osteons are about 40µm diameter and allow blood vessels, nerves and lymphatic fluid to circulate within cortical bone. Lacunae are cavities which host osteocyte cells between the lamellae, and which are linked through a network of canals of 0.2µm diameter called canaliculi. The oriented structure of osteons makes cortical bone an highly anisotropic material [Cowin, 2001]. In contrast trabecular bone is isotropic, highly porous (up to 0.95), and has a "rod and plate" characteristic structure. The volume of the cavities houses the main part of the body's bone marrow where most of the bone metabolic functions happen. Trabecular bone is found at the epiphysis (extremity parts) of long bone and in the core of short bones.

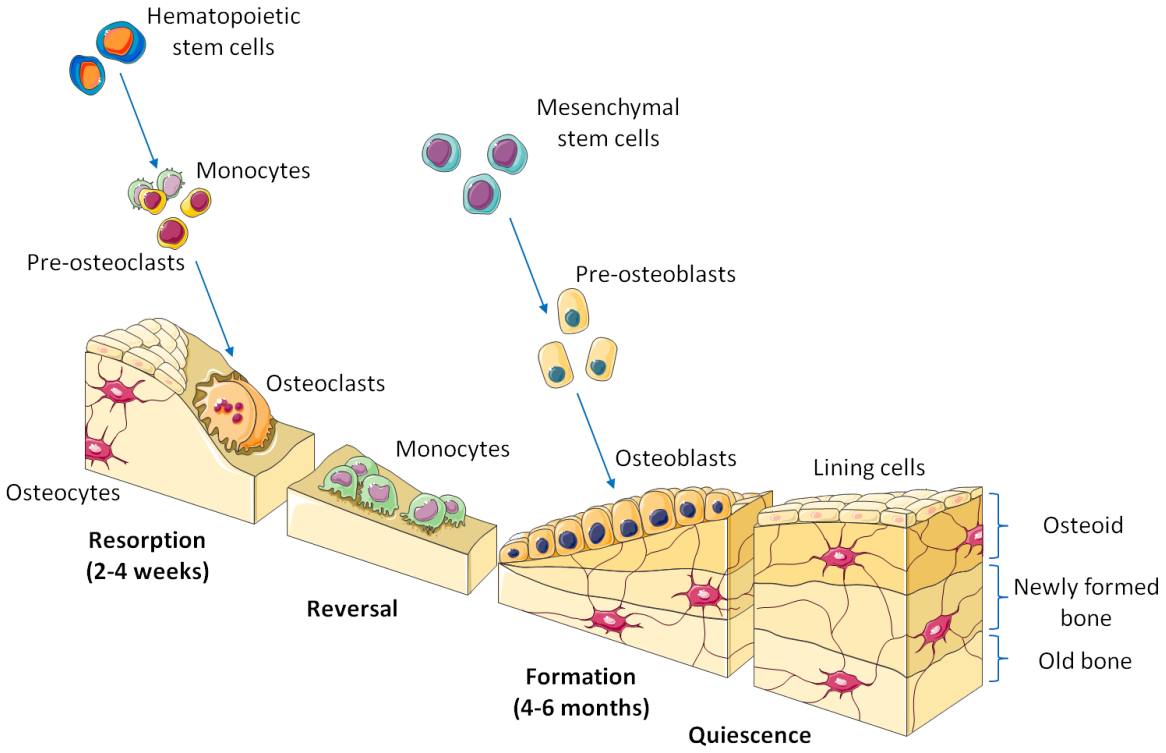

Figure 1.2 – Illustration of bone remodeling sequence supported by cellular activity[1]

Bone is a dynamic structure constantly developing, regenerating and remodeling. These processes are complexly regulated by a multitude of different growth and transcription factors which coordinate the interactions of cells and matrix in response to external or internal stimuli. Several types of cells can be found in bone tissue, but its functional integrity is ensured by mainly three cell types which play a well defined role in the remodeling process [Buckwalter et al., 1995b]. Osteoblast cells are responsible for bone matrix deposition, they produce alkaline phosphatase (ALP) which plays a role in bone mineralization. Osteoclast cells are in charge of bone resorption by producing H^+ ions and tartrate-resistant acid phosphatase (TRAP) which degrade hydroxilapatite and organic matrix respectively. Finaly, osteocytes are mechanosensible cells that regulate the remodeling process by interacting with osteoblasts and osteoclasts via extracellular signaling. Osteocalsts are mature osteoblasts that are embedded within the bone matrix in cavities called lacuanae. They communicate with each other thanks to gap junctions, made possible by a network of long cytoplasmic extensions going through the canaliculi. They also participate, although much less than osteoblasts, in the production of bone extracellular matrix.

This three cell types are very functional cells but have a relatively limited proliferative ability. In the scope of cell based therapies for bone reconstruction it may be useful to explore their origins, differentiation and maturation. Stem cells are responsible for the renewal of all tissue in the body during repair and remodeling. Biochemical and biophysical signals

[1] Illustration built from the free PowerPoint image bank Servier Medical Art http://smart.servier.fr/servier-medical-art

control their activation, proliferation, migration, differentiation and survival. Stem cells give rise to progenitor cells through asymmetric division, in which a mother stem cell divides into one daughter stem cell and one daughter progenitor cell [Muschler et al., 2004]. That way the overall population of stem cell is conserved while progenitor cells are destined to progressively differentiate into more functional cells. Mesenchymal stem cells (MSCs) have the ability to differentiate into divers connective tissues cells such as osteoblasts (bone), chondrocytes (cartilage), adipocytes (adipose tissue), myocytes (muscles) and even neurons. In the case of bone lineage, they first differentiate into pre-osteoblasts, which have good proliferative capabilities, before to progress into osteoblasts. Osteoblasts are responsible for the deposition of collagen extracellular matrix (ECM) during bone formation phase (Fig. 1.2). After about 40 days, osteoblasts have three possible fates : they may differentiate into ostocytes if they are trapped in the forming bone, they may mature in lining cells on the surface of mature bone, or they may die by apoptosis. Finally, osteocytes and lining cells may survive for more than 20 years in the cortical bone until a new remodeling cycle is initiated in the region they reside [Buckwalter et al., 1995a; Muschler et al., 2004]. Osteoclasts does not originate from MSC but from hematopoietic stem cells (HSC). This later cells are the origin of all blood cells and are located in the bone marrow. They indirectly differentiate into monocytes which, when in presence with osteoblasts and MSCs, can self-fusion to produce osteoclasts [Buckwalter et al., 1995a].

1.2 Bone tissue repair

When damaged, bone has a unique ability to heal and remodel without leaving any scar. The healing of a fracture is a natural physiological process that results in bone union. However 5 to 10% of fractures face difficulties to restore, resulting in delayed union or even non-union [Calori et al., 2011]. In these cases, clinical treatments may be needed in order to restore physiological functionality.

1.2.1 Natural healing and remodeling

The first reaction to bone fracture is an inflamatory response due to damaged blood vessels, leading to the formation of an hematoma. Many signaling molecules released during inflammation (e.g. FGFs, BMPs, PDGF) are also involved in new bone formation [Frohlich et al., 2008]. In the three first days MSCs are recruited and start proliferating and differentiating into pre-osteoblasts and osteoblasts. During the first week, surrounding soft tissues stabilize the fracture by formation of a callus, which will be transformed in cartilaginous tissue during chondrogenesis (Fig. 1.3). Additionally angiogenesis is initiated to provide blood supply in the damaged zone. After the second week cell proliferation decreases, but intense osteoblastic activity continues. The callus is mineralized then resorbed by chondroclast cells while osteoblasts form new woven bone, a disorganized bone characteristic of initial bone formation. Finally the mechanical continuity is restored by the remodeling process in which

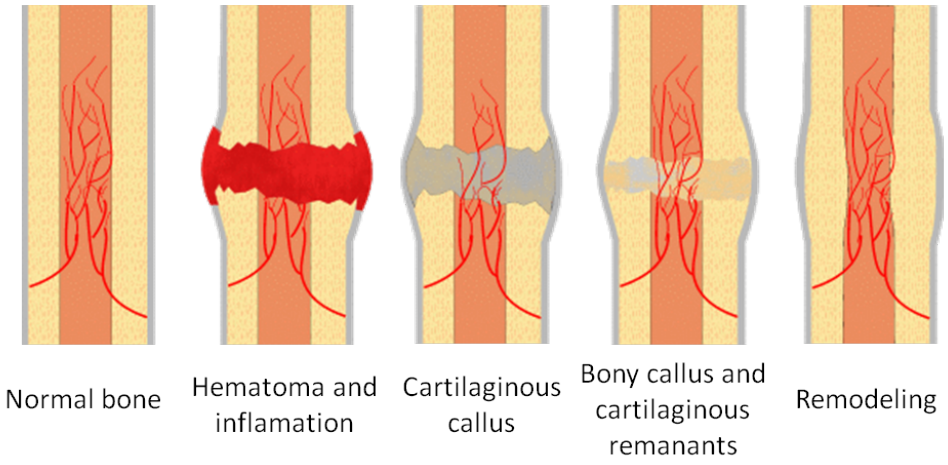

Figure 1.3 – Illustration of stages in bone healing after a fracture

osteocytes, ostoclasts and osteoblasts replace woven bone by lamellar bone [Dimitriou et al., 2005].

1.2.2 Current clinical treatments

In general, the excellent healing ability of bone, combined with external restoration of alignment and stable fixation, suffice for the reconstruction of most fracture [Frohlich et al., 2008]. However in certain clinical situations such as high energy traumatic events, large resections following a pathology (e.g. tumor, infection), or complex non-union defects, natural bone repair may be too slow or inadequate. For instance, in the case of long bones, critical defects are considered for a length of bone loss of 3cm in the forearm, 5cm in the femur and tibia, and 6cm in the humerus [Calori et al., 2011]. In these challenging orthopedic cases, some form of grafting is required.

The functions of a bone graft are to fill the space of the defect, provide support, and enhance biological repair. The biological properties of a bone graft are often discussed in terms of osteoinductivity (ability to promote bone formation), osteoconductivity (ability to promote vascularization and cell colonization within the graft), and osetogeniticity (ability to host bone-forming cells within the bone graft) [Giannoudis et al., 2005].

Nowadays, the best graft material is autologous bone graft. The technique consists in harvesting trabecular bone from a healthy site of the patient (usually the iliac crest in the pelvic girdle), and implant it directly in the bone defect. This procedure is widely applied, and the reported successful healing rate is 60 to 100% [Calori et al., 2011]. Autologous bone graft is safe, cheap, available to every surgeon, and present the three desirable properties of a graft material : osteoinductivity , osteoconductivity and osteogeniticity. Nevertheless autologous grafting has significant disadvantages. First the harvesting operation is often associated with complications such as bleeding, hematoma, infections and prolonged pain. Second, the donor site morbidity increases with the amount of harvested bone, and in the case of large or multiple reconstructions, the volume of bone material available is insufficient [Kneser et al., 2006].

Finally, the cost of the additional intervention may be equivalent to the cost of commercially available bone substitutes [Calori et al., 2011].

Allogenic (from a human donor) and xenogenic (from an animal donor) bone grafts are the main alternatives to autologous graft. They present the advantage of avoiding the harvesting of bone on the patient and all its possible complications, risks and costs. These grafts have ideal osteoconductivity and biomechanical properties, and are relatively easy to obtain through tissue banks [Kneser et al., 2006]. To avoid immune response, freezing and irradiation processes are applied to eliminate the cellular phase of the graft. Even though the osteoconductivity is conserved, the process dramatically weaken the osteoinductive capabilities of the graft. Moreover risks of viral and bacterial transmission remain [Giannoudis et al., 2005]. Allografts and xenografts are donor and process dependent, yielding to variable clinical results. The lack of osteogenesis delays osteointegration and vascularization, which in large grafts may lead to remaining non-vital regions [Frohlich et al., 2008].

Several other types of material are used for the reconstruction of bone defects. The main material families are biomaterial (e.g. demineralized bone matrix, collagen), ceramic (e.g. calcium phosphate and apatite based cements), bioactive glasse (e.g. silicon-based cements), and non-biologic (e.g. polymers, metals) substrates [Giannoudis et al., 2005; Calori et al., 2011]. Nevertheless, most of these substitutes are only osteoconductive, there mechanical support can be weak, and present mixed clinical results [Giannoudis et al., 2005]. While the osteoconductivity of a biomaterial is directed by its composition, surface physicochemical properties and internal structure, osteoinductivity can be provided with the aid of osteoinducitve substances (e.g. transforming growth factor (TGF-β), insuline-like growth factor (IGF I and II), platelet derived growth factor (PDGF), fibroblast growth factor (FGF), various bone morphogenic proteins (BMPs)) [Janicki & Schmidmaier, 2011]. The use of growth factors in combination with the above filling materials has been tested clinically, but still few studies have yet been reported, and the applications protocols are not yet standardized [Kneser et al., 2006].

Further osteogenicity can be improved with the introduction of osteocompetent cells within the filling material. This is the aim of bone tissue engineering, and the specificities of this field are discussed in the next section.

1.3 Tissue engineering

Tissue engineering is an interdisciplinary field which aims to repair damaged tissues or to restore a defect by combining *in vitro* biomaterials, cells and/or signaling molecules. If cells are used, expansion and tissue specific cell differentiation may request an *in vitro* culture period ranging from a couple of days to several months. The obtained constructs must be developed in parallel with well elaborated surgical concepts in order to lead to successful *in vivo* applications [Kneser et al., 2006]. In this section, the main components for the development of bone substitutes, in the frame of tissue engineering, are reviewed.

1.3.1 Scaffold design

Three-dimensional porous scaffolds play an important role in tissue engineering strategies. During *in vitro* culture, it serves as a support for cells attachment, migration, proliferation and differentiation and may be a provider of osteoinductive substances. Upon transplantation it is the vehicle for delivery of cells to the defect site. The porous structure lets void for tissue ingrowth and vascularization while maintaining mechanical integrity [Muschler et al., 2004]. The scaffold must be made from biocompatible material, and should biodegrade and bioresorb at a controlled rate, following new tissue formation. The development of scaffolds for tissue engineering is an intense and prolific research field, and several possibilities are already available for clinical use. In this section, the variety of existing scaffolds is discussed along the following main characteristics : the bulk material composition, the geometrical architecture, the mechanical properties, the surface chemistry and the *in vivo* degradation properties.

The *bulk materials* used in bone tissue engineering are inherited from orthopedic clinical practices. It includes biological-derived material (e.g. processed allograft, coral), biological polymers (e.g. collagen, chitin), ceramics or mineral-based material (e.g. tricalcium phosphate (TCP), hydroxyapatite (HA), calcium phosphate), metals (e.g. titanium, tantalum) and synthetic biodegradable polymers (e.g. polyglycolide (PGA), polylactides (PLLA, PDLA), polycaprolactone (PCL)) [Hutmacher, 2000; Muschler et al., 2004]. Composite scaffolds made of two or more of the above cited material are also in use.

The three-dimensional *porous architecture* of the scaffold is critical since it influences mechanical properties, cellular fate, nutrient supply, vascularization and tissue ingrowth. The pore size is usually in the range of 100 - 500µm. Even though the ideal size has been estimated around 350µm [Murphy et al., 2010], it is believed that larger pore sizes support deeper cell proliferation and tissue penetration [Muschler et al., 2004]. Concerning the pore structure, the geometry can be dictated by the fabrication process (for instance in the case of biological based scaffold), or arbitrary chosen when the synthesis method allows it (Fig. 1.4). Most of these scaffolds are homogeneous porous media with isotropic transport properties. Considering the recent advances in fabrication techniques (e.g. 3D-printing, stereolithography), it may be possible to produce controlled scaffolds with hierarchical microstructures and oriented channels to guide the patterns of cell migration, fluid flow and diffusion through the construct [Hutmacher, 2000; Khademhosseini et al., 2006; Sprio et al., 2011]. Finally the nanostructural architecture of the scaffold should be considered since the substrate rigidity and rugosity is known to influence cell adhesion, differentiation and migration [Engler et al., 2006; Yoon et al., 2012].

The required *mechanical properties* of the scaffold depends on the graft site physiological load and bone property. For instance, defects on load-bearing long bones require the restoration of high mechanical stability, while the mechanical loads involved in craniofacial reconstructions does not necessitate such mechanical performances [Kneser et al., 2006]. On the other hand, the use of rigid non-degradable material such as metals, protects adjacent tissue from mechanical loads, resulting in a change of the stress environment that may lead to a loss of local tissue mechanical properties. Cortical bone has a Young's modulus of 15-20GPa

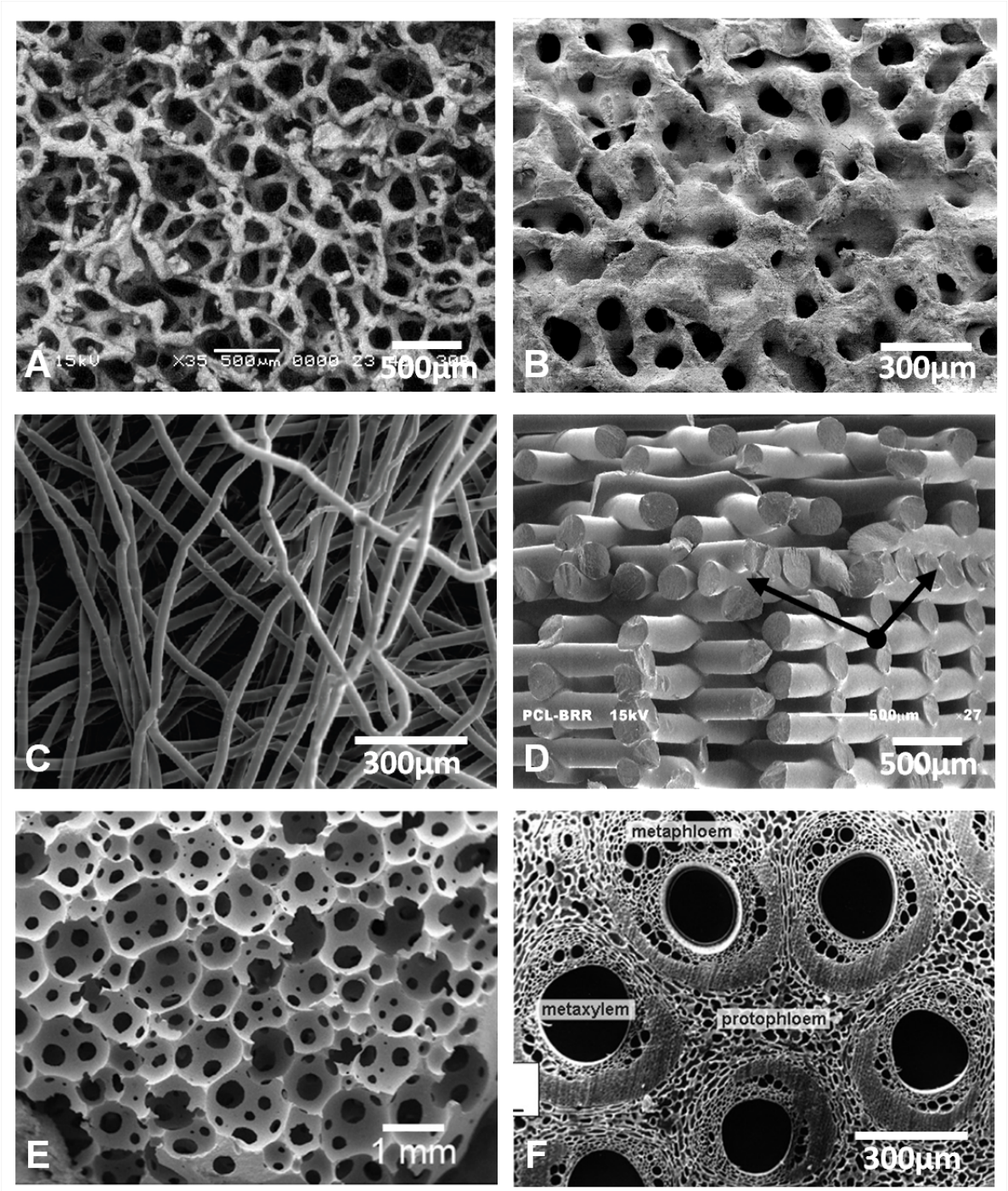

Figure 1.4 – Scanning electron microscope (SEM) images of various scaffold structures used in bone tissue engineering. (A) Partial deproteinized bone [Wu et al., 2010]. (B) Natural coral (*porites*) [David et al., 2014]. (C) Nonwoven PLLA fiber mesh [VanGordon et al., 2010]. (D) Polymer fiber mesh (PCL) built by fused deposition modeling (FDM) [Hutmacher, 2000]. (E) Hydroxyapatite scaffold obtained by foaming method [Sprio et al., 2011]. (F) Wood-derived ceramic structure [Sprio et al., 2011]

and a compressive strength of 100-200MPa, while trabecular bone has a Young's modulus of 0.1-2GPa and a compressive strength of 2-20MPa [Cowin, 2001]. A summary of scaffolds mechanical properties of different materials and architectures can be found in [Bose et al., 2012]. The scaffold should present similar mechanical properties to the local bone, therefor ceramic based scaffolds are appropriate to replace cortical bone, while polymers may be better suited for trabecular bone. Another key factor related to mechanical properties of the scaffold is the decrease in mechanical support during *in vivo* resorption. In order to avoid mechanical failure of the implant (fracture), the degradation rate of the scaffold material must match the regeneration rate of the the replacing bone [Hutmacher, 2000]. Finally, the mechanical stimuli playing an important role in the differentiation of bone marrow stem cells, the scaffold should transmit an appropriate stress environment within the graft site [Pioletti, 2013].

The *surface chemistry* of the scaffold directs its interactions with cells. Surface properties are influenced by the bulk material, but are mainly dependent on the adsorbed proteins and lipids. These biomolecules that come from coating solutions, culture medium, biological fluids and/or cell metabolism, cover the surface of the scaffold and are the primary mediator of cellular response to the material [Muschler et al., 2004]. This can be put to profit to direct cell attachment, survival, proliferation and differentiation by precoating the scaffold with bioactive proteins such as fibronectin or various growth factors [Bose et al., 2012].

Finally, the *degradation properties* of the scaffold must be considered with care. First the resorption rate should be control to match tissue formation and mechanical load transfer from the biodegrading scaffold to the tissue. Typical degradation times range from 3 to 12 month depending on the application [Bose et al., 2012]. Second, degradable materials release degradation products within the implantation site. This products, when released too quickly, may influence local pH and and reach toxic concentrations, leading to inflammatory reactions. The control of the pH environment during scaffold resorption can be addressed by the use of composite material. Indeed, synthetic polymer materials (PGA, PDLA, PLLA) release acidic by-products, while ceramic materials (TCP, HA) produce basic resorption products. Therefore a adequate combination of the two types of material could avoid the production of unfavorable environment for the cells [Hutmacher, 2000].

1.3.2 Cell choice

Tissue engineering strategies combine three-dimensional scaffolds with cells, in order to build a functional tissue and/or to recruit and attract other cell types toward the construct. The ideal cells should be easily isolated and expended, have stable phenotype of interest and show long term safety.

In the aim of producing bone substitutes, the cell type must present an osteogenic phenotype, which include mesenchymal stem cells (MSCs) (Fig. 1.5), bone marrow stromal cells (BMSCs), periosteal cells and osteoblasts [Kneser et al., 2006]. MSCs are particularly promising since they have the ability to differentiate into osteoprogenitors and mature osteoblasts, they are easily isolated, expanded, and show a stable phenotype up to 50 population doubling [Frohlich et al., 2008]. Several autologous sources of MSCs are known (e.g. cartilage, fat), but

bone marrow aspirates provide the higher density of stem cells, are relatively safe, and easy to proceed [Muschler et al., 2004; Colnot, 2011]. Nevertheless the number of cells and the quality of the aspirate are patient dependent, with an observed decrease in MSC concentration with age, motivating *in vitro* cellular expansion before seeding or transplantation.

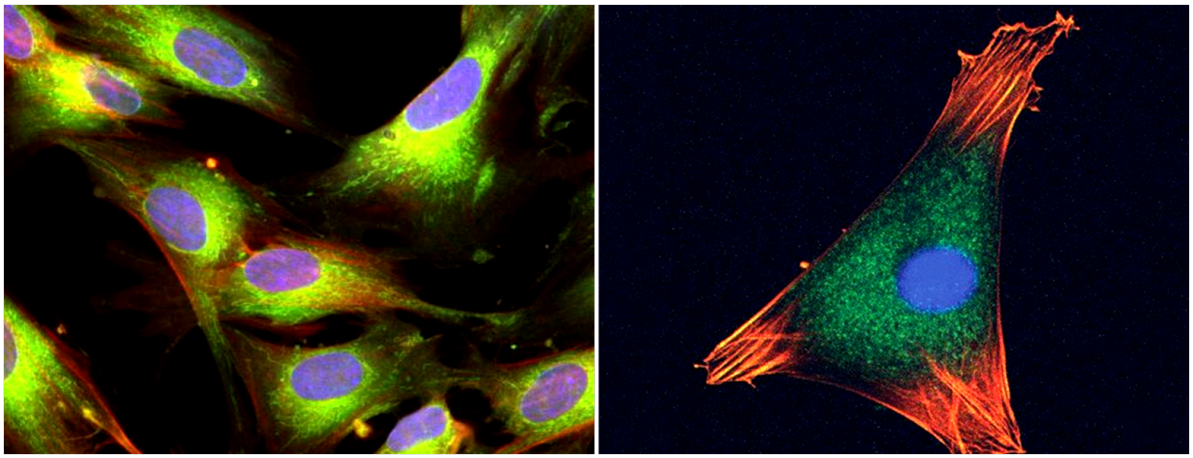

Figure 1.5 – Mesenchymal stem cells stained with fluorescent dyes[2]. Nucleus are in blue, microtubules in green, and actin filaments in red.

During early stages of scaffold and device testing, the use of human or animal immortalized cell lines are a reasonable choice (e.g. murine osteoblasts MC3T3-E1 [Cartmell et al., 2003], murine mesenchymal cells C3H10T1/2 [David et al., 2011], human osteoblast-like cells MG63 [Olivier et al., 2007]). These are populations of cells issued from a multicellular organism, which have lost their natural senescence due to mutation or human intervention. Therefore they can be grown *in vitro* for prolonged periods. From a practical research point of view, they present the advantages of being easily available and easy to maintain in any basic cell culture facilities. However, as soon as the proof of concept has been established for a given process, more clinical oriented cells must be selected.

1.3.3 *In vitro* culture conditions

Once the scaffold and the cell type are selected, the appropriate culture conditions have to be maintain to optimize cell proliferation, differentiation into the appropriate lineage, migration and matrix deposition.

The importance of the seeding method must not be underestimated if an homogeneous initial distribution of cells is intended (Fig. 1.6). When the scaffold is introduced in cell suspension and let to rest, sedimentation process drives the cells to the surface. This means that regions with higher ratio of suspension volume to scaffold surface will have a high cell density once attached on the wall. This occurs particularly for heterogeneous porous scaffolds

[2]Left : https://globalmedicaldiscovery.com/wp-content/uploads/2014/04/Human-mesenchymal-stem-cell.jpg Right : http://news.softpedia.com/news/New-Technique-for-Tracking-Stem-Cells-Developed-405076.shtml

(including scaffolds made of multiple porous granules), and on the edge of the scaffolds, close to the bulk cell suspension. It results in an initial heterogenous distribution of the cells within the scaffold, with more cells on the surrounding of the scaffold than in its center. To overcome this issue, multistep seeding [Grayson et al., 2008] or dynamic seeding methods [Vunjak-Novakovic et al., 1998] have been proposed.

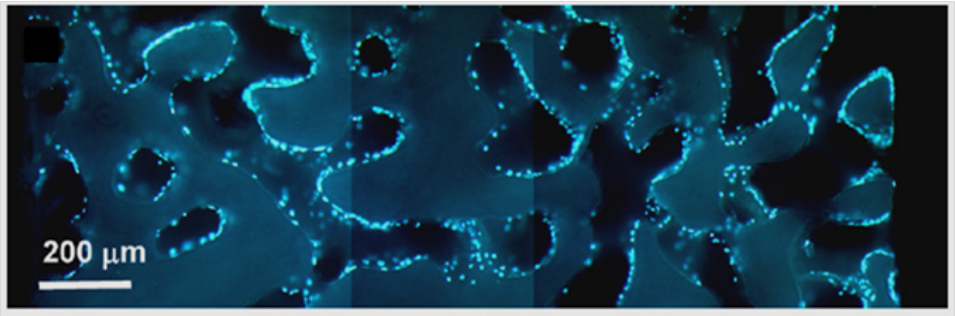

Figure 1.6 – Fluorescent microscope pictures of 20µm sections of coral scaffolds seeded with Hoechst stained human MSC (adapted from [Mygind et al., 2007])

Once the cells seeded and attached to the scaffold, the construct is usually maintained *in vitro* in a bath of culture medium within an incubator. It has been shown that the first days/weeks after seeding, cellular adherence, growth and differentiation is dominated by surface phenomena due to cell/material interactions [Kommareddy et al., 2010]. Then in a second time, cells produce extracellular matrix (ECM) which allows them to grow three-dimensional. From that point, the pore geometry of the scaffold becomes important since it is shared between forming tissue and culture medium.

When the culture medium is at rest, the culture is said to be in *static* conditions, as opposed to *dynamic* culture conditions. The role of culture medium is to provide the necessary nutrient and oxygen levels to support cellular activity. It can be supplemented with osteoinductive substances to promote cell differentiation, division and matrix deposition. In static culture conditions, diffusion is the only transport process, and the cell consumption may induce large concentration gradients leading to regions with nutrient and/or oxygen depletion. This mass transport limitation occurs especially at the core of large constructs, and at high cell density where there is competition for resources [Malda et al., 2004]. Cells in these regions may enter in a quiescent state or in necrosis due to lack of nutrients or hypoxic (lack of oxygen) conditions. Nevertheless, it has been suggested that MSCs can survive for long periods (up to 12 days) in sever hypoxia as long as glucose is available [Deschepper et al., 2011], and that hypoxic conditions may be a stimulus for cell differentiation or migration toward a more favorable environment [Muschler et al., 2004].

Mass transport limitations together with the need to produce more easily larger and cheaper bone substitutes have motivated the development of bioreactors for bone tissue engineering. The next chapter is dedicated to this subject, with a focus on bioreactors using hydrodynamic environments.

CHAPTER 2

BIOREACTORS FOR BONE TISSUE ENGINEERING

AS DISCUSSED in the previous chapter, tissue engineering sets the ground principles of cellular based therapy for the reconstruction of tissues and organs. Nevertheless most of this processes are not yet ready to be used in practical applications because of insufficient substitute quality and reproducibility, high production time and cost, and difficulties to implement in clinical applications [Salter et al., 2012]. By adopting an approach based on process engineering, bioreactors systems are a promising tool to address this issues. In the present chapter, the different principles of bioreactors for bone tissue engineering are examined, and the prerequisites for translation to clinical applications are reviewed. Finally the double porosity bioreactor developed in [David et al., 2011] is detailed.

Bioreactors are generally used to facilitate, monitor and control biological, biochemical and biophysical processes. The parameters influencing cell growth within a bioreactor include temperature, pH, concentration in nutrient, growth factors and oxygen, and biophysical stimuli. These systems are usually constituted of biologically inert and non-corrosive material to avoid cytotoxic responses. Furthermore the components must be able to support sterilization techniques, and the bioreactor should be convenient to be manipulated in aseptic conditions.

Bioreactor systems must efficiently provide nutrients, oxygen and biophysical stimuli in order to optimize cell proliferation, differentiation and matrix deposition. Possibilities to enhance mass transport are culture medium flow, integration of membranes or hollow fibers within the scaffold, or pre-vascularization. In the case of bone forming cells, the relevant biophysical stimuli are mechanical solicitations (hydrodynamic shear stress, mechanical strain) and electromagnetic fields. Each design of bioreactor for bone substitute presented bellow applies one or more of this solutions to produce bone substitutes.

2.1 Bioreactors using hydrodynamic stimuli

The principle behind the application of hydrodynamic culture conditions is to make use of culture medium flow to address mass transport limitations and to apply mechanical stimuli to the cells.

In vitro constructs are usually not vascularised, and in that case, culture medium is the only source of oxygen and nutrients. Thus diffusion from the exterior of the construct to its core is the main process responsible for species supply of the inner cells. Simple calculations can show that cells at more than 500-1000 µm in the depth of the construct can be very quickly in hypoxic conditions (lack of oxygen) [Muschler et al., 2004], which could lead to necrosis at the center of the construct. Moreover static culture conditions lead to inhomogeneous concentrations fields due to local consumption of nutrients in zones of higher cell density. These limitations can be partially solved by the use of hydrodynamic conditions where convective effects enhance mass transport around and within the construct.

In addition to improve mass transport, hydrodynamic culture conditions are a means to stimulate mechanically the cells. Particularly, bone cells have been shown to be more sensitive to mechanical strain than other cell types [Meyer et al., 1999]. In everyday life, *in vivo* mechanical stress stimulates osteocyte and osteoblast cells present in bones, and is thus a key factor in the control of bone remodeling [Cowin, 2007]. Similarly, in a hydrodynamic bioreactor, fluid flow induced mechanical stimuli influence cell differentiation and proliferation [Glowacki et al., 1998; Bancroft et al., 2002; Cartmell et al., 2003; Raimondi et al., 2006; Grayson et al., 2010; McCoy & O'Brien, 2010]. In bone tissue engineering studies, the mechanical parameter of interest is the fluid flow induced *shear stress* [Hung et al., 1995; Goldstein et al., 2001; Sikavitsas et al., 2003; Raimondi et al., 2006; Leclerc et al., 2006; Pedersen et al., 2007, 2010; Jungreuthmayer et al., 2009a; Park et al., 2010; McCoy & O'Brien, 2010; Grayson et al., 2011]. To be more precise, the main known effects of fluid flow influencing cell fate, are the deformation of cytoskeleton [Horikawa et al., 2000; McGarry et al., 2004; Kwon & Jacobs, 2007], the activation of stretch-sensitive ion channels in the membrane [Jacobs et al., 2010], and the stimulation of primary cilia [Hoey et al., 2012; Delaine-Smith et al., 2014]. These solicitations induce complex chains of biophysical and biochemical processes, called mechanotransduction, that lead to cell response [Ingber, 2006]. Since all of these solicitations are considered to be the effect of shear stress, which has the advantage to be easily computed and quantified, the fluid flow mechanical stimuli are assumed to be limited to this stress.

Parameters influencing spacial distribution and intensity of local shear stress within a three-dimensional scaffold are, the bioreactor and scaffold geometries (which include the scaffold porosity, isotropy, pore size and interconnectivity) as well as the fluid flow rate and physical properties. The distribution of the shear stress on the scaffold walls are extremely hard to determine experimentally, however different fluid mechanics models have been successfully developed to address this question (see Sec. 3.1). Concerning the intensity of the shear stress, the values found in the literature vary greatly from a study to another, depending on the cell line, the support material or whether the cells are grown in two or three dimensions

[Jungreuthmayer et al., 2009b; McCoy & O'Brien, 2010]. For three-dimensional cell cultures, it is observed that a first range of shear stress values yields to an enhanced cell proliferation. Then for increasing values of shear stress, cell division slows down while differentiation and production of extracellular matrix are improved. Finally for very high values, shear stress is damageable for the cell survival and attachment, and fluid flow may wash them off the scaffold [Cartmell et al., 2003; Mygind et al., 2007].

Several bioreactor designs make use of hydrodynamic culture environments to improve cell proliferation, differenciation and matrix deposition [Rauh et al., 2011]. The types of system reviewed below are the spinner flask bioreactor [Vunjak-Novakovic et al., 1998], the rotating wall bioreactor [Freed & Vunjak-Novakovic, 1995], and the perfusion bioreactor [Mueller et al., 1999].

2.1.1 Spinner flask bioreactors

The simplest and cheapest way to provide hydrodynamic stimuli to a biohybrid, is to suspend the seeded scaffold in a flask filled with culture medium, and to agitate the liquid using a magnetic bar. The bioreactors based on that principle are called spinner flask bioreactors (Fig. 2.1). The system is placed in an incubator which maintains adequate temperature, humidity and CO_2 content. Apertures with filters are present at the top of the flask to allow gas exchange between the bioreactor and the incubator without risks of contamination. The level of applied shear stress is dependent of the stirring speed, which has typical values of 30 to 50rpm for flasks of 120mL [Rauh et al., 2011].

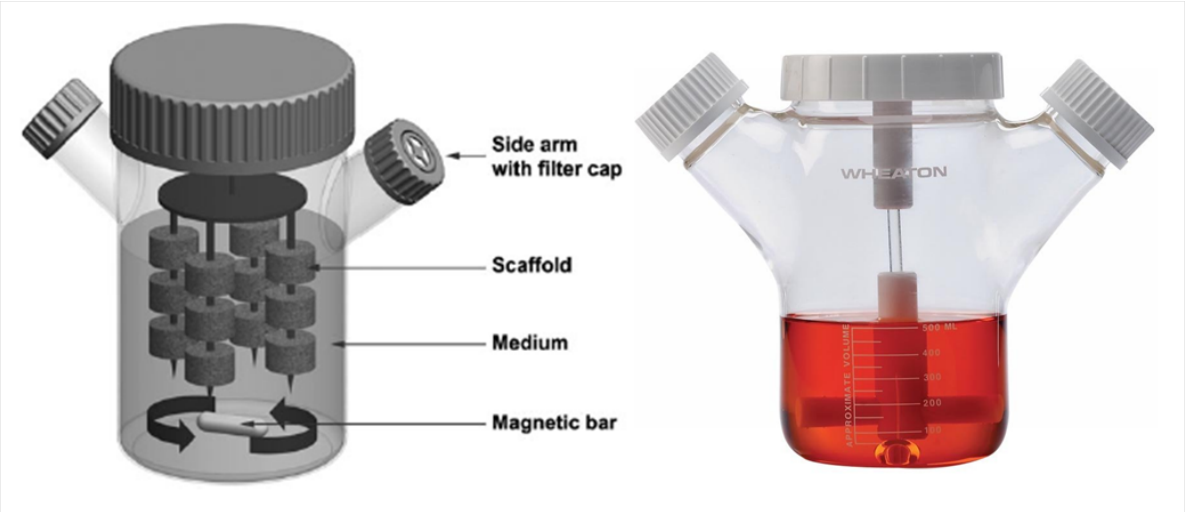

Figure 2.1 – The spinner flask bioreactor. Left : Schematic representation [Rauh et al., 2011]. Right : Wheaton Celstir® spinner flask

Cultures in spinner flask bioreactors lead to very good results in term of cell proliferation and production of osteogenic markers, compared to static conditions [Sikavitsas et al., 2002; Mygind et al., 2007]. Using coral scaffold of mean pore size of 200µm and 500µm, Mygind et al. [2007] obtain a better proliferation, differenciation and homogeneity of human MSC in

a spinner flask bioreactor than in static culture. Moreover the 200µm pore constructs showed better osteogenic differentiation than the 500µm pore constructs, while this later had a higher number of cell indicating a better proliferation. This results suggest that lower shear stress (in larger pore size) enhance cell division, while higher shear stress (in smaller pores) stimulates cell differentiation.

Despite its inexpensiveness and good results, the spinner flask bioreactors present several disadvantages. The most important drawback is the complex hydrodynamics in the flask making difficult the precise evaluation of applied levels of shear stress. Moreover the velocity field is inhomogeneous within the bioreactor, leading to stimuli dependent on the location of the construct, and bad repeatability between experiments [Goldstein et al., 2001].

2.1.2 Rotating wall bioreactors

Rotating wall bioreactors have been initially design by the National Aeronautics and Space Administration (NASA) to study cellular growth in micro-gravity environment. It is composed of a horizontal cylindrical vessel, put in rotation along its axis my an external motor. The closed bioreactor contains culture medium and constructs in suspension. Rotation of the vessel induces laminar flow by inertial effects (Fig. 2.2). Although mass transport limitations are solved by the culture medium flow, it seems that the level of shear stress remains very low, probably because the constructs follow the movement of the fluid. The results of cell culture in rotating wall bioreactors in the frame of bone tissue engineering are controversial. While some authors find improved cell proliferation and osteogenic markers productions [Botchwey et al., 2001; Song et al., 2008], other observe a decrease in cell survival compared to static conditions [Goldstein et al., 2001; Sikavitsas et al., 2002].

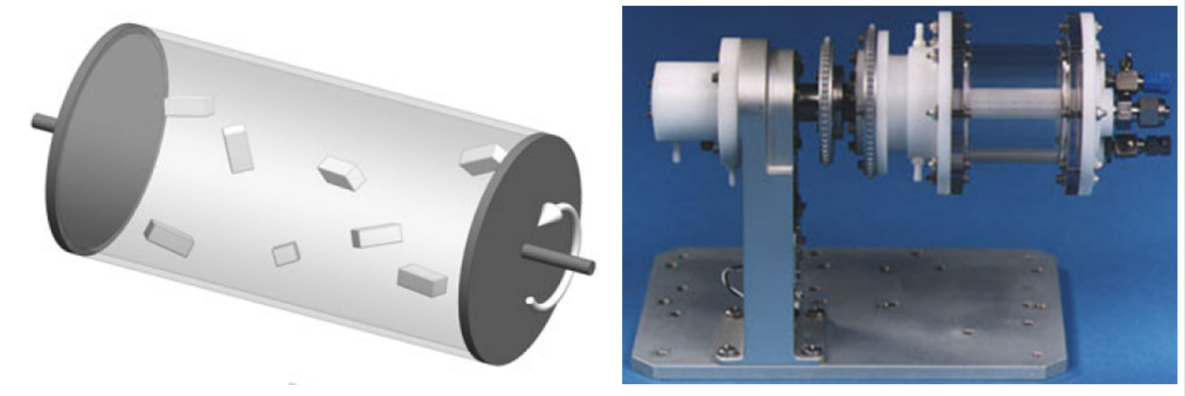

Figure 2.2 – The rotating wall bioreactor. Left : Schematic representation [Rauh et al., 2011]. Right : One of the first rotating wall bioreactor prototype developed by the NASA[1]

The divergence in the results obtained with rotating wall bioreactors can partly be explained by the weaknesses of the system. To start with, the material density of the scaffold

[1] http://science.nasa.gov/science-news/science-at-nasa/1999/msad05oct99_1/

and its size play an important role in the way the construct will be moved by the fluid. If the density of the scaffold is close to the density of the culture medium, the construct will stay in suspension, limiting collisions with the walls or other constructs. But if the density is different from the culture medium, the construct may have turbulent movements within the vessel, increasing risks of damages by collisions. Some modifications to the bioreactor have been proposed to address this issue, by fixing the construct to the walls of the vessel [Song et al., 2008]. This has the advantage of keeping the biohybrid in the peripheric zone of the vessel, where the main hydrodynamic effects take place. Yet, rotating wall bioreactors have limited volume of production, and the heterogeneous levels of shear stress applied to the biohybrides remain a clear restriction to its use in laboratory.

2.1.3 Perfusion bioreactors

The limitations of the previously presented bioreactors motivated the development of perfusion bioreactors [Yeatts & Fisher, 2011]. This design takes advantage of laminar flow to enhance mass transport and distribute shear stress in the whole construct. The perfusion systems are usually constituted of a chamber in which one or more seeded scaffolds are placed, and through which the culture medium is perfused with the help of pump and tubing systems. Two main categories of perfusion bioreactors are met, direct perfusion systems force the culture medium through the construct, while indirect perfusion systems allow the culture medium to flow around the construct (Fig. 2.3).

In indirect perfusion bioreactors, the culture medium can follow the path of less resistance around the construct, inducing less flow in the core than on the surrounding of the scaffold [Janssen et al., 2006; David et al., 2011]. Shear stress is thus mainly located at the periphery of the biohybrid, and the benefits of the perfusion on mass transport may be limited at the center. This may result in preferential cell proliferation at the surrounding of the scaffold, and hypoxic and starving conditions at the core, leading to necrosis. In contrast, direct perfusion bioreactors enhance mass transport and shear stress distribution within the construct [Bancroft et al., 2002; Cartmell et al., 2003; Grayson et al., 2008, 2011]. Nevertheless it necessitates the use of sufficiently permeable scaffolds in order to limit too high local stresses which could harm the cells. Moreover at long culture times, cell proliferation decrease the porosity of the construct, intensifying the level of shear stress which could lead to a maximal state of tissue growth, or even detachment of cell aggregates.

The design of perfusion bioreactors varies widely from a team to another. The culture medium can either flow in a closed loop or go from a reservoir to a waste flask. Perfusion modes can be oscillatory, pulsed or continuous [Jaasma & O'Brien, 2008; Wu et al., 2010]. Additional equipments can be adapted to mechanically stimulate the construct [El Haj et al., 1990], monitor the mineralization, or measure the concentration of species of interest (oxygen, osteogenic markers...) [Janssen et al., 2006]. Typical continuous flow rates range from 1 to 600mL/h, and the volume of the produced constructs are usually of few milliliters. Yet the transfer to clinic applications requires volumes up to 300mL of bone substitutes.

One proposed strategy to increase the produced volume is to use larger scaffolds [Olivier

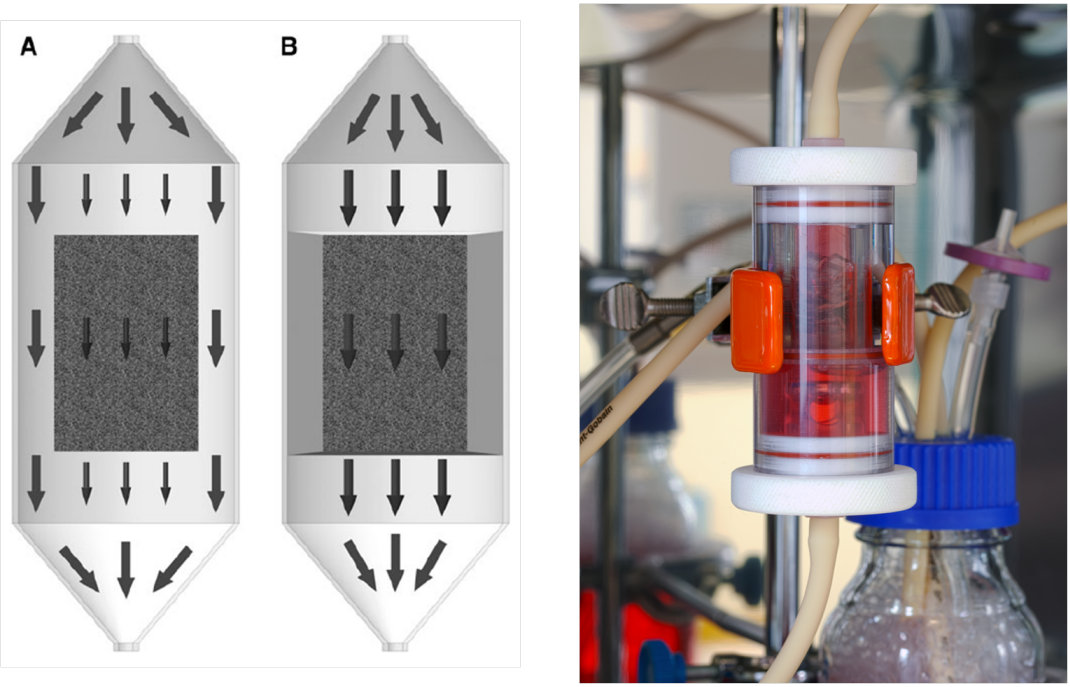

Figure 2.3 – The perfusion bioreactor. Left : Schematic representation of (A) indirect perfusion, (B) direct perfusion [Rauh et al., 2011]. Right : Photography of a perfusion bioreactor prototype used in our team.

et al., 2007], but this often leads to higher heterogeneities in cell proliferation. An alternative strategy is to multiply the number of millimeter size scaffolds in the chamber [Janssen et al., 2006; David et al., 2011]. The resulting construct shows a very good cellular proliferation and differentiation, and the scaffolds are covered with interconnected and dense layer of extracellular matrix. However the core of the individual scaffolds still present a lack of proliferative cells, probably due to mass transport limitations. Although, these studies succeed in increasing the volume of the final construct of a factor 10, another factor 10 is needed in order to face all clinical needs.

2.2 Bioreactors based on other principles

Bioreactors using hydrodynamic stimuli are the most widely used systems in bone tissue engineering, mainly because it deals with mechanical stimuli as well as mass transport limitations. However other types of designs based on different physical and biological principles have been proposed.

Several other possibilities than hydrodynamic culture exist to provide mechanical stimuli. An intuitive and more biomimetic approach is to strain the scaffold so that the stress is transmitted to the attached cells. Machines originally fabricated for material testing have been adapted to apply compression [El Haj et al., 1990; Wartella & Wayne, 2009; Baas et al., 2010] or bending [Mauney et al., 2004] strain to the construct. These result in an increase

of ostegenic markers and matrix deposition compared to unloaded samples. Alternatively, cell stretching systems have been developed to study the effect of tensile strain on bone cells. Cells are embedded in a collagen matrix, which is fixed on a silicon dish. This silicon support is cyclically stretched uniaxially or biaxially using piloted motors [Neidlinger-Wilke et al., 1994; Ignatius et al., 2005]. Stretching stimulus seems to mainly increase bone cell proliferation. Interestingly cells where found to be oriented along the axis of the applied mechanical stress. Nevertheless, severe drawbacks exist for these direct mechanical stress systems. Indeed, any force producing mechanism that invades the bioreactor (piston, silicon sheet...) are a possible cause of infection. Additionally the scaffold material must transmit the force to the cells, and this implies that they must be strong enough in compression or bending systems, and soft enough in silicon stretching systems. This constraints may lead to incompatibilities with the prerequisites for biodegradation times of the scaffolds [El Haj & Cartmell, 2010]. Finally mass transport limitations are present in this types of bioreactors, and they may have to be coupled with perfusion systems [Bölgen et al., 2008].

Electromagnetic fields have been used in clinical studies to treat various bone pathologies [Aaron et al., 2006]. The underlying idea is that *in vivo* mechanical deformations in bones cause piezoelectricity, generating electric potentials. Vibration and movement of human muscles induce mechanical strains and currents of specific frequencies to which bone cells are sensitive. Bioreactor systems based on this principle use magnetic coils to generate pulsed electromagnetic fields of controlled intensity to stimulate growing constructs [Bodamyali et al., 1998]. The results show enhanced osteogenesis [Schwartz et al., 2008; Sun et al., 2010] and in certain cases better proliferation [Tsai et al., 2007] compared to control samples. Although electromagnetic fields systems are non-invasive, which is an advantage to reduce contamination risks, the high cost of the equipment is a clear limitation.

Instead of trying to reproduce *in vitro* the ideal biochemical and biophysical conditions of bone growth, *in vivo* bioreactors tend to make use of a host organism to supply the adequate nutrients, growth factor, and physiological environment to the construct. This method consists of implanting a cell-loaded scaffold material within a living organism, in order to initiate vascularization and the creation of more mature bone structures. Different animal models have been developed [Petite et al., 2000; Stevens et al., 2005; Holt et al., 2005] resulting in vascularized neo-bone formation. A recent exploratory study has been carried on a man as an *in vivo* bioreactor to replace a large part of his mandible [Warnke et al., 2004]. A titanium cage filled with bone mineral scaffold, autologous bone marrow and growth factor (BMP-7), has been implanted in one of the patient's dorsal muscle (right latissimus dorsi muscle). After 7 weeks the construct was transplanted to repair the mandibular defect (Fig. 2.4). The formation of new bone leaded in an improvement of the patient quality of life [Warnke et al., 2006], until his death from heart failure 15 month after the mandible replacement. Although the application of *in vivo* bioreactor concept has shown success in some individual cases, they currently imply very heavy, risky and expansive surgical operations.

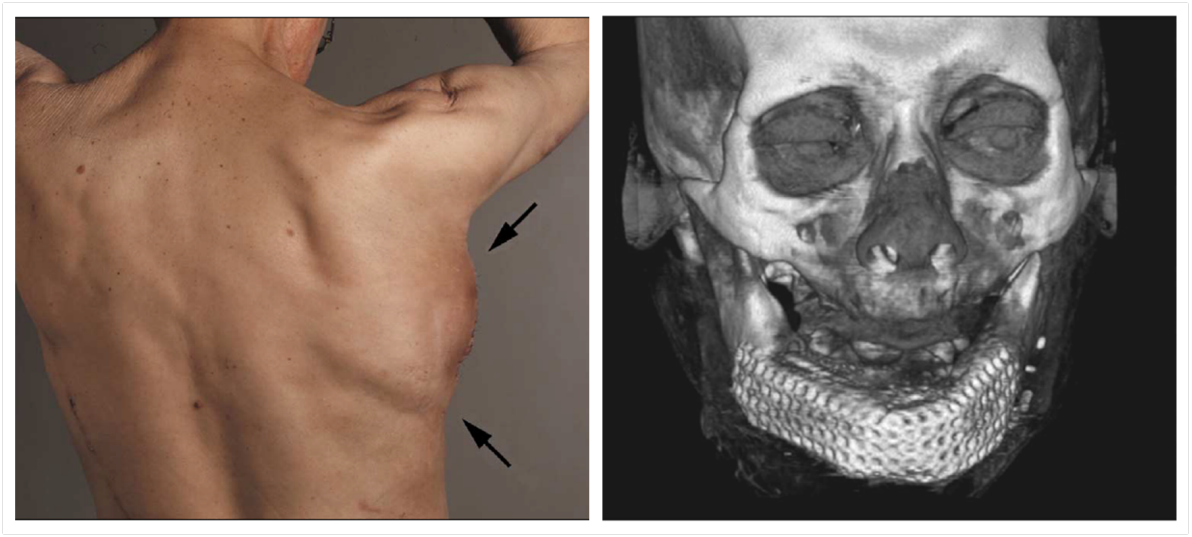

Figure 2.4 – Left : Dorsal view of mandibular replacement 3 weeks after implantation. Arrows point to the implantation site. Right : 3D computed tomography scan after transplantation of the *in vivo* cultured mandibular substitute. Figures adapted from [Warnke et al., 2004]

2.3 The double porosity bioreactor [David et al., 2011]

In the frame of the present thesis, the double porosity bioreactor developed by David et al. [2011] is studied. We seek to analyze the effects of culture medium perfusion on mass transport as well as on cell proliferation and tissue development. In this section the bioreactor's principal characteristics and results are presented.

The primary goal of the development of the double porosity bioreactor is to produce clinically relevant volumes of bone substitute in a limited time. This necessitates to enhance the proliferation and differentiation of osteo-competent cells within a bioresorbable three-dimensional scaffold. The design is partly inspired from fluidized bed reactors [Legallais et al., 2000; David et al., 2004] to tackle mass transport limitations and to provide optimal mechanical stimuli to the growing construct.

The bioreactor system is composed of a vertical cylindrical tube (inside diameter 3.3cm, height 21cm) containing the construct, and connected in a closed loop to a culture medium flask. Perfusion is ensured by a peristaltic pump and silicon tubing (Fig. 2.5). Except for the pump, the whole system is placed in an incubator and maintained at 37°C during culture. The silicon tubing are permeable to gas exchange between the culture medium and the incubator environment, providing oxygen and CO_2 during the whole duration of the experiment. Culture medium flow rate has been tested for values ranging between 1 to 100mL/min, and best results in terms of proliferation has been found for 10mL/min. The flask of culture medium is changed every three days in aseptic conditions.

The scaffold is constituted of a stack of cube shaped decellularized coral (approximately 140 microporous granules of $3\times3\times3\text{mm}^3$). This material has been widely used as bone sub-

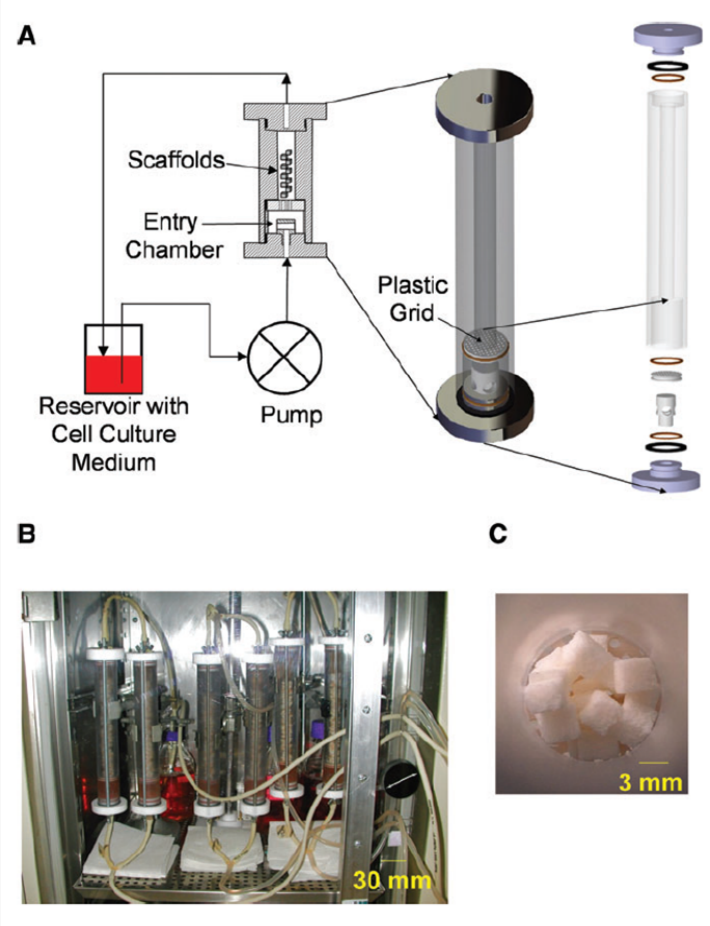

Figure 2.5 – Experimental set-up of the double perfusion bioreactor. (A) Schema of the set-up. (B) Several bioreactors perfused in parallel inside an incubator. (C) A stack of coral scaffold cubes

stitute for the past 10 years in orthopedic and maxilofacial surgery. It has the advantage of being biocompatible, osteoconductor, and bioresorbable. Two types of corals with different geometrical properties have been used : *Porites* which has a porosity of roughly 50% and mean pore size of approximately 80µm, and *Acropora* which presents a porosity of 12% for a mean pore size of 500µm. The scaffold cubes are staked randomly in the bioreactor, allowing the culture medium to flow in the space between the cubes, and assuring a relative isotropy. The double porosity composed of the inner coral porosity, and the staking of the cubes, gives its name to the bioreactor.

In the original article, the cell line used for the experiments are pluripotent stem cells derived from mouse embryos (C3H10T1/2) and transfected with green fluorescent protein (GFP). Coral cubes are precoated with culture medium before to be seeded with 10^6cell/mL cell suspension. Cells are kept at rest 24 hours in an incubator to allow proper attachment, and are then transfered in the bioreactor. At a flow rate of 10ml/min, the wall shear stress in the scaffold is roughly estimated between 0.01 and 10mPa. Cell number per cube is evaluated after 3, 6, 9, 12, 15, 18 and 21 days of culture by a destructive method. Basically each con-

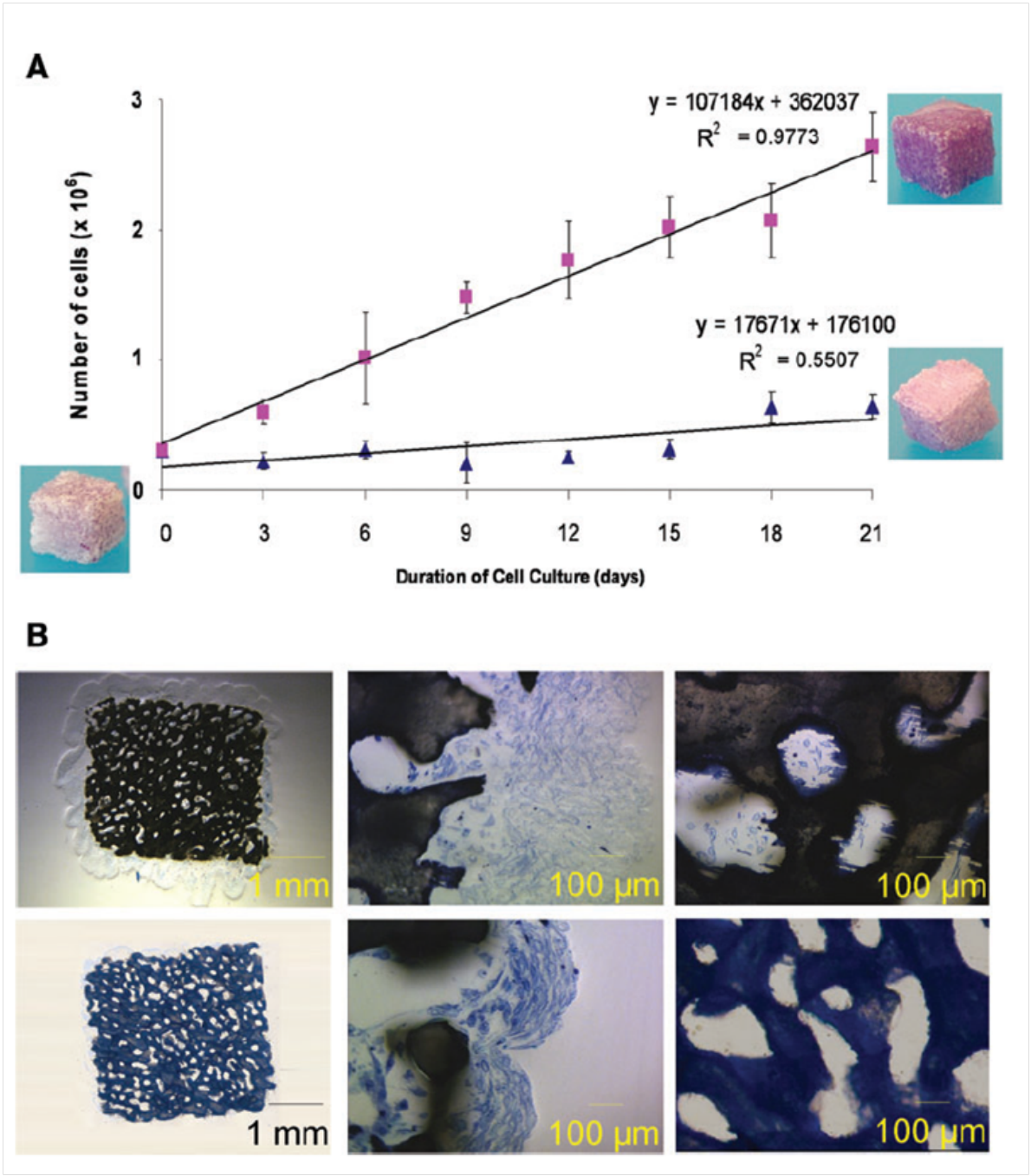

Figure 2.6 – Effect of culture medium fluid flow on cell proliferation. (A) Cell proliferation under static conditions (blue triangles), and under 10mL/min perfusion (pink squares). (B) Histological slices (Stevenel blue) of biohybrid cultured under 10mL/min perfusion for 3 weeks (top line) and in static conditions (lower line). Middle pictures show the periphery of the construct while right pictures show the center.

struct is crushed in a lysis buffer, and cell number is deduced by correlation with fluorescence intensity.

Results show a limited cell proliferation in static conditions with an observed plateau from the 6th day, whereas cell population in dynamic conditions is still increasing at 21 days of culture (Fig. 2.6A). After three weeks of culture, perfused constructs contain more than four times more cells than static cultured constructs. It is also important to note that the number of cells within a coral cube is independent of its location in the chamber, indicating an homogeneous cell proliferation along the bioreactor. Histological observations of the construct cultured for 21 days at 10mL/min flow rate show a thick (600µm) layer of cells at the periphery of the coral cubes, but only few isolated cell at the core of the scaffold (Fig. 2.6B). Cells at the center of the scaffold present morphological signs of necrosis. In contrast, constructs cultured in static conditions exhibit smaller external cell layer and almost no cell at the core of the scaffold.

Lastly, the bioreactor is tested with sheep MSCs, and the resulting construct is implanted subcutaneously for 8 weeks in sheep. Newly formed bone are observed on the surface of the explanted constructs, with the presence of osteocytes inside and a layer of osteoblasts around.

In this study, the double porosity bioreactor proves to be able to produce up to 30mL of bone substitutes. Although cell proliferation is homogeneous within the bioreactor, the cores of individual cubes remain poorly populated. This is due to the layer of cells forming a impermeable barrier at the periphery of the granules, and limiting nutrient transport to the core. In order to solve this issue and to meet the requirements to clinical applications, further developments are needed as well as a better understanding of mechanisms leading to the formation of bone substitute.

2.4 Requirements for a translational bioreactor

Despite the promising results obtained in the last 20 years with the use of bioreactors for bone tissue engineering, these systems have only been used anecdotally in clinical context [Warnke et al., 2004]. Here the requirements for the translation of bioreactors technologies to clinical applications are reviewed.

In order to be routinely used in clinical procedures, bone substitutes produced with bioreactors must represent a viable and competitive alternative over current cell based technologies. This condition may be satisfied identifying and addressing key challenges inherent to current bioreactors for tissue engineering.

- *Reproducibility of the produced construct.* Although the variety of protocols used by different research teams makes difficult the systematic reproduction of the results, the main source of variability is the behavior of human cells. Indeed they are extremely dependent on the donor batch (e.g. age, sex, health, antecedents), and may present different sensitivity to perturbations in the culture environment.

- *Minimization of operator dependency* which leads to inconsistency and lack of quality control between produced construct.
- *Scaling-up the production of substitutes.* Proof of the concept of bioreactor made substitute has been made. However the volume produced are still too low to face all clinical needs, and no large-scale production systems are yet proposed.
- *Cost effectiveness.* For bioreactor based treatments to be clinically introduced, the price of the overall process, from the provenance of the cells to the grafting of the construct into patient, should be competitive compared to other clinical procedures.
- *Compliance with regulatory specifications.* With the introduction of bioreactor systems in clinical treatments, complex regulatory frameworks are likely to be developed. A global reflection on safety regulation, risk assessment and validation of production processes is essential [Martin et al., 2009]. Currently the quality assurance system for medicinal products is insured by the Good Manufacturing Practice[2] (GMP) guidelines.

The three first challenges above can be partially solved through the development of automated sensor-based bioreactor systems [Martin et al., 2004, 2009]. By monitoring and controlling in real time the biochemical and biophysical parameters, the produced constructs can be standardized, making the process more robust and stable. This implies the development of on-line, non-invasive sensing techniques for culture parameters, together with a better understanding of the fundamental cellular and molecular processes leading to bone substitute production. Ideally the automation of the bioreactor system should lead to a user interface restricted to non-technical considerations. This would facilitate the manipulation by traditional hospital staff and decrease operator dependency [Salter et al., 2012]. It has also been suggested that the monitored parameters could be integrated in real time to a computational model of the bioreactor in order to predict the development of the tissue with time, helping scheduling of maintenance operations and surgery planning [Martin et al., 2004].

The cost effectiveness challenge may be the most critical in translating bioreactor processes to clinical applications. The evaluation of the price of such a treatment must take into account the cost of the bioreactor design and building, the scaffold, the cells, the culture media, the control essays (biochemical analysis and imaging), the labor, and the occasional failures in the process. Including these parameters in their estimation, Salter et al. [2012] determined that the cost of a bone graft made with a bioreactor would range from $10,000 to 15,000. They conclude that bioengineered bone substitutes are more expensive than allografts (free bone graft), but are a cost equivalent alternative to other current cell based therapies.

It is worth mentioning here that, even though there are yet no commercial offers of bone engineered substitutes, several private companies propose ready to use bioreactors to facilitate the production and the monitoring of cell growth and mineralized bone constructs. For example, spinner flask bioreactors are available from Bellco Biotechnology, Wheaton, or Corning® Lifesciences. Bioreactors based on the design of the rotating wall bioreactor can be purchased from Synthecon, Inc., Zellwerk GmbH or B. Braun Biotech International GmbH. A variety of perfusion bioreactors are offered by MINUCELLS and MINUTISSUE GmbH, while ten-

[2] http://ec.europa.eu/health/documents/eudralex/vol-4/index_en.htm

sion and compression systems are proposed by Flexcell International Corporation. A lot of these products are autoclavable and/or disposable systems. Moreover a variety of additional features are offered by some companies, such as online monitoring of oxygen, pH and glucose levels (Synthecon, Inc.), modules and softwares to control pulsatile hydrostatic pressure (Tissue Growth Technologies), or microscope stages allowing the observation of real time cell signaling response to mechanical stimuli (Flexcell International Corporation).

CHAPTER 3

MODELING PERFUSION BIOREACTORS

A LARGE VARIETY of bioreactors for bone tissue engineering has been developed by independent research teams. Most of them show good results in terms of cell proliferation, differentiation and extracellular matrix deposition. Among the prerequisites for translation of biorector technology to clinical application, one key challenge is the improvement of the fundamental knowledge about phenomena influencing cell fate within such system. Nonetheless the development of bioreactors has been largely based on an experimental trial and error spirit, and a deep understanding of the underlying mechanisms determining the efficiency of the different methods is still missing.

A quantitative assessment and prediction of relevant culture parameters (e.g. glucose concentration, fluid velocity, cell division rate) is required where current experimental approaches fail to this task. In this context, modeling methods are promising tools to study and predict biochemical and biophysical phenomena at the cell or tissue scale.

Cell fate within a bioreactor depends on an almost infinite number of parameters. Since no one is yet ready to capture the whole complexity of life within a model, the large majority of bioreactor modeling studies are focused on the medium culture flow, mass transport, and their respective influence on cell proliferation and differentiation. In the present chapter, the scientific literature is discussed in regard to these three aspects.

3.1 Modeling transport phenomena

The importance of hydrodynamics in bioreactors for bone tissue engineering has been assessed in Sec. 2.1. The flow of culture medium has a double role, enhancing mass transport through the construct via convective effects, and stimulating mechanically cell proliferation, differentiation and extracellular matrix (ECM) deposition. Despite its importance in many bioreactor systems, the fluid flow induced shear stress is often roughly estimated [Goldstein et al., 2001; David et al., 2011]. And yet, the values of the fluid velocity, and thus of the shear stress, may vary on a large range due to the complicated porous geometry of the scaffold.

This means that the shear stress experienced by cells at different locations may vary of several orders of magnitude.

A crucial aspect concerning transport of momentum (fluid flow) ans mass (species) in a bioreactor, is the coupling between cell/tissue growth and transport processes. Cell proliferation, migration and ECM deposition are dictated by velocity fields inducing mechanical stimuli, and concentration profiles. In return, culture medium flow and mass transport are modified by the developing tissue, resulting in a time evolving coupled process. Luckily the time scale separation between tissue growth and transport phenomena is usually large enough to consider the tissue geometry to be quasi-static in regard to the other processes.

3.1.1 Modeling momentum transport

Biophysical stimuli influencing osteocompetent cells proliferation, differentiation, migration and ECM deposition, include pressure and shear stress. The large quantity of experimental studies has assessed the decisive effect of shear on tissue development. In this section, several models aiming to evaluate the shear stress intensity and distribution within tissue engineering scaffolds are presented.

Studies focusing on the modeling of momentum transport in tissue engineering aim to evaluate the wall shear stress induced by the culture medium flow. Since the shear is a pore scale parameter, all the simulations presented below characterize the pore scale. Some analytic models evaluate the mean shear stress, however homogenized models of momentum transport are of interest mainly for the computation of convection in mass transport, and these will be presented in Sec. 3.1.2.

Analytical models

In practical conditions met in bioreactors (incompressible fluid and wall fluid velocity null), the mean shear stress is a function of the entrance fluid velocity, the fluid properties, and the scaffold geometrical characteristics. If the two first are easily available for a given experiment, the detailed scaffold architecture may be more difficult to obtain. Nevertheless, mean pore size, porosity and permeability of a scaffold can be measured providing relatively inexpensive experimental setups. For instance, porosity can be evaluated by imbibition methods or by mercure intrusion, while permeability can be estimated with a permeation test by correlation with Darcy's law [Dias et al., 2012]. Thus it is appealing for experimentalists to find simple models relating shear stress to scaffold porosity and permeability.

As a first approach, fluid velocity and shear stress within the pores of a porous scaffold can be estimated analytically providing simplifications on the geometry. Supposing the porous medium composed of identical parallel cylinders oriented along the flow, and an incompressible fluid satisfying Stokes equation, a quick analyze in cylindrical coordinates leads to a mean wall shear stress τ_m in the form [Goldstein et al., 2001]

$$\tau_m = \mu_f U_m \frac{8}{\varepsilon d} \tag{3.1}$$

where U_m is the mean seepage velocity (superficial average), μ_f the dynamic viscosity of the fluid, ε is the scaffold porosity, and d the pores diameter. U_m can be easily computed knowing the entrance flow rate and the geometry of the bioreactor chamber. Because of its extreme simplicity, this model is widely used in experimental studies to evaluate the order of magnitude of the imposed shear stress in a specific set-up [Goldstein et al., 2001; Vance et al., 2005; Grayson et al., 2011]. However the geometry of the scaffold is highly idealized, leading to overestimation of the average shear stress [Jungreuthmayer et al., 2009a].

In order to avoid simplification hypothesis on the scaffold architecture, it is appealing to take into account the geometry through the permeability. To this purpose, several authors [Wang & Tarbell, 2000; Boschetti et al., 2006; Cioffi et al., 2006; Voronov et al., 2010a,b; Pham et al., 2012] use the model proposed by Wang & Tarbell [1995]

$$\tau_m = \mu_f U_m \frac{1}{\sqrt{K}} \tag{3.2}$$

where K is interpreted as the scaffold permeability. Yet, this model has been originally developed for the evaluation of wall shear stress around smooth muscle cells embedded in a porous ECM, with K being the permeability of the ECM, not of the porous media constituted by the cells [Wang & Tarbell, 1995]. In a subsequent study [Wang & Tarbell, 2000] and without any justification, the same author (J.M. Tarbell, the two Wang are different) incorporates the overall permeability (ECM + cells) within K. This has contributed to the misinterpretation of the permeability in the above cited works.

In a more recent letter, Warren & Stepanek [2008] approximate the mean wall shear stress by the mean wall stress ($\tau_m = \varepsilon(\nabla p)_m/S$), and express it as function of the permeability and mean fluid velocity using Darcy's law

$$\tau_m = \mu_f U_m \frac{\varepsilon}{KS} \tag{3.3}$$

where S is the specific surface area of the porous medium, and $(\nabla p)_m$ is the mean pressure gradient at the wall. They examine the validity of Eq. (3.3) in the case of a random sphere packing ($S = 6(1-\varepsilon)/l$ with l the characteristic sphere size), by comparing with direct computations (lattice-Boltzmann method). They conclude that a factor $\alpha \simeq 0.6 - 0.8$ must be included in Eq. (3.3) in order to approximate properly the mean wall shear stress.

The above models are dependent of strong simplifications, and give only an average shear stress. However cells are subject to local shear, and the distribution of the mechanical loads in the scaffold may be useful. This motivates the use of numerical tools to evaluate the detailed fluid velocity profile within the porous scaffold.

Computational models

Computational fluid dynamics (CFD) represents a powerful tool to compute fluid flow, and thus shear, within a given structure. However the main difficulties related to porous scaffold architectures remain : (i) obtaining the detailed realistic geometry, (ii) generating a discrete domain representing such complicated porous architectures, and (iii) solving the conservation equations on this domain at a reasonable computational cost.

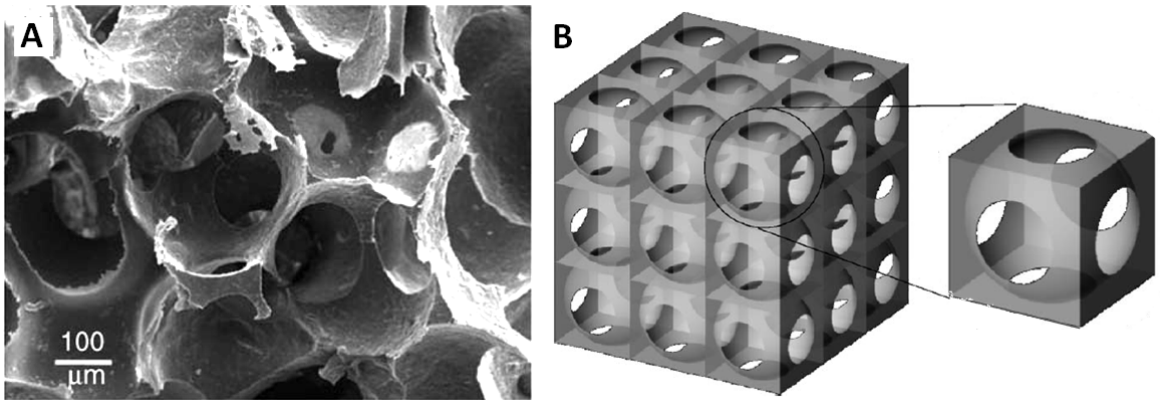

Figure 3.1 – Regular scaffold used in [Boschetti et al., 2006]. A : SEM image of a PDLLA scaffold made by particulate leaching. B : Idealized representation of the scaffold

Concerning the definition of the geometry, some artificially made scaffolds have regular and homogeneous characteristics [Hutmacher, 2000; Singh et al., 2005], allowing to use basic CAD tools to build idealized 3D computational structures, as shown in Fig. 3.1 [Boschetti et al., 2006]. Nevertheless, even when the scaffold is designed to be regular, current fabrication techniques still induce variation from the theoretical geometry, leading to unpredictable deviations of the transport properties [Hendrikson et al., 2014]. In order to take into account the specific architecture of a scaffold, three-dimensional imaging techniques must be applied. Micro X-ray computed tomography (µCT) is, from far, the most widely used 3D imaging technique to virtually reconstruct scaffolds architecture [Voronov et al., 2010b]. This technique is popular due to its relatively low cost, high resolution (up to 4µm [Cioffi et al., 2006]), and rapidity. The obtained scan can be easily reconstructed and analyzed to give access to structural data such as porosity, pore size distribution and isotropy (Fig. 3.2). Note that the obtained µCT images are in grayscales, and a threshold must be applied to discriminate solid from void space. This choice in the threshold may highly influence the values of the structural data and subsequent computations.

The order of magnitude of scanned volumes is of the order of $10mm^3$, however computational costs limit the volume used for CFD simulations to few millimeters cube [Maes et al., 2009]. Indeed, most CFD methods (e.g. finite volume, finite element, finite difference) require to approximate the fluid volume by a discrete domain or mesh. And since the geometries of the scanned scaffolds are complicated and irregular, the meshed domains get very quickly heavy with increasing volumes. Scaffolds with high porosity (>70%) and larger pore size tend to have a simpler geometry and to be more easily meshable. Discretization can be conducted with pre-processing softwares such as AMIRA (TGS, San Diego, CA, USA) [Cioffi et al., 2006], Ansys (Ansys Software, Canonsburg, PA, USA) [Acosta Santamaría et al., 2013], Gambit (Fluent Inc., Lebanon, NH, USA) [Boschetti et al., 2006] or Mimics (Materialise, Leuven, Belgium) combined with Patran (MSC Software, Newport Beach, CA, USA) [Sandino et al., 2008]. Conditions imposed at the boundaries are usually no-slip at the fluid/solid interface, constant velocity at the entrance (ranging from 1 to 300µm/s) and null pressure at the exit. Finally the culture medium is modeled as an incompressible newtonian

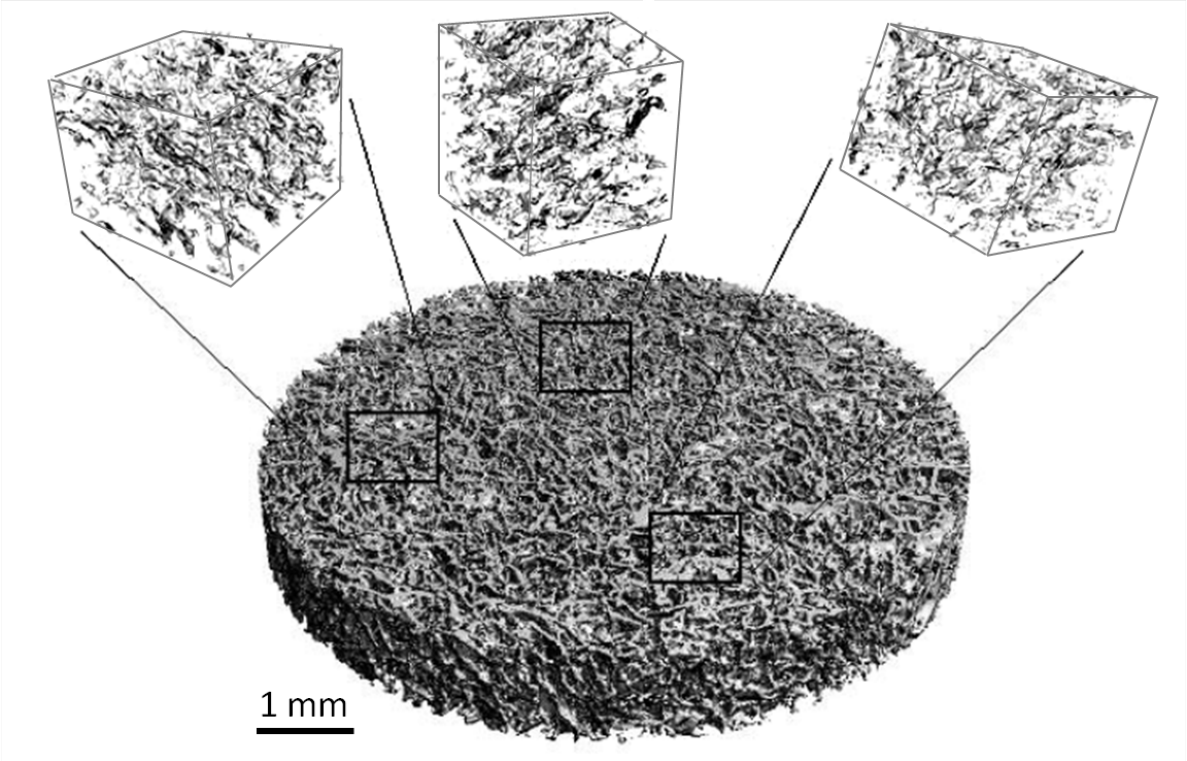

Figure 3.2 – µCT scan of a collagen-glycosaminoglycan scaffold, and three randomly chosen sub-volumes of 640µm×640µm×480µm (adapted from [Jungreuthmayer et al., 2009a])

fluid, and laminar Stokes flow is solved either by finite volume method with softwares such as FLUENT (Fluent Inc., Lebanon, USA) [Raimondi et al., 2006; Boschetti et al., 2006; Cioffi et al., 2006, 2008; Pham et al., 2012], OpenFOAM (OpenCFD Ltd., Bracknell, UK) [Jungreuthmayer et al., 2009a,b] or Ansys CFX (Ansys Software, Canonsburg, PA, USA) [Stops et al., 2010; Acosta Santamaría et al., 2013; Zermatten et al., 2014], or finite element method with for instance Marc-Mentat (MSC Software, Newport Beach, CA, USA) [Sandino et al., 2008].

Alternatively, the lattice Boltzmann method (LBM) [d'Humieres, 1992; Lallemand & Luo, 2000] is a CFD method that does not require a meshed geometry, and thus skips the delicate preprocessing steps. The geometry obtained by µCT being a grayscale 3D matrix, only a threshold has to be applied to determine the solid from the fluid sites, and the binary matrice is directly used as an input to generate the regular lattice. In brief, the LBM consists in assigning at each fluid node a population of fluid particles with a velocity distribution function. Then at each time step, the particles propagate to neighboring nodes according to their velocity function, which is then updated through collision rules. After a sufficient number of iterations, the macroscopic system converges to an incompressible Stokes flow. To our knowledge, Porter et al. [2005] are the first to take advantage of µCT to reconstruct the 3D geometry of trabecular bone, and to solve the flow within this porous structure with the LBM (µCT resolution 34µm, LBM element size 68µm, lattice of 2.5 million elements including 1.2

million fluid elements). The shear stress is evaluated by multiplying the symmetrical part of the gradient of the velocity tensor by the dynamic viscosity. Subsequent studies using LBM in tissue engineering scaffolds include [Galbusera et al., 2007; Zhao et al., 2007; VanGordon et al., 2010; Voronov et al., 2010a,b; Gao et al., 2012], with the smallest LBM element size being 6µm [Gao et al., 2012].

Evaluation of the wall shear stress

CFD simulations are operated in order to quantify the flow field, which determines wall shear stress and influence mass transport. While the field of wall shear stress is accessible from simulations, it is of little practical interest since it can be used only for the specific computed structure. The mean shear stress computed on a realistic scaffold architecture, with experimentally relevant flow rates, has first been evaluated by Porter et al. [2005] using the LBM. Cioffi et al. [2006, 2008] confirm this result with the finite volume method, and are the first to compute the wall shear stress distribution within a scaffold. Interestingly, using a regular CAD scaffold made of spherical pores, Boschetti et al. [2006] compute the fluid flow and shear stress distribution for varying porosity (59 to 89%) and pore size (sphere diameter of 50 to 150µm), and conclude that while both porosity and pore size influence the shear stress distribution, its intensity is mainly dependent on the pore size. This observations are further confirmed by a LBM study on various µCT based scaffolds, showing that for a given flow rate, the shear stress distribution is more influenced by the architecture than by the porosity [Voronov et al., 2010a]. In a subsequent study, Voronov et al. [2010b] compute the probability distribution function of the wall shear stress for 36 µCT based scaffold geometries. Adding to their database results from the literature [Cioffi et al., 2006; Jungreuthmayer et al., 2009a], they show that the probability density function of the wall shear stress in a porous scaffold can be well fitted with a three-parameters gamma distribution (Fig. 3.3). This distribution is valid for a variety of regular and irregular architectures, and for porosities as low as 50% [Pham et al., 2012].

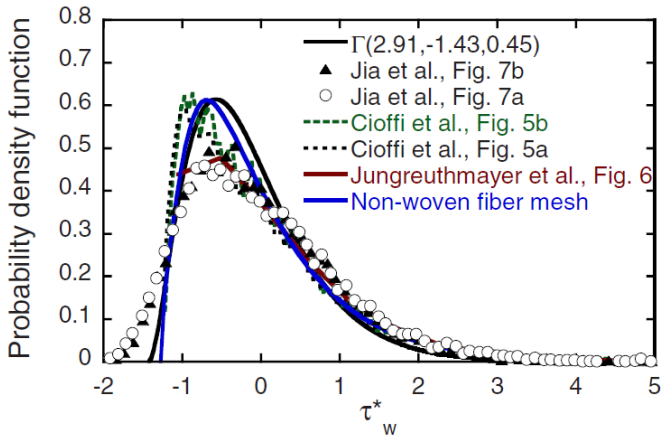

Figure 3.3 – Comparison between probability distribution functions of wall shear stress from various studies, and three-parameters gamma distribution [Voronov et al., 2010b]

3.1.2 Modeling mass transport

In addition to provide a mechanical stimuli supporting cell proliferation, differentiation and ECM deposition, the flow of culture medium enhances mass transport by convective effects. Indeed, due to diffusion limitations, regions in the scaffold located few millimeters away from the bulk nutritive medium, may present depletion in oxygen, nutrient or osteoinductive substances. It has been observed experimentally that dynamic culture conditions reduce this issue (see Sec. 2.1), however the effect of culture medium flow on mass transport and cell proliferation remains to be quantified.

Since mass transport occurs both in the culture medium, and in the cell/tissue region, a lot of models on species diffusion, convection and reaction within a bioreactor also focus on cell proliferation. In this section, only mass transport is discussed, modeling of cell growth will be the subject of Sec. 3.2.

At the pore scale, mass transport in the culture medium within a scaffold can be computed for a given pore geometry by a classical diffusion-convection transport equation [Pierre & Oddou, 2007; Galbusera et al., 2007, 2008; Cioffi et al., 2008]. The input velocity in the convective term is the solution of the momentum transport problem obtained by methods presented in Sec. 3.1.1. However, since in most cases the characteristic length on which the concentration varies, is larger than the pore size, the detailed knowledge of the concentration field at the scaffold may not be essential. Instead, homogenized models can be employed to describe macroscopic mass transport, saving considerable computational costs [Cioffi et al., 2008].

Although several studies solve homogenized mass transport models for tissue engineering applications [Botchwey et al., 2003; Pathi et al., 2005; Sengers et al., 2005; Zhao et al., 2005, 2007; Cioffi et al., 2008; Chung et al., 2010; Nikolaev et al., 2010; Yu, 2012], these are often based on heuristic considerations, and very few establish the theoretical basis of such macroscopic models [Galban & Locke, 1999a,b; Lasseux et al., 2004]. The structure of the mass transport equation is conserved through up-scaling, facilitating its use in simulations. However special care has to be taken with the definition of the effective diffusion-dispersion tensor. Depending on the complexity of the model, the effective diffusion coefficient is taken equal to the bulk fluid diffusion coefficient [Botchwey et al., 2003; Sengers et al., 2005; Cioffi et al., 2008], the Maxwell formulation [Sacco et al., 2010; Yu, 2012], or an analytic formulation derived in Ochoa [1988] [Pathi et al., 2005]. Note that none of this study takes into account dispersive effects arising from momentum transport. The velocity field must also be the solution of an homogenized momentum transport problem such as Darcy [Botchwey et al., 2003; Cioffi et al., 2008], Brinkman [Zhao et al., 2007; Sacco et al., 2010], or even Forchheimer [Yu, 2012] equations.

The only way to capture concentration depletion in the core of the scaffold is to incorporate cell consumption. This is generally done by adding a reaction term which acts as a sink, within the mass transport equation. Whatever the transported species (e.g. oxygen, glucose), the consumption kinetic is modeled through a Michaelis-Menten kinetic of the form [Cioffi et al., 2008; Galbusera et al., 2008, 2007; Nikolaev et al., 2010; Sengers et al., 2005; Zhao

et al., 2005]

$$R = \frac{R_c C}{K_c + C} \varepsilon_{cell} \tag{3.4}$$

where C is the average species concentration, R_c and K_c are the maximal consumption rate and half saturation constant respectively, and ε_{cell} is the volume fraction of cells in the representative volume.

Considering the large variety of modeled bioreactor and cell parameters, general conclusions on mass transport alone are difficult to draw. Nevertheless coupling mass transport with the cellular activity is the key point to understand tissue growth kinetic and heterogeneous formation. The next section reviews the existing strategies to model cell proliferation in response to biochemical and biophysical stimuli encountered in tissue engineering processes.

3.2 Modeling cell proliferation

The construct, constituted of the scaffold, cells and secreted ECM, is a constantly evolving material. In a bioreactor, tissue growth modifies momentum and mass transport during the whole culture time. In return, cell proliferation, survival and activity highly depend on the biochemical and biophysical environment induced by these transport processes. In order to understand the mechanisms influencing the evolution of the construct, the strong coupling between cell proliferation, culture medium flow and species transport must be studied. This motivates the development of dynamic cell models in tissue engineering applications.

Early cell growth mathematical models were developed to predict bacterial colony formation [Contois, 1959]. Thereafter, modeling of cell proliferation has been widely supported by medical motivations such has the study of tumor growth, embryogenesis, and biological tissue behavior [Araujo & McElwain, 2004; Jones & Chapman, 2012]. Two main categories of cell growth models can be drawn (Fig. 3.4). On one hand, *individual cell based models* (IBMs) have been developed to simulate small-scale phenomena in which the properties of the cells vary over distances comparable to the size of the cell. On the other hand, *continuum models*, based on heuristic diffusion-reaction structures or mechanical considerations, have been built to represent large scale phenomena where the properties of the cell/tissue vary over distances of several cell diameters [Byrne & Drasdo, 2008]. Although IBMs capture cellular scale physics that can be directly linked to experimentally measured parameters, its computational cost is prohibitive when the number of individuals become large. Moreover, at the tissue scale, the detailed cell informations (e.g. individual cell track, state of mitotic cycle) may not be pertinent, and the averaged parameters may be sufficient to represent relevant phenomena. This allows to use continuum models, saving considerable computational resources. Ideally, large scale models should be rigorously up-scaled from cellular scale experimental data or IBMs, although this is rarely the case [Codling et al., 2008]. In the present section, IBMs and continuum models are discussed in the scope of bioreactors for tissue engineering.

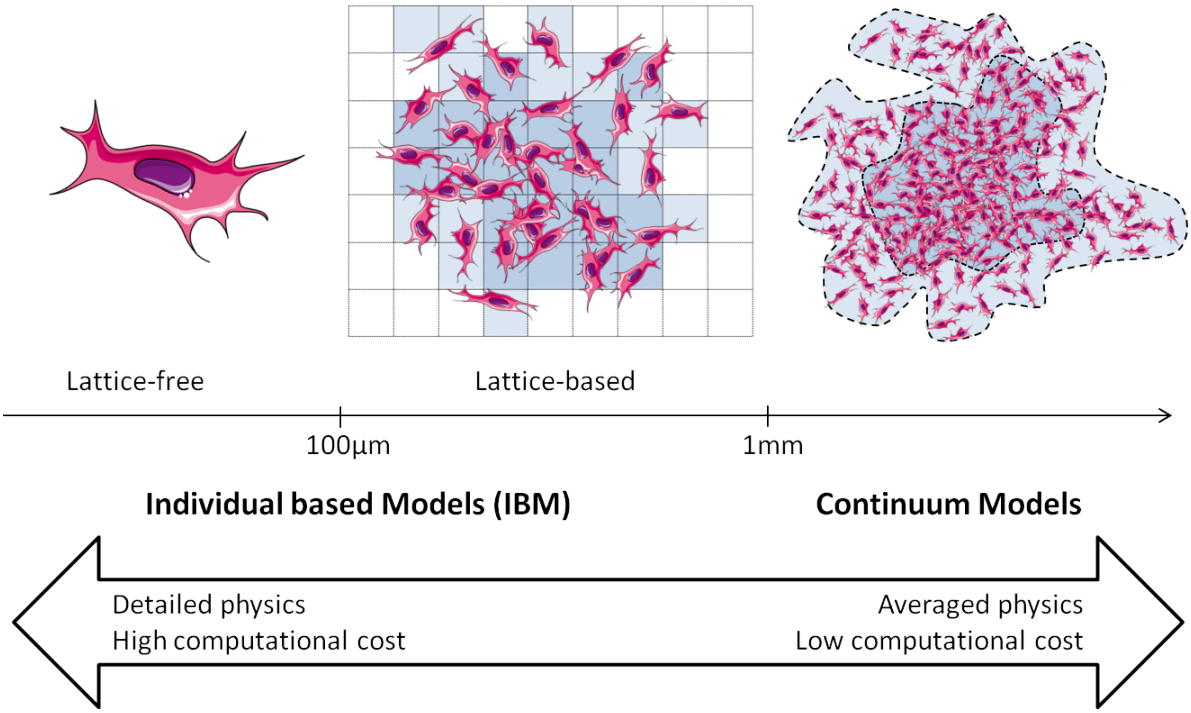

Figure 3.4 – Length scales associated with cell proliferation modeling approaches

3.2.1 Individual based models

Individual based models (IBMs) can be divided in two subgroups : lattice-free and lattice-based models [Plank & Simpson, 2012]. In the first case, a single cell is represented by several elements of the lattice, allowing the implementation of realistic biophysical and biochemical parameters. In the second case, each node of the lattice represents one or more cells, and the complicated and computationally expensive physical laws directing cell behavior are approached by a series of simple rules that are easily computed. Cellular automata (CA) are the most popular class of lattice-based models, where time, space and state are discrete[1]. Although there is a substantial lost in information between lattice-free and lattice-based models, the gain in computational time is of the order of 10^3 [Byrne & Drasdo, 2008].

Lattice-free models usually model cells by elastic spheres or ellipses, interacting with each other and with the support through attraction and repulsion forces [Galbusera et al., 2008; Jungreuthmayer et al., 2009b]. Division time can be defined as a function of the internal cell cycle and external conditions (range of nutrient concentration, mechanical stimuli) [Byrne & Drasdo, 2008]. Cell motility may be modeled following a random walk pattern, with or without preferential direction depending on chemotaxis. Remarkable degrees of complexity can be reached with this kind of model. For instance, Hoffmann et al. [2011] add a system of pods to spherical cells. The number of pods is dependent of the number of neighboring cells, and allows migration by attachment to the support and traction of the spherical cell body. This

[1] Actually any computer simulation is discrete in time, space, and state, but numerical algorithms are usually built such as to overcome artifacts due to discretization.

model is able to capture cell orientation at high cellular density, and is highly mechanically realistic. Nevertheless this degree of fidelity is of few interest at the tissue scale, and its complexity as well as its computational cost direct the use of lattice-based model for tissue engineering applications.

Early lattice-based models of cell proliferation have been developed to reproduce two-dimensional growth of cell colony in Petri dishes [Zygourakis et al., 1991a,b; Lee et al., 1995]. Briefly, a cellular automaton (CA) is built of a two-dimensional regular square lattice, where each node is an automaton defined by a finite number of state. A node can be either a cell or a void. At every time step, each automaton occupied by a cell follows a set of rules determining division and migration as a function of the neighborhood. At high cell density, the limited space naturally imposes contact inhibition for division and migration. Adjustable parameters include the number of time steps between two divisions, the number of time steps before changing the migration direction (the static state is a direction), the probability transition between one migration direction to another, and the migration velocity. This parameters include stochastic aspects in order to represent biological variability, and are adjusted with statistical treatments of experimental data [Lee, 1994; Garijo et al., 2012]. This model has been further extended to three-dimensional growth to represent tissue formation [Cheng et al., 2006], assessing the importance of homogeneous seeding and cell migration for uniform proliferation.

In order to understand the influence of cell population dynamic on the oxygen concentration field, Galbusera et al. [2007] introduce a coupling between the previously developed CA and a diffusion-convection-reaction equation. A regular scaffold geometry is modeled, and cells evolve in the fluid region. The velocity field is obtained with the lattice-Boltzmann method (LBM), while mass transport is solved by the finite difference method. Cell oxygen uptake is modeled by Michaelis-Menten kinetics. In this model, the CA is totally independent of the external stimuli. The oxygen concentration field is computed as a function of cell proliferation stage. Although this study proves the feasibility of coupling different numerical methods to model a dynamic multiphysics system, it provides limited conclusions due to the small computational domain imposed by the explicit representation of the scaffold geometry.

More recent models include the influence of the concentration field on cell fate [Cheng et al., 2009; Chung et al., 2010]. In this works, a homogenized construct maintained in a static culture medium bath is considered. A diffusion-reaction equation is solved by the finite difference method, and cell proliferation is based on the previously described CA [Cheng et al., 2006]. Cell division time is set according to a distribution from which the mean value is a Monod kinetic function of the local nutrient concentration. Then during cell migration, this division time can be increased or decreased as a function of the local concentration experienced on the way. These models are able to capture the dynamic formation of heterogeneous fields of concentration and cell density (Fig. 3.5).

Despite the above cited successful applications in tissue engineering, numerous limitations are associated with the use of CA. To begin with, data obtained with CA models are often difficult to extrapolate in relevant and quantitative macroscopic information. Moreover, when a large number of automaton is modeled, the computational costs often necessitate to have recourse to parallel computing, canceling one of the main advantage of CA : its simple

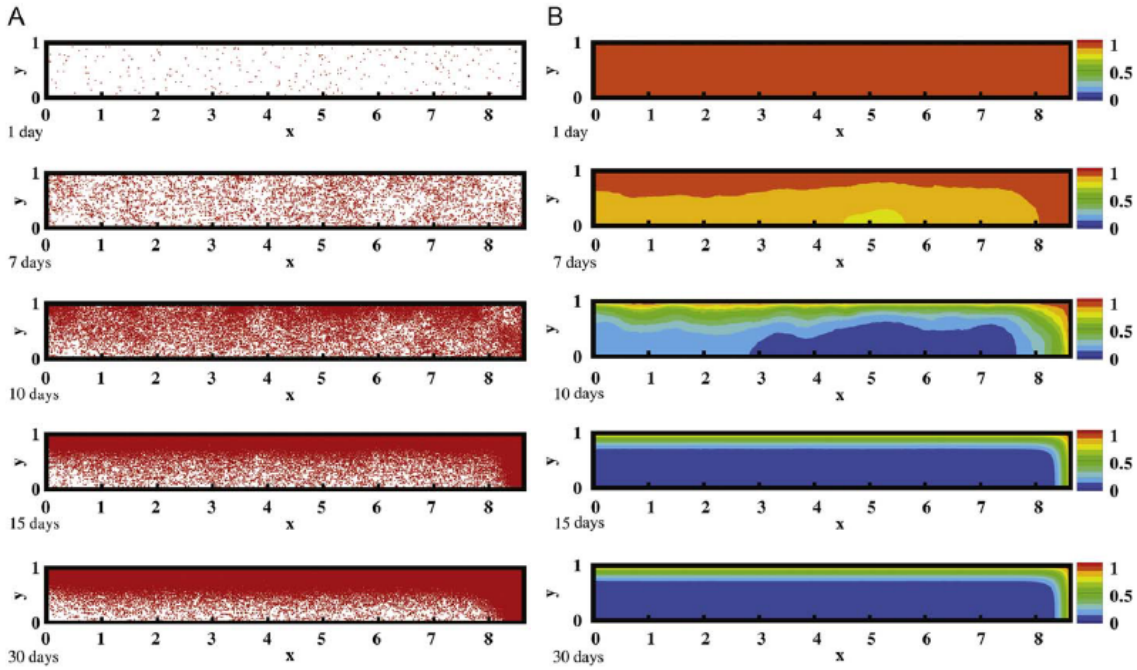

Figure 3.5 – Time evolution of the cell distribution (A) and nutrient contours (B) of the top right corner of the construct [Chung et al., 2010]

conceptual representation and implementation. Finally, the multiphysics aspect of the problem, often require to couple different solving methods (for instance coupling a CA for cell proliferation, with the finite difference method for diffusion, and/or the finite element method for fluid flow). In the literature, this types of representations are termed "hybrid models". The transport processes in these models are very often homogenized, and their length scale compatibility with CA may be questionable. In the next section, models where the cellular properties are averaged in order to represent tissue behavior in the form of continuum models are discussed.

3.2.2 Continuum models

Pioneer continuum models of cell proliferation in tissue engineering process are based on the volume averaging method [Galban & Locke, 1997, 1999a,b]. In this studies, culture medium is represented by one phase, while the scaffold, cells and ECM are all considered to form a unique homogeneous biomass region. An average diffusion-consumption equation is obtained on the hypothesis of local mass equilibrium, and both effective diffusion coefficient and reaction rate are derived as a function of the biomass volume fraction. An average mass balance equation for the biomass is defined as a function of different growth rates. Three types of growth kinetics dependent on nutrient concentration are solved and compared with experimental results of cartilage growth Freed et al. [1994]. The best fit is obtained for a Contois kinetic [Contois, 1959] modified to take into account cell contact inhibition (thanks

to $\rho_c \epsilon_c$ in the denominator)

$$r_c(\epsilon_c, C) = \frac{k_g C}{k_s \rho_c \epsilon_c + C} - r_d \tag{3.5}$$

where C is the nutrient concentration, ϵ_c the biomass volume fraction, k_g and k_s the maximal specific growth rate and the half saturation constant respectively, ρ_c the biomass density, and r_d the cell death rate due to apoptosis. Interestingly, the effective diffusion coefficient is shown to vary of an order of magnitude between low and high density regions.

Continuum models are by definition homogenized models. Even though the derivation of the governing equations should be based on rigorous up-scaling of microscopic processes, they are often "guessed" and applied without verification of their domain of validity. For instance, the form of the cell proliferation rate as a function of the concentration and cell number can be linear [Lewis et al., 2005], exponential [Zhao et al., 2005], logistic [Dunn et al., 2006], or modified Contois type [Coletti et al., 2006]. Most recent models include "diffusive like" terms to biomass conservation equations in order to represent tissue expansion [Chung et al., 2007, 2008; Jeong et al., 2011].

In all the above cited works, cell proliferation kinetic is dependent on concentration, and cell density. Mechanical stimuli is introduced by Sacco et al. [2010] who propose to modify the modified Contois kinetic (Eq. (3.5)) in order to introduce a dependency of the maximal growth rate on the shear stress

$$r(\epsilon_c, C, \tau_m, \xi) = \frac{k_g(\tau, \xi) C}{k_s \rho_c \epsilon_c + C} - r_d \tag{3.6}$$

where τ_m is the mean shear stress, and ξ a parameter specific to the cell type, that has to be experimentally calibrated [Raimondi et al., 2006]. As a first hypothesis, a linear relation between k_g and τ_m is chosen. The mean shear stress is obtained through Eq. (3.2), where the permeability is computed by the Carman-Kozeny equation. The model is solved in a two-domensional domain, and the results show an increase of biomass volume fraction with increasing perfusion flow rates.

An alternative approach based on the multiphase porous flow mixture theory has been proposed by Lemon et al. [2006]. They present a general model with an arbitrary number of phase, and apply it to tissue growth within a scaffold. Each tissue component is modeled by mass and force balance equations, and can deform through constitutive relations. The dynamics of the cellular phases is studied as a function of initial conditions, and cell-cell and cell-scaffold affinity. This model is further developed to take into account nutrient transport limitations on tissue growth [Lemon & King, 2007]. A three-phase system in considered composed of motile cells, culture medium (called "water" in the article), and scaffold, and growth process is investigated for two initial seeding conditions. O'Dea et al. [2008, 2010] extend the model to represent perfusion of the culture medium. The three parameters influencing tissue formation are cell density, pressure and fluid shear stress. Depending on their intensity, the growth rate in response to these parameters is either in a quiescence stage, proliferation and ECM deposition stage, or apoptosis stage (Fig. 3.6). This model is solved analytically in one-dimension, and numerically in two-dimensions [Osborne et al., 2010], revealing the importance of including geometrical effects to capture relevant tissue growth behavior.

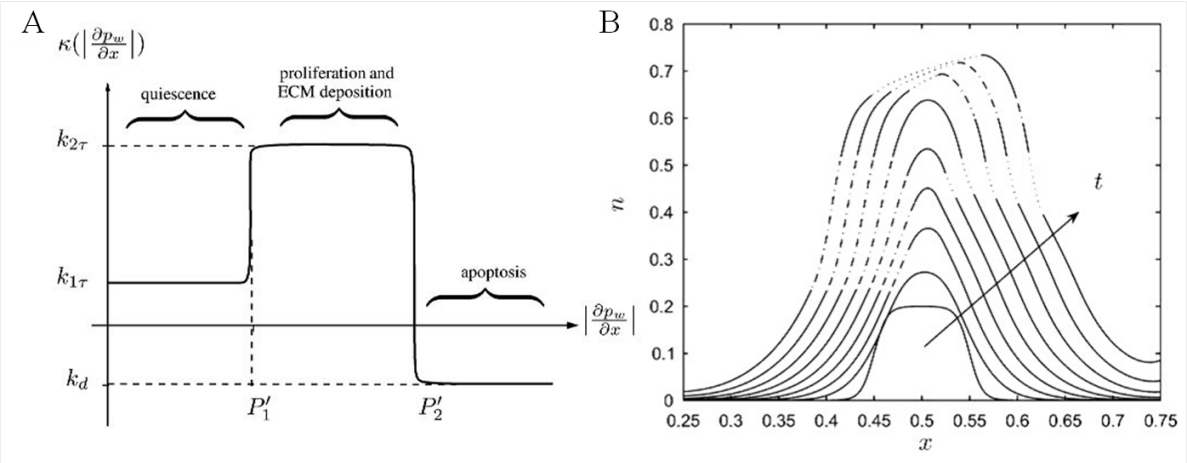

Figure 3.6 – Figures adapted from O'Dea et al. [2010]. (A) Representation of tissue growth kinetic in response to flow induced shear stress. (B) Time evolution of the cell volume fraction as a function of the position in the bioreactor.

Some authors choose to model tissue growth by a moving boundary formulation [Galban & Locke, 1997]. In this kind of model, the growth mechanism happens exclusively at the boundary between the tissue and the culture medium, and the velocity of the interface is dependent on interfacial parameters only. Lappa [2003] uses the level set method to represent two-dimensional cartilage growth as a function of the interfacial concentration and shear stress. More recently, Nava et al. [2013] predict three-dimensional tissue growth with an arbitrary Lagrangian-Eulerian technique which allows to re-mesh the geometry at each tissue proliferation step. Although these models permit the visualization of all the stages of tissue growth, there is no experimental clue that tissue expansion is an interfacial process. Additionally, the tissue being a homogenized region, the boundary with the culture medium is not clearly defined, and the understanding of the transport processes taking place at such interface are not established yet [Goyeau et al., 2003; Valdés-Parada et al., 2006].

CHAPTER 4

DISCUSSION AND CHALLENGES

THE DEVELOPMENT of bioreactors for bone tissue engineering is a very active research field. A plethora of experimental studies using hydrodynamic culture environment has been proposed, enhancing mass transport and mechanical stimuli, and leading to improved cell proliferation, differentiation and extracellular matrix deposition. Yet, the translation of this biotechnology to routine clinical applications is still restrained by a lack of knowledge of the underlying phenomena leading to the production of relevant volumes of bone substitutes.

In an attempt to overcome this limitation, mathematical models have been developed to analyze the parameters inaccessible to experimental measurement, and to predict substitute formation. As depicted in Fig. 4.1, these studies have investigated momentum transport (including the evaluation of fluid flow induced mechanical forces), nutrient transport, and cell/tissue growth. Thanks to X-ray micro-tomography (μCT) technology, a lot of work has been carried on the evaluation of wall shear stress induced by the flow of culture medium in porous scaffolds. On the other hand, several studies analyze biomass growth in regard to nutrient transport. The multiphysics aspect of the problem is still a challenge to model all transport phenomena and its influences on cell dynamics. Moreover very few models include the influence of fluid flow induced mechanical stimuli on cell proliferation. Among them, those based on the mixture theory [O'Dea et al., 2008, 2010; Osborne et al., 2010] have the advantage of being the result of a rigorous mathematical development, able to represent force interactions between the cells, the culture medium and the scaffold. However the structure at the pore/cell scale is not included in this theory, and effective transport parameters (e.g. tissue permeability, diffusion tensor) are not defined. Models based on a moving boundary formulation [Lappa, 2003; Nava et al., 2013] are purely tissue scale models, and fail in relating cell scale physics to tissue production. Finally, Sacco et al. [2010] propose a comprehensive model coupling momentum and mass transport to tissue growth kinetic. Although they claim to base their analysis on the volume averaging method, the effective transport parameters are not obtained from a closure problem, but from external phenomenological laws, disconnecting their model from the pore/cell structure.

It is crucial to highlight the multiscale nature of bioreactor systems for tissue engineering. The production of macroscopic subtitutes is the result of an infinite number of biological,

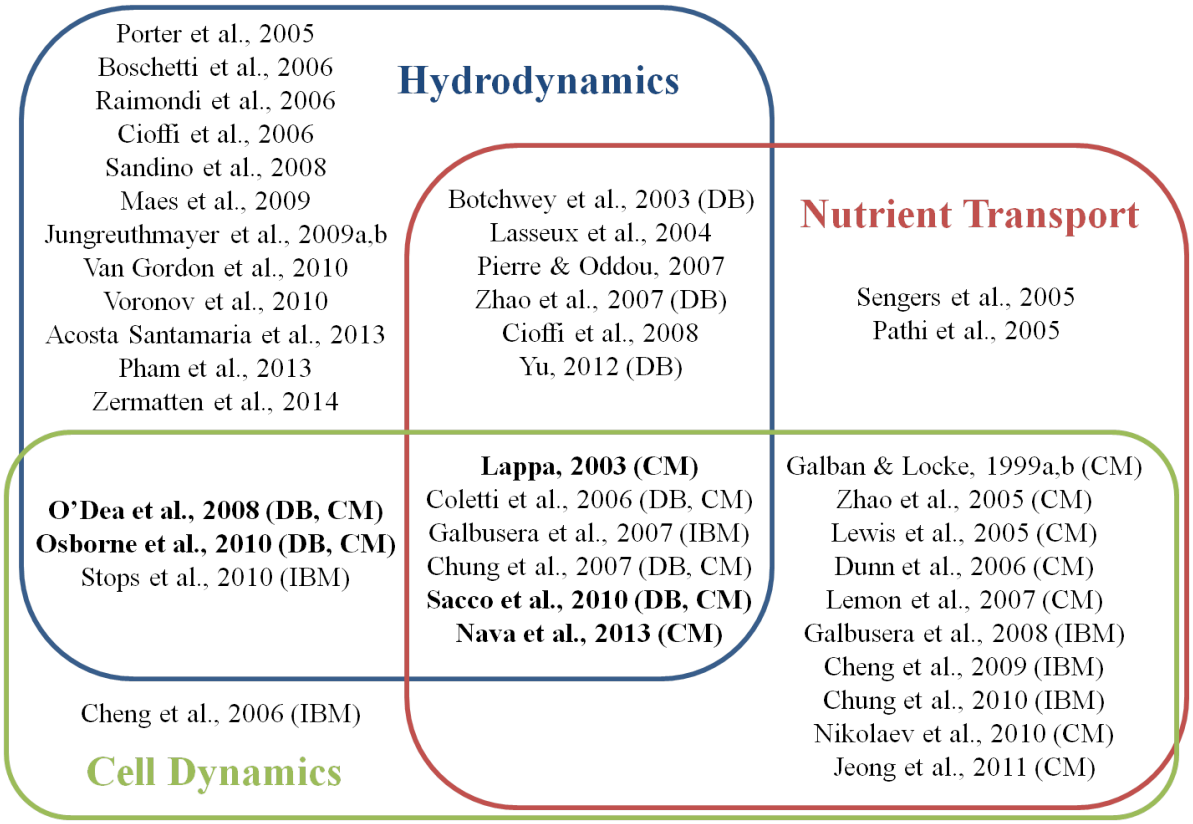

Figure 4.1 – Synthesis of the main modeling studies on bioreactors. (DB) : Darcy or Darcy-Brinkman flow, (CM) : Continuum model, (IBM) : Individual based model. References in **bold** include the effect of shear stress on cell dynamics.

biochemical and biophysical mechanisms occurring at the cell scale and below. Thus mathematical models aiming to describe tissue growth in a bioreactor must represent either cell scale phenomena, leading to high computational costs, either tissue scale processes, loosing information about the microscopic physics. All the challenge of homogenization methods, lies in managing the information lost through the up-scaling process.

Considering the scale at which the tissue grows, continuum models are the most suitable approach to describe substitute formation at the bioreactor level. However the validity of this type of representation should be discussed in terms of the following problematics :

- *How to correctly predict tissue growth when its origin phenomena are at the cell scale?* Continuum models are homogenized models, and their relevance at the tissue scale can only be assessed by a rigorous up-scaling of the phenomena occurring at the cellular scale. Although several homogenization methods exist, the quality of a continuum model is conditioned by the understanding of the cell scale physics. This necessitate experimental characterizations of cellular response to specific stimuli.
- *How to quantify cell response to specific stimuli?* The difficulty to control a distinct stimulus, and monitor its effects on a population of cells within a bioreactor motivates the use of specific experimental setups. To this purpose miniaturized bioreactors

have been designed [Laganà & Raimondi, 2012], however microfluidic systems offer a higher degree of control on the cell culture environment [Kreke & Goldstein, 2004; Leclerc et al., 2006; Korin et al., 2007; Scaglione et al., 2008; Park et al., 2010; Altmann et al., 2011; Chabanon et al., 2012]. In order to apprehend biological variability, advanced statistical analysis may be used to deduce representative cell behaviors and laws. This laws may be the basis for upscaling methods, or implemented in individual based models (IBMs).

- *How does tissue growth models can be validated?* Once solved, the tissue growth model must be confronted to reference solutions. In the case of homogenized models, direct numerical simulations (DNS) can be used as reference, but this mainly (in)validate the up-scaling procedure, not the fundamental physical assumptions. Ideally, the model solution should be confronted to experimental results. This implies good interactions between the mathematical and experimental models in order to define and compare relevant quantitative parameters that are accessible from both approaches.

The aim of this thesis is to investigate, through a combined modeling and experimental approach, tissue formation within a perfusion bioreactor based on David et al. [2011] (for a summary of the study, see Sec. 2.3).

From a modeling point of view, this bioreactor presents several challenging features related to transport in porous media. First, the double porosity architecture, which characteristic length scales are clearly separated, constitutes a heterogeneous porous media. The determination of the transport properties of this type of bi-structured system has several applications in industrial processes or in soil engineering [Soulaine et al., 2013]. Moreover the boundary between the porous granules and the culture medium around the cubes, forms a porous/fluid interface, which is a lively research problematic in momementum and mass transport [Goyeau et al., 2003; Valdés-Parada et al., 2013]. Second, the biological material is also a multiscale system with heterogeneous characteristics. Additionally, it is a reactive media (due to nutrient consumption and protein synthesis) with time evolving structure and parameters. Finally, there exists a strong interdependence between the three main phenomena : momentum transport, mass transport, and tissue growth (cell proliferation and ECM production).

From the experimental point of view, a number of challenges are related to the study of cell/tissue growth under perfusion within the bioreactor. Few reproducible methodologies allows the quantification in time and space of the biomass production, and most of them are destructive, necessitating time consuming experimental campaigns. Moreover, the question of what quantity should be measured is not trivial. Ideally, indicators representative of cell proliferation and tissue production should be defined. This indicators should be evaluated through a reproducible methodology, and facilitate the comparison and discussion with the modeling approach.

In the light of this discussion, the present thesis is developed on the following approach. First, a simplified bioreactor is defined, facilitating the study of the relevant phenomena related to cell/tissue growth under perfusion. Second, based on multiple upscaling procedures, a bioreactor scale theoretical model is built for momentum and mass transport. This macroscopic representation is shown to depend on relevant cell scale informations. Moreover, its

development allows the computation of the bioreactor effective properties through the resolution of a series of closure problems. Then an experimental methodology is proposed to quantify cell and tissue growth within the perfusion bioreactor. After introducing a biomass growth kinetic in the theoretical model, the comparison between the computed and experimental results is discussed.

PART II

MODELING MOMENTUM AND MASS TRANSPORT IN A PERFUSION BIOREACTOR

CHAPTER 5

INTRODUCTION ON THE MODELING APPROACH

DYNAMIC CULTURE SYSTEMS for the production of bone substitutes [El Haj et al., 1990; Janssen et al., 2006; Grayson et al., 2008, 2011; David et al., 2011] or cartilaginous substitutes [Freed et al., 1994; Cartmell et al., 2003; Raimondi et al., 2006], make use of culture medium perfusion through the biohybride in order to enhance the formation of homogeneous tissue. The circulation of culture medium promotes convection, improving transport of nutritive species in zones of the bio-material where diffusion is limited and optimal cell growth conditions are not met. Moreover fluid flow induces mechanical constraints on the tissue and stimulates cell proliferation and matrix deposition [Meyer et al., 1999; Korin et al., 2007; Park et al., 2010; McCoy & O'Brien, 2010]. Nevertheless, experimental results show that managing homogeneous nutritive supply and adequate mechanical stimuli within the bioreactor, is still the main challenge in order to improve the production of substitutes [David et al., 2011; Hansmann et al., 2013].

In this part of the thesis, a theoretical framework is developed, in order to characterize the influence of transport phenomena on the production of bone substitute in a perfusion bioreactor. The whole analysis is based on the double porosity bioreactor [David et al., 2011] described in Sec. 2.3. This system is a complex hierarchical structure, where the scaffold is made of a stack of microporous coral cubes, and where the biological phase evolves within and around the scaffold. Given the multitude of length scales at which transport phenomena influence growth mechanisms in the bioreactor, it appears necessary to take into account the multiscale aspect of the system. Yet, the existing studies on transport in bioreactors, either focus on the tissue/pore scale [Botchwey et al., 2003; Lasseux et al., 2004; Boschetti et al., 2006; Cioffi et al., 2008; Jungreuthmayer et al., 2009a; Chung et al., 2010; Yu, 2012] or the cellular scale [Fleury et al., 2006; Pedersen et al., 2007, 2010; Tarbell & Shi, 2013]. The challenge consists in providing a "macroscopic" model (i.e. at the bioreactor scale), which includes both the geometrical characteristics and the physical phenomena arising from the different lower scales. In order to deal with this objective, several upscaling procedures have been developed in the past [Cushman et al., 2002]. Among them, the volume averaging method has been extensively used in the last twenty years, to study mass transport phenomena

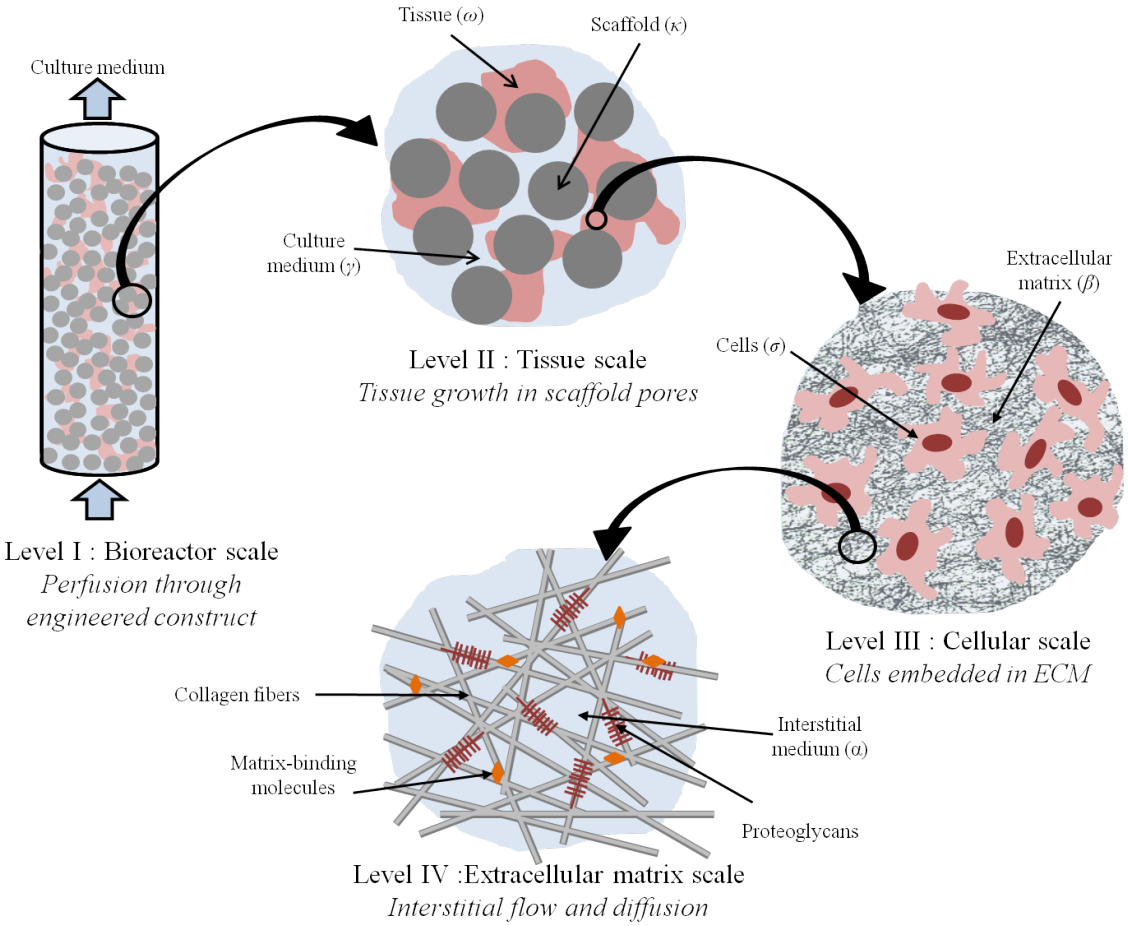

Figure 5.1 – Hyerarchy of the scales involved in a perfusion bioreactor

at biological interfaces. Although the literature on this method is quite furnished considering studies on biofilms [Ochoa et al., 1986; Wood & Whitaker, 1998, 1999, 2000; Wood et al., 2002, 2007, 2011; Golfier et al., 2009; Orgogozo et al., 2009, 2010; Davit et al., 2010], much less attention has been drawn to engineered tissues [Galban & Locke, 1999a,b; Lasseux et al., 2004; Pathi et al., 2005; Chung et al., 2007; Sacco et al., 2010].

As a first step toward the understanding of the complex transport and growth phenomena in the double porosity bioreactor, a slightly modified bioreactor model is proposed as the basis of this study. A detailed description and justification of the setup is presented along with the experimental study in Chap. 9. The main simplification has been to suppress the micro-porosity of the coral cube by using impermeable glass beads of 2mm diameter instead. Random sphere packing is a well characterized structure, and this geometry will facilitate the evaluation of the transport and cell growth mechanism in the porous media. Note that this configuration is conceptually the same than for a direct perfusion bioreactor.

As depicted in Fig. 5.1, this study is based on the definition of four scales, in order to represent the relevant transport phenomena influencing cell proliferation in the bioreactor. The bioreactor scale (level I), is the scale where the substitute is seen as a continuous material.

At the tissue scale (level II), three distinct regions are present, the growing biological tissue, the solid glass beads, and the culture medium. Yet the tissue is itself a complicated porous medium, constituted, at the cellular scale (level III), of cells and extracellular matrix (ECM). The study is pushed down to the ECM scale (level IV), where the influence of the fibrous structure of ECM on the transport properties are determined.

In the present part, the volume averaging method is extensively applied, in order to up-scale the momentum and mass transport from the ECM scale (level IV) up to the bioreactor scale (level I). The effective transport properties are evaluated at each scale, through the resolution of the corresponding closure problems.

CHAPTER 6

THE EXTRACELLULAR MATRIX SCALE

LET US START the modeling study of momentum and mass transport in the bioreactor, at the extracellular matrix scale. The tissue is composed of cells embedded in the extracellular matrix (ECM) (Fig. 5.1). Cells produce and interact with ECM trough binding protein complexes and membrane receptors. The porous aspect of ECM allows diffusion and convection of chemical species, as well as interstitial flow induced stimulation of the cells. The ECM serves as a physical support for the cells to evolve in space, and plays a role in the transmission of extracellular signals through binding proteins. Its composition can vary strongly from a type of tissue to another, but the main constituents are collagen fibers (2/3 of ECM proteins), proteoglycan, laminin and fibrin [Swartz & Fleury, 2007]. These proteins are arranged in a fibrous network filed with interstitial fluid, which can be plasma for *in vivo* soft tissues, or culture medium for *in vitro* engineered tissues. In both cases, the fluid is likely to be in movement due to physiological phenomena (e.g. pressure gradient between blood and lymphatic capillaries in soft tissues, dynamic compression in cartilage and bone) or experimental conditions (e.g. perfusion of culture medium in a bioreactor). A summary of the orders of magnitude related to mass and momentum transport in biological tissues is reported in Tab. 6.1.

The question of keeping convection into account when modeling mass transport in ECM is of great importance. Depending on the type of tissue and on the application, the order of magnitude of the Péclet number in the tissue can vary from 10^{-3} to 10^{-1} [Swartz & Fleury, 2007; Ng & Swartz, 2003, 2006]. Even though this relatively low values indicate that diffusion is the predominant process influencing mass transport, recent studies tend to point out the importance of convection induced by interstitial flow on cellular activity. Interstitial flow can influence cell fate by modifying its mechanical and its biochemical environment. Numerous articles showed the significant effects of shear stress stimulation on cell proliferation, even at very low values [Tardy et al., 1997; Leclerc et al., 2006; Garanich et al., 2007; Park et al., 2010; Luo et al., 2011]. The interactions between cells and the ECM are highly complex and play a critical role on the understanding of cells fate [Swartz & Fleury, 2007]. For example, it has been shown that under interstitial flow, cells rearrange the orientation od ECM collagen fibers in order to regulate the level of constraint they are experiencing [Ng & Swartz, 2006; Pedersen et al., 2010]. Fleury et al. [2006] showed that even at low Péclet number, interstitial

Parameters	**Order of magnitude**	**References**
Cell diameter (m)	10^{-5}	–
ECM fibers diameter (m)	10^{-7}	[Pedersen et al., 2007, 2010]
Interstitial flow velocity ($m.s^{-1}$)	0.1 - 2 $\times$ 10^{-6}	[Chary & Jain, 1989; Dafni et al., 2002; Jain, 1999; Swartz & Fleury, 2007; Tarbell & Shi, 2013]
Interstitial medium dynamic viscosity (except synovial fluid) ($Pa.s$)	0.75 - 2.2 $\times$ 10^{-4}	[Swartz & Fleury, 2007; Fournier, 2011]
Interstitial medium specific gravity	1 - 1.05	[Swartz & Fleury, 2007; Fournier, 2011]
Effective tissue diffusion coefficient ($m^2.s^{-1}$)	1 - 100 $\times$ 10^{-12}	[Malda et al., 2004; Swartz & Fleury, 2007]
Effective tissue permeability (m^2)	10^{-12} - 10^{-18}	[Levick, 1987; Swartz & Fleury, 2007; Fournier, 2011; Tarbell & Shi, 2013]

Table 6.1 – Orders of magnitude of ECM parameters

flow can induce subtle chemokine and morphogene gradients that can be sensed by cells and influence their migration. Intersitial flow is a significant phenomenon for the transport of macromolecules for which the diffusivity is limited, and for smaller molecules in the case of higher permeability matrices such that hydrogels. Moreover in the case of inflammatory environment and in some pathological tissues where permeability can be larger, the increase in lymphatic activity amplifies interstitial flow leading to higher Péclet numbers [Rutkowski & Swartz, 2007]. Under these considerations, in order to represent a wide range of experimental conditions, the convective effects of interstitial flow is included in our model of mass transport in the ECM.

6.1 Derivation of the ECM transport properties

In the present work, scale IV is considered in order to characterize the transport properties of ECM. Therefore the ECM fibrous structure is represented by a non-deformable, homogeneous and inert matrix (the η-phase). The interstitial medium, in our case culture medium, is modeled as an incompressible fluid constituting the α-phase (Fig. 6.1). For the seek of simplicity, a unique transported species A representing a nutritive element (e.g. glucose) is considered in this work, although the derivation of a multiple species model could be easily done following the same methodology (see for example [Wood & Whitaker, 1999, 2000]).

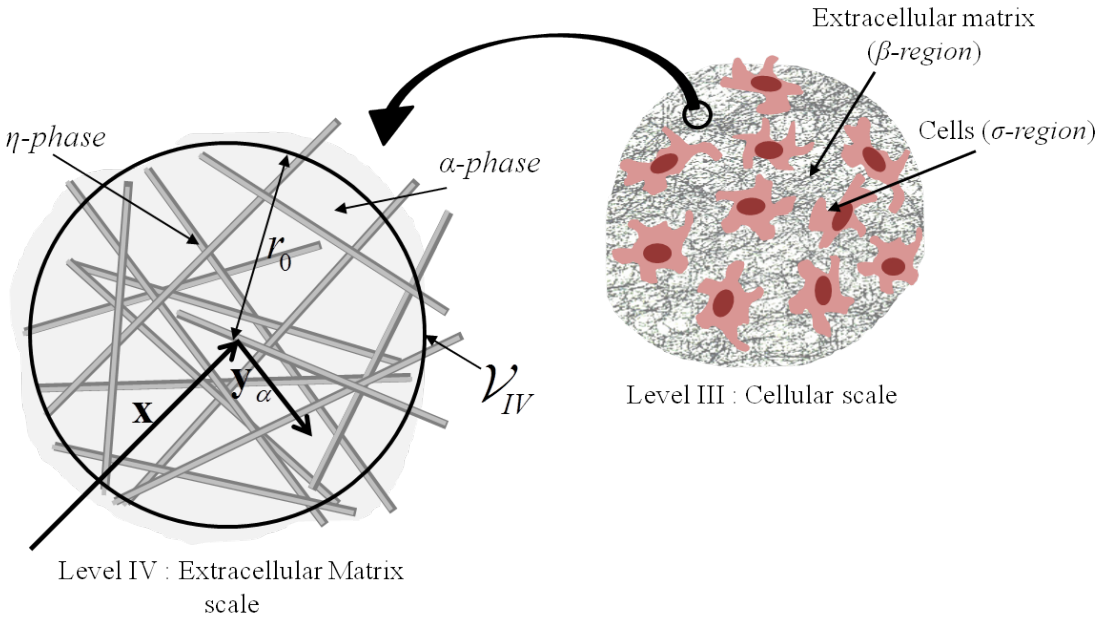

Figure 6.1 – Definition of the phases and length scales associated with the ECM averaging volume

The problem at the ECM scale (level IV) is formulated as a transient diffusion-convection problem coupled with a transient incompressible laminar flow

Level IV local problem :

$$\nabla.\mathbf{v}_\alpha = 0 \qquad \text{in the } \alpha\text{-phase} \tag{6.1}$$

$$\rho_\alpha \frac{\partial \mathbf{v}_\alpha}{\partial t} = -\nabla p_\alpha + \mu_\alpha \nabla^2 \mathbf{v}_\alpha + \rho_\alpha \mathbf{g} \qquad \text{in the } \alpha\text{-phase} \tag{6.2}$$

$$\frac{\partial c_{A\alpha}}{\partial t} + \nabla.\left(\mathbf{v}_\alpha c_{A\alpha}\right) = \nabla.(D_{A\alpha}\nabla c_{A\alpha}) \qquad \text{in the } \alpha\text{-phase} \tag{6.3}$$

$$\text{BC1}: \quad \mathbf{v}_\alpha = 0 \qquad \text{at } A_{\alpha\eta} \tag{6.4}$$

$$\text{BC2}: \quad \mathbf{n}_{\alpha\eta}.(D_{A\alpha}\nabla c_{A\alpha}) = 0 \qquad \text{at } A_{\alpha\eta} \tag{6.5}$$

where $\mathbf{v}_\alpha$ and p_α are the interstitial velocity and pressure respectively, and $c_{A\alpha}$ is the concentration of species A. ρ_α, μ_α and $D_{A\alpha}$ are respectively the density, dynamic viscosity and diffusivity coefficient of species A in the α-phase. $\mathbf{g}$ is the gravitational acceleration, $A_{\alpha\eta}$ is the interfacial area and $\mathbf{n}_{\alpha\eta}$ is the normal vector oriented from the α-phase toward the η-phase.

The problem described by Eqs. (6.2) to (6.5) has to be homogenized in order to obtain the transport equations and properties of the ECM equivalent region at level III. Following the volume averaging method [Whitaker, 1999], for a given quantity ψ_α associated with the α-phase, the *superficial average* is defined as

$$\langle \psi_\alpha \rangle = \frac{1}{\mathcal{V}_{IV}} \int_{V_\alpha} \psi_\alpha dV \tag{6.6}$$

where $\mathcal{V}_{IV}$ is the averaging volume associated with the ECM scale (Fig. 6.1). Because it is often more convenient to deal with an average defined only in one phase (and because this is the actual measured quantity), the *intrinsic average* is defined by

$$\langle \psi_\alpha \rangle^\alpha = \frac{1}{V_\alpha} \int_{V_\alpha} \psi_\alpha dV \tag{6.7}$$

where V_α is the volume of the α-phase within $\mathcal{V}_{IV}$. The superficial and intrinsic averages are related by the α-phase volume fraction $\varepsilon_\alpha = V_\alpha/\mathcal{V}_{IV}$ such as

$$\langle \psi_\alpha \rangle = \varepsilon_\alpha \langle \psi_\alpha \rangle^\alpha \tag{6.8}$$

Once the averaging operators applied to the conservation equations, the *general transport* and the *spacial averaging theorems* [Howes & Whitaker, 1985] need to be used

$$\left\langle \frac{\partial \psi_\alpha}{\partial t} \right\rangle = \frac{\partial \langle \psi_\alpha \rangle}{\partial t} - \frac{1}{\mathcal{V}_{IV}} \int_{A_{\alpha\eta}} \mathbf{n}_{\alpha\eta}.\mathbf{w}_{\alpha\eta}\psi_\alpha dA \tag{6.9}$$

$$\langle \nabla \psi_\alpha \rangle = \nabla \langle \psi_\alpha \rangle + \frac{1}{\mathcal{V}_{IV}} \int_{A_{\alpha\eta}} \mathbf{n}_{\alpha\eta}\psi_\alpha dA \tag{6.10}$$

$$\langle \nabla.\boldsymbol{\psi}_\alpha \rangle = \nabla.\langle \boldsymbol{\psi}_\alpha \rangle + \frac{1}{\mathcal{V}_{IV}} \int_{A_{\alpha\eta}} \mathbf{n}_{\alpha\eta}.\boldsymbol{\psi}_\alpha dA \tag{6.11}$$

where $\boldsymbol{\psi}_\alpha$ is a tensor quantity associated with the α-phase, $\mathbf{w}_{\alpha\eta}$ is the velocity of the interface $A_{\alpha\eta}$. The main prerequisite for all upscaling method is the separations between the characteristic length scales. Here we have

$$l_\alpha \ll r_0 \ll l_\beta \tag{6.12}$$

where l_α, r_0 and l_β are the length scales of the α-phase, the averaging volume and the ECM length scale at level III (Fig. 6.1) respectively.

On this basis, averaging the system described by Eqs. (6.2) to (6.5) is a classic problem [Whitaker, 1986a; Quintard & Whitaker, 1994c,b; Whitaker, 1999] and only the results are reported here (see App. A for more details on the derivation). Considering ρ_α, μ_α and $D_{A\alpha}$ constant within the averaging volume $\mathcal{V}_{IV}$, the *closed averaged equations* for momentum and mass transport are

$$\nabla.\langle \mathbf{v}_\alpha \rangle^\alpha = 0 \tag{6.13}$$

$$\rho_\alpha \varepsilon_\alpha^{-1} \frac{\partial \left(\varepsilon_\alpha \langle \mathbf{v}_\alpha \rangle^\alpha\right)}{\partial t} = -\nabla \langle p_\alpha \rangle^\alpha - \frac{\mu_\alpha}{\mathbf{K}_\beta^{\mathrm{III}}} \varepsilon_\alpha \langle \mathbf{v}_\alpha \rangle^\alpha + \mu_\alpha \nabla^2 \langle \mathbf{v}_\alpha \rangle^\alpha + \rho_\alpha \mathbf{g} \tag{6.14}$$

$$\frac{\partial \left(\varepsilon_\alpha \langle c_{A\alpha} \rangle^\alpha\right)}{\partial t} + \varepsilon_\alpha \langle \mathbf{v}_\alpha \rangle^\alpha . \nabla \langle c_{A\alpha} \rangle^\alpha = \nabla . \left(\mathbf{D}_{A\beta}^{\mathrm{III}} . \nabla \langle c_{A\alpha} \rangle^\alpha\right) \tag{6.15}$$

The capital exponent in the effective parameters $\mathbf{K}_\beta^{\mathrm{III}}$ and $\mathbf{D}_{A\beta}^{\mathrm{III}}$ reminds the level at which the parameters are valid, while the subscripts define the phase from which they are evaluated. One can recognize here the non-stationary form of Darcy-Brinkman equation [Brinkman, 1947] and a diffusion-dispersion transport equation. This set of equations is valid in the β-region at the cellular scale (level III) (Fig. 6.1), where the transport phenomena are influenced by the ECM scale (level IV) through the permeability $\mathbf{K}_\beta^{\mathrm{III}}$ and diffusion/dispersion tensor $\mathbf{D}_{A\beta}^{\mathrm{III}}$ defined as

$$\varepsilon_\alpha \mathbf{K}_\beta^{\mathrm{III}-1} = -\frac{1}{V_\alpha} \int_{A_{\alpha\sigma}} \mathbf{n}_{\alpha\eta} . \left(-\mathbf{I}\mathbf{b}_\alpha + \nabla \mathbf{B}_\alpha\right) dA \tag{6.16}$$

$$\mathbf{D}_{A\beta}^{\mathrm{III}} = D_{A\alpha} \left(\varepsilon_\alpha \mathbf{I} + \frac{1}{\mathcal{V}_{\mathrm{IV}}} \int_{A_{\alpha\eta}} \mathbf{n}_{\alpha\eta} \mathbf{d}_\alpha dA \right) - \langle \tilde{\mathbf{v}}_\alpha \mathbf{d}_\alpha \rangle \tag{6.17}$$

In Eqs. (6.16) and (6.17), $\mathbf{b}_\alpha$, $\mathbf{B}_\alpha$, and $\mathbf{d}_\alpha$ are the closure variables that have to fulfill the ECM scale (level IV) closure problems:

Closure problem for momentum transport (scale IV)

$$\nabla.\mathbf{B}_\alpha = 0 \tag{6.18}$$

$$0 = -\nabla \mathbf{b}_\alpha + \nabla^2 \mathbf{B}_\alpha + \varepsilon_\alpha \mathbf{K}_\beta^{\mathrm{III}-1} \tag{6.19}$$

$$\mathbf{B}_\alpha = -\mathbf{I} \qquad \text{at } A_{\alpha\eta} \tag{6.20}$$

$$\mathbf{B}_\alpha(\mathbf{x}) = \mathbf{B}_\alpha(\mathbf{x} + l_i) \qquad i = 1,2,3 \tag{6.21}$$

$$\mathbf{b}_\alpha(\mathbf{x}) = \mathbf{b}_\alpha(\mathbf{x} + l_i) \qquad i = 1,2,3 \tag{6.22}$$

$$\langle \mathbf{B}_\alpha \rangle^\alpha = 0 \tag{6.23}$$

Closure problem for mass transport (scale IV)

$$\tilde{\mathbf{v}}_\alpha + \mathbf{v}_\alpha . \nabla \mathbf{d}_\alpha = D_{A\alpha} \nabla^2 \mathbf{d}_\alpha \tag{6.24}$$

$$-\mathbf{n}_{\alpha\eta} . \nabla \mathbf{d}_\alpha = \mathbf{n}_{\alpha\eta} \qquad \text{at } A_{\alpha\eta} \tag{6.25}$$

$$\mathbf{d}_\alpha(\mathbf{x}) = \mathbf{d}_\alpha(\mathbf{x} + l_i) \qquad i = 1,2,3 \tag{6.26}$$

$$\langle \mathbf{d}_\alpha \rangle^\alpha = 0 \tag{6.27}$$

These closure problems are considered here to be quasi-static by assuming the spacial and time scales to be well separated [Goyeau et al., 1999]. To replace the unknown boundary conditions of the averaging volume, the closure variables are solved in a spatially periodic unit cell of dimension l_i (Eqs. (6.21), (6.22) and (6.26)). Assuming the unit cells to be spatially periodic does not imply the ECM to be periodic, however it has to be homogeneous. Finally, the averages of the closure variables are shown to be null, and this constraints are required for solvability.

The solution of these two closure problems on a representative unit cell allow us to compute the ECM permeability $\mathbf{K}_\beta^{\mathrm{III}}$ and diffusion/dispersion tensor $\mathbf{D}_{A\beta}^{\mathrm{III}}$. The following section present the numerical resolution procedures and results.

6.2 Computation of the ECM transport properties

In this section the effective transport parameters of the ECM are computed. The ECM permeability and the diffusion/dispersion tensor are obtained by solving the closure problem for momentum (Eqs. (6.18) to (6.23)) and mass transport (Eqs. (6.24) to (6.27)) respectively.

6.2.1 ECM permeability

The closure problem for momentum transport given by Eqs. (6.18) to (6.23) is an integro-differential problem which is delicate to solve numerically. In order to write it in a more computationally convenient form, a variable change is proceeded [Whitaker, 1999, Chap. 4]

$$\mathbf{B'}_\alpha = \varepsilon_\alpha^{-1}\left(\mathbf{B}_\alpha + \mathbf{I}\right).\mathbf{K}_\beta^{\mathrm{III}} \tag{6.28}$$

$$\mathbf{b'}_\alpha = \varepsilon_\alpha^{-1}\mathbf{b}_\alpha.\mathbf{K}_\beta^{\mathrm{III}} \tag{6.29}$$

so the closure problem can be written in the form of an incompressible static stokes flow problem

$$0 = -\nabla\mathbf{b'}_\alpha + \nabla^2\mathbf{B'}_\alpha + \mathbf{I} \qquad \text{in the } \alpha\text{-phase} \tag{6.30}$$

$$\nabla.\mathbf{B'}_\alpha = 0 \qquad \text{in the } \alpha\text{-phase} \tag{6.31}$$

$$\mathbf{B'}_\alpha = 0 \qquad \text{at } A_{\alpha\eta} \tag{6.32}$$

$$\mathbf{B'}_\alpha(\mathbf{x}) = \mathbf{B'}_\alpha(\mathbf{x} + l_i) \qquad i = 1,2,3 \tag{6.33}$$

$$\mathbf{b'}_\alpha(\mathbf{x}) = \mathbf{b'}_\alpha(\mathbf{x} + l_i) \qquad i = 1,2,3 \tag{6.34}$$

$$\langle\mathbf{B'}_\alpha\rangle^\alpha = \varepsilon_\alpha^{-1}\mathbf{K}_\beta^{\mathrm{III}} \tag{6.35}$$

The boundary value problem given by Eqs. (6.30) to (6.34) can be solved in a given geometry with any standard routine capable of dealing with a Stokes flow. Moreover permeability can directly be obtained with Eq. (6.35).

The ECM is a fibrous structure, and we aim to solve the closure problem on a representative fibrous geometry. The main difficulty of numerical computation on complicated geometries

such as fibrous mediums, is the mesh generation at the interfaces between the fluid and the solid. To facilitate this, we adopt a *penalty method* where Eqs. (6.30) and (6.32) are substituted by a "Brinkman like" transport equation valid in the whole domain (α and η phases)

$$0 = -\nabla \mathbf{b}' + \nabla^2 \mathbf{B}' + \mathbf{I} + \frac{\mathbf{B}'}{K_{\text{num}}} \tag{6.36}$$

where $\mathbf{B}'$ and $\mathbf{b}'$ are variables both defined in the α and η phases, and which tend to ${\mathbf{B}'}_\alpha$ and ${\mathbf{b}'}_\alpha$ respectively in the α-phase. K_{num} is an artificial variable that is used to numerically penalize the $\mathbf{B}'$-field in the solid η-phase. When K_{num} tends to infinity (in the α-phase), Eq. (6.36) reduces to the Stokes flow equation (Eq. (6.30)), and when K_{num} tends to zero (in the η-phase), the last term in Eq. (6.36) tends to plus infinity implying the $\mathbf{B}'$-field to be null in order to fulfill the equality. Thus we define K_{num} as an heavy-side function such as

$$K_{\text{num}} = \begin{cases} 10^{20} & \text{in the } \alpha\text{-phase} \\ 10^{-20} & \text{in the } \eta\text{-phase} \end{cases} \tag{6.37}$$

and solve the one domain problem

$$0 = -\nabla \mathbf{b}' + \nabla^2 \mathbf{B}' + \mathbf{I} + \mathbf{B}' K_{\text{num}}^{-1} \tag{6.38}$$

$$\nabla . \mathbf{B}' = 0 \tag{6.39}$$

$$\mathbf{B}'(\mathbf{x}) = \mathbf{B}'(\mathbf{x} + l_i) \qquad i = 1, 2, 3 \tag{6.40}$$

$$\mathbf{b}'(\mathbf{x}) = \mathbf{b}'(\mathbf{x} + l_i) \qquad i = 1, 2, 3 \tag{6.41}$$

$$\langle \mathbf{B}' \rangle^\alpha = \varepsilon_\alpha^{-1} \mathbf{K}_\beta^{\text{III}} \tag{6.42}$$

Note here that in the one domain approach, the boundary condition Eq. (6.32) is automatically satisfied.

Eqs. (6.38) to (6.42) are solved using the finite element method software Comsol Multiphysics 4.3b with iterative solver GMRES and left preconditioning. In order to validate the quality of our numerical solution, a comparison is first performed with the analytic solution of the drag coefficient around a sphere in a cubic domain [Zick & Homsy, 1982]. A mesh convergence study is carried out for different radius of the sphere (thus different ε_α), leading to relative errors on the velocity field under 0.5%. Fig. 6.2 shows the comparison of our results with those of Zick & Homsy [1982]. The drag coefficient C is related to the permeability through

$$C = \frac{2}{9} \frac{r^2}{1 - \varepsilon_\alpha} \frac{1}{K_\beta^{\text{III}}} \tag{6.43}$$

where $r = [3/4\pi(1 - \varepsilon_\alpha)]^{1/3}$ is the radius of the sphere. Fig. 6.2 shows a perfect agreement with the analytic solution.

We now wish to study the influence of the fibrous structure on the ECM permeability. To that purpose, five different random fibrous media are constituted by constructing various sets of cylinders. A Matlab script is used to generate a list of random coordinates for N points and vectors comprised in a unit cube of size l_α. The list is then imported in Comsol Multiphysics 4.3b, and set as parameters for the cylinders positions. The heights are fixed ($H = l_\alpha$) and

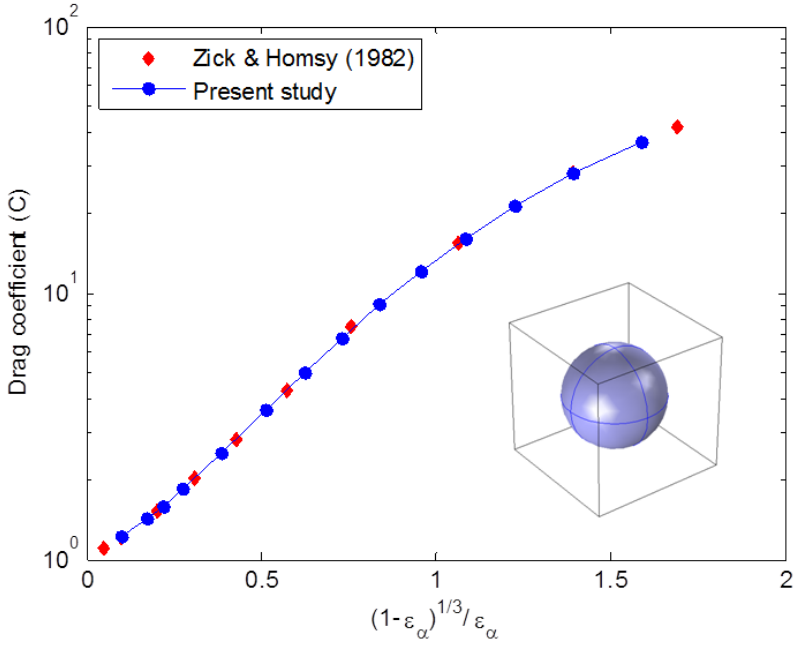

Figure 6.2 – Solution of the one domain closure problem. Validation of the resolution scheme (The drag coefficient is related to the permeability through Eq. (6.43))

all the cylinders have the same radius (R). Since the closure problem is solved on a periodic unit cell, the fibrous media has to be periodic. This is done by generating an array of unit periodicity with all the cylinders, and subtracting this array to a unit cube (see Fig. 6.3). The geometry modeling in Comsol is done with the "CAD import module kernel". The interstitial fluid volume fraction ε_α is modified either by taking $N = 10$ cylinders and varying their radius R between $0.02l_\alpha$ and $0.14l_\alpha$, or by increasing the number of cylinder N for a constant radius $R = 0.04l_\alpha$. In order to avoid very small elements in the meshing process, some cylinders have to be manually rotated along their axes to facilitate the intersections of the surfaces. Total meshes are composed of 100 000 to 700 000 tetrahedral elements.

The one domain closure problem (Eqs. (6.38) to (6.42)) is solved for each geometry, and all the components of $\mathbf{K}_\beta^{\mathrm{III}}$ are obtained. For all the configurations, the diagonal components of the permeability tensor lay in the same order of magnitude. This confirms the isotropy of the randomly generated fibrous mediums. Fig. 6.4 shows the longitudinal component of the permeability ($K_{\alpha xx}^{\mathrm{III}}$) for the different porous fibrous mediums. For comparison, the permeabilities of porous mediums composed of spheres in Cubic Simple (CS) or Cubic Centered (CC) arrangements are displayed. All the fibrous mediums permeabilities are in the same range and shows a similar dependence to the fluid volume fraction. However the permeability of the CS porous medium is two times higher than for the CC porous medium, which is five to ten times higher than the permeabilities of the fibrous porous mediums. Moreover, the permeability of the fibrous porous mediums increases slower with ε_α than the spherical porous mediums. These differences can be interpreted in term of tortuosity (which is actually the integral of $\mathbf{n}_{\alpha\eta}\mathbf{b}_\alpha$ in the definition of the permeability in Eq. (6.16)). Indeed fibrous mediums are, for a given porosity, more tortuous than the spherical porous mediums, thus they

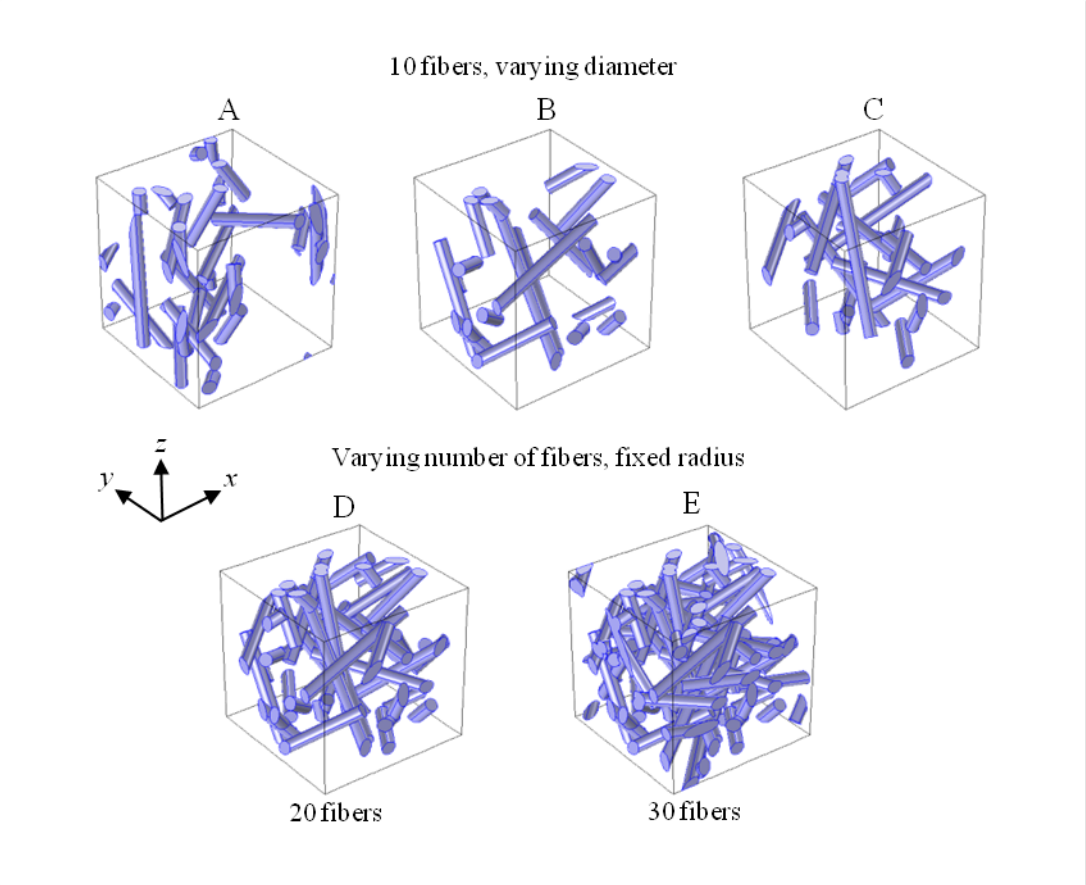

Figure 6.3 – The five different configurations of random fibrous medium unit cells used for the computations of $\mathbf{K}_{\beta}^{\mathrm{III}}$

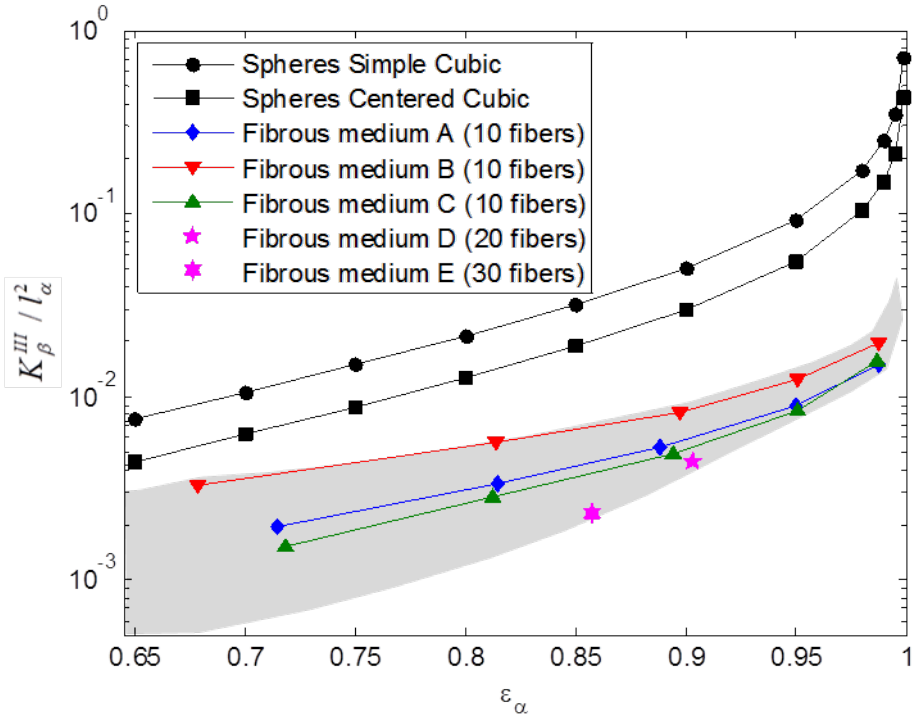

Figure 6.4 – Normalized permeability of random fibrous medium ($\mathbf{K}_\beta^{\mathrm{III}}$) as a function of the interstitial medium volume fraction (ε_α). The grey zone represent the range of permeability of the fibrous mediums

are less permeable. Similarly, the CC porous mediums are more tortuous than the CS porous mediums, giving rise to lower permeabilities.

6.2.2 ECM diffusion-dispersion tensor

Next, the diffusion-dispersion tensor $\mathbf{D}_{A\beta}^{\mathrm{III}}$ is computed by solving the closure problem for mass transport (Eqs. (7.61) to (7.67)). To that purpose, the problem is written in its dimensionless form

$$\mathrm{Pe}_\alpha \left(\tilde{\mathbf{v}}'_\alpha + \mathbf{v}'_\alpha . \nabla \mathbf{d}'_\alpha\right) = \nabla^2 \mathbf{d}'_\alpha \tag{6.44}$$

$$-\mathbf{n}_{\alpha\eta} . \nabla \mathbf{d}'_\alpha = \mathbf{n}_{\alpha\eta} \qquad \text{at } A_{\alpha\eta} \tag{6.45}$$

$$\mathbf{d}'_\alpha(\mathbf{x}) = \mathbf{d}'_\alpha(\mathbf{x} + l_i) \qquad i = 1, 2, 3 \tag{6.46}$$

$$\langle \mathbf{d}'_\alpha \rangle^\alpha = 0 \tag{6.47}$$

where the dimensionless variables are defined as

$$\mathbf{d}'_\alpha = \frac{\mathbf{d}_\alpha}{l_\alpha} \qquad \tilde{\mathbf{v}}'_\alpha = \frac{\tilde{\mathbf{v}}_\alpha}{\|v_\alpha\|} \qquad \mathbf{v}'_\alpha = \frac{\mathbf{v}_\alpha}{\|v_\alpha\|} \tag{6.48}$$

and

$$\|v_\alpha\| = \left(\langle \mathbf{v}_\alpha \rangle^\alpha . \langle \mathbf{v}_\alpha \rangle^\alpha\right)^{1/2} \tag{6.49}$$

The Péclet number at the ECM scale (level IV), represents the relative contributions of mass transport due to convective and diffusive effects in the α-phase. It is defined as

$$\mathrm{Pe}_\alpha = \frac{\|v_\alpha\| l_\alpha}{D_{A\alpha}} \tag{6.50}$$

This formulation of the closure problem allows to compute the diffusion-dispersion tensor for different Péclet numbers, without having to solve the velocity field each time. For a known $\mathbf{v}_\alpha$-field, and supposing a stationary Stokes flow, the solution of Eqs. (6.44) to (6.47) is obtained and the dimensionless diffusion-dispersion tensor is computed as

$$\frac{\mathbf{D}^{\mathrm{III}}_{A\beta}}{D_{A\alpha}} = \left(\varepsilon_\alpha \mathbf{I} + \frac{1}{\mathcal{V}_{\mathrm{IV}}} \int_{A_{\alpha\eta}} \mathbf{n}_{\alpha\eta} \mathbf{d}'_\alpha dA \right) - \mathrm{Pe}_\alpha \langle \tilde{\mathbf{v}}'_\alpha \mathbf{d}'_\alpha \rangle \tag{6.51}$$

Once again the method of penalty is adopted to facilitate the resolution in complicated geometries. A diffusion coefficient of $10^{-20} D_{A\alpha}$ is imposed in the κ-phase canceling the diffusion in the solid. The accuracy of the solution is first tested on a two-dimensional square unit cell with a square solid inclusion (Fig. 6.5). An excellent agreement with the results of Amaral Souto & Moyne [1997] is observed.

Returning to the fibrous geometries, Eqs. (6.44) to (6.47) are solved in the random fibrous medium A for a Péclet number varying from 0.1 to 1000. Fig. 6.6 shows the diagonal components of the diffusion-dispersion tensor for a flow along the x-direction. As expected, two distinct regimes are observed. For a Péclet number under 1, diffusion is the dominant process and $\mathbf{D}^{\mathrm{III}}_{A\beta}$ is a constant determined only by the molecular diffusion coefficient. For higher Péclet, dispersion occurs and $\mathbf{D}^{\mathrm{III}}_{A\beta}$ increases up to two orders of magnitude in the longitudinal direction. The transverse components of $\mathbf{D}^{\mathrm{III}}_{A\beta}$ are slightly higher in the dispersive regime than in the diffusive regime. A small difference between the y and z components of the transverse dispersion can be observed, due to the anisotropy of the fibrous geometry. Yet, this variation is negligible compared to the longitudinal dispersion, and it is reasonable to conclude that the fibrous medium is isotropic in regard to dispersive effects.

In practical cases, the interstitial flow in the ECM gives rise to Péclet of the order of 10^{-3} to 10^{-1} [Swartz & Fleury, 2007; Ng & Swartz, 2003, 2006]. This indicates, in regard to the results presented in Fig. 6.6, that dispersion does not occur in the ECM. Thus this process will not be investigated further at scale IV, and for the rest of the study, $\mathbf{D}^{\mathrm{III}}_{A\beta}$ is supposed independent of the fluid flow intensity.

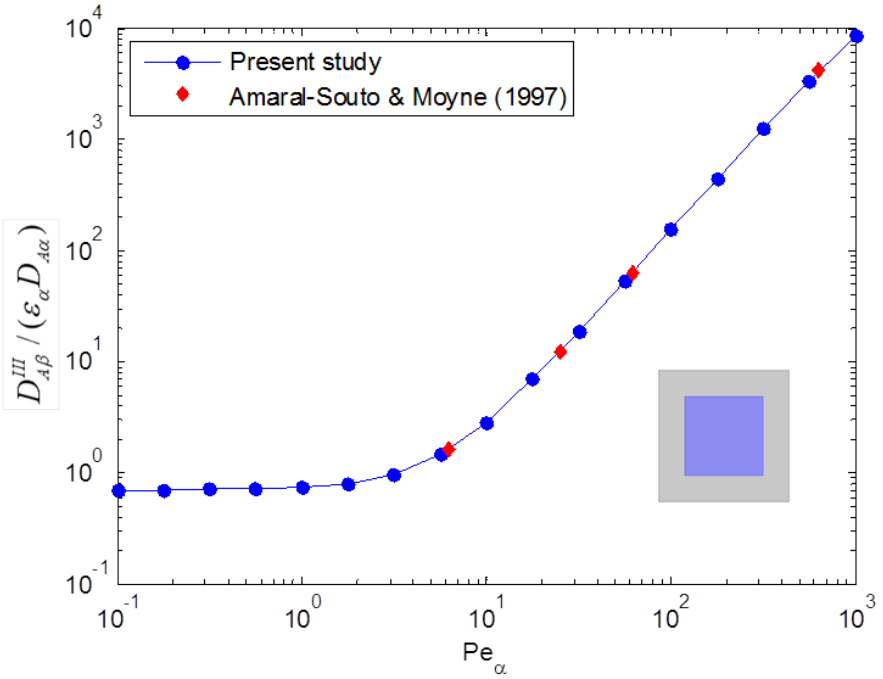

Figure 6.5 – Solution of the one domain closure problem for mass transport. Diffusion-dispersion around in-line square cylinders, validation of the closure resolution scheme ($\varepsilon_\alpha = 0.64$)

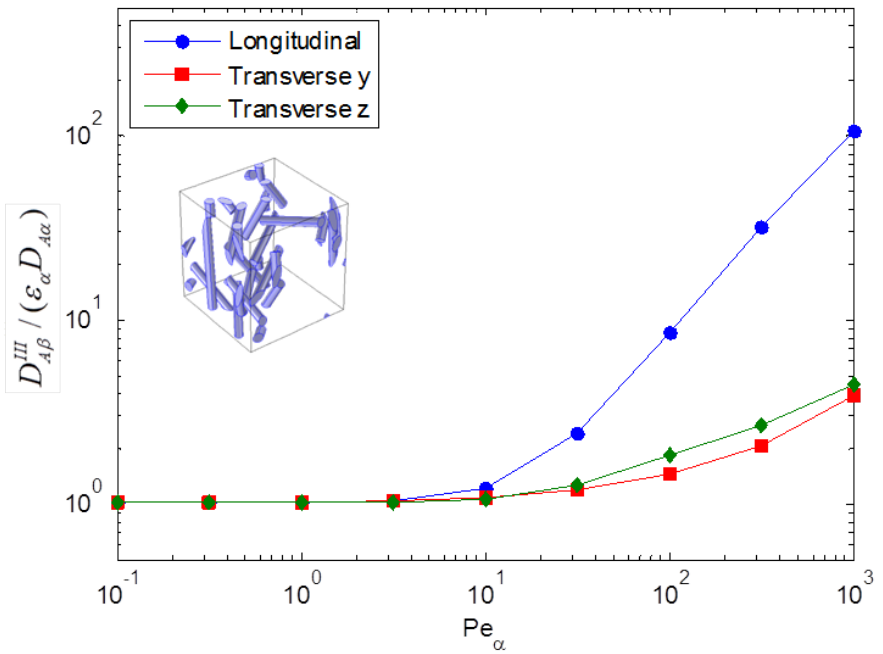

Figure 6.6 – Diagonal components of the diffusion-dispersion tensor in the random fibrous medium A (10 fibers, $R = 0.2l_\alpha$, $\varepsilon_\alpha = 0.9503$)

CHAPTER 7

THE CELLULAR SCALE

NOW THAT the ECM transport properties have been evaluated, we are ready to describe the cellular scale (level III) in terms of momentum and mass transport. Then a second upscaling is carried to determine the tissue effective transport properties (level II). After solving the closure problems related to these properties, the dependencies between level IV and level III effective parameters are shown.

One of the main difference with the previous section, is that the cell is likely to evolve due to division, migration or death. This implies that the volume fractions at the cellular scale are not constant anymore, and that special care as to be taken about the velocity of the interface between the cells and the ECM.

7.1 Local description of the cellular scale

The cellular scale (level III) is composed of cells embedded in ECM (Fig. 7.1). Two regions are represented : the ECM region (β) where species are transported via diffusion and convection, and the cellular region (σ) where species are transported by diffusion, and where reactions occurs (consumption or production of species).

Although the extracellular region (β) is a complex fibrous medium at level IV, at the cellular scale (level III) it is considered as a continuous and homogeneous equivalent region. The conservation equations for momentum and mass transport as well as the effective parameters in the β-region have been determined in Chap. 6.

But before using Eqs. (6.13) to (6.15) as local equations describing mass and momentum transport in the β-region, attention should be paid to the continuity equation Eq. (6.13). Indeed, at the cellular scale, cell growth is present and the interfacial velocity between the cells (σ-phase) and the ECM (β-region) is not null in general. For this reason a more general form of Eq. (6.13) should be taken at the cellular scale. To that purpose, let us go back to the ECM scale (level IV), and write down the general form of the mass conservation equations

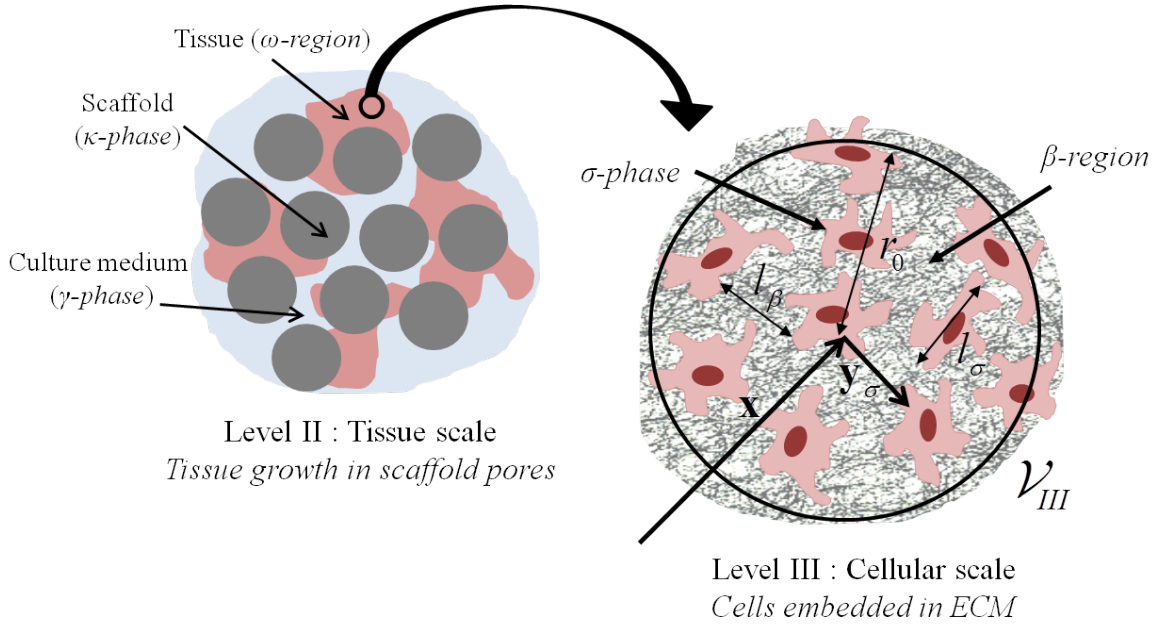

Figure 7.1 – Definition of the phases and length scales associated with the cellular averaging volume

for the α and η-phases.

$$\frac{\partial \rho_\alpha}{\partial t} + \nabla.(\rho_\alpha \mathbf{v}_\alpha) = 0 \quad \text{in the } \alpha\text{-phase} \tag{7.1}$$

$$\frac{\partial \rho_\eta}{\partial t} = Q_\eta \quad \text{in the } \eta\text{-phase} \tag{7.2}$$

where ρ_η is the density of the solid η-phase, and Q_η is the production rate of collagen fibers. The ECM is produced by cells, and we expect Q_η to be dependent on the cell density, and on the concentration of species A in the cellular region. While in the present part Q_η is kept general, it will be explicitly defined in Chap. 10, where the tissue growth kinetic will be introduced. Note that, since the collagen fibers are considered as solids, the velocity in the η-phase is null. In order to obtain the cellular scale mass conservation equation in the β-region, Eqs. (7.1) and (7.2) are averaged. Using the general transport and the spacial averaging theorems, we obtain

$$\frac{\partial (\varepsilon_\alpha \langle \rho_\alpha \rangle^\alpha)}{\partial t} + \nabla.(\varepsilon_\alpha \langle \rho_\alpha \mathbf{v}_\alpha \rangle^\alpha) = -\frac{1}{\mathcal{V}_{\text{IV}}} \int_{A_{\alpha\eta}} \mathbf{n}_{\alpha\eta}.(\mathbf{v}_\alpha - \mathbf{w}_{\alpha\eta})\, \rho_\alpha dA \tag{7.3}$$

$$\frac{\partial (\varepsilon_\eta \langle \rho_\eta \rangle^\eta)}{\partial t} = \langle Q_\eta \rangle + \frac{1}{\mathcal{V}_{\text{IV}}} \int_{A_{\eta\alpha}} \mathbf{n}_{\eta\alpha}.\mathbf{w}_{\alpha\eta} \rho_\eta dA \tag{7.4}$$

Where $\mathbf{w}_{\alpha\eta}$ is the velocity of interface between the α and η phases. It is very reasonable to assume that, within the averaging volume $\mathcal{V}_{\text{IV}}$, the density of each phase is constant within its phase

$$\rho_\alpha = \langle \rho_\alpha \rangle^\alpha \qquad \rho_\eta = \langle \rho_\eta \rangle^\eta \tag{7.5}$$

This allows, after adding up the two averaged equations, to write the mass conservation equation in the β-region in the form

$$\frac{\partial(\varepsilon_\alpha\rho_\alpha+\varepsilon_\eta\rho_\eta)}{\partial t}+\nabla.(\varepsilon_\alpha\rho_\alpha\langle\mathbf{v}_\alpha\rangle^\alpha)=\langle Q_\eta\rangle-\frac{1}{\mathcal{V}_{\text{IV}}}\int_{A_{\alpha\eta}}\mathbf{n}_{\alpha\eta}.\left[(\mathbf{v}_\alpha-\mathbf{w}_{\alpha\eta})\,\rho_\alpha+\mathbf{w}_{\alpha\eta}\rho_\eta\right]dA \tag{7.6}$$

Here, the surface integral represents the mass transfer at the interface between the α and η phases. Since the mass is conserved at $A_{\alpha\eta}$, that is to say

$$\mathbf{n}_{\alpha\eta}.\left(\mathbf{v}_\alpha-\mathbf{w}_{\alpha\eta}\right)\rho_\alpha=-\mathbf{n}_{\alpha\eta}.\mathbf{w}_{\alpha\eta}\rho_\eta \qquad \text{at } A_{\alpha\eta} \tag{7.7}$$

The last term in Eq. (7.6) is null, allowing to write the averaged mass conservation equation in the ECM as

$$\frac{\partial(\varepsilon_\alpha\rho_\alpha+\varepsilon_\eta\rho_\eta)}{\partial t}+\nabla.(\rho_\alpha\langle\mathbf{v}_\alpha\rangle)=\langle Q_\eta\rangle \tag{7.8}$$

The first term on the left hand side represents the conservation of the β-region density, and this equation will be used at the cellular scale as the mass conservation equation in the β-region.

For sake of simplicity in the subscripts, we will use the following notation correspondences to link the ECM and cellular scales

$$\mathbf{v}_\beta\equiv\langle\mathbf{v}_\alpha\rangle \qquad \text{in the } \beta\text{-region} \tag{7.9}$$
$$p_\beta\equiv\langle p_\alpha\rangle^\alpha \qquad \text{in the } \beta\text{-region} \tag{7.10}$$
$$c_{A\beta}\equiv\langle c_{A\alpha}\rangle \qquad \text{in the } \beta\text{-region} \tag{7.11}$$
$$\rho_\beta\equiv\varepsilon_\alpha\rho_\alpha+\varepsilon_\eta\rho_\eta \qquad \text{in the } \beta\text{-region} \tag{7.12}$$
$$Q_\beta\equiv\langle Q_\eta\rangle \qquad \text{in the } \beta\text{-region} \tag{7.13}$$

One has to keep in mind that $\mathbf{v}_\beta$ and $c_{A\beta}$ are *superficial* averages of $\mathbf{v}_\alpha$ and $c_{A\alpha}$ respectively, while p_β is an *intrinsic* average of p_α.

Using these notations, the closed averaged conservation Eqs. (6.14), (6.15) and (7.8), can be written in the form of local conservation equations in the β-region

$$\frac{\partial\rho_\beta}{\partial t}+\nabla.\left(\rho_\alpha\mathbf{v}_\beta\right)=Q_\beta \quad \text{in the } \beta\text{-region} \tag{7.14}$$

$$\rho_\alpha\varepsilon_\alpha^{-1}\frac{\partial\mathbf{v}_\beta}{\partial t}=-\nabla p_\beta-\frac{\mu_\alpha}{\mathbf{K}_\beta^{\text{III}}}\mathbf{v}_\beta+\mu_\alpha\varepsilon_\alpha^{-1}\nabla^2\mathbf{v}_\beta+\rho_\alpha\mathbf{g} \qquad \text{in the } \beta\text{-region} \tag{7.15}$$

$$\varepsilon_\alpha\frac{\partial c_{A\beta}}{\partial t}+\nabla.\left(\mathbf{v}_\beta c_{A\beta}\right)=\nabla.(\mathbf{D}_{A\beta}^{\text{III}}.\nabla c_{A\beta}) \qquad \text{in the } \beta\text{-region} \tag{7.16}$$

Momentum transport in the β-region is modeled via a Darcy-Brinkman equation [Brinkman, 1947] taking into account the fibrous structure of the ECM. The effective parameters $\mathbf{K}_\beta^{\text{III}}$ and $\mathbf{D}_{A\beta}^{\text{III}}$ defined in Eqs. (6.16) and (6.17) are dependent on the structure of the ECM at level IV through the closure problem (Eqs. (6.18) to (6.22)). In Eq. (7.17), cell metabolism is represented by the consumption of the species through a Michaelis-Menten reaction kinetic [Chung et al., 2007; Ma et al., 2006; Nikolaev et al., 2010; Sacco et al., 2010; Zhao et al.,

2005; Wood & Whitaker, 1998, 1999, 2000; Wood et al., 2002, 2007; Golfier et al., 2009; Orgogozo et al., 2009, 2010].

Transport equations must now be defined in the σ-phase. The cellular region is actually a structured medium compartmentalized into organelles with specific functions and properties. This organelles are themselves enveloped by simple (peroxisomes, endoplasmic reticulum, golgi apparatus, lysosomes) or double (nucleus, mitochondrion) membranes which act as barriers for solutes. Some of this organelles such as the endoplasmic reticulum and the golgi apparatus present a folded like porous structure. The disposition and geometry of the organelles, their membrane properties end the cytoskeleton structure are parameters that influence mass transport inside the cells [Kühn et al., 2011; Höfling & Franosch, 2013]. The representation of the heterogenity and the complexity of these transport processes is out of the scope of this study, and only simple diffusion and reaction of the species A is considered in this work. Here the intracellular σ-region is supposed to be a continuous and homogeneous phase where only diffusion and reaction take place. This is represented by the following mass conservation equations

$$\frac{\partial c_{A\sigma}}{\partial t} = \nabla.(D_{A\sigma}\nabla c_{A\sigma}) - k_A \frac{c_{A\sigma}}{c_{A\sigma} + K_A} \qquad \text{in the } \sigma\text{-phase} \tag{7.17}$$

$$\frac{\partial \rho_\sigma}{\partial t} = Q_\sigma \qquad \text{in the } \sigma\text{-phase} \tag{7.18}$$

where $c_{A\sigma}$ is the species point concentration in the σ-phase. $D_{A\sigma}$ is the diffusion coefficient, k_A and K_A are respectively the specific degradation rate of species A and half saturation constant of the reaction kinetic. ρ_σ and Q_σ are the mass density and the cell production rate in the σ-phase respectively. It should be emphasized that, since we do not know the specific transport mechanism inside the cells, the velocity within the σ-phase is supposed null. The cell production rate Q_σ is the source of cell growth, and should be a function of the σ-phase concentration, as well as the velocity in the β-region inducing shear stress at $A_{\beta\sigma}$. The primary goal of this chapter, is the assessment of the transport properties of the tissue, and the definition of Q_σ in regard to cell/tissue production will be further discussed in Chap. 10.

The system remains to be completed with appropriate boundary conditions at the interface between the β-region and the σ-phase. Animal cells membranes are composed of phospholipids arranged in bilayer. Because of the hydrophobic nature of the inner part of this layer, the membrane is a barrier to the movement of many solutes such as hydrophilic ions and sugar. In order to control the transport of this molecules across the membrane, channel and carrier proteins are present in the bilayer. This transporter proteins have specific mechanisms, gates and kinetics [Ashcroft, 1999]. At the contrary, small uncharged molecules such as oxygen, carbon dioxide and some hormones can dissolve through the membrane and pass across it by simple diffusion. In the case of glucose, facilitated diffusion from the extracellular region to the cytoplasm is mediated by fourteen known membrane transporters called Glut proteins [Thorens & Mueckler, 2010]. Not all of their mechanisms and functions are yet fully known, but each has a specific role in the control of glucose intracellular concentration. This level of complexity is out of the scope of this study, and a single carrier model representing facilitated transport of the species A through cell membrane is adopted [Wood & Whitaker, 1998, 1999,

2000; Wood et al., 2002]

$$\text{BC1}: \quad -\mathbf{n}_{\beta\sigma}.\left(\mathbf{D}^{\text{III}}_{A\beta}.\nabla c_{A\beta}+\mathbf{w}_{\beta\sigma}c_{A\beta}\right)=\frac{E_0\left(c_{A\beta}-\alpha_0 c_{A\sigma}\right)}{\alpha_1+\alpha_2 c_{A\beta}+\alpha_3 c_{A\sigma}+\alpha_4 c_{A\beta}c_{A\sigma}} \quad \text{at } A_{\beta\sigma} \tag{7.19}$$

where $\mathbf{w}_{\beta\sigma}$ is the interface velocity, $\mathbf{n}_{\beta\sigma}$ is the unit normal vector directed from the β-region toward the σ-phase, $A_{\beta\sigma}$ is the interfacial area between the two phases. E_0 is the surface concentration of transporter proteins, α_0 is an equilibrium coefficient and $\alpha_{2,3,4,5}$ are membrane transport parameters. This boundary condition is well suited for molecules that need simple membrane carrier such as glucose [Ashcroft, 1999; Thorens & Mueckler, 2010]. Additionally, the following boundary conditions are necessary

$$\text{BC2}: \quad -\mathbf{n}_{\beta\sigma}.\left(\mathbf{D}^{\text{III}}_{A\beta}.\nabla c_{A\beta}+\left(\mathbf{w}_{\beta\sigma}-\mathbf{v}_{\beta}\right)c_{A\beta}\right)= -\mathbf{n}_{\beta\sigma}.\left(D_{A\sigma}\mathbf{I}.\nabla c_{A\sigma}+\mathbf{w}_{\beta\sigma}c_{A\sigma}\right) \quad \text{at } A_{\beta\sigma} \tag{7.20}$$

$$\text{BC3}: \quad \mathbf{n}_{\beta\sigma}.\left(\mathbf{v}_{\beta}-\mathbf{w}_{\beta\sigma}\right)\rho_{\alpha}=-\mathbf{n}_{\beta\sigma}.\mathbf{w}_{\beta\sigma}\rho_{\sigma} \quad \text{at } A_{\beta\sigma} \tag{7.21}$$

Eq. (7.21) is an interfacial mass conservation condition where the velocity of the σ-phase is neglected. Note that the transport quantity in the left hand side is in ρ_{α}, and this is consistent with Eqs. (7.14) and (7.15). Eq. (7.21) can be written in the form

$$\text{BC3}: \quad \mathbf{n}_{\beta\sigma}.\mathbf{v}_{\beta}=\mathbf{n}_{\beta\sigma}.\left(1-\frac{\rho_{\sigma}}{\rho_{\alpha}}\right)\mathbf{w}_{\beta\sigma} \quad \text{at } A_{\beta\sigma} \tag{7.22}$$

where one can identify the term between brackets as the volume change parameter [Bousquet-Melou et al., 2002]. It is assumed here that the densities in the σ and the α phases are equivalent, thus the right hand side of Eq. (7.22) is discarded. Since the no slip condition implies that the projection of $\mathbf{v}_{\beta}$ on the tangent plane to $A_{\beta\sigma}$ is null, a classical no-slip boundary condition is obtained from Eq. (7.22)

$$\text{BC3}: \quad \mathbf{v}_{\beta}=0 \quad \text{at } A_{\beta\sigma} \tag{7.23}$$

Finally, the local problem at the cellular scale (level III) is constituted by Eqs. (7.14) to (7.17), (7.19), (7.20) and (7.23). In the following sections, the momentum and mass transport problems are up-scaled using the volume averaging method, and the tissue effective properties are evaluated through the resolution of the corresponding closure problems.

7.2 Upscaling momentum transport to the tissue scale

In the present section, momentum transport is up-scaled from the cellular scale (level III) to the tissue scale (level II), based on the volume averaging theory. This development leads to the definition of an effective tissue permeability, which explicitly include the ECM permeability. The inter-scale dependency between this two permeabilities is finally investigated through a numerical resolution of the associated closure problem.

7.2.1 Theoretical development

The process of averaging the momentum transport problem at the cellular scale (Eqs. (7.14), (7.15) and (7.23)), is very similar to the derivation described at the ECM scale (Chap. 6, App. A). Considering the effective density $\rho_\alpha \varepsilon_\alpha^{-1}$ and viscosity $\mu_\alpha \varepsilon_\alpha^{-1}$ of the culture medium, and the effective permeability tensor $\mathbf{K}_\beta^{\text{III}}$ to be constant in space within the averaging volume $\mathcal{V}_{\text{III}}$, the superficial average of Eq. (7.15) is

$$\rho_\alpha \varepsilon_\alpha^{-1} \left\langle \frac{\partial \mathbf{v}_\beta}{\partial t} \right\rangle = -\left\langle \nabla p_\beta \right\rangle - \frac{\mu_\alpha}{\mathbf{K}_\beta^{\text{III}}} \left\langle \mathbf{v}_\beta \right\rangle + \mu_\alpha \varepsilon_\alpha^{-1} \left\langle \nabla^2 \mathbf{v}_\beta \right\rangle + \left\langle \rho_\alpha \mathbf{g} \right\rangle \tag{7.24}$$

Only the Darcy term differs from the average of a Stokes equation, but given its linearity, it is straight forward to derive the *non-closed averaged equation for momentum transport* in the β-region

$$\begin{aligned} \rho_\alpha \varepsilon_\alpha^{-1} \frac{\partial \left(\varepsilon_\beta \langle \mathbf{v}_\beta \rangle^\beta \right)}{\partial t} &= -\varepsilon_\beta \nabla \left\langle p_\beta \right\rangle^\beta - \frac{\mu_\alpha}{\mathbf{K}_\beta^{\text{III}}} \varepsilon_\beta \left\langle \mathbf{v}_\beta \right\rangle^\beta \\ &+ \mu_\alpha \varepsilon_\alpha^{-1} \varepsilon_\beta \nabla^2 \left\langle \mathbf{v}_\beta \right\rangle^\beta + \varepsilon_\beta \rho_\alpha \mathbf{g} + \frac{1}{\mathcal{V}_{\text{III}}} \int_{A_{\beta\sigma}} \mathbf{n}_{\beta\sigma} . \left(-\mathbf{I} \tilde{p}_\beta + \mu_\alpha \varepsilon_\alpha^{-1} \nabla \tilde{\mathbf{v}}_\beta \right) dA \end{aligned} \tag{7.25}$$

where $\mathcal{V}_{\text{III}}$ is the averaging volume at the cell scale (see Fig. 7.1). Here Gray decomposition [Gray, 1975] has been introduced for the velocity and pressure in the β-region

$$\mathbf{v}_\beta = \langle \mathbf{v}_\beta \rangle^\beta + \tilde{\mathbf{v}}_\beta \tag{7.26}$$

$$p_\beta = \langle p_\beta \rangle^\beta + \tilde{p}_\beta \tag{7.27}$$

Note that the averaged Eq. (7.25) is valid under the classical length scale constraints

$$l_\beta \ll r_0 \qquad r_0^2 \ll L_\varepsilon L_{p1} \qquad r_0^2 \ll L_\varepsilon L_{v1} \qquad r_0^2 \ll L_\varepsilon L_{v2} \tag{7.28}$$

where l_β, r_0, L_ε, L_{p1}, L_{v1} and L_{v2} are the characteristic length scales of the β-region, the averaging volume $\mathcal{V}_{\text{III}}$, the volume fraction variation, the pressure gradient variation, the velocity gradient variation and the velocity laplacian variation respectively.

Now turning our attention to the mass conservation equations (Eqs. (7.14) and (7.18)), the general transport and spacial averaging theorems are applied to get

$$\frac{\partial (\varepsilon_\beta \langle \rho_\beta \rangle^\beta)}{\partial t} + \nabla . (\varepsilon_\beta \langle \rho_\alpha \mathbf{v}_\beta \rangle^\beta) = \langle Q_\beta \rangle + \frac{1}{\mathcal{V}_{\text{III}}} \int_{A_{\beta\sigma}} \mathbf{n}_{\beta\sigma} . \left(\rho_\beta \mathbf{w}_{\beta\sigma} - \rho_\alpha \mathbf{v}_\beta \right) dA \tag{7.29}$$

$$\frac{\partial (\varepsilon_\sigma \langle \rho_\sigma \rangle^\sigma)}{\partial t} = \langle Q_\sigma \rangle + \frac{1}{\mathcal{V}_{\text{III}}} \int_{A_{\sigma\beta}} \mathbf{n}_{\sigma\beta} . \rho_\sigma \mathbf{w}_{\beta\sigma} dA \tag{7.30}$$

Adding up these two averaged equations we have

$$\begin{aligned} \frac{\partial (\varepsilon_\beta \langle \rho_\beta \rangle^\beta + \varepsilon_\sigma \langle \rho_\sigma \rangle^\sigma)}{\partial t} + \nabla . (\varepsilon_\beta \langle \rho_\alpha \mathbf{v}_\beta \rangle^\beta) &= \langle Q_\beta + Q_\sigma \rangle \\ &+ \frac{1}{\mathcal{V}_{\text{III}}} \int_{A_{\beta\sigma}} \mathbf{n}_{\beta\sigma} . \left[(\rho_\beta - \rho_\sigma) \mathbf{w}_{\beta\sigma} - \rho_\alpha \mathbf{v}_\beta \right] dA \end{aligned} \tag{7.31}$$

Here we need to make the hypothesis that the density in the β-region is close to the density in the α-phase. In practice this is not a strong assumption, and when used together with the previous hypothesis that the density of a phase is constant within its phase, we obtain the simplification

$$\rho_\alpha = \langle \rho_\alpha \rangle^\alpha \quad \simeq \quad \rho_\beta = \langle \rho_\beta \rangle^\beta \quad \simeq \quad \rho_\sigma = \langle \rho_\sigma \rangle^\sigma \tag{7.32}$$

Under this conditions, the mass conservation boundary condition Eq. (7.21) allows to neglect the right hand side of Eq. (7.31). The *averaged mass conservation equation* can finally be written in the form

$$\frac{\partial(\varepsilon_\beta \rho_\beta + \varepsilon_\sigma \rho_\sigma)}{\partial t} + \nabla.(\varepsilon_\beta \rho_\alpha \langle \mathbf{v}_\beta \rangle^\beta) = \langle Q_\beta + Q_\sigma \rangle \tag{7.33}$$

At this point we have the averaged equations for momentum transport and mass conservation (Eqs. (7.25) and (7.33)). Eq. (7.25) still includes local quantities represented by the deviation terms. In order to close this equation we need to build a problem for the deviations, and this is done by subtracting Eqs. (7.25) to (7.15) and using the spacial decompositions (Eqs. (7.26) and (7.27)) we have

$$\begin{aligned} \rho_\alpha \varepsilon_\alpha^{-1} \frac{\partial \tilde{\mathbf{v}}_\beta}{\partial t} - \rho_\alpha \varepsilon_\alpha^{-1} \langle \mathbf{v}_\beta \rangle^\beta \frac{\partial \varepsilon_\beta}{\partial t} = -\nabla \tilde{p}_\beta - \frac{\mu_\alpha}{\mathbf{K}_\beta^{\mathrm{III}}} \tilde{\mathbf{v}}_\beta + \mu_\alpha \varepsilon_\alpha^{-1} \nabla^2 \tilde{\mathbf{v}}_\beta \\ - \frac{1}{V_\beta} \int_{A_{\beta\sigma}} \mathbf{n}_{\beta\sigma}. \left(-\mathbf{I} \tilde{p}_\beta + \mu_\alpha \varepsilon_\alpha^{-1} \nabla \tilde{\mathbf{v}}_\beta \right) dA \quad \text{in the } \beta\text{-region} \end{aligned} \tag{7.34}$$

Some simplifications can be done when evaluating the orders of magnitude of the terms

$$\rho_\alpha \varepsilon_\alpha^{-1} \frac{\partial \tilde{\mathbf{v}}_\beta}{\partial t} = O\left(\rho_\alpha \varepsilon_\alpha^{-1} \frac{\langle \mathbf{v}_\beta \rangle^\beta}{t_v} \right) \tag{7.35}$$

$$\rho_\alpha \varepsilon_\alpha^{-1} \langle \mathbf{v}_\beta \rangle^\beta \frac{\partial \varepsilon_\beta}{\partial t} = O\left(\rho_\alpha \varepsilon_\alpha^{-1} \frac{\langle \mathbf{v}_\beta \rangle^\beta}{t_\varepsilon} \right) \tag{7.36}$$

$$\mu_\alpha \varepsilon_\alpha^{-1} \nabla^2 \tilde{\mathbf{v}}_\beta = O\left(\mu_\alpha \varepsilon_\alpha^{-1} \frac{\langle \mathbf{v}_\beta \rangle^\beta}{l_\beta^2} \right) \tag{7.37}$$

where t_v and t_ε are the characteristic time for change in the velocity and volume fraction respectively. In this study, the evolution of the cellular structure is supposed to be much slower than the variation in fluid velocity in the ECM. This means that $t_v \ll t_\varepsilon$ so the second term on the left hand side can be neglected. In addition, the first term on the left hand side can be neglected over the viscous diffusion term when

$$\frac{\mu_\alpha \varepsilon_\alpha^{-1}}{\rho_\alpha \varepsilon_\alpha^{-1}} \frac{t_v}{l_\beta^2} \gg 1 \tag{7.38}$$

This simplifications lead to a static *deviation problem for momentum transport* in the β-region of the form

$$\nabla.\tilde{\mathbf{v}}_\beta = 0 \qquad \text{in the } \beta\text{-region} \tag{7.39}$$

$$0 = -\nabla\tilde{p}_\beta - \frac{\mu_\alpha}{\mathbf{K}_\beta^{\mathrm{III}}}\tilde{\mathbf{v}}_\beta + \mu_\alpha\varepsilon_\alpha^{-1}\nabla^2\tilde{\mathbf{v}}_\beta - \frac{1}{V_\beta}\int_{A_{\beta\sigma}}\mathbf{n}_{\beta\sigma}.\left(-\mathbf{I}\tilde{p}_\beta + \mu_\alpha\varepsilon_\alpha^{-1}\nabla\tilde{\mathbf{v}}_\beta\right)dA$$

in the β-region (7.40)

$$\tilde{\mathbf{v}}_\beta = -\langle\mathbf{v}_\beta\rangle^\beta \qquad \text{at } A_{\beta\sigma} \tag{7.41}$$

Here, Eq. (7.39) has been obtained from Eq. (7.33), under the same length scale constraints and assumptions than the ones needed to derive Eq. (7.40). Additionally, it has been assumed that the time scale associated with the average production rates, is much larger than the time scale associated with momentum transport. In other words, cell growth is so slow that is does not influence the deviation problem for momentum transport.

The only source term in the momentum deviation problem (Eqs. (7.39) to (7.41)) is given by the boundary condition Eq. (7.41). In order to link the deviation problem to the non-closed averaged problem, a relation between the deviations and the averages is proposed in the form

$$\tilde{\mathbf{v}}_\beta = \mathbf{B}_\beta.\langle\mathbf{v}_\beta\rangle^\beta \tag{7.42}$$

$$\tilde{p}_\beta = \mu_\alpha\varepsilon_\alpha^{-1}\mathbf{b}_\beta.\langle\mathbf{v}_\beta\rangle^\beta \tag{7.43}$$

where $\mathbf{B}_\beta$ and $\mathbf{b}_\beta$ are the colosure variables for momentum transport in the β-region. Substituting these definitions in the averaged momentum transport equation Eq. (7.25) we obtain

$$\rho_\alpha\varepsilon_\alpha^{-1}\varepsilon_\beta^{-1}\frac{\partial\left(\varepsilon_\beta\langle\mathbf{v}_\beta\rangle^\beta\right)}{\partial t} = -\nabla\langle p_\beta\rangle^\beta + \mu_\alpha\varepsilon_\alpha^{-1}\nabla^2\langle\mathbf{v}_\beta\rangle^\beta + \rho_\alpha\mathbf{g}$$
$$-\mu_\alpha\varepsilon_\alpha^{-1}\left[\frac{\varepsilon_\alpha}{\mathbf{K}_\beta^{\mathrm{III}}} - \frac{1}{V_\beta}\int_{A_{\beta\sigma}}\mathbf{n}_{\beta\sigma}.\left(-\mathbf{I}\mathbf{b}_\beta + \nabla\mathbf{B}_\beta\right)dA\right]\langle\mathbf{v}_\beta\rangle^\beta \tag{7.44}$$

One can identify a classical form of the permeability tensor depending on the closure variables in the β-region

$$\varepsilon_\beta\mathbf{K}_\beta^{\star-1} = -\frac{1}{V_\beta}\int_{A_{\beta\sigma}}\mathbf{n}_{\beta\sigma}.\left(-\mathbf{I}\mathbf{b}_\beta + \nabla\mathbf{B}_\beta\right)dA \tag{7.45}$$

This definition allows to represent the tissue effective permeability as a function of two permeabilities

$$\varepsilon_\alpha\varepsilon_\beta\mathbf{K}_\omega^{\mathrm{II}-1} = \varepsilon_\alpha\mathbf{K}_\beta^{\mathrm{III}-1} + \varepsilon_\beta\mathbf{K}_\beta^{\star-1} \tag{7.46}$$

and the *closed macroscopic momentum transport equation* in the β-region takes the form

$$\rho_\alpha\varepsilon_\alpha^{-1}\varepsilon_\beta^{-1}\frac{\partial\left(\varepsilon_\beta\langle\mathbf{v}_\beta\rangle^\beta\right)}{\partial t} = -\nabla\langle p_\beta\rangle^\beta - \frac{\mu_\alpha}{\mathbf{K}_\omega^{\mathrm{II}}}\varepsilon_\beta\langle\mathbf{v}_\beta\rangle^\beta + \mu_\alpha\varepsilon_\alpha^{-1}\nabla^2\langle\mathbf{v}_\beta\rangle^\beta + \rho_\alpha\mathbf{g} \tag{7.47}$$

Note that Eq. (7.47) is a Darcy-Brinkman equation, whose effective permeability tensor $\mathbf{K}_\omega^{\mathrm{II}}$ is a function of the ECM permeability $\mathbf{K}_\beta^{\mathrm{III}}$, and of the permeability arising from the cellular structure $\mathbf{K}_\beta^\star$.

Eq. (7.47) appears different from the one developed in the context of large scale averaging [Quintard & Whitaker, 1996a, 1998a] for two reasons : (i) in the work of Quintard & Whitaker [1996a, 1998a] the fluid is slightly compressible, allowing to express the boundary value

problem in terms of the pressure only. This gives rise to higher order governing equations and thus higher order closure variables. (ii) the momentum transport equation is treated in the form of Darcy's law [Darcy, 1856] and the Brinkman corrections are neglected. In this form the authors chose to distribute $\mathbf{K}_\beta^{\mathrm{III}}$ into two effective coefficients defined in Eqs. (125g) and (135) of [Quintard & Whitaker, 1996a].

Although Eq. (7.45) does not depend explicitly on $\mathbf{K}_\beta^{\mathrm{III}}$, it is influenced by the ECM permeability through the solution of the closure problem

$$\nabla.\mathbf{B}_\beta = 0 \tag{7.48}$$

$$0 = -\nabla\mathbf{b}_\beta - \varepsilon_\alpha \mathbf{K}_\beta^{\mathrm{III}-1}\mathbf{B}_\beta + \nabla^2\mathbf{B}_\beta + \varepsilon_\beta \mathbf{K}_\beta^{\star-1} \tag{7.49}$$

$$\mathbf{B}_\beta = -\mathbf{I} \quad \text{at } A_{\beta\sigma} \tag{7.50}$$

$$\mathbf{B}_\beta(\mathbf{x}+l_i) = \mathbf{B}_\beta(\mathbf{x}) \qquad i=1,2,3 \tag{7.51}$$

$$\mathbf{b}_\beta(\mathbf{x}+l_i) = \mathbf{b}_\beta(\mathbf{x}) \qquad i=1,2,3 \tag{7.52}$$

Note that the interstitial fluid volume fraction ε_α plays a role in the microscopic closure problem. The resolution of this closure problem for momentum transport allows to compute the effective tissue permeability $\mathbf{K}_\omega^{\mathrm{II}}$, and this is done in the following section.

7.2.2 Computation of the tissue effective permeability

The closure problem for momentum transport at the cellular scale (level III) is given by Eqs. (7.48) to (7.66). Because of $\mathbf{K}_\beta^\star$ in the conservation equation, we are facing an integro-differential problem. Similarly to what have been done in Sec. 6.2.1, a series of variable changes is proposed to develop a problem more convenient to solve numerically.

First a new tensor is defined

$$\mathbf{B}_\beta^\sharp = \mathbf{B}_\beta + \mathbf{I} \tag{7.53}$$

allowing to write the closure problem in the form

$$\nabla.\mathbf{B}_\beta^\sharp = 0 \tag{7.54}$$

$$0 = -\nabla\mathbf{b}_\beta - \varepsilon_\alpha \mathbf{K}_\beta^{\mathrm{III}-1}\mathbf{B}_\beta^\sharp + \nabla^2\mathbf{B}_\beta^\sharp + \varepsilon_\alpha \mathbf{K}_\beta^{\mathrm{III}-1} + \varepsilon_\beta \mathbf{K}_\beta^{\star-1} \tag{7.55}$$

$$\mathbf{B}_\beta^\sharp = 0 \quad \text{at } A_{\beta\sigma} \tag{7.56}$$

$$\mathbf{B}_\beta^\sharp(\mathbf{x}+l_i) = \mathbf{B}_\beta^\sharp(\mathbf{x}) \quad i=1,2,3 \tag{7.57}$$

$$\mathbf{b}_\beta(\mathbf{x}+l_i) = \mathbf{b}_\beta(\mathbf{x}) \quad i=1,2,3 \tag{7.58}$$

We see here the effective tissue permeability (Eq. (7.46)) appearing in the right hand side of Eq. (7.54). This suggests to define new vector and tensor fields according to

$$\mathbf{b}'_\beta = \varepsilon_\alpha^{-1}\varepsilon_\beta^{-1}\mathbf{b}_\beta.\mathbf{K}_\omega^{\mathrm{II}} \tag{7.59}$$

$$\mathbf{B}'_\beta = \varepsilon_\alpha^{-1}\varepsilon_\beta^{-1}\mathbf{B}_\beta^\sharp.\mathbf{K}_\omega^{\mathrm{II}} \tag{7.60}$$

And the closure problem can be set to the form of an incompressible Darcy-Brinkman flow problem

$$\nabla.\mathbf{B}'_\beta = 0 \tag{7.61}$$

$$0 = -\nabla \mathbf{b}'_\beta - \varepsilon_\alpha \mathbf{K}_\beta^{\mathrm{III}-1}\mathbf{B}'_\beta + \nabla^2 \mathbf{B}'_\beta + \mathbf{I} \tag{7.62}$$

$$\mathbf{B}'_\beta = 0 \qquad \text{at } A_{\beta\sigma} \tag{7.63}$$

$$\mathbf{B}'_\beta(\mathbf{x}+l_i) = \mathbf{B}'_\beta(\mathbf{x}) \quad i=1,2,3 \tag{7.64}$$

$$\mathbf{b}'_\beta(\mathbf{x}+l_i) = \mathbf{b}'_\beta(\mathbf{x}) \quad i=1,2,3 \tag{7.65}$$

And the tissue effective permeability can be obtained using the fact that the superficial average of deviation of the velocity is null (average of Eq. (7.26)). This implies that

$$\langle \mathbf{B}_\beta \rangle^\beta = 0 \tag{7.66}$$

and when the variable change is applied, we obtain

$$\langle \mathbf{B}'_\beta \rangle^\beta = \varepsilon_\alpha^{-1}\varepsilon_\beta^{-1}\mathbf{K}_\omega^{\mathrm{II}} \tag{7.67}$$

The form of the above problem is similar to the usual closure problem for momentum transport [Whitaker, 1999], except for the Darcy term where the interstitial fluid volume fraction is present. The inputs needed to solve the closure problem at the cellular scale are, the ECM volume fraction ε_β, the interstital fluid volume fraction ε_α, and its resulting ECM effective permeability $\mathbf{K}_\beta^{\mathrm{III}}$.

In order to investigate the influence of the above parameters on the tissue effective permeability $\mathbf{K}_\omega^{\mathrm{II}}$, an intuitive two step approach would be : first, evaluate $\mathbf{K}_\beta^{\mathrm{III}}$ by solving the ECM scale closure problem (Eqs. (6.30) to (6.35)) on a given geometry ; second, solve the cellular scale closure problem (Eqs. (7.61) to (7.67)). Yet, this has the disadvantage of explicitly coupling the values of $\mathbf{K}_\beta^{\mathrm{III}}$ to ε_α. Thus, in order to have access to a larger range of values, the couple $(\varepsilon_\alpha, \mathbf{K}_\beta^{\mathrm{III}})$ is arbitrarily set, allowing to isolate more easily the inter-scale dependency. This supposes that for any finite value of $(\varepsilon_\alpha, \mathbf{K}_\beta^{\mathrm{III}})$, a geometry of the unit cell exists.

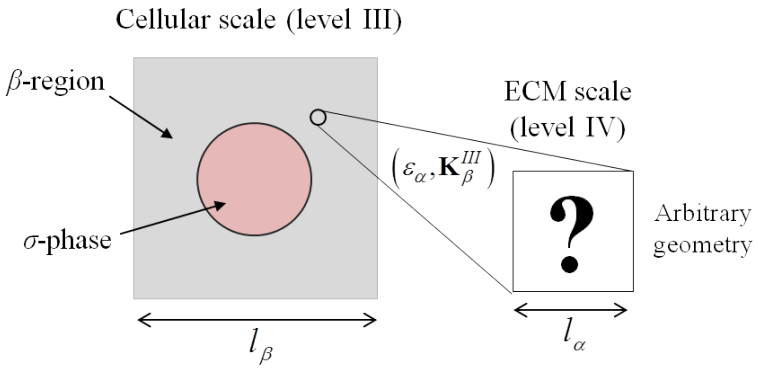

Figure 7.2 – Unit cell used to investigate the inter-scale dependency between the ECM ($\mathbf{K}_\beta^{\mathrm{III}}$) and the tissue ($\mathbf{K}_\omega^{\mathrm{II}}$) permeabilities.

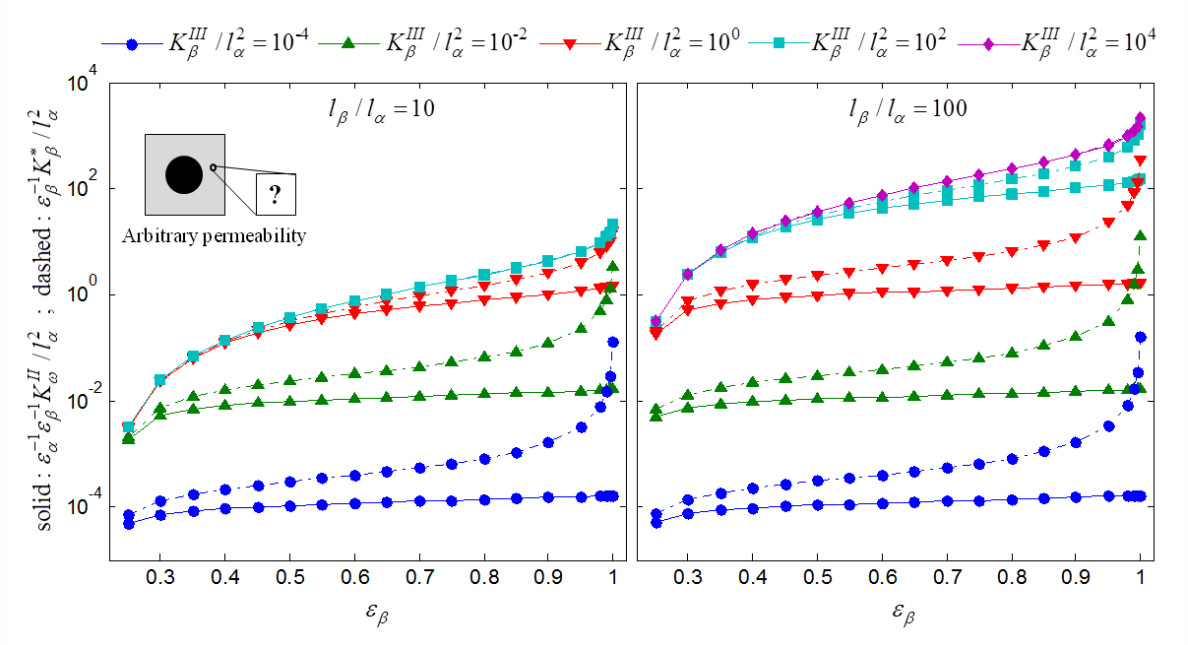

Figure 7.3 – Tissue effective permeability as a function of the ECM permeability ($\varepsilon_\alpha = 0.6$)

The cell scale closure problem for momentum transport (Eqs. (7.61) to (7.67)), is solved on the two-dimensional unit cell represented in Fig. 7.2. Numerical results illustrating the inter-scale dependency are show in Fig. 7.3. The tissue effective permeability, $\mathbf{K}_\omega^{\mathrm{II}}$ (solid lines) and the permeability arising from the cellular scale structure, $\mathbf{K}_\beta^\star$ (dashed lines) are plotted for different permeability values of the ECM scale (scale IV), and for two ratio of the characteristic cell sizes. The interstitial fluid volume fraction, ε_α, is kept equal to 0.6. First, it can be seen that the ECM permeability $\mathbf{K}_\beta^{\mathrm{III}}$ strongly influences the tissue permeability coefficient. For large values of the ECM volume fraction ε_β, and thus cell structure permeability $\mathbf{K}_\beta^\star$, the inequality $\mathbf{K}_\beta^{\mathrm{III}}\varepsilon_\alpha^{-1} \ll \mathbf{K}_\beta^\star\varepsilon_\beta^{-1}$ is satisfied, and, from Eq. (7.46), $\mathbf{K}_\omega^{\mathrm{II}}$ tends to $\varepsilon_\beta\mathbf{K}_\beta^{\mathrm{III}}$ (microporous behavior). On the other hand, we verify that $\mathbf{K}_\omega^{\mathrm{II}}$ logically tends toward $\mathbf{K}_\beta^\star$ for small ε_β values, and obviously, for large $\mathbf{K}_\omega^{\mathrm{II}}$ (fluid behavior). Note that these observations are verified whatever the ratio l_β/l_α.

In order to validate the effective permeability obtained by double volume averaging, semi-direct numerical computations (sDNS) are carried for the explicitly defined hierarchical structure shown in Fig. 7.4. The term "semi-direct" is used because only a unit cell of the tissue is considered (instead of a whole region) with the geometry a the cell and ECM scale explicitly represented. At both level, a two-dimensional structure composed of in-line cylinders are considered. The closure problem at the ECM scale (Eqs. (6.30) to (6.35)) is solved for various values of the interstitial fluid volume fraction ε_α, and the corresponding ECM permeabilities $\mathbf{K}_\beta^{\mathrm{III}}$ are obtained. These values are then used in the cellular scale closure problem (Eqs. (7.61) to (7.67)) to determine the tissue effective permeability $\mathbf{K}_\omega^{\mathrm{II}}$ for different values of the ECM volume fraction ε_β. The results are presented in Fig. 7.5, and compared with sDNS in the case $l_\beta/l_\alpha = 20$. sDNS and double volume averaged solutions are in excellent agreement, validating the use of the double averaging for the evaluation of the tissue permeability. Yet,

for very low values of the ECM volume fraction ε_β, the sDNS permeability slightly deviates from the double averaging permeability. This suggests that in the sDNS, the elementary representative volume of the ECM is not well represented between the cellular obstacles, leading to inaccuracies. This results allow to conclude that, for the geometries considered, the distance between two cellular obstacles must be at least equal to $5l_\alpha$ in order for the length scale separations to be valid (which is consistent with [Goyeau et al., 1997]).

In the above results, a large range of parameters values have been investigated, in order to study the momentum transport characteristics related to a hierarchical porous media. Yet, in practice, this parameters are unlikely to vary that much in a tissue grown within a perfusion bioreactor. The evaluation of a more realistic tissue effective permeability will be carried in Chap. 10. But first, let us treat the mass transport problem.

7.3 Upscaling mass transport to the tissue scale

Here, mass transport at the cellular scale (level III) is up-scaled in order to obtain the mass transport properties at the tissue scale (level II). By supposing local mass equilibrium between the ECM and the intracellular region, a one-equation model for mass transport is derived. Then the tissue effective diffusion-dispersion coefficient will be investigated in regard to membrane transport, fluid intensity, and ECM permeability, by solving the associated closure problem.

7.3.1 Theoretical development

Let us recall the local equations describing mass transport at the cellular scale (see Sec. 7.1 for the discussion on their choice)

$$\varepsilon_\alpha \frac{\partial c_{A\beta}}{\partial t} + \nabla.\left(\mathbf{v}_\beta c_{A\beta}\right) = \nabla.(\mathbf{D}^{\mathrm{III}}_{A\beta}.\nabla c_{A\beta}) \qquad \text{in the } \beta\text{-region} \tag{7.68}$$

$$\frac{\partial c_{A\sigma}}{\partial t} = \nabla.(D_{A\sigma}\nabla c_{A\sigma}) - k_A \frac{c_{A\sigma}}{c_{A\sigma} + K_A} \qquad \text{in the } \sigma\text{-phase} \tag{7.69}$$

$$\text{BC1}: \quad -\mathbf{n}_{\beta\sigma}.\left(\mathbf{D}^{\mathrm{III}}_{A\beta}.\nabla c_{A\beta} + \left(\mathbf{w}_{\beta\sigma} - \mathbf{v}_\beta\right) c_{A\beta}\right) = \frac{E_0\left(c_{A\beta} - \alpha_0 c_{A\sigma}\right)}{\alpha_1 + \alpha_2 c_{A\beta} + \alpha_3 c_{A\sigma} + \alpha_4 c_{A\beta} c_{A\sigma}} \quad \text{at } A_{\beta\sigma} \tag{7.70}$$

$$\text{BC2}: \quad -\mathbf{n}_{\beta\sigma}.\left(\mathbf{D}^{\mathrm{III}}_{A\beta}.\nabla c_{A\beta} + \left(\mathbf{w}_{\beta\sigma} - \mathbf{v}_\beta\right) c_{A\beta}\right) = -\mathbf{n}_{\beta\sigma}.\left(D_{A\sigma}\mathbf{I}.\nabla c_{A\sigma} + \mathbf{w}_{\beta\sigma} c_{A\sigma}\right) \quad \text{at } A_{\beta\sigma} \tag{7.71}$$

It is important to keep in mind that $\mathbf{D}^{\mathrm{III}}_{A\beta}$ is a diffusion-dispersion tensor whose value depends on the Péclet number at level IV, and thus to the $\mathbf{v}_\beta$-field (see Eqs. (6.50) and (7.9)).

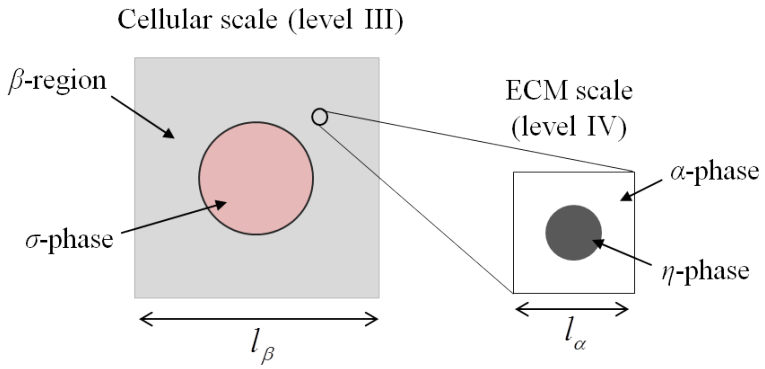

Figure 7.4 – Unit cells with explicitly defined hierarchical structure, used for comparision with the semi-direct numerical simulations.

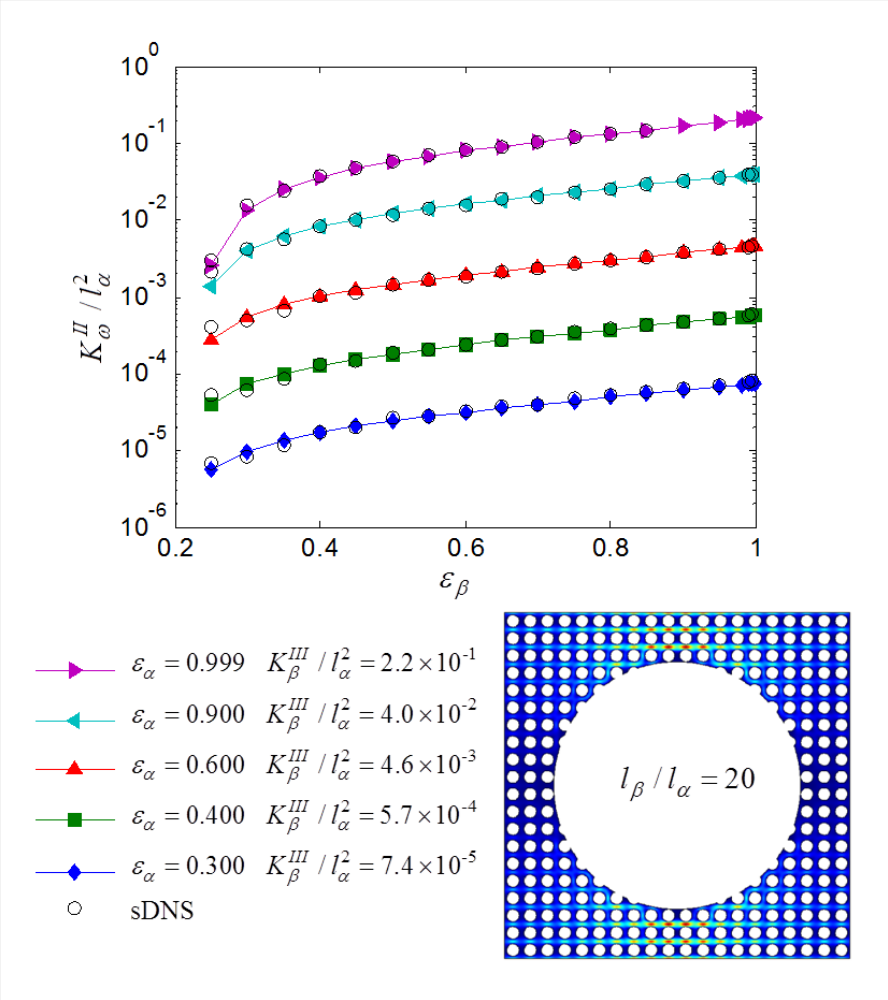

Figure 7.5 – Comparison of the results of the tissue effective permeability, from double volume averaging (colored figures) and semi-direct numerical simulations (black circles). Hierarchical structure composed of in-line cylinders at the two levels, for $l_\beta/l_\alpha = 20$. The bottom-right figure shows the intensity of the longitudinal fluid velocity for a sDNS where $\varepsilon_\alpha = 0.6$ and $\varepsilon_\beta = 0.6$.

Since in the general case, $\mathbf{v}_\beta$ can vary within $\mathcal{V}_{\text{III}}$, $\mathbf{D}^{\text{III}}_{A\beta}$ is subject to spacial variations at the cellular scale. Moreover its values can range over several orders of magnitude between the diffusive and dispersive regime, depending on Pe_α-field in $\mathcal{V}_{\text{III}}$. The theory of large-scale volume averaging deals with this kind of heterogeneous dispersion by introducing the spatial deviation of the dispersion tensor [Quintard & Whitaker, 1998b; Ahmadi et al., 1998; Quintard et al., 2001; Cherblanc et al., 2003]. However since the applications are usually large fields in geosciences, the flow is modeled with Darcy equation, neglecting the variability in the velocity profile. In our case, momentum transport is modeled with a Darcy-Brinkman equation, and heterogeneous dispersion is susceptible to occur. A detailed study of the dispersive effects in hierarchical bi-porous media is presented in App. B. Nonetheless experimental evidences [Swartz & Fleury, 2007; Ng & Swartz, 2003, 2006] point out that in biological tissues Pe_α is of the order of 10^{-3} to 10^{-1}. In regard to the results presented in Sec. 6.2.2, it is very reasonable to assume that $\mathbf{D}^{\text{III}}_{A\beta}$ lays in the diffusive regime and that its variations within $\mathcal{V}_{\text{III}}$ are negligible.

The form of the membrane transport described by Eq. (7.70) has been first derived by Wood & Whitaker [1998] on the basis of [Ochoa et al., 1986]. It represents transport through a lipid bi-layer, where the mechanism is driven by the concentration difference between the β and σ-regions. Specific kinetics characteristic of the membrane lipid layers are taken into account in the denominator. The non-linear nature of this equation presents difficulties in the upscaling, and simplifications will be needed to deal with it in the closure problem.

For generality, the two boundary conditions Eqs. (7.70) and (7.71) include the fluid velocity in the β-region. Since we have a no slip boundary condition at the cell membrane (Eq. (7.23)), $\mathbf{v}_\beta$ is discarded at $A_{\beta\sigma}$ in the rest of the development.

Following the volume averaging method described in Chap. 6 and App. A, the *non-closed volume averaged equations* for mass transport in the β and σ phases are obtained

$$\varepsilon_\alpha \frac{\partial\left(\varepsilon_\beta \left\langle c_{A\beta}\right\rangle^\beta\right)}{\partial t} + \varepsilon_\beta \left\langle \mathbf{v}_\beta\right\rangle^\beta .\nabla \left\langle c_{A\beta}\right\rangle^\beta = \nabla.\left[\mathbf{D}^{\text{III}}_{A\beta}.\left(\varepsilon_\beta \nabla \left\langle c_{A\beta}\right\rangle^\beta + \frac{1}{\mathcal{V}_{\text{III}}}\int_{A_{\beta\sigma}} \mathbf{n}_{\beta\sigma}\tilde{c}_{A\beta}dA\right)\right] + \frac{1}{\mathcal{V}_{\text{III}}}\int_{A_{\beta\sigma}} \mathbf{n}_{\beta\sigma}.\left(\mathbf{D}^{\text{III}}_{A\beta}.\nabla c_{A\beta} + \mathbf{w}_{\beta\sigma}c_{A\beta}\right)dA - \nabla.\left\langle\tilde{\mathbf{v}}_\beta\tilde{c}_{A\beta}\right\rangle \quad \text{in the } \beta\text{-region} \tag{7.72}$$

$$\frac{\partial\left(\varepsilon_\sigma \left\langle c_{A\sigma}\right\rangle^\sigma\right)}{\partial t} = \nabla.\left[D_{A\sigma}\left(\varepsilon_\sigma \nabla \left\langle c_{A\sigma}\right\rangle^\sigma + \frac{1}{\mathcal{V}_{\text{III}}}\int_{A_{\sigma\beta}} \mathbf{n}_{\sigma\beta}\tilde{c}_{A\sigma}dA\right)\right] + \frac{1}{\mathcal{V}_{\text{III}}}\int_{A_{\sigma\beta}} \mathbf{n}_{\sigma\beta}.\left(D_{A\sigma}\nabla c_{A\sigma} + \mathbf{w}_{\beta\sigma}c_{A\sigma}\right)dA - \varepsilon_\sigma\left\langle k_A\frac{c_{A\sigma}}{c_{A\sigma}+K_A}\right\rangle^\sigma \quad \text{in the } \sigma\text{-phase} \tag{7.73}$$

where the spacial deviations for the concentrations have been introduced.

$$c_{A\beta} = \left\langle c_{A\beta}\right\rangle^\beta + \tilde{c}_{A\beta} \qquad c_{A\sigma} = \left\langle c_{A\sigma}\right\rangle^\sigma + \tilde{c}_{A\sigma} \tag{7.74}$$

In order to take into account cell growth and thus variation of ε_σ during time, the development of Eqs. (7.72) and (7.73) does not require ε_β and ε_σ to be constant in time or in space (only

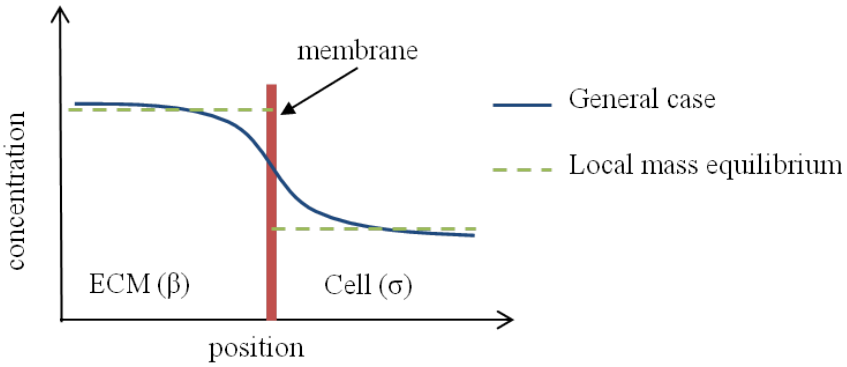

Figure 7.6 – Representation of the concentration profile close to the interface $A_{\beta\sigma}$ in the general case and at local mass equilibrium

ε_α is a constant). Compared to Eq. (A.35) where the porous structure is inert, Eqs. (7.72) and (7.73) present additional interfacial terms involving the cell membrane velocity $\mathbf{w}_{\beta\sigma}$.

We remind that Eqs. (7.72) and (7.73) are valid under the following length scale constraints

$$l_\beta << r_0 \qquad r_0^2 << L_\varepsilon L_{c_{\beta 1}} \qquad l_\sigma << r_0 \qquad r_0^2 << L_\varepsilon L_{c_{\sigma 1}} \tag{7.75}$$

where l_σ, $L_{c_{\beta 1}}$ and $L_{c_{\sigma 1}}$ are the characteristic length scales of the σ-phase and of the concentration gradient variation in the β and σ phases respectively.

To this point, one averaged mass transport equation has been developed for each of the σ-phase and β-region. The dependent variables for these averaged equations are linked to two different concentrations, one for each phase. In the general case, a two equation model is best suited to describe the averaged mass transport process, although a one equation non-equilibrium model as been recently proposed [Davit et al., 2010]. However, in the case where the time-scales associated with transport phenomena in the two phases are close enough [Wood & Whitaker, 1998], the gradient of the average concentration vary sufficiently slowly for the system to be supposed at local mass equilibrium (Fig. 7.6). This hypothesis is supported by the fact that the diffusion coefficients measured in the ECM and in the cell are of the same order of magnitude, and that convective transport in the ECM is usually small [Mastro et al., 1984; Swartz & Fleury, 2007]. This allows to develop a one-equation mass equilibrium model which simplifies further development [Ochoa et al., 1986; Galban & Locke, 1999b; Wood & Whitaker, 2000; Lasseux et al., 2004; Golfier et al., 2009]. In that case, Eq. (7.19) indicates that averaged concentrations are related by

$$\langle c_{A\beta}\rangle^\beta = \alpha_0 \langle c_{A\sigma}\rangle^\sigma \quad \text{at local mass equilibrium} \tag{7.76}$$

Adding up the two non-closed averaged transport Eqs. (7.72) and (7.73), making use of the boundary condition Eq. (7.20), and noticing that $\mathbf{n}_{\sigma\beta} = -\mathbf{n}_{\beta\sigma}$ and $A_{\sigma\beta} = A_{\beta\sigma}$ we get

$$\frac{\partial\left(\varepsilon_\sigma \langle c_{A\sigma}\rangle^\sigma + \varepsilon_\alpha\varepsilon_\beta \langle c_{A\beta}\rangle^\beta\right)}{\partial t} + \varepsilon_\beta \langle \mathbf{v}_\beta\rangle^\beta . \nabla \langle c_{A\beta}\rangle^\beta = \nabla . \left[\varepsilon_\sigma D_{A\sigma}\mathbf{I}.\nabla \langle c_{A\sigma}\rangle^\sigma + \varepsilon_\beta \mathbf{D}^{\mathrm{III}}_{A\beta}.\nabla \langle c_{A\beta}\rangle^\beta\right] + \nabla .(\mathbf{f}_\sigma + \mathbf{f}_\beta) + \varepsilon_\sigma \langle R_\sigma\rangle^\sigma \tag{7.77}$$

where $\langle R_\sigma \rangle^\sigma$ is the intrinsic average of the reaction term, and $\mathbf{f}_\sigma$ and $\mathbf{f}_\beta$ are non-closed vectors representing the dispersive flux

$$\langle R_\sigma \rangle^\sigma = -\left\langle k_A \frac{c_{A\sigma}}{c_{A\sigma} + K_A} \right\rangle^\sigma \tag{7.78}$$

$$\mathbf{f}_\sigma = D_{A\sigma}\mathbf{I}.\left(\frac{1}{\mathcal{V}_{\text{III}}}\int_{A_{\sigma\beta}} \mathbf{n}_{\sigma\beta}\tilde{c}_{A\sigma}dA\right) \tag{7.79}$$

$$\mathbf{f}_\beta = \mathbf{D}^{\text{III}}_{A\beta}.\left(\frac{1}{\mathcal{V}_{\text{III}}}\int_{A_{\beta\sigma}} \mathbf{n}_{\beta\sigma}\tilde{c}_{A\beta}dA\right) - \langle \tilde{\mathbf{v}}_\beta \tilde{c}_{A\beta}\rangle \tag{7.80}$$

The reaction rate has a non-linear form, and the treatment of such a term in upscaling methods is still an active research field. Following Wood & Whitaker [2000], it is possible to prove that under the length scale constraints encountered in the present study, Eq. (7.78) can be written in the form

$$\langle R_\sigma \rangle^\sigma = -k_A \frac{\langle c_{A\sigma}\rangle^\sigma}{\langle c_{A\sigma}\rangle^\sigma + K_A} \tag{7.81}$$

In order to build a one equation mass equilibrium model, an equilibrium weighted average concentration is proposed [Ochoa et al., 1986; Wood & Whitaker, 1998; Golfier et al., 2009]

$$\{c_A\} = \varepsilon_\beta \langle c_{A\beta}\rangle^\beta + \alpha_0 \varepsilon_\sigma \langle c_{A\sigma}\rangle^\sigma \tag{7.82}$$

When the local mass equilibrium is met, Eq. (7.76) is valid in the whole averaging volume $\mathcal{V}_{\text{III}}$, and we get

$$\{c_A\} = \alpha_0 \langle c_{A\sigma}\rangle^\sigma = \langle c_{A\beta}\rangle^\beta \tag{7.83}$$

It is then possible to write Eq. (7.77) as a function of the weighted concentration only to obtain the *non-closed average equation at local mass equilibrium*

$$\frac{\partial\left[\left(\alpha_0^{-1}\varepsilon_\sigma + \varepsilon_\alpha\varepsilon_\beta\right)\{c_A\}\right]}{\partial t} + \varepsilon_\beta \langle \mathbf{v}_\beta\rangle^\beta .\nabla\{c_A\} = \nabla.\left[\left(\varepsilon_\sigma\alpha_0^{-1}D_{A\sigma}\mathbf{I} + \varepsilon_\beta\mathbf{D}^{\text{III}}_{A\beta}\right).\nabla\{c_A\}\right] + \nabla\cdot\left(\mathbf{f}_\sigma + \mathbf{f}_\beta\right) + \varepsilon_\sigma\langle R_\sigma\rangle^\sigma \tag{7.84}$$

At local mass equilibrium, the weighted average concentration is equivalent to the intrinsic average concentration in the β-region (Eq. (7.83)), and Eq. (7.84) can also be formulated in terms of $\langle c_{A\beta}\rangle^\beta$ only.

Eq. (7.84) still includes deviation terms in $\mathbf{f}_\beta$ and $\mathbf{f}_\sigma$, and to close this equation we need to build a problem for $\tilde{c}_\beta$ and $\tilde{c}_\sigma$. But first the interface convective term in Eqs. (7.72) and (7.73) need to be simplified on the basis that the diffusive transport is much more important than the transport of species A due the velocity of the cell wall $\mathbf{w}_{\beta\sigma}$

$$\mathbf{n}_{\beta\sigma}.\left(\mathbf{w}_{\beta\sigma}c_{A\beta}\right) \ll \mathbf{n}_{\beta\sigma}.\left(\mathbf{D}^{\text{III}}_{A\beta}.\nabla c_{A\beta}\right) \qquad \mathbf{n}_{\sigma\beta}.\left(\mathbf{w}_{\beta\sigma}c_{A\sigma}\right) \ll \mathbf{n}_{\sigma\beta}.\left(D_{A\sigma}\nabla c_{A\sigma}\right) \tag{7.85}$$

Then making use of the spacial decompositions (Eq. (7.74)), the general deviation problem is derived. The averaged mass transport equations (Eqs. (7.72) and (7.73)) are divided by

ε_β and ε_σ respectively, and subtracted to the point mass conservation equations (Eqs. (7.68) and (7.69) respectively).

$$\frac{\partial \tilde{c}_{A\beta}}{\partial t} - \langle c_{A\beta}\rangle^\beta \varepsilon_\beta^{-1}\frac{\partial \varepsilon_\beta}{\partial t} + \tilde{\mathbf{v}}_\beta.\nabla\langle c_{A\beta}\rangle^\beta + \mathbf{v}_\beta.\nabla\tilde{c}_{A\beta} = \nabla.\left(\mathbf{D}^{\mathrm{III}}_{A\beta}.\nabla\tilde{c}_{A\beta}\right) - \varepsilon_\beta^{-1}\nabla.\left(\mathbf{D}^{\mathrm{III}}_{A\beta}.\frac{1}{\mathcal{V}_{\mathrm{III}}}\int_{A_{\beta\sigma}}\mathbf{n}_{\beta\sigma}\tilde{c}_{A\beta}dA\right) - \frac{1}{V_\beta}\int_{A_{\beta\sigma}}\mathbf{n}_{\beta\sigma}.\left(\mathbf{D}^{\mathrm{III}}_{A\beta}.\nabla\tilde{c}_{A\beta}\right)dA + \varepsilon_\beta^{-1}\nabla.\langle\tilde{\mathbf{v}}_\beta\tilde{c}_{A\beta}\rangle \qquad \text{in the } \beta\text{-phase} \tag{7.86}$$

$$\frac{\partial \tilde{c}_{A\sigma}}{\partial t} - \langle c_{A\sigma}\rangle^\sigma \varepsilon_\sigma^{-1}\frac{\partial \varepsilon_\sigma}{\partial t} = \nabla.\left(D_{A\sigma}\nabla\tilde{c}_{A\sigma}\right) - \varepsilon_\sigma^{-1}\nabla.\left(D_{A\sigma}\mathbf{I}.\frac{1}{\mathcal{V}_{\mathrm{III}}}\int_{A_{\sigma\beta}}\mathbf{n}_{\sigma\beta}\tilde{c}_{A\sigma}dA\right) - \frac{1}{V_\sigma}\int_{A_{\sigma\beta}}\mathbf{n}_{\sigma\beta}.\left(D_{A\sigma}\nabla\tilde{c}_{A\sigma}\right)dA + R_\sigma - \langle R_\sigma\rangle^\sigma \qquad \text{in the } \sigma\text{-phase} \tag{7.87}$$

Some simplifications can be done to Eqs. (7.86) and (7.87). First, under the constraints Eq. (7.75), the non-local diffusion (second term on the RHS) is much smaller than the diffusive term [Whitaker, 1999]. Second, Wood & Whitaker [1998] showed that in most biofilms (and by extension most tissues), the diffusive term is larger than the accumulation and the consolidation terms (first and second terms on the LHS respectively). Moreover the reaction term is also shown to be much smaller than the diffusion term. The constraints related to these simplifications can be found in [Wood & Whitaker, 1998, Appendix A & B]. The deviation problem can now be simplified to a static integro-differential problem

$$\tilde{\mathbf{v}}_\beta.\nabla\{c_A\} + \mathbf{v}_\beta.\nabla\tilde{c}_{A\beta} = \nabla.\left(\mathbf{D}^{\mathrm{III}}_{A\beta}.\nabla\tilde{c}_{A\beta}\right) - \frac{1}{V_\beta}\int_{A_{\beta\sigma}}\mathbf{n}_{\beta\sigma}.\left(\mathbf{D}^{\mathrm{III}}_{A\beta}.\nabla\tilde{c}_{A\beta}\right)dA \qquad \text{in the } \beta\text{-region} \tag{7.88}$$

$$0 = \nabla.\left(D_{A\sigma}\nabla\tilde{c}_{A\sigma}\right) - \frac{1}{V_\sigma}\int_{A_{\sigma\beta}}\mathbf{n}_{\sigma\beta}.\left(D_{A\sigma}\nabla\tilde{c}_{A\sigma}\right)dA \qquad \text{in the } \sigma\text{-phase} \tag{7.89}$$

$$\text{BC1}: \quad -\mathbf{n}_{\beta\sigma}.\left(\mathbf{D}^{\mathrm{III}}_{A\beta}.\nabla\tilde{c}_{A\beta} - \mathbf{D}^{\mathrm{III}}_{A\beta}.\nabla\{c_A\}\right) = \frac{E_0}{\Gamma}\left(\tilde{c}_{A\beta} - \alpha_0\tilde{c}_{A\sigma}\right) \quad \text{at } A_{\beta\sigma} \tag{7.90}$$

$$\text{BC2}: \quad \mathbf{n}_{\beta\sigma}.\left(\mathbf{D}^{\mathrm{III}}_{A\beta}.\nabla\tilde{c}_{A\beta} - D_{A\sigma}\mathbf{I}.\nabla\tilde{c}_{A\sigma}\right) = -\mathbf{n}_{\beta\sigma}.\left[\left(\mathbf{D}^{\mathrm{III}}_{A\beta} - \alpha_0^{-1}D_{A\sigma}\mathbf{I}\right).\nabla\{c_A\}\right] \quad \text{at } A_{\beta\sigma} \tag{7.91}$$

with

$$\Gamma = \alpha_1 + \alpha_2\langle c_{A\beta}\rangle^\beta + \alpha_3\langle c_{A\sigma}\rangle^\sigma + \alpha_4\langle c_{A\beta}\rangle^\beta\langle c_{A\sigma}\rangle^\sigma \tag{7.92}$$

The derivation of the mass transfer boundary condition Eq. (7.90) is described in detail in Wood & Whitaker [1998, 2000].

Only a source term of the first order is present in Eqs. (7.88), (7.90) and (7.91). In order to solve the deviation problem, one need to relate the deviation quantities to the average values. Considering the form of these source terms, we propose

$$\tilde{c}_{A\beta} = \mathbf{d}_\beta.\nabla\langle c_{A\beta}\rangle^\beta = \mathbf{d}_\beta.\nabla\{c_A\} \tag{7.93}$$

$$\tilde{c}_{A\sigma} = \mathbf{d}_\sigma.\nabla\langle c_{A\sigma}\rangle^\sigma = \alpha_0^{-1}\mathbf{d}_\sigma.\nabla\{c_A\} \tag{7.94}$$

where $\mathbf{d}_\beta$ and $\mathbf{d}_\sigma$ are the closure variables. Substituting the representations Eqs. (7.93) and (7.94) in the averaged equation Eq. (7.84), the *closed macroscopic mass transport equation* is deduced

$$\frac{\partial\left[\left(\alpha_0^{-1}\varepsilon_\sigma+\varepsilon_\alpha\varepsilon_\beta\right)\{c_A\}\right]}{\partial t}+\varepsilon_\beta\left\langle\mathbf{v}_\beta\right\rangle^\beta.\nabla\{c_A\}=\nabla.\left(\mathbf{D}_{A\omega}^{\mathrm{II}}.\nabla\{c_A\}\right)-\varepsilon_\sigma k_A\frac{\{c_A\}}{\{c_A\}+\alpha_0 K_A} \tag{7.95}$$

where the effective tissue diffusion-dispersion tensor is defined by

$$\begin{aligned}\mathbf{D}_{A\omega}^{\mathrm{II}}=&\left(\varepsilon_\sigma\alpha_0^{-1}D_{A\sigma}\mathbf{I}+\varepsilon_\beta\mathbf{D}_{A\beta}^{\mathrm{III}}\right)\\&+\alpha_0^{-1}D_{A\sigma}\mathbf{I}.\frac{1}{\mathcal{V}_{\mathrm{III}}}\int_{A_{\sigma\beta}}\mathbf{n}_{\sigma\beta}\mathbf{d}_\sigma dA+\mathbf{D}_{A\beta}^{\mathrm{III}}.\frac{1}{\mathcal{V}_{\mathrm{III}}}\int_{A_{\beta\sigma}}\mathbf{n}_{\beta\sigma}\mathbf{d}_\beta dA-\left\langle\tilde{\mathbf{v}}_\beta\mathbf{d}_\beta\right\rangle\end{aligned} \tag{7.96}$$

Whilst the three first terms of $\mathbf{D}_{A\omega}^{\mathrm{II}}$ represent the influence of the cellular scale structure on the tissue effective transport properties, the last term of Eq. (7.96) shows the contribution of the fluid velocity to dispersion.

The only cellular scale variables present in Eq. (7.95), are the $\mathbf{d}_\beta$ and $\mathbf{d}_\sigma$ included in the effective diffusion tensors $\mathbf{D}_{A\omega}^{\mathrm{II}}$. In order to be evaluated, a problem for the closure variables must be built, and this is done by introducing Eqs. (7.93) and (7.94) into the deviation problem (Eqs. (7.88) to (7.91))

$$\tilde{\mathbf{v}}_\beta+\mathbf{v}_\beta.\nabla\mathbf{d}_\beta=\mathbf{D}_{A\beta}^{\mathrm{III}}.\nabla^2\mathbf{d}_\beta-\frac{1}{V_\beta}\int_{A_{\beta\sigma}}\mathbf{n}_{\beta\sigma}.\left(\mathbf{D}_{A\beta}^{\mathrm{III}}\nabla\mathbf{d}_\beta\right)dA\qquad\text{in the }\beta\text{-region} \tag{7.97}$$

$$0=D_{A\sigma}\nabla^2\mathbf{d}_\sigma-\frac{1}{V_\sigma}\int_{A_{\sigma\beta}}\mathbf{n}_{\sigma\beta}.\left(D_{A\sigma}\nabla\mathbf{d}_\sigma\right)dA\qquad\text{in the }\sigma\text{-phase} \tag{7.98}$$

$$\text{BC1}:\quad\mathbf{d}_\beta-\mathbf{d}_\sigma=-\mathbf{n}_{\beta\sigma}.\frac{\Gamma}{E_0}\mathbf{D}_{A\beta}^{\mathrm{III}}.\left(\mathbf{I}+\nabla\mathbf{d}_\beta\right)\qquad\text{at }A_{\beta\sigma} \tag{7.99}$$

$$\text{BC2}:\quad\mathbf{n}_{\beta\sigma}.\left(\mathbf{D}_{A\beta}^{\mathrm{III}}.\nabla\mathbf{d}_\beta-\alpha_0^{-1}D_{A\sigma}\mathbf{I}.\nabla\mathbf{d}_\sigma\right)=-\mathbf{n}_{\beta\sigma}.\left(\mathbf{D}_{A\beta}^{\mathrm{III}}-\alpha_0^{-1}D_{A\sigma}\mathbf{I}\right)\qquad\text{at }A_{\beta\sigma} \tag{7.100}$$

$$\mathbf{d}_\beta(\mathbf{x}+l_i)=\mathbf{d}_\beta(\mathbf{x})\qquad i=1,2,3 \tag{7.101}$$

$$\mathbf{d}_\sigma(\mathbf{x}+l_i)=\mathbf{d}_\sigma(\mathbf{x})\qquad i=1,2,3 \tag{7.102}$$

$$\left\langle\mathbf{d}_\beta\right\rangle^\beta=0 \tag{7.103}$$

$$\left\langle\mathbf{d}_\sigma\right\rangle^\sigma=0 \tag{7.104}$$

Once again, periodicity has been supposed to replace the unknown boundary condition at the limit of the averaging volume. This does not suppose the tissue to be periodic, only that the distribution of the cells within the tissue, varies on long distances compared to the size of the averaging volume (homogeneous tissue).

7.3.2 Computation of the tissue diffusion-dispersion tensor

Here we wish to investigate mass transport in the tissue, in regard to (i) the relative diffusivity between the β-region and σ-phase, (ii) the active membrane transport parameter, (iii) the permeability in the β-region.

The closure problem for mass transport at the cellular scale is defined by Eqs. (7.97) to (7.104). Following the same approach than in Sec. 6.2.2, its dimensionless form is

$$\mathrm{Pe}_\beta \left(\tilde{\mathbf{v}}'_\beta + \mathbf{v}'_\beta.\nabla \mathbf{d}'_\beta\right) = \nabla^2 \mathbf{d}'_\beta - \frac{1}{V_\beta}\int_{A_{\beta\sigma}} \mathbf{n}_{\beta\sigma}.\mathbf{d}'_\beta dA \qquad \text{in the } \beta\text{-region} \tag{7.105}$$

$$0 = D_{\sigma\beta}\nabla^2 \mathbf{d}'_\sigma - \frac{1}{V_\sigma}\int_{A_{\sigma\beta}} \mathbf{n}_{\sigma\beta}.\left(D_{\sigma\beta}\nabla \mathbf{d}'_\sigma\right) dA \qquad \text{in the } \sigma\text{-phase} \tag{7.106}$$

$$\text{BC1}: \quad \mathbf{d}'_\beta - \mathbf{d}'_\sigma = -\mathbf{n}_{\beta\sigma}.\left[\gamma_\beta\left(\mathbf{I} + \nabla \mathbf{d}'_\beta\right)\right] \qquad \text{at } A_{\beta\sigma} \tag{7.107}$$

$$\text{BC2}: \quad \mathbf{n}_{\beta\sigma}.\left(\nabla \mathbf{d}'_\beta - D_{\sigma\beta}\mathbf{I}.\nabla \mathbf{d}'_\sigma\right) = -\mathbf{n}_{\beta\sigma}.\left(\mathbf{I} - D_{\sigma\beta}\mathbf{I}\right) \qquad \text{at } A_{\beta\sigma} \tag{7.108}$$

$$\mathbf{d}'_\beta(\mathbf{x} + l_i) = \mathbf{d}'_\beta(\mathbf{x}) \qquad i = 1,2,3 \tag{7.109}$$

$$\mathbf{d}'_\sigma(\mathbf{x} + l_i) = \mathbf{d}'_\sigma(\mathbf{x}) \qquad i = 1,2,3 \tag{7.110}$$

$$\langle \mathbf{d}'_\beta \rangle^\beta = 0 \tag{7.111}$$

$$\langle \mathbf{d}'_\sigma \rangle^\sigma = 0 \tag{7.112}$$

where the dimensionless variables are defined as

$$\mathbf{d}'_\beta = \frac{\mathbf{d}_\beta}{l_\beta} \quad ; \quad \mathbf{d}'_\sigma = \frac{\mathbf{d}_\sigma}{l_\beta} \quad ; \quad \tilde{\mathbf{v}}'_\beta = \frac{\tilde{\mathbf{v}}_\beta}{\|v_\beta\|} \quad ; \quad \mathbf{v}'_\beta = \frac{\mathbf{v}_\beta}{\|v_\beta\|} \tag{7.113}$$

with

$$\|v_\beta\| = \left(\langle \mathbf{v}_\beta \rangle^\beta.\langle \mathbf{v}_\beta \rangle^\beta\right)^{1/2} \tag{7.114}$$

One can see three dimensionless parameters arising from this problem : the cellular scale Péclet number (Pe_β) which represents the relative contributions between the fluid flow and the diffusion of the species A in the β-region ; the relative diffusivity ($D_{\sigma\beta}$) between the β-region and the σ-phase ; and the relative membrane transport parameter (γ_β) which represents the relative contribution between the membrane transport and the diffusion in the β-region. These dimensionless parameters are defined as

$$\mathrm{Pe}_\beta = \frac{\|v_\beta\| l_\beta}{D^{\mathrm{III}}_{A\beta}} \quad ; \quad D_{\sigma\beta} = \frac{\alpha_0^{-1} D_{A\sigma}}{D^{\mathrm{III}}_{A\beta}} \quad ; \quad \gamma_\beta = \frac{\Gamma}{E_0}\frac{D^{\mathrm{III}}_{A\beta}}{l_\beta} \tag{7.115}$$

Here we suppose to remain in the diffusive regime at the ECM scale (Fig. 6.6), so the diffusion-dispersion tensor in the β-region can be written $\mathbf{D}^{\mathrm{III}}_{A\beta} = D^{\mathrm{III}}_{A\beta}\mathbf{I}$. With these definitions, the diffusion-dispersion tensor at the tissue scale (Eq. (7.96)) can be written in its dimensionless form

$$\frac{\mathbf{D}^{\mathrm{II}}_{A\omega}}{D^{\mathrm{III}}_{A\beta}} = \left(\varepsilon_\sigma D_{\sigma\beta} + \varepsilon_\beta\right)\mathbf{I} + \frac{D_{\sigma\beta}}{\mathcal{V}_{\mathrm{III}}}\int_{A_{\sigma\beta}} \mathbf{n}_{\sigma\beta}\mathbf{d}'_\sigma dA + \frac{1}{\mathcal{V}_{\mathrm{III}}}\int_{A_{\beta\sigma}} \mathbf{n}_{\beta\sigma}\mathbf{d}'_\beta dA - \mathrm{Pe}_\beta\langle \tilde{\mathbf{v}}'_\beta \mathbf{d}'_\beta\rangle \tag{7.116}$$

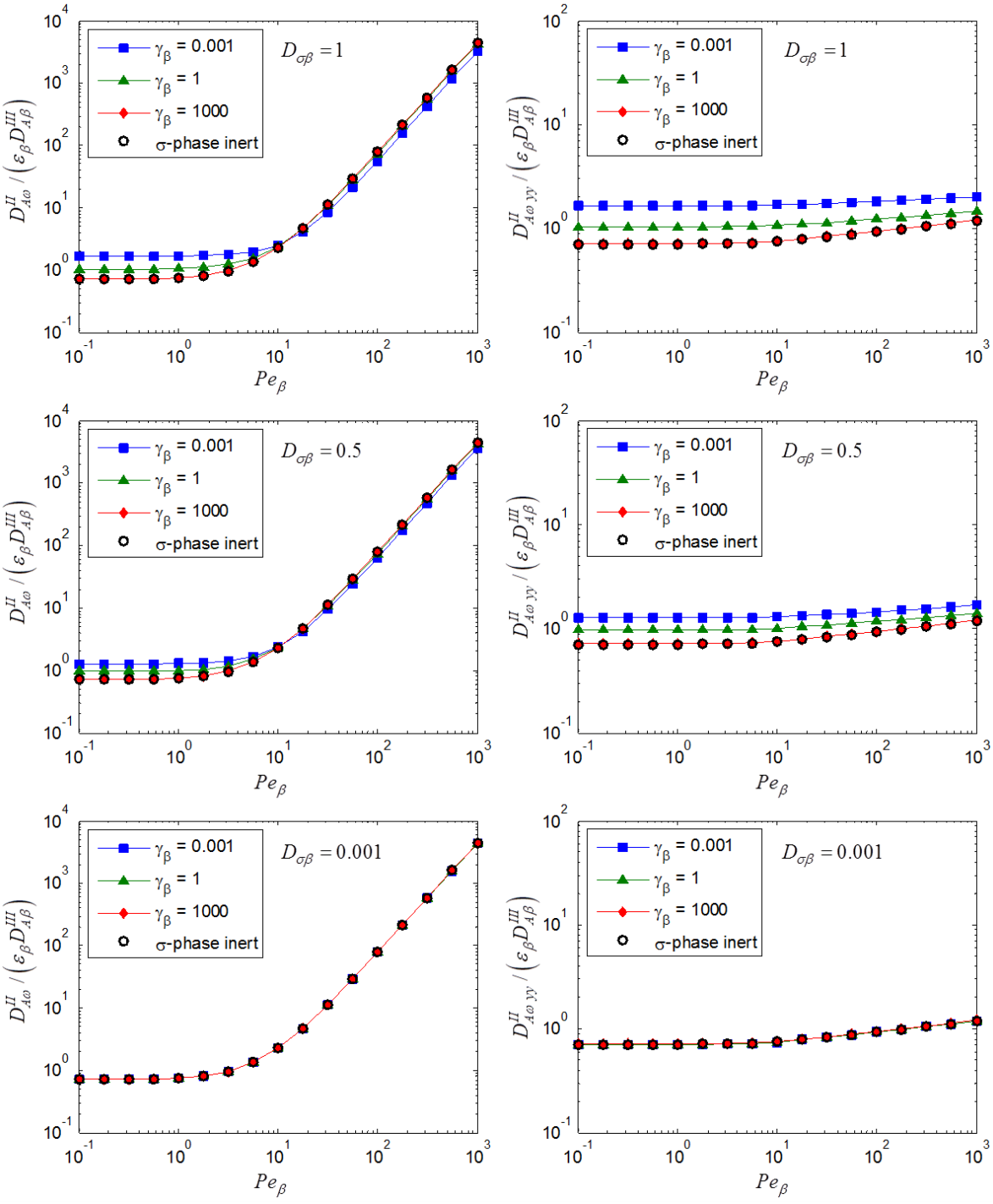

Figure 7.7 – Influence of the relative diffusivity $D_{\sigma\beta}$ and the membrane transport parameter γ_β on the longitudinal (left) and transverse (right) dispersion. Stokes flow around in-line diffusive cylinders ($\varepsilon_\beta = 0.6$)

One can argue that using $D_{A\alpha}$ instead of $D^{\text{III}}_{A\beta}$ in the definition of the dimensionless parameters is more appropriate. However this would introduce one more diffusivity in the representation of the closure problem, and complexify the definition of $D_{\sigma\beta}$. In the present case, this is not an issue since $D^{\text{III}}_{A\beta}$ lays in the diffusive regime, and is thus proportional to $D_{A\alpha}$. The reader is directed to App. B for an example where this simplification is not valid.

The closure problem for mass transport at the cellular scale (Eqs. (7.105) to (7.112)) is valid for known fluid velocity field $\mathbf{v}_\beta$. In order to study mass transport independently of the effects of the permeability, we first suppose an incompressible Stokes flow in the β-region. This corresponds to the limit case where $\mathbf{K}^{\text{III}}_\beta$ tends to plus infinity. The diffusion closure problem is solved using the finite element software Comsol Multiphysics, on a two-dimensional unit cell representing an in-line array of cylinders, with the β-region being fluid and ε_β fixed to 0.6. Fig. 7.7 shows the results of the longitudinal and transverse effective diffusion-dispersion tensor $\mathbf{D}^{\text{II}}_{A\omega}$, for various values of the dimensionless parameters Pe_β, $D_{\sigma\beta}$, and γ_β. For all the longitudinal diffusion-dispersion coefficients, a classical two regimes behavior is observed : at values of Péclet number lower than 10, mass transport is directed by diffusive effects, while for larger values of the Péclet number, mass transport is dominated by the convective effects, leading to dispersion. One can note that the transverse component of the diffusion-dispersion tensor $D^{\text{II}}_{\omega yy}$ is almost independent of the Péclet number.

Turning our attention to the membrane transport parameter γ_β, the results show that it influences the effective diffusion-dispersion coefficient, $\mathbf{D}^{\text{II}}_{A\omega}$, essentially in the diffusive regime. For very large values of γ_β, the membrane transport is negligible compared to the diffusion process, and the boundary condition Eq. (7.107) reduces to a no-flux condition at $A_{\beta\sigma}$. This has for consequence that the tissue effective diffusion $\mathbf{D}^{\text{II}}_{A\omega}$, behaves as if the σ-phase is inert. On the other hand, when γ_β tends to zero, Eq. (7.107) reduces to an interfacial continuity equation, enhancing the effective tissue diffusion. Finally, it has to be noted that for very low values of the relative diffusivity $D_{\sigma\beta}$, the diffusion in the σ-phase is very small compared to mass transport in the β-region. This has for consequence that the cellular region is inert in regard to mass transport, making negligible the influence of the interfacial transport parameter, γ_β, on the diffusion-dispersion tensor $\mathbf{D}^{\text{II}}_{A\omega}$.

We now wish to study the influence of the ECM permeability $\mathbf{K}^{\text{III}}_\beta$, on the tissue effective diffusion-dispersion coefficient $\mathbf{D}^{\text{II}}_{A\omega}$. To this purpose, the velocity field in the β-region is now described by an incompressible Darcy-Brinkman flow. The values of the ECM permeability $\mathbf{K}^{\text{III}}_\beta$ are determined from the solution of the closure problem for momentum transport (Eqs. (6.30) to (6.35)), on a two-dimensional unit cell representing an array of in-line cylinder. Considering the numerous parameters implied in the system, only intermediate values of the transport parameters are investigated ($D_{\sigma\beta} = 0.5$, $\gamma_\beta = 1$). As shown in Fig. 7.8, the ECM permeability $\mathbf{K}^{\text{III}}_\beta$ influences the longitudinal diffusion-dispersion tensor $D^{\text{II}}_{A\omega}$ only in the dispersive regime, where the flow of the fluid is important compared to the diffusive transport. For a given Péclet number, lower values of the permeability in the β-region, result in a lower dispersion, until a minimum is reach.

One has to keep in mind that, in the present section, no dispersive effects have been considered within the β-region. Under this hypothesis, the conclusions of this numerical study are that the tissue effective diffusion dispersion coefficient $\mathbf{D}^{\text{II}}_{A\omega}$, is influenced by the mem-

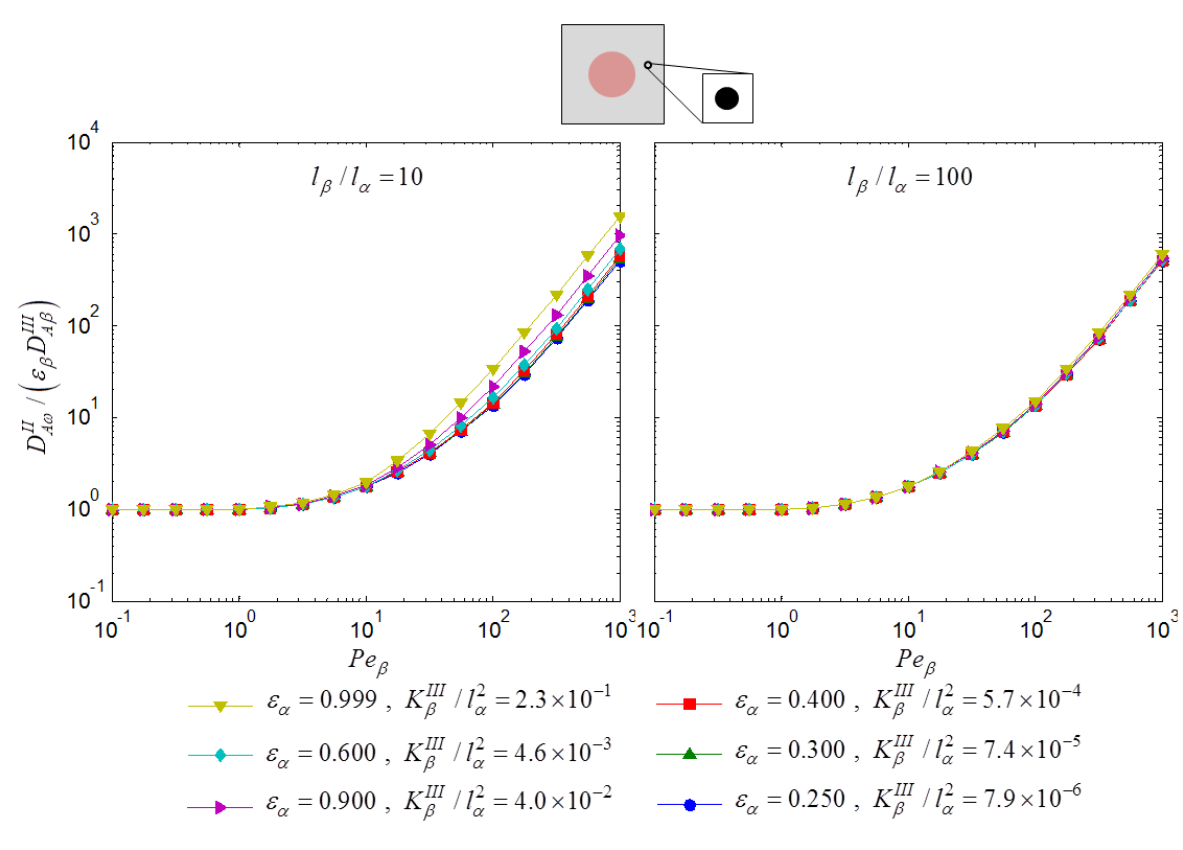

Figure 7.8 – Influence of the β-region permeability $\mathbf{K}^{\mathrm{III}}_\beta$ on the longitudinal tissue diffusion-dispersion coefficient $\mathbf{D}^{\mathrm{II}}_{A\omega}$. ($\varepsilon_\beta = 0.6$, $D_{\sigma\beta} = 0.5$, $\gamma_\beta = 1$)

brane transport properties γ_β, essentially at low Péclet values, while dependent on the ECM effective permeability $\mathbf{K}^{\mathrm{III}}_\beta$ only at high Péclet. Nevertheless, at high Pe_β, cell scale dispersion is likely to appear. This is not a problem in the case of mass transport in biological tissues, where the velocity in the ECM is very low. Yet, in the general case, the effects of dispersion at level III must be taken into account when computing the effective diffusion-dispersion coefficient at level II, and this is done in App. B.

In this chapter, momentum and mass transport at the cellular scale have been upscaled, leading to a system of equations describing transport at the tissue scale. These equations include effective properties, which have been numerically computed for a large range of cell scale parameters. The next step toward the development of a macroscopic model, is the upscaling of transport phenomena from the tissue to the bioreactor scale, and this is the subject of the next chapter.

CHAPTER 8

THE TISSUE SCALE

IN THE PREVIOUS chapters, the transport properties of the biological tissue have been evaluated through two successive upscalings. The inter-scale dependencies have been shown, and realistic tissue effective permeability and diffusion-dispersion coefficients have been computed. In the present chapter, the final upscaling from the tissue scale (level II) to the bioreactor scale (level I) is developed. As depicted in Fig. 8.1, the tissue scale system is composed of three regions, the κ-region defining the glass beads, the ω-region representing the tissue, and the γ-region characterizing the liquid culture medium. In practice, the velocity of the culture medium in the bioreactor (γ-region) is much larger than the velocity of the fluid within the tissue (ω-region). This motivates the derivation of non-equilibrium transport models for both, momentum and mass transport.

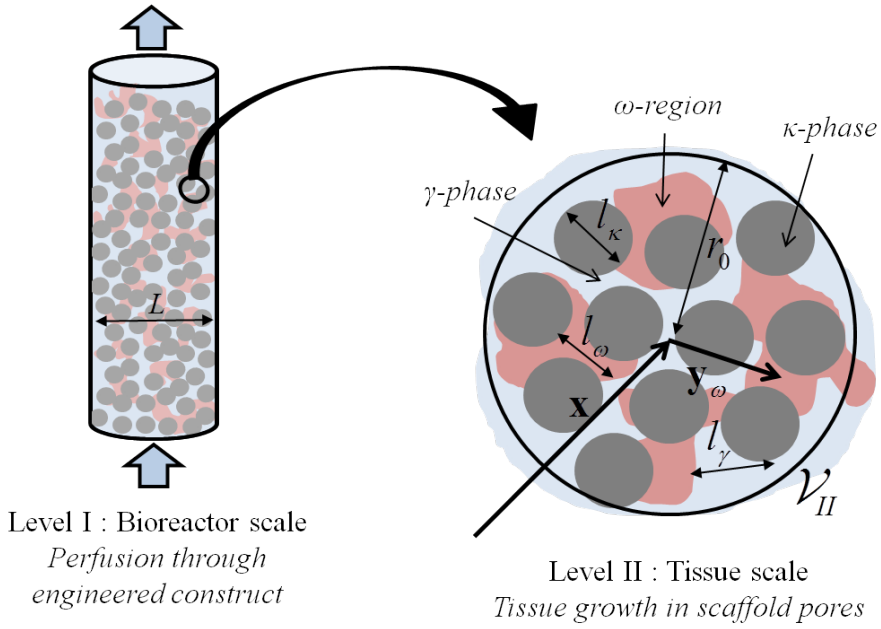

Figure 8.1 – Definition of the phases and length scales associated with the tissue averaging volume

8.1 Local description of the tissue scale

We are now facing a three-phase system where the κ-region is a rigid and inert phase, and the γ-region is a fluid phase where momentum and mass transport take place. Even though we have shown in the previous developments of this study that the ω-region is a complex hierarchical structure at the lower scales, it is considered at the tissue scale as a continuous and homogeneous region. The transport properties of the tissue (ω-region) have been derived through two successive homogenization steps (Chaps. 6 and 7) resulting in a set of conservation equations for momentum (Eqs. (7.33) and (7.47)) and mass (Eq. (7.95)) transport. Following Chap. 7, we use notation equivalences to link the tissue averaged quantities to lower scales point variables

$$\mathbf{v}_\omega \equiv \langle \mathbf{v}_\beta \rangle_\omega = \langle \langle \mathbf{v}_\alpha \rangle_\beta \rangle_\omega \tag{8.1}$$

$$p_\omega \equiv \langle p_\beta \rangle_\omega^\beta = \left\langle \langle p_\alpha \rangle_\beta^\alpha \right\rangle_\omega^\beta \tag{8.2}$$

$$c_{A\omega} \equiv \{c_A\}_\omega = \langle \langle c_{A\alpha} \rangle_\beta \rangle_\omega + \alpha_0 \langle c_{A\sigma} \rangle_\omega \tag{8.3}$$

$$\rho_\omega \equiv \rho_\beta \varepsilon_\beta + \rho_\sigma \varepsilon_\sigma = (\rho_\alpha \varepsilon_\alpha + \rho_\eta \varepsilon_\eta)\varepsilon_\beta + \rho_\sigma \varepsilon_\sigma \tag{8.4}$$

$$\varepsilon_{\text{III}} \equiv \alpha_0^{-1} \varepsilon_\sigma + \varepsilon_\alpha \varepsilon_\beta \tag{8.5}$$

$$R_\omega = -\varepsilon_\sigma k_A \frac{\{c_A\}_\omega}{\{c_A\}_\omega + \alpha_0 K_A} \tag{8.6}$$

$$Q_\omega \equiv \langle Q_\beta + Q_\sigma \rangle_\omega = \langle \langle Q_\eta \rangle_\beta + Q_\sigma \rangle_\omega \tag{8.7}$$

Here subscripts have been added to recall in which region the quantities are averaged. Beside saving considerable space, this definitions show clearly the underlying hierarchical property of the tissue and the relation between the different scales. It is now possible to write the conservation equations for momentum and mass transport (Eqs. (7.33), (7.47) and (7.95)) in the ω-region, in the local form

$$\frac{\partial \rho_\omega}{\partial t} + \nabla.(\rho_\alpha \mathbf{v}_\omega) = Q_\omega \quad \text{in the } \omega\text{-region} \tag{8.8}$$

$$\rho_\alpha \varepsilon_\alpha^{-1} \varepsilon_\beta^{-1} \frac{\partial \mathbf{v}_\omega}{\partial t} = -\nabla p_\omega - \frac{\mu_\alpha}{\mathbf{K}_\omega^{\text{II}}} \mathbf{v}_\omega + \mu_\alpha \varepsilon_\alpha^{-1} \varepsilon_\beta^{-1} \nabla^2 \mathbf{v}_\omega + \rho_\alpha \mathbf{g} \quad \text{in the } \omega\text{-region} \tag{8.9}$$

$$\frac{\partial}{\partial t}(\varepsilon_{\text{III}} c_{A\omega}) + \nabla.(\mathbf{v}_\omega c_{A\omega}) = \nabla.(\mathbf{D}_{A\omega}^{\text{II}}.\nabla c_{A\omega}) + R_\omega \quad \text{in the } \omega\text{-region} \tag{8.10}$$

We recall that the tissue permeability $\mathbf{K}_\omega^{\text{II}}$ and diffusion-dispersion tensor $\mathbf{D}_{A\omega}^{\text{II}}$ are defined in Eqs. (7.46) and (7.96), and have been computed through the solution of their respective closure problem.

The fluid constituting the γ-phase is the same culture medium than in the α-phase (level IV), however we keep the subscripts γ when referring to the fluid velocity $\mathbf{v}_\gamma$, pressure p_γ and species A concentration $c_{A\gamma}$ in this region. This is consistent with the use of notation equivalences (Eqs. (7.9) to (7.11) and Eqs. (8.1) to (8.7)) in the sense that these are variables of the α-phase in the γ-region. An estimation of the bioreactor set-up parameters ($\|v_\gamma\| \sim 10^{-3}$m/s, $l_\gamma \sim 10^{-3}$m, $\rho_\alpha \sim 10^3$kg/m^3 and $\mu_\alpha \sim 10^{-2}$Pa.s), leads to a Reynolds number

related to the flow in the γ-phase of the order of 1 to 10. This range is usually associated to the transition zone toward a flow regime where inertia effects are dominant [Nield & Bejan, 2006]. The consequences of including inertia in the γ-region would lead to a Forchheimer term at the bioreactor scale, whose contribution is laborious to evaluate theoretically and computationally [Lasseux et al., 2011]. Inertial effects are not the focus of this study, and considering the range of the Reynolds number, it is a reasonable assumption to neglect it. Therefore momentum transport in the γ-phase is modeled by an incompressible Stokes flow, while mass transport is represented by a diffusion-convection equation

$$\frac{\partial \rho_\alpha}{\partial t} + \nabla.(\rho_\alpha \mathbf{v}_\gamma) = 0 \quad \text{in the } \gamma\text{-phase} \tag{8.11}$$

$$\rho_\alpha \frac{\partial \mathbf{v}_\gamma}{\partial t} = -\nabla p_\gamma + \mu_\alpha \nabla^2 \mathbf{v}_\gamma + \rho_\alpha \mathbf{g} \quad \text{in the } \gamma\text{-phase} \tag{8.12}$$

$$\frac{\partial c_{A\gamma}}{\partial t} + \nabla.\left(\mathbf{v}_\gamma c_{A\gamma}\right) = \nabla.(D_{A\alpha} \nabla c_{A\gamma}) \quad \text{in the } \gamma\text{-phase} \tag{8.13}$$

Here the bulk culture medium density ρ_α, viscosity μ_α and diffusivity $D_{A\alpha}$ are supposed to be equal to the ones in the α-phase (level IV). In practice this may not be exact since the ECM interstitial medium may contain higher concentrations of biomolecules and fragments produced by cellular activity, which could modify the interstitial fluid properties from the clear culture medium [Swartz & Fleury, 2007]. However in this study we will assume that the variations of ρ_α, μ_α and $D_{A\alpha}$ are negligible between the γ and α-phases.

This system needs to be completed with boundary conditions at the three interfaces $A_{\gamma\kappa}$, $A_{\omega\kappa}$ and $A_{\gamma\omega}$. Since the κ-phase is an inert solid, the two first interfaces are easy to describe with boundary conditions similar to the ones used in the previous chapters

$$\text{BC1}: \quad \mathbf{v}_\gamma = 0 \quad \text{at } A_{\gamma\kappa} \tag{8.14}$$

$$\text{BC2}: \quad \mathbf{v}_\omega = 0 \quad \text{at } A_{\omega\kappa} \tag{8.15}$$

$$\text{BC3}: \quad -\mathbf{n}_{\gamma\kappa}.\left(D_{A\alpha} \nabla c_{A\gamma}\right) = 0 \quad \text{at } A_{\gamma\kappa} \tag{8.16}$$

$$\text{BC4}: \quad -\mathbf{n}_{\omega\kappa}.\left(\mathbf{D}^{\text{II}}_{A\omega}.\nabla c_{A\omega}\right) = 0 \quad \text{at } A_{\omega\kappa} \tag{8.17}$$

Where $\mathbf{n}_{\gamma\kappa}$ (respectively $\mathbf{n}_{\omega\kappa}$) is the unit normal vector pointing from the γ-phase (respectively ω-region) toward the κ-phase. These equations represent no-slip and no-flux boundary conditions at the interfaces with the solid κ-phase.

The remaining interface is between the fluid γ-phase and the porous ω-region. Transport phenomena at a fluid-porous interface is still a vibrant research area and a general description of the physics in such a system is still missing. Concerning momentum transport in a fluid/porous channel, pioneer work from Beavers & Joseph [1967] proposes a semi-empirical jump condition to link a Stokes flow in the fluid phase, to a Darcy flow in the porous region. This condition has been later adapted for a Brinkman flow in the porous region, allowing the continuity on both the velocity field and the viscous stress [Neale & Nader, 1974]. In order to get rid of the semi-empirical coefficient in the previous jump conditions, Ochoa-Tapia &

Whitaker [1995] take advantage of the volume averaging technique to develop a jump condition on the stress, which can be determined through the resolution of a closure problem. However in this later model the continuity on the velocity field is still assumed, and the difficulty of the resolution of the closure problem prohibitive. Alternatively, a fluid-porous system can be modeled via the one-domain approach, where the spacial variations of the interface properties are taken into account within space dependent parameters of a generalized transport equation, valid in the two regions [Goyeau et al., 2003; Chandesris & Jamet, 2006]. Introducing the macroscopic velocity deviations of the two-domain with respect to the one-domain approach, Valdés-Parada et al. [2013] develop a velocity and a stress jump boundary condition whose coefficients are determined by the solution of a macroscopic closure problem. In all this models, the underlying questions are on the position of the dividing surface and the spacial evolution of the properties in the inter-region. Although the above cited studies give material to deal with these issues in the case of uni-dimensional flow, we are still far from a definitive answer in the general case.

In the present problem, the exact location and properties of the interface between the tissue (ω-region) and the culture medium (γ-phase) are unknown, and time dependent. Therefore the continuity of the fluid velocity and the viscous stress is assumed at the fluid-porous interface

$$\text{BC5}: \quad \mathbf{v}_\gamma = \mathbf{v}_\omega \quad \text{at } A_{\gamma\omega} \tag{8.18}$$

$$\begin{aligned}\text{BC6}: \quad \mathbf{n}_{\gamma\omega}.\left[-p_\gamma \mathbf{I} + \mu_\alpha \left(\nabla \mathbf{v}_\gamma + \nabla \mathbf{v}_\gamma^T\right)\right] = \\ \mathbf{n}_{\gamma\omega}.\left[-p_\omega \mathbf{I} + \mu_\alpha \varepsilon_\alpha^{-1} \varepsilon_\beta^{-1} \left(\nabla \mathbf{v}_\omega + \nabla \mathbf{v}_\omega^T\right)\right] \quad \text{at } A_{\gamma\omega}\end{aligned} \tag{8.19}$$

Note that for consistence with the averaged tissue transport equations, the effective viscosity in the ω-region is $\mu_\alpha \varepsilon_\alpha^{-1} \varepsilon_\beta^{-1}$. The stress continuity boundary condition Eq. (8.19) is actually similar to the jump condition proposed by Ochoa-Tapia & Whitaker [1995] with zero jump coefficients. This form has also been used in studies of multiphase fluid flow [Whitaker, 1986b; Lasseux et al., 1996], with an additional surface tension term. Assuming Eqs. (8.18) and (8.19) is consistent with recent models on momentum transport at biological interfaces [Yu, 2012; Kapellos et al., 2012].

Only the mass transport boundary conditions at $A_{\gamma\omega}$ remain to be defined

$$\begin{aligned}\text{BC7}: \quad -\mathbf{n}_{\gamma\omega}.\left[\left(\mathbf{w}_{\gamma\omega} - \mathbf{v}_\gamma\right) c_{A\gamma} + D_{A\alpha} \nabla c_{A\gamma}\right] = \\ -\mathbf{n}_{\gamma\omega}.\left[\left(\mathbf{w}_{\gamma\omega} - \mathbf{v}_\omega\right) c_{A\omega} + \mathbf{D}_{A\omega}^{\text{II}}.\nabla c_{A\omega}\right] \quad \text{at } A_{\gamma\omega}\end{aligned} \tag{8.20}$$

$$\text{BC8}: \quad c_{A\gamma} = c_{A\omega} \quad \text{at } A_{\gamma\omega} \tag{8.21}$$

While Eq. (8.20) represents the flux conservation at the interface $A_{\gamma\omega}$, Eq. (8.21) assumes the continuity of the concentration fields between the γ and ω-regions [Davit et al., 2010; Wood et al., 2011].

The local problem at the tissue scale (level II) is now fully defined by Eqs. (8.8) to (8.21). As discussed in Sec. 7.3.1, for a system where transport is present in two distinct regions, the general averaging model yields to two macroscopic equations, with coupling tensors, and multiple closure problems. Despite the large range of conditions for which these two-equations

models are valid, the complexity of their development and resolution remain fastidious. In some specific cases, it is possible to link the physics in the two regions by an equilibrium constant. This allows to define a special average variable (velocity, pressure or concentration) and to develop a one-equation equilibrium model. For instance, mechanical equilibrium in momentum transport between two porous media has been studied in [Quintard & Whitaker, 1998a], while mass equilibrium is widely assumed in tissue engineering [Lasseux et al., 2004] and biofilm models [Golfier et al., 2009; Wood et al., 2011]. Although this types of model are easier to develop and to solve, their domain of validity is restricted to the cases where the characteristic time and length scales related to the transport phenomena in the two regions are sufficiently close [Wood & Whitaker, 1998; Golfier et al., 2009].

In the next sections, it will be shown that, at the tissue scale (level II), equilibrium conditions between the γ and ω-regions are neither met for momentum nor mass transport. A one-equation model in non equilibrium condition has been recently proposed for time asymptotic mass transport [Davit et al., 2010]. In the case of a perfusion bioreactor, this approach is an interesting alternative to two-equation models, since the time scale associated with transport phenomena are very long. Following this idea, a one-equation non-equilibrium model for momentum transport has been developed, and is presented in App. C. Unfortunately, this approach gives access to a weighted average only, and if one aims to couple the model for mass and momentum transport, to a tissue growth model, a solution for the tissue average is requested. For this reason, in the following sections, two-equation models for momentum and mass transport are developed, and the effective properties (main and coupling tensors) are evaluated by solving a series of closure problems.

8.2 Upscaling momentum transport to the bioreactor scale

In this section the momentum transport problem described at the tissue scale (level II) by Eqs. (8.8), (8.9), (8.11), (8.12), (8.14), (8.15), (8.18) and (8.19) is averaged, leading to a two-equation macroscopic model. A set of permeability tensors are defined, and corresponding closure systems are developed in order to allow their evaluation.

8.2.1 Theoretical development

The bioreactor is perfused with culture medium at 10mL/min. Given the geometry of the bioreactor, and that the porosity of a random sphere packing is about 40-50%, the order of magnitude of culture medium velocity in the γ-region is $\|v_\gamma\| \sim 10^{-3}$m/s. Considering the low permeability of the tissue ($K_\omega^{\mathrm{II}} \sim 10^{-14}\mathrm{m}^2$ [Levick, 1987; Swartz & Fleury, 2007; Fournier, 2011; Tarbell & Shi, 2013]), it is reasonable to suppose that the order of magnitude of the fluid velocity in the ω-region is much lower than in the γ-region.

$$\|v_\omega\| \ll \|v_\gamma\| \tag{8.22}$$

This indicates that the development of a mechanical equilibrium model is not suitable for the present problem [Quintard & Whitaker, 1998a]. Non-equilibrium models for momentum transport have been developed in the case of multiphase flow in porous medium [Whitaker, 1986b; Lasseux et al., 1996], for dual porosity systems [Quintard & Whitaker, 1996a,b] and fluid/porous systems [Soulaine et al., 2013]. They result in a two-equation macroscopic model with several permeability tensors (at least four), and multiple closure problems. These models, although representing well the physics of the problem for a wide range of conditions, are rarely used in practice due to their prohibitive complexity. In an attempt to overcome this limitation, a one-equation non-equilibrium model for momentum transport has been derived based on weighted averages. The derivation of such a model is presented in App. C. Yet, this model does not give access to the average velocity in the tissue region. Therefore, in the present section, a two-equation non-equilibrium model is developed to facilitate the coupling with a tissue growth model.

Mass conservation equations

Let us begin the averaging procedure with the mass conservation equations. Applying the averaging theorems on Eqs. (8.8) and (8.11) leads to

$$\frac{\partial}{\partial t}\left(\varepsilon_\gamma \rho_\alpha\right) + \nabla.\left(\rho_\alpha \varepsilon_\gamma \langle \mathbf{v}_\gamma \rangle^\gamma\right) = \dot{m}_\gamma \tag{8.23}$$

$$\frac{\partial}{\partial t}\left(\varepsilon_\omega \langle \rho_\omega \rangle^\omega\right) + \nabla.\left(\rho_\alpha \varepsilon_\omega \langle \mathbf{v}_\omega \rangle^\omega\right) = \dot{m}_\omega + \varepsilon_\omega \langle Q_\omega \rangle^\omega \tag{8.24}$$

where $\dot{m}_\gamma$ and $\dot{m}_\omega$ are the interfacial mass exchange rates defined as

$$\dot{m}_\gamma = -\sum_{i=\omega,\kappa} \frac{1}{\mathcal{V}_{\text{II}}} \int_{A_{\gamma i}} \mathbf{n}_{\gamma i}.\left(\mathbf{v}_\gamma - \mathbf{w}_{\gamma i}\right) \rho_\alpha dA \tag{8.25}$$

$$\dot{m}_\omega = -\sum_{i=\gamma,\kappa} \frac{1}{\mathcal{V}_{\text{II}}} \int_{A_{\omega i}} \mathbf{n}_{\omega i}.\left(\mathbf{v}_\omega \rho_\alpha - \mathbf{w}_{\omega i} \rho_\omega\right) dA \tag{8.26}$$

Note that both ρ_α and ρ_ω are present in the definition of $\dot{m}_\omega$. This is due to the fact that, Eq. (8.8) represents the total mass conservation in the tissue, and not only the mass of the transported α-phase. Consequently, the presence of ρ_ω indicates that the mass of the α, η, and σ phases are conserved in the tissue (see Eq. (8.4)).

The mass exchange rates still include local velocities, so the spacial deviations

$$\mathbf{v}_\gamma = \langle \mathbf{v}_\gamma \rangle^\gamma + \tilde{\mathbf{v}}_\gamma \qquad \mathbf{v}_\omega = \langle \mathbf{v}_\omega \rangle^\omega + \tilde{\mathbf{v}}_\omega \tag{8.27}$$

are introduced. Then expanding the average velocities in Taylor series, and applying the geometrical theorems, we get

$$\dot{m}_\gamma = \nabla \varepsilon_\gamma \rho_\alpha \langle \mathbf{v}_\gamma \rangle^\gamma - \sum_{i=\omega,\kappa} \frac{1}{\mathcal{V}_{\text{II}}} \int_{A_{\gamma i}} \mathbf{n}_{\gamma i}.\left(\tilde{\mathbf{v}}_\gamma - \mathbf{w}_{\gamma i}\right) \rho_\alpha dA \tag{8.28}$$

$$\dot{m}_\omega = \nabla \varepsilon_\omega \rho_\alpha \langle \mathbf{v}_\omega \rangle^\omega - \sum_{i=\gamma,\kappa} \frac{1}{\mathcal{V}_{\text{II}}} \int_{A_{\omega i}} \mathbf{n}_{\omega i}.\left(\tilde{\mathbf{v}}_\omega \rho_\alpha - \mathbf{w}_{\omega i} \rho_\omega\right) dA \tag{8.29}$$

If the macroscopic properties of the bioreactor evolve over a length scale L, much larger than the length scale of the deviation of the velocity ($L \gg l_\gamma$ and $L \gg l_\omega$), the gradients of the volume fractions become negligible compared to the other terms, and we obtain

$$\dot{m}_\gamma = -\sum_{i=\omega,\kappa} \frac{1}{\mathcal{V}_{\text{II}}} \int_{A_{\gamma i}} \mathbf{n}_{\gamma i} . \left(\tilde{\mathbf{v}}_\gamma - \mathbf{w}_{\gamma i}\right) \rho_\alpha dA \tag{8.30}$$

$$\dot{m}_\omega = -\sum_{i=\gamma,\kappa} \frac{1}{\mathcal{V}_{\text{II}}} \int_{A_{\omega i}} \mathbf{n}_{\omega i} . \left(\tilde{\mathbf{v}}_\omega \rho_\alpha - \mathbf{w}_{\omega i} \rho_\omega\right) dA \tag{8.31}$$

Finally, introducing back the mass exchange rates into Eqs. (8.23) and (8.24), the non-closed average mass conservation equations are deduced. Let us now turn our attention to the averaging of the momentum transport equations.

Momentum transport equations

The momentum problem at the tissue scale (level II) is described by Eqs. (8.8), (8.9), (8.11), (8.12), (8.14), (8.15), (8.18) and (8.19) Following the main steps of the volume averaging method presented in Sec. 7.2.1, the momentum equation in the γ-phase is written

$$\rho_\alpha \frac{\partial(\varepsilon_\gamma \langle \mathbf{v}_\gamma \rangle^\gamma)}{\partial t} - \sum_{i=\omega,\kappa} \rho_\alpha \frac{1}{\mathcal{V}_{\text{II}}} \int_{A_{\gamma i}} \mathbf{n}_{\gamma i} . \left(\mathbf{w}_{\gamma i} \mathbf{v}_\gamma\right) dA = -\varepsilon_\gamma \nabla \langle p_\gamma \rangle^\gamma + \rho_\alpha \varepsilon_\gamma \mathbf{g} + \mu_\alpha \varepsilon_\gamma \nabla^2 \langle \mathbf{v}_\gamma \rangle^\gamma + \sum_{i=\omega,\kappa} \frac{1}{\mathcal{V}_{\text{II}}} \int_{A_{\gamma i}} \mathbf{n}_{\gamma i} . \left(-\tilde{p}_\gamma + \mu_\alpha \nabla \tilde{\mathbf{v}}_\gamma\right) dA \tag{8.32}$$

where the spacial decompositions of the γ-phase velocity and pressure have been introduced. In Eq. (8.32), the only differences with the previous chapters are the multiple surface integrals due to the three-phase system, and the convective term at $A_{\gamma\omega}$ which cannot be discarded due to the velocity continuity. In order to treat this term, the surface integrals on the left hand side of Eq. (8.32) are developed using Gray's spacial decomposition for the fluid velocity

$$\sum_{i=\omega,\kappa} \frac{1}{\mathcal{V}_{\text{II}}} \int_{A_{\gamma i}} \mathbf{n}_{\gamma i} . \left(\mathbf{w}_{\gamma i} \mathbf{v}_\gamma\right) dA = \sum_{i=\omega,\kappa} \frac{1}{\mathcal{V}_{\text{II}}} \int_{A_{\gamma i}} \mathbf{n}_{\gamma i} . \left(\mathbf{w}_{\gamma i} \langle \mathbf{v}_\gamma \rangle^\gamma\right) dA + \sum_{i=\omega,\kappa} \frac{1}{\mathcal{V}_{\text{II}}} \int_{A_{\gamma i}} \mathbf{n}_{\gamma i} . \left(\mathbf{w}_{\gamma i} \tilde{\mathbf{v}}_\gamma\right) dA \tag{8.33}$$

The intrinsic averages are expanded in Taylor series, and using the usual length scale constraints and the general transport theorem, the interfacial convective terms are written

$$\sum_{i=\omega,\kappa} \frac{1}{\mathcal{V}_{\text{II}}} \int_{A_{\gamma i}} \mathbf{n}_{\gamma i} . \left(\mathbf{w}_{\gamma i} \mathbf{v}_\gamma\right) dA = \frac{\partial \varepsilon_\gamma}{\partial t} \langle \mathbf{v}_\gamma \rangle^\gamma + \sum_{i=\omega,\kappa} \frac{1}{\mathcal{V}_{\text{II}}} \int_{A_{\gamma i}} \mathbf{n}_{\gamma i} . \left(\mathbf{w}_{\gamma i} \tilde{\mathbf{v}}_\gamma\right) dA \tag{8.34}$$

When this form of the interfacial convection is introduced back in Eq. (8.32), the unclosed average equation for momentum transport in the γ-phase is obtained

$$\rho_\alpha \frac{\partial(\varepsilon_\gamma \langle \mathbf{v}_\gamma \rangle^\gamma)}{\partial t} - \rho_\alpha \frac{\partial \varepsilon_\gamma}{\partial t} \langle \mathbf{v}_\gamma \rangle^\gamma - \rho_\alpha \frac{1}{\mathcal{V}_{\text{II}}} \int_{A_{\gamma\omega}} \mathbf{n}_{\gamma\omega} . (\mathbf{w}_{\gamma\omega} . \tilde{\mathbf{v}}_\gamma) \, dA =$$
$$- \varepsilon_\gamma \nabla \langle p_\gamma \rangle^\gamma + \rho_\alpha \varepsilon_\gamma \mathbf{g} + \mu_\alpha \varepsilon_\gamma \nabla^2 \langle \mathbf{v}_\gamma \rangle^\gamma + \sum_{i=\omega,\kappa} \frac{1}{\mathcal{V}_{\text{II}}} \int_{A_{\gamma i}} \mathbf{n}_{\gamma i} . (-\tilde{p}_\gamma + \mu_\alpha \nabla \tilde{\mathbf{v}}_\gamma) \, dA \quad (8.35)$$

The second term on the left hand side, represents the consolidation of the tissue, and it can be discarded when the first term on the left hand side is developed. Nevertheless, it will not be done here because the superficial form of the average equation is sought.

The same development can be drawn for momentum transport in the ω-region, and the unclosed average equation takes the form

$$\rho_\alpha \varepsilon_\alpha^{-1} \varepsilon_\beta^{-1} \frac{\partial(\varepsilon_\omega \langle \mathbf{v}_\omega \rangle^\omega)}{\partial t} - \rho_\alpha \varepsilon_\alpha^{-1} \varepsilon_\beta^{-1} \frac{\partial \varepsilon_\omega}{\partial t} \langle \mathbf{v}_\omega \rangle^\omega - \rho_\alpha \varepsilon_\alpha^{-1} \varepsilon_\beta^{-1} \frac{1}{\mathcal{V}_{\text{II}}} \int_{A_{\omega\gamma}} \mathbf{n}_{\omega\gamma} . (\mathbf{w}_{\omega\gamma} . \tilde{\mathbf{v}}_\omega) \, dA =$$
$$- \varepsilon_\omega \nabla \langle p_\omega \rangle^\omega - \frac{\mu_\alpha}{\mathbf{K}_\omega^{\text{II}}} \varepsilon_\omega \langle \mathbf{v}_\omega \rangle^\omega + \rho_\alpha \varepsilon_\omega \mathbf{g} + \mu_\alpha \varepsilon_\alpha^{-1} \varepsilon_\beta^{-1} \varepsilon_\omega \nabla^2 \langle \mathbf{v}_\omega \rangle^\omega$$
$$+ \sum_{i=\gamma,\kappa} \frac{1}{\mathcal{V}_{\text{II}}} \int_{A_{\omega i}} \mathbf{n}_{\omega i} . \left(-\tilde{p}_\omega + \mu_\alpha \varepsilon_\alpha^{-1} \varepsilon_\beta^{-1} \nabla \tilde{\mathbf{v}}_\omega\right) dA \quad (8.36)$$

At this point we have two average equations for momentum transport at the bioreactor scale (level I). If the transport properties concerning the flow in the two regions are close enough, it would be possible to hypothesis mechanical equilibrium [Quintard & Whitaker, 1998a] the same way mass equilibrium has been supposed for mass transport at the cellular scale (Sec. 7.3.1). However in our case the transport equations in the two regions are different (Stokes in the γ-region, Darcy-Brinkman in the ω-region), and the fluid velocity is much higher in the culture medium region than in the tissue. Thus it is not possible to assume mechanical equilibrium here, and the two averaged equations for momentum transport have to be kept.

Eqs. (8.35) and (8.36) still include local terms due to the presence of the velocity and pressure deviations. The next step is to build a problem for the four deviations $\tilde{\mathbf{v}}_\gamma$, $\tilde{p}_\gamma$, $\tilde{\mathbf{v}}_\omega$ and $\tilde{p}_\omega$, and this is done by subtracting the unclosed averaged equations Eqs. (8.35) and (8.36) to the local equations Eqs. (8.8) and (8.9). Starting with the γ-phase we obtain

$$\rho_\alpha \frac{\partial \tilde{\mathbf{v}}_\gamma}{\partial t} + \rho_\alpha \frac{1}{V_\gamma} \int_{A_{\gamma\omega}} \mathbf{n}_{\gamma\omega} . (\mathbf{w}_{\gamma\omega} . \tilde{\mathbf{v}}_\gamma) \, dA = -\nabla \tilde{p}_\gamma + \mu_\alpha \nabla^2 \tilde{\mathbf{v}}_\gamma$$
$$- \sum_{i=\omega,\kappa} \frac{1}{V_\gamma} \int_{A_{\gamma i}} \mathbf{n}_{\gamma i} . (-\tilde{p}_\gamma + \mu_\alpha \nabla \tilde{\mathbf{v}}_\gamma) \, dA \quad \text{in the } \gamma\text{-phase} \quad (8.37)$$

The order of magnitude of the two terms on the left hand side are compared with the viscous diffusion term

$$\rho_\alpha \frac{\partial \tilde{\mathbf{v}}_\gamma}{\partial t} = O\left(\rho_\alpha \frac{\langle \mathbf{v}_\gamma \rangle^\gamma}{t_v}\right) \quad (8.38)$$

$$\rho_\alpha \frac{1}{V_\gamma}\int_{A_{\gamma\omega}} \mathbf{n}_{\gamma\omega}.\mathbf{w}_{\gamma\omega}.\tilde{\mathbf{v}}_\gamma dA = O\left(\rho_\alpha \frac{1}{l_\gamma}\frac{l_\gamma}{t_\mathbf{w}}\langle \mathbf{v}_\gamma\rangle^\gamma\right) \tag{8.39}$$

$$\mu_\alpha \nabla^2 \tilde{\mathbf{v}}_\gamma = O\left(\frac{\mu_\alpha \langle \mathbf{v}_\gamma\rangle^\gamma}{l_\gamma^2}\right) \tag{8.40}$$

One sees that if the time scale associated with the velocity of the tissue interface (t_ω), is much larger than the time scale associated with the deviation of the velocity in the γ-phase ($t_\mathbf{w} \gg t_v$), the second term of the left hand side of Eq. (8.37) can be discarded. Moreover the closure problem can be supposed stationary when the length scale constraint $(\rho_\alpha l_\gamma^2)/(\mu_\alpha t_v) \ll 1$ is satisfied. These two hypothesis have been made in the previous developments of Chaps. 6 and 7, and when they are also respected for the γ region, the *deviation problem for momentum transport at the tissue scale* takes the form

$$\rho_\alpha \nabla.\tilde{\mathbf{v}}_\gamma = -\varepsilon_\gamma^{-1}\dot{m}_\gamma \quad \text{in the } \gamma\text{-phase} \tag{8.41}$$

$$0 = -\nabla\tilde{p}_\gamma + \mu_\alpha\nabla^2\tilde{\mathbf{v}}_\gamma - \sum_{i=\omega,\kappa}\frac{1}{V_\gamma}\int_{A_{\gamma i}} \mathbf{n}_{\gamma i}.\left(-\tilde{p}_\gamma + \mu_\alpha\nabla\tilde{\mathbf{v}}_\gamma\right)dA \quad \text{in the } \gamma\text{-phase} \tag{8.42}$$

$$\rho_\alpha \nabla.\tilde{\mathbf{v}}_\omega = -\varepsilon_\omega^{-1}\dot{m}_\omega \quad \text{in the } \omega\text{-region} \tag{8.43}$$

$$0 = -\nabla\tilde{p}_\omega + \mu_\alpha\varepsilon_\alpha^{-1}\varepsilon_\beta^{-1}\nabla^2\tilde{\mathbf{v}}_\omega - \frac{\mu_\alpha}{\mathbf{K}_\omega^{\mathrm{II}}}\tilde{\mathbf{v}}_\omega - \sum_{i=\gamma,\kappa}\frac{1}{V_\omega}\int_{A_{\omega i}} \mathbf{n}_{\omega i}.\left(-\tilde{p}_\omega + \mu_\alpha\varepsilon_\alpha^{-1}\varepsilon_\beta^{-1}\nabla\tilde{\mathbf{v}}_\omega\right)dA$$
$$\text{in the } \omega\text{-region} \tag{8.44}$$

$$\tilde{\mathbf{v}}_\gamma = -\langle \mathbf{v}_\gamma\rangle^\gamma \quad \text{at } A_{\gamma\kappa} \tag{8.45}$$

$$\tilde{\mathbf{v}}_\omega = -\langle \mathbf{v}_\omega\rangle^\omega \quad \text{at } A_{\omega\kappa} \tag{8.46}$$

$$\tilde{\mathbf{v}}_\gamma = \tilde{\mathbf{v}}_\omega - \left(\langle \mathbf{v}_\gamma\rangle^\gamma - \langle \mathbf{v}_\omega\rangle^\omega\right) \quad \text{at } A_{\gamma\omega} \tag{8.47}$$

$$\mathbf{n}_{\gamma\omega}.\left[-\tilde{p}_\gamma + \mu_\gamma(\nabla\tilde{\mathbf{v}}_\gamma + \nabla\tilde{\mathbf{v}}_\gamma^T)\right] = \mathbf{n}_{\gamma\omega}.\left[-\tilde{p}_\omega + \mu_\alpha\varepsilon_\alpha^{-1}\varepsilon_\beta^{-1}(\nabla\tilde{\mathbf{v}}_\omega + \nabla\tilde{\mathbf{v}}_\omega^T)\right]$$
$$+ \mathbf{n}_{\gamma\omega}.\left(\langle p_\gamma\rangle^\gamma - \langle p_\omega\rangle^\omega\right) \quad \text{at } A_{\gamma\omega} \tag{8.48}$$

The mass conservation Eqs. (8.41) and (8.43) have been derived by subtracting Eqs. (8.23) and (8.24) to Eqs. (8.8) and (8.11), then supposing that the production rate of tissue is much slower than the variation of the velocity deviations, and under the same time and length scale constraints than for the development of the transport equations, the above relations are obtained. Finally, for the development of boundary condition Eq. (8.48), the length scale separation $(l_\gamma, l_\omega) \ll L$ has been used to neglect the gradient of the velocity deviations in regards to the gradient of the velocity averages.

The deviation problem defined by Eqs. (8.41) to (8.48) involves source terms in $\langle \mathbf{v}_\gamma\rangle^\gamma$ (Eqs. (8.45) and (8.47)) , $\langle \mathbf{v}_\omega\rangle^\omega$ (Eqs. (8.46) and (8.47)) and $\langle p_\gamma\rangle^\gamma - \langle p_\omega\rangle^\omega$ (Eq. (8.48)). This motivates the following relations between the deviations and the averages

$$\tilde{\mathbf{v}}_\gamma = \mathbf{B}_{\gamma\gamma}.\langle \mathbf{v}_\gamma\rangle^\gamma + \mathbf{B}_{\gamma\omega}.\langle \mathbf{v}_\omega\rangle^\omega + \mu_\alpha^{-1}\mathbf{B}_\gamma\left(\langle p_\gamma\rangle^\gamma - \langle p_\omega\rangle^\omega\right) \tag{8.49}$$

$$\tilde{\mathbf{v}}_\omega = \mathbf{B}_{\omega\gamma}.\langle\mathbf{v}_\gamma\rangle^\gamma + \mathbf{B}_{\omega\omega}.\langle\mathbf{v}_\omega\rangle^\omega + \mu_\alpha^{-1}\varepsilon_\alpha\varepsilon_\beta\mathbf{B}_\omega\left(\langle p_\gamma\rangle^\gamma - \langle p_\omega\rangle^\omega\right) \tag{8.50}$$

$$\mu_\alpha^{-1}\tilde{p}_\gamma = \mathbf{b}_{\gamma\gamma}.\langle\mathbf{v}_\gamma\rangle^\gamma + \mathbf{b}_{\gamma\omega}.\langle\mathbf{v}_\omega\rangle^\omega + \mu_\alpha^{-1}b_\gamma\left(\langle p_\gamma\rangle^\gamma - \langle p_\omega\rangle^\omega\right) \tag{8.51}$$

$$\mu_\alpha^{-1}\varepsilon_\alpha\varepsilon_\beta\tilde{p}_\omega = \mathbf{b}_{\omega\gamma}.\langle\mathbf{v}_\gamma\rangle^\gamma + \mathbf{b}_{\omega\omega}.\langle\mathbf{v}_\omega\rangle^\omega + \mu_\alpha^{-1}\varepsilon_\alpha\varepsilon_\beta b_\omega\left(\langle p_\gamma\rangle^\gamma - \langle p_\omega\rangle^\omega\right) \tag{8.52}$$

where the closure variables $\mathbf{B}_{ij}$ are 2nd order tensors, $\mathbf{B}_i$ and $\mathbf{b}_{ij}$ are 1st order tensors, and b_i $(i,j = \gamma,\omega)$ are scalar variables. These can be seen as mapping tensors in which the first subscript recalls the region in which they are defined, and the second subscript, when it exists, indicates which velocity is being mapped onto the spatial deviation. When substituting Eqs. (8.49) to (8.52) into the unclosed macroscopic equations, it is possible to define six bioreactor effective permeabilities

$$\varepsilon_\gamma\mathbf{K}_\gamma^{\mathrm{I}-1} = -\frac{1}{V_\gamma}\int_{A_{\gamma\omega}}\mathbf{n}_{\gamma\omega}.\left(-\mathbf{I}\mathbf{b}_{\gamma\gamma} + \nabla\mathbf{B}_{\gamma\gamma}\right)dA - \frac{1}{V_\gamma}\int_{A_{\gamma\kappa}}\mathbf{n}_{\gamma\kappa}.\left(-\mathbf{I}\mathbf{b}_{\gamma\gamma} + \nabla\mathbf{B}_{\gamma\gamma}\right)dA \tag{8.53}$$

$$\varepsilon_\omega\mathbf{K}_{\gamma\omega}^{\mathrm{I}-1} = \frac{1}{V_\gamma}\int_{A_{\gamma\omega}}\mathbf{n}_{\gamma\omega}.\left(-\mathbf{I}\mathbf{b}_{\gamma\omega} + \nabla\mathbf{B}_{\gamma\omega}\right)dA + \frac{1}{V_\gamma}\int_{A_{\gamma\kappa}}\mathbf{n}_{\gamma\kappa}.\left(-\mathbf{I}\mathbf{b}_{\gamma\omega} + \nabla\mathbf{B}_{\gamma\omega}\right)dA \tag{8.54}$$

$$\mathbf{\Pi}_\gamma^{\mathrm{I}} = \frac{1}{V_\gamma}\int_{A_{\gamma\omega}}\mathbf{n}_{\gamma\omega}.\left(-\mathbf{I}b_\gamma + \nabla\mathbf{B}_\gamma\right)dA + \frac{1}{V_\gamma}\int_{A_{\gamma\kappa}}\mathbf{n}_{\gamma\kappa}.\left(-\mathbf{I}b_\gamma + \nabla\mathbf{B}_\gamma\right)dA \tag{8.55}$$

$$\begin{aligned}\varepsilon_\alpha\varepsilon_\beta\varepsilon_\omega\mathbf{K}_\omega^{\mathrm{I}-1} &= \varepsilon_\alpha\varepsilon_\beta\mathbf{K}_\omega^{\mathrm{II}-1} \\ &- \frac{1}{V_\omega}\int_{A_{\omega\gamma}}\mathbf{n}_{\omega\gamma}.\left(-\mathbf{I}\mathbf{b}_{\omega\omega} + \nabla\mathbf{B}_{\omega\omega}\right)dA - \frac{1}{V_\omega}\int_{A_{\omega\kappa}}\mathbf{n}_{\omega\kappa}.\left(-\mathbf{I}\mathbf{b}_{\omega\omega} + \nabla\mathbf{B}_{\omega\omega}\right)dA\end{aligned} \tag{8.56}$$

$$\varepsilon_\alpha\varepsilon_\beta\varepsilon_\gamma\mathbf{K}_{\omega\gamma}^{\mathrm{I}-1} = \frac{1}{V_\omega}\int_{A_{\omega\gamma}}\mathbf{n}_{\omega\gamma}.\left(-\mathbf{I}\mathbf{b}_{\omega\gamma} + \nabla\mathbf{B}_{\omega\gamma}\right)dA + \frac{1}{V_\omega}\int_{A_{\omega\kappa}}\mathbf{n}_{\omega\kappa}.\left(-\mathbf{I}\mathbf{b}_{\omega\gamma} + \nabla\mathbf{B}_{\omega\gamma}\right)dA \tag{8.57}$$

$$\mathbf{\Pi}_\omega^{\mathrm{I}} = \frac{1}{V_\omega}\int_{A_\omega}\mathbf{n}_{\omega\gamma}.\left(-\mathbf{I}b_\omega + \nabla\mathbf{B}_\omega\right)dA + \frac{1}{V_\omega}\int_{A_{\omega\kappa}}\mathbf{n}_{\omega\kappa}.\left(-\mathbf{I}b_\omega + \nabla\mathbf{B}_\omega\right)dA \tag{8.58}$$

and when at the bioreactor scale, the culture medium flow is considered to be much faster than the tissue growth process, the *closed averaged equations for momentum transport* in the bioreactor are finally expressed as

$$\begin{aligned}\rho_\alpha\varepsilon_\gamma^{-1}\frac{\partial(\varepsilon_\gamma\langle\mathbf{v}_\gamma\rangle^\gamma)}{\partial t} &= -\nabla\langle p_\gamma\rangle^\gamma + \rho_\alpha\mathbf{g} + \mu_\alpha\nabla^2\langle\mathbf{v}_\gamma\rangle^\gamma \\ &- \frac{\mu_\alpha}{\mathbf{K}_\gamma^{\mathrm{I}}}\varepsilon_\gamma\langle\mathbf{v}_\gamma\rangle^\gamma + \frac{\mu_\alpha}{\mathbf{K}_{\gamma\omega}^{\mathrm{I}}}\varepsilon_\omega\langle\mathbf{v}_\omega\rangle^\omega + \mathbf{\Pi}_\gamma^{\mathrm{I}}\left(\langle p_\gamma\rangle^\gamma - \langle p_\omega\rangle^\omega\right)\end{aligned} \tag{8.59}$$

$$\begin{aligned}\rho_\alpha\varepsilon_\alpha^{-1}\varepsilon_\beta^{-1}\varepsilon_\omega^{-1}\frac{\partial(\varepsilon_\omega\langle\mathbf{v}_\omega\rangle^\omega)}{\partial t} &= -\nabla\langle p_\omega\rangle^\omega + \rho_\alpha\mathbf{g} + \mu_\alpha\varepsilon_\alpha^{-1}\varepsilon_\beta^{-1}\nabla^2\langle\mathbf{v}_\omega\rangle^\omega \\ &- \frac{\mu_\alpha}{\mathbf{K}_\omega^{\mathrm{I}}}\varepsilon_\omega\langle\mathbf{v}_\omega\rangle^\omega + \frac{\mu_\alpha}{\mathbf{K}_{\omega\gamma}^{\mathrm{I}}}\varepsilon_\gamma\langle\mathbf{v}_\gamma\rangle^\gamma + \mathbf{\Pi}_\omega^{\mathrm{I}}\left(\langle p_\gamma\rangle^\gamma - \langle p_\omega\rangle^\omega\right)\end{aligned} \tag{8.60}$$

Note here that the permeabilities of the lower scales are present through $\mathbf{K}^{\mathrm{I}}_{\omega}$, and for convenience we will use the additional notation

$$\varepsilon_{\omega}\mathbf{K}^{\mathrm{I}\star-1}_{\omega} = -\frac{1}{V_{\omega}}\int_{A_{\omega\gamma}} \mathbf{n}_{\omega\gamma}.\left(-\mathbf{I}\mathbf{b}_{\omega\omega} + \nabla\mathbf{B}_{\omega\omega}\right) dA - \frac{1}{V_{\omega}}\int_{A_{\omega\kappa}} \mathbf{n}_{\omega\kappa}.\left(-\mathbf{I}\mathbf{b}_{\omega\omega} + \nabla\mathbf{B}_{\omega\omega}\right) dA \tag{8.61}$$

so that Eq. (8.56) can be written in a similar form to Eq. (7.46)

$$\varepsilon_{\alpha}\varepsilon_{\beta}\varepsilon_{\omega}\mathbf{K}^{\mathrm{I}-1}_{\omega} = \varepsilon_{\alpha}\varepsilon_{\beta}\mathbf{K}^{\mathrm{II}-1}_{\omega} + \varepsilon_{\omega}\mathbf{K}^{\mathrm{I}\star-1}_{\omega} \tag{8.62}$$

The definitions of $\mathbf{K}^{\mathrm{I}}_{\gamma}$ and $\mathbf{K}^{\mathrm{I}}_{\omega}$ are similar to the definitions of the permeability tensors at the lower scales, however there is now a coupling between the two phases through $\mathbf{K}^{\mathrm{I}}_{\gamma\omega}$, $\mathbf{K}^{\mathrm{I}}_{\omega\gamma}$, $\mathbf{\Pi}^{\mathrm{I}}_{\gamma}$ and $\mathbf{\Pi}^{\mathrm{I}}_{\omega}$. The definitions of these coupling tensors (Eqs. (8.54), (8.55), (8.57) and (8.58)) are slightly different from those usually met in the literature [Whitaker, 1986b; Lasseux et al., 1996; Soulaine et al., 2013] only because these authors seek the Darcy form of the momentum transport equation. Here we keep into account the non-stationarity of the macroscopic equations as well as the Brinkman correction. The tensors $\mathbf{\Pi}^{\mathrm{I}}_{\gamma}$ and $\mathbf{\Pi}^{\mathrm{I}}_{\omega}$ are related to the mass transfer between the γ-phase and the ω-region, due to the macroscopic pressure difference. Macroscopic models often neglect the coupling tensors over the main permeability tensors ($\mathbf{K}^{\mathrm{I}}_{ij}, \mathbf{\Pi}^{\mathrm{I}}_{i} \ll \mathbf{K}^{\mathrm{I}}_{i}$). As emphasized by Soulaine et al. [2013], this may be a reasonable assumption for configurations where the interface between the two regions is small, and parallel to the main flow. Yet, in the general case, the coupling tensors may play a critical role on momentum transport. Consequently they will be retained in the rest of this study.

The effective bioreactor permeabilities (Eqs. (8.53) to (8.58)) are defined by the closure variables (Eqs. (8.49) to (8.52)), and their respective closure problem remain to be built. Introducing the closure variables into the deviation problem (Eqs. (8.41) to (8.48)) results in the definition of three *closure problems*, one for each source term of the deviation problem

Problem I (in $\langle\mathbf{v}_{\gamma}\rangle^{\gamma}$) :

$$\nabla.\mathbf{B}_{\gamma\gamma} = \varepsilon_{\gamma}^{-1}\chi_{\gamma\gamma} \quad \text{in the } \gamma\text{-phase} \tag{8.63}$$

$$0 = -\nabla\mathbf{b}_{\gamma\gamma} + \nabla^2\mathbf{B}_{\gamma\gamma} + \varepsilon_{\gamma}\mathbf{K}^{\mathrm{I}-1}_{\gamma} \quad \text{in the } \gamma\text{-phase} \tag{8.64}$$

$$\nabla.\mathbf{B}_{\omega\gamma} = \varepsilon_{\omega}^{-1}\chi_{\omega\gamma} \quad \text{in the } \omega\text{-region} \tag{8.65}$$

$$0 = -\nabla\mathbf{b}_{\omega\gamma} + \nabla^2\mathbf{B}_{\omega\gamma} - \varepsilon_{\alpha}\varepsilon_{\beta}\mathbf{K}^{\mathrm{II}-1}_{\omega}\mathbf{B}_{\omega\gamma} - \varepsilon_{\alpha}\varepsilon_{\beta}\varepsilon_{\gamma}\mathbf{K}^{\mathrm{I}-1}_{\omega\gamma} \quad \text{in the } \omega\text{-region} \tag{8.66}$$

$$\mathbf{B}_{\gamma\gamma} = \mathbf{B}_{\omega\gamma} - \mathbf{I} \quad \text{at } A_{\gamma\omega} \tag{8.67}$$

$$\mu_{\alpha}\mathbf{n}_{\gamma\omega}.\left[-\mathbf{b}_{\gamma\gamma} + \left(\nabla\mathbf{B}_{\gamma\gamma} + \nabla\mathbf{B}^{T}_{\gamma\gamma}\right)\right] = \mu_{\alpha}\varepsilon_{\alpha}^{-1}\varepsilon_{\beta}^{-1}\mathbf{n}_{\gamma\omega}.\left[-\mathbf{b}_{\omega\gamma} + \left(\nabla\mathbf{B}_{\omega\gamma} + \nabla\mathbf{B}^{T}_{\omega\gamma}\right)\right] \quad \text{at } A_{\gamma\omega} \tag{8.68}$$

$$\mathbf{B}_{\gamma\gamma} = -\mathbf{I} \quad \text{at } A_{\gamma\kappa} \tag{8.69}$$

$$\mathbf{B}_{\omega\gamma} = 0 \quad \text{at } A_{\omega\kappa} \tag{8.70}$$

$$\mathbf{B}_{\gamma\gamma}(\mathbf{x} + l_i) = \mathbf{B}_{\gamma\gamma}(\mathbf{x}) \qquad \mathbf{B}_{\omega\gamma}(\mathbf{x} + l_i) = \mathbf{B}_{\omega\gamma}(\mathbf{x}) \qquad i = 1, 2, 3 \tag{8.71}$$

$$\mathbf{b}_{\gamma\gamma}(\mathbf{x} + l_i) = \mathbf{b}_{\gamma\gamma}(\mathbf{x}) \qquad \mathbf{b}_{\omega\gamma}(\mathbf{x} + l_i) = \mathbf{b}_{\omega\gamma}(\mathbf{x}) \qquad i = 1, 2, 3 \tag{8.72}$$

$$\langle\mathbf{B}_{\gamma\gamma}\rangle^{\gamma} = 0 \qquad \langle\mathbf{B}_{\omega\gamma}\rangle^{\omega} = 0 \tag{8.73}$$

Problem II (in $\langle \mathbf{v}_\omega \rangle^\omega$) :

$$\nabla.\mathbf{B}_{\gamma\omega} = \varepsilon_\gamma^{-1}\chi_{\gamma\omega} \quad \text{in the } \gamma\text{-phase} \tag{8.74}$$

$$0 = -\nabla \mathbf{b}_{\gamma\omega} + \nabla^2\mathbf{B}_{\gamma\omega} - \varepsilon_\omega \mathbf{K}_{\gamma\omega}^{\mathrm{I}-1} \quad \text{in the } \gamma\text{-phase} \tag{8.75}$$

$$\nabla.\mathbf{B}_{\omega\omega} = \varepsilon_\omega^{-1}\chi_{\omega\omega} \quad \text{in the } \omega\text{-region} \tag{8.76}$$

$$0 = -\nabla \mathbf{b}_{\omega\omega} + \nabla^2\mathbf{B}_{\omega\omega} - \varepsilon_\alpha\varepsilon_\beta \mathbf{K}_\omega^{\mathrm{II}-1}\mathbf{B}_{\omega\omega} + \varepsilon_\omega \mathbf{K}_\omega^{\mathrm{I}\star-1} \quad \text{in the } \omega\text{-region} \tag{8.77}$$

$$\mathbf{B}_{\gamma\omega} = \mathbf{B}_{\omega\omega} + \mathbf{I} \quad \text{at } A_{\gamma\omega} \tag{8.78}$$

$$\mu_\alpha \mathbf{n}_{\gamma\omega}.\left[-\mathbf{b}_{\gamma\omega} + (\nabla\mathbf{B}_{\gamma\omega} + \nabla\mathbf{B}_{\gamma\omega}^T)\right] = \mu_\alpha\varepsilon_\alpha^{-1}\varepsilon_\beta^{-1}\mathbf{n}_{\gamma\omega}.\left[-\mathbf{b}_{\omega\omega} + (\nabla\mathbf{B}_{\omega\omega} + \nabla\mathbf{B}_{\omega\omega}^T)\right] \quad \text{at } A_{\gamma\omega} \tag{8.79}$$

$$\mathbf{B}_{\gamma\omega} = 0 \quad \text{at } A_{\gamma\kappa} \tag{8.80}$$

$$\mathbf{B}_{\omega\omega} = -\mathbf{I} \quad \text{at } A_{\omega\kappa} \tag{8.81}$$

$$\mathbf{B}_{\gamma\omega}(\mathbf{x} + l_i) = \mathbf{B}_{\gamma\omega}(\mathbf{x}) \qquad \mathbf{B}_{\omega\omega}(\mathbf{x} + l_i) = \mathbf{B}_{\omega\omega}(\mathbf{x}) \qquad i = 1, 2, 3 \tag{8.82}$$

$$\mathbf{b}_{\gamma\omega}(\mathbf{x} + l_i) = \mathbf{b}_{\gamma\omega}(\mathbf{x}) \qquad \mathbf{b}_{\omega\omega}(\mathbf{x} + l_i) = \mathbf{b}_{\omega\omega}(\mathbf{x}) \qquad i = 1, 2, 3 \tag{8.83}$$

$$\langle \mathbf{B}_{\gamma\omega} \rangle^\gamma = 0 \qquad \langle \mathbf{B}_{\omega\omega} \rangle^\omega = 0 \tag{8.84}$$

Problem III (in $\langle p_\gamma \rangle^\gamma - \langle p_\omega \rangle^\omega$) :

$$\nabla.\mathbf{B}_\gamma = \varepsilon_\gamma^{-1} h_\gamma \quad \text{in the } \gamma\text{-phase} \tag{8.85}$$

$$0 = -\nabla b_\gamma + \nabla^2\mathbf{B}_\gamma - \mathbf{\Pi}_\gamma^{\mathrm{I}} \quad \text{in the } \gamma\text{-phase} \tag{8.86}$$

$$\nabla.\mathbf{B}_\omega = \varepsilon_\omega^{-1} h_\omega \quad \text{in the } \omega\text{-region} \tag{8.87}$$

$$0 = -\nabla b_\omega + \nabla^2\mathbf{B}_\omega - \varepsilon_\alpha\varepsilon_\beta \mathbf{K}_\omega^{\mathrm{II}-1}\mathbf{B}_\omega - \mathbf{\Pi}_\omega^{\mathrm{I}} \quad \text{in the } \omega\text{-region} \tag{8.88}$$

$$\mathbf{B}_\gamma = \mathbf{B}_\omega \quad \text{at } A_{\gamma\omega} \tag{8.89}$$

$$\mathbf{n}_{\gamma\omega}.\left[-\mathbf{I}b_\gamma + (\nabla\mathbf{B}_\gamma + \nabla\mathbf{B}_\gamma^T)\right] = \mathbf{n}_{\gamma\omega}.\left[-\mathbf{I}b_\omega + (\nabla\mathbf{B}_\omega + \nabla\mathbf{B}_\omega^T)\right] - \mathbf{n}_{\gamma\omega}.\mathbf{I} \quad \text{at } A_{\gamma\omega} \tag{8.90}$$

$$\mathbf{B}_\gamma = 0 \quad \text{at } A_{\gamma\kappa} \tag{8.91}$$

$$\mathbf{B}_\omega = 0 \quad \text{at } A_{\omega\kappa} \tag{8.92}$$

$$\mathbf{B}_\gamma(\mathbf{x} + l_i) = \mathbf{B}_\gamma(\mathbf{x}) \qquad \mathbf{B}_\omega(\mathbf{x} + l_i) = \mathbf{B}_\omega(\mathbf{x}) \qquad i = 1, 2, 3 \tag{8.93}$$

$$b_\gamma(\mathbf{x} + l_i) = b_\gamma(\mathbf{x}) \qquad b_\omega(\mathbf{x} + l_i) = b_\omega(\mathbf{x}) \qquad i = 1, 2, 3 \tag{8.94}$$

$$\langle \mathbf{B}_\gamma \rangle^\gamma = 0 \qquad \langle \mathbf{B}_\omega \rangle^\omega = 0 \tag{8.95}$$

Here the following notations have been used in the continuity equations [Soulaine et al., 2013]

$$\chi_{\gamma\gamma} = \sum_{i=\omega,\kappa} \frac{1}{\mathcal{V}_{\mathrm{II}}} \int_{A_{\gamma i}} \mathbf{n}_{\gamma i}.\mathbf{B}_{\gamma\gamma} dA \qquad \chi_{\omega\gamma} = \sum_{i=\gamma,\kappa} \frac{1}{\mathcal{V}_{\mathrm{II}}} \int_{A_{\omega i}} \mathbf{n}_{\omega i}.\mathbf{B}_{\omega\gamma} dA \tag{8.96}$$

$$\chi_{\omega\gamma} = \sum_{i=\omega,\kappa} \frac{1}{\mathcal{V}_{\mathrm{II}}} \int_{A_{\gamma i}} \mathbf{n}_{\gamma i}.\mathbf{B}_{\omega\gamma} dA \qquad \chi_{\omega\omega} = \sum_{i=\gamma,\kappa} \frac{1}{\mathcal{V}_{\mathrm{II}}} \int_{A_{\omega i}} \mathbf{n}_{\omega i}.\mathbf{B}_{\omega\omega} dA \tag{8.97}$$

and

$$h_\gamma = \sum_{i=\omega,\kappa} \frac{1}{\mathcal{V}_{\text{II}}} \int_{A_{\gamma i}} \mathbf{n}_{\gamma i}.\mathbf{B}_\gamma dA \qquad h_\omega = \sum_{i=\gamma,\kappa} \frac{1}{\mathcal{V}_{\text{II}}} \int_{A_{\omega i}} \mathbf{n}_{\omega i}.\mathbf{B}_\omega dA \tag{8.98}$$

Due to the quasi-stationary nature of the closure problem, the velocities of the interfaces have been neglected in the continuity equations. Moreover, making use of the boundary conditions, and of the averaging theorem, one can show that

$$\chi_{\gamma\gamma} = -\chi_{\omega\gamma} \qquad \chi_{\omega\omega} = -\chi_{\gamma\omega} \tag{8.99}$$

and

$$h_\gamma = -h_\omega \tag{8.100}$$

The h_i may be seen as mass exchange coefficient, while the χ_{ij} have the dimension of a velocity. Note that in the above closure problems, additional constraints on the $\mathbf{b}_{ij}$ and b_i are required to guarantee the uniqueness of the solutions. Thus we choose to impose

$$\langle \mathbf{b}_{\gamma\gamma} \rangle^\gamma = 0 \qquad \langle \mathbf{b}_{\omega\gamma} \rangle^\omega = 0 \tag{8.101}$$
$$\langle \mathbf{b}_{\gamma\omega} \rangle^\gamma = 0 \qquad \langle \mathbf{b}_{\omega\omega} \rangle^\omega = 0 \tag{8.102}$$
$$\langle b_\gamma \rangle^\gamma = 0 \qquad \langle b_\omega \rangle^\omega = 0 \tag{8.103}$$

Solving this three closure problems, allows to evaluate the six macroscopic parameters influencing momentum transport at the bioreactor scale. Yet, in the current state, these closure problems are challenging to solve numerically. In the next section, some simplifications concerning the mass exchange rate will be done, allowing, after some manipulations, to write the closure problems in simpler forms.

8.2.2 Computation of the effective parameters

The three closure problems above are integro-differential problems, and their resolution in the current state is highly discouraging. Fortunately, with the help of adequate variable changes, some algebra, and a little bit of patience, it is possible to transform this problems into Stokes and Brinkman flow problems.

Simplification of the closure problems

First, let us write the mass exchange rates in their closed form. Substituting Eqs. (8.49) and (8.50) into Eqs. (8.30) and (8.31) yields to

$$\frac{\dot{m}_\gamma}{\rho_\alpha} = -\chi_{\gamma\gamma}\langle \mathbf{v}_\gamma \rangle^\gamma - \chi_{\gamma\omega}\langle \mathbf{v}_\omega \rangle^\omega - \frac{h_\gamma}{\mu_\alpha}\left(\langle p_\gamma \rangle^\gamma - \langle p_\omega \rangle^\omega\right) + \frac{1}{\mathcal{V}_{\text{II}}} \int_{A_{\gamma\omega}} \mathbf{n}_{\gamma\omega}.\mathbf{w}_{\gamma\omega} dA \tag{8.104}$$

$$\frac{\dot{m}_\omega}{\rho_\alpha} = -\chi_{\omega\gamma}\langle \mathbf{v}_\gamma \rangle^\gamma - \chi_{\omega\omega}\langle \mathbf{v}_\omega \rangle^\omega - \frac{h_\omega}{\mu_\alpha \varepsilon_\alpha^{-1} \varepsilon_\beta^{-1}}\left(\langle p_\gamma \rangle^\gamma - \langle p_\omega \rangle^\omega\right) + \frac{1}{\mathcal{V}_{\text{II}}} \int_{A_{\omega\gamma}} \mathbf{n}_{\omega\gamma}.\mathbf{w}_{\gamma\omega} \rho_\alpha^{-1} \rho_\omega dA \tag{8.105}$$

These equations can be simplified by comparing the relative contribution of the different terms to the mass exchange rates. To start with, considering the small values of the interface velocity $\mathbf{w}_{\gamma\omega}$, in regard to the other quantities, it is easy to neglect the influence of the last term on the mass exchange rate. Furthermore, the macroscopic velocities in the bioreactor, like in most fluid flow in porous media, are driven by the gradient of the macroscopic pressure. This means that the two first terms on the right hand side, are of the second order in regard to the macroscopic pressures. Thus, following Soulaine et al. [2013], we assume that the mass exchange rate between the γ and ω regions, is dominated by the macroscopic pressure difference. This allows to neglect the χ_{ij} over the h_i, and Eqs. (8.104) and (8.105) can be approximated as

$$\frac{\dot{m}_\gamma}{\rho_\alpha} = -\frac{h_\gamma}{\mu_\alpha}\left(\langle p_\gamma\rangle^\gamma - \langle p_\omega\rangle^\omega\right) \tag{8.106}$$

$$\frac{\dot{m}_\omega}{\rho_\alpha} = -\frac{h_\omega}{\mu_\alpha \varepsilon_\alpha^{-1}\varepsilon_\beta^{-1}}\left(\langle p_\gamma\rangle^\gamma - \langle p_\omega\rangle^\omega\right) \tag{8.107}$$

Introducing this forms of the mass exchange rates into the conservation equations (Eqs. (8.23) and (8.24)), their closed forms read

$$\frac{\partial}{\partial t}\left(\varepsilon_\gamma\rho_\alpha\right) + \nabla.\left(\rho_\alpha\varepsilon_\gamma\langle\mathbf{v}_\gamma\rangle^\gamma\right) = -\rho_\alpha\frac{h_\gamma}{\mu_\alpha}\left(\langle p_\gamma\rangle^\gamma - \langle p_\omega\rangle^\omega\right) \tag{8.108}$$

$$\frac{\partial}{\partial t}\left(\varepsilon_\omega\langle\rho_\omega\rangle^\omega\right) + \nabla.\left(\rho_\alpha\varepsilon_\omega\langle\mathbf{v}_\omega\rangle^\omega\right) = -\rho_\alpha\frac{h_\omega}{\mu_\alpha\varepsilon_\alpha^{-1}\varepsilon_\beta^{-1}}\left(\langle p_\gamma\rangle^\gamma - \langle p_\omega\rangle^\omega\right) + \varepsilon_\omega\langle Q_\omega\rangle^\omega \tag{8.109}$$

When the interfacial mass transfer is significant at the bioreactor scale, h_γ and h_ω have to be evaluated through the closure problem III.

Returning to problems I and II, we first note that, the simplification leading to Eq. (8.106) implies that the χ_{ij} are also neglected in the closure problems, such that the $\mathbf{B}_{ij}$ recover solenoidal properties. Then, the following variable change is proposed [Whitaker, 1994; Lasseux et al., 1996]

$$\mathbf{B}_{\gamma\gamma} = -\mathbf{I} - \varepsilon_\gamma\left(\mathbf{B}^0_{\gamma\gamma}\mathbf{K}^{\mathrm{I}-1}_\gamma - \mathbf{B}^0_{\gamma\omega}\mathbf{K}^{\mathrm{I}-1}_{\omega\gamma}\right) \tag{8.110}$$

$$\mathbf{B}_{\omega\gamma} = -\varepsilon_\alpha\varepsilon_\beta\varepsilon_\gamma\left(\mathbf{B}^0_{\omega\gamma}\mathbf{K}^{\mathrm{I}-1}_\gamma - \mathbf{B}^0_{\omega\omega}\mathbf{K}^{\mathrm{I}-1}_{\omega\gamma}\right) \tag{8.111}$$

$$\mathbf{b}_{\gamma\gamma} = -\varepsilon_\gamma\left(\mathbf{b}^0_{\gamma\gamma}\mathbf{K}^{\mathrm{I}-1}_\gamma - \mathbf{b}^0_{\gamma\omega}\mathbf{K}^{\mathrm{I}-1}_{\omega\gamma}\right) \tag{8.112}$$

$$\mathbf{b}_{\omega\gamma} = -\varepsilon_\alpha\varepsilon_\beta\varepsilon_\gamma\left(\mathbf{b}^0_{\omega\gamma}\mathbf{K}^{\mathrm{I}-1}_\gamma - \mathbf{b}^0_{\omega\omega}\mathbf{K}^{\mathrm{I}-1}_{\omega\gamma}\right) \tag{8.113}$$

$$\mathbf{B}_{\gamma\omega} = -\varepsilon_\omega\left(\mathbf{B}^0_{\gamma\omega}\mathbf{K}^{\mathrm{I}-1}_\omega - \mathbf{B}^0_{\gamma\gamma}\mathbf{K}^{\mathrm{I}-1}_{\gamma\omega}\right) \tag{8.114}$$

$$\mathbf{B}_{\omega\omega} = -\mathbf{I} - \varepsilon_\alpha\varepsilon_\beta\varepsilon_\omega\left(\mathbf{B}^0_{\omega\omega}\mathbf{K}^{\mathrm{I}-1}_\omega - \mathbf{B}^0_{\omega\gamma}\mathbf{K}^{\mathrm{I}-1}_{\gamma\omega}\right) \tag{8.115}$$

$$\mathbf{b}_{\gamma\omega} = -\varepsilon_\omega\left(\mathbf{b}^0_{\gamma\omega}\mathbf{K}^{\mathrm{I}-1}_\omega - \mathbf{b}^0_{\gamma\gamma}\mathbf{K}^{\mathrm{I}-1}_{\gamma\omega}\right) \tag{8.116}$$

$$\mathbf{b}_{\omega\omega} = -\varepsilon_\alpha\varepsilon_\beta\varepsilon_\omega\left(\mathbf{b}^0_{\omega\omega}\mathbf{K}^{\mathrm{I}-1}_\omega - \mathbf{b}^0_{\omega\gamma}\mathbf{K}^{\mathrm{I}-1}_{\gamma\omega}\right) \tag{8.117}$$

The introduction of these transformations into problems I and II leads to simpler closure problems of the form

Problem I' :

$$0 = -\nabla \mathbf{b}^0_{\gamma\gamma} + \nabla^2 \mathbf{B}^0_{\gamma\gamma} - \mathbf{I} \quad \text{in the } \gamma\text{-phase} \tag{8.118}$$

$$\nabla . \mathbf{B}^0_{\gamma\gamma} = 0 \quad \text{in the } \gamma\text{-phase} \tag{8.119}$$

$$0 = -\nabla \mathbf{b}^0_{\omega\gamma} + \nabla^2 \mathbf{B}^0_{\omega\gamma} - \varepsilon_\alpha \varepsilon_\beta \mathbf{K}^{\mathrm{II}-1}_\omega \mathbf{B}^0_{\omega\gamma} \quad \text{in the } \omega\text{-region} \tag{8.120}$$

$$\nabla . \mathbf{B}^0_{\omega\gamma} = 0 \quad \text{in the } \omega\text{-region} \tag{8.121}$$

$$\mathbf{B}^0_{\gamma\gamma} = \mathbf{B}^0_{\omega\gamma} \quad \text{at } A_{\gamma\omega} \tag{8.122}$$

$$\mathbf{n}_{\gamma\omega} . \left[-\mathbf{b}^0_{\gamma\gamma} + (\nabla \mathbf{B}^0_{\gamma\gamma} + \nabla \mathbf{B}^{0\ T}_{\gamma\gamma}) \right] = \mathbf{n}_{\gamma\omega} . \left[-\mathbf{b}^0_{\omega\gamma} + (\nabla \mathbf{B}^0_{\omega\gamma} + \nabla \mathbf{B}^{0\ T}_{\omega\gamma}) \right] \quad \text{at } A_{\gamma\omega} \tag{8.123}$$

$$\mathbf{B}^0_{\gamma\gamma} = 0 \quad \text{at } A_{\gamma\kappa} \tag{8.124}$$

$$\mathbf{B}^0_{\omega\gamma} = 0 \quad \text{at } A_{\omega\kappa} \tag{8.125}$$

$$\mathbf{B}^0_{\gamma\gamma}(\mathbf{x} + l_i) = \mathbf{B}^0_{\gamma\gamma}(\mathbf{x}) \qquad \mathbf{B}^0_{\omega\gamma}(\mathbf{x} + l_i) = \mathbf{B}^0_{\omega\gamma}(\mathbf{x}) \qquad i = 1, 2, 3 \tag{8.126}$$

$$\mathbf{b}^0_{\gamma\gamma}(\mathbf{x} + l_i) = \mathbf{b}^0_{\gamma\gamma}(\mathbf{x}) \qquad \mathbf{b}^0_{\omega\gamma}(\mathbf{x} + l_i) = \mathbf{b}^0_{\omega\gamma}(\mathbf{x}) \qquad i = 1, 2, 3 \tag{8.127}$$

$$\langle \mathbf{B}^0_{\gamma\gamma} \rangle^\gamma = -\varepsilon_\gamma^{-1} \mathbf{K}^*_{\gamma\gamma} \qquad \langle \mathbf{B}^0_{\omega\gamma} \rangle^\omega = -\varepsilon_\alpha^{-1} \varepsilon_\beta^{-1} \varepsilon_\omega^{-1} \mathbf{K}^*_{\omega\gamma} \tag{8.128}$$

Problem II' :

$$0 = -\nabla \mathbf{b}^0_{\gamma\omega} + \nabla^2 \mathbf{B}^0_{\gamma\omega} \quad \text{in the } \gamma\text{-phase} \tag{8.129}$$

$$\nabla . \mathbf{B}^0_{\gamma\omega} = 0 \quad \text{in the } \gamma\text{-phase} \tag{8.130}$$

$$0 = -\nabla \mathbf{b}^0_{\omega\omega} + \nabla^2 \mathbf{B}^0_{\omega\omega} - \varepsilon_\alpha \varepsilon_\beta \mathbf{K}^{\mathrm{II}-1}_\omega \mathbf{B}^0_{\omega\omega} - \mathbf{I} \quad \text{in the } \omega\text{-region} \tag{8.131}$$

$$\nabla . \mathbf{B}^0_{\omega\omega} = 0 \quad \text{in the } \omega\text{-region} \tag{8.132}$$

$$\mathbf{B}^0_{\gamma\omega} = \mathbf{B}^0_{\omega\omega} \quad \text{at } A_{\gamma\omega} \tag{8.133}$$

$$\mathbf{n}_{\gamma\omega} . \left[-\mathbf{b}^0_{\gamma\omega} + (\nabla \mathbf{B}^0_{\gamma\omega} + \nabla \mathbf{B}^{0\ T}_{\gamma\omega}) \right] = \mathbf{n}_{\gamma\omega} . \left[-\mathbf{b}^0_{\omega\omega} + (\nabla \mathbf{B}^0_{\omega\omega} + \nabla \mathbf{B}^{0\ T}_{\omega\omega}) \right] \quad \text{at } A_{\gamma\omega} \tag{8.134}$$

$$\mathbf{B}^0_{\gamma\omega} = 0 \quad \text{at } A_{\gamma\kappa} \tag{8.135}$$

$$\mathbf{B}^0_{\omega\omega} = 0 \quad \text{at } A_{\omega\kappa} \tag{8.136}$$

$$\mathbf{B}^0_{\gamma\omega}(\mathbf{x} + l_i) = \mathbf{B}^0_{\gamma\omega}(\mathbf{x}) \qquad \mathbf{B}^0_{\omega\omega}(\mathbf{x} + l_i) = \mathbf{B}^0_{\omega\omega}(\mathbf{x}) \qquad i = 1, 2, 3 \tag{8.137}$$

$$\mathbf{b}^0_{\gamma\omega}(\mathbf{x} + l_i) = \mathbf{b}^0_{\gamma\omega}(\mathbf{x}) \qquad \mathbf{b}^0_{\omega\omega}(\mathbf{x} + l_i) = \mathbf{b}^0_{\omega\omega}(\mathbf{x}) \qquad i = 1, 2, 3 \tag{8.138}$$

$$\langle \mathbf{B}^0_{\gamma\omega} \rangle^\gamma = -\varepsilon_\gamma^{-1} \mathbf{K}^*_{\gamma\omega} \qquad \langle \mathbf{B}^0_{\omega\omega} \rangle^\omega = -\varepsilon_\alpha^{-1} \varepsilon_\beta^{-1} \varepsilon_\omega^{-1} \mathbf{K}^*_{\omega\omega} \tag{8.139}$$

Where the following notations have been introduced

$$\mathbf{K}^*_{\gamma\gamma} = \left(\mathbf{K}^{\mathrm{I}-1}_\gamma - \mathbf{K}^{\mathrm{I}-1}_{\gamma\omega} \mathbf{K}^{\mathrm{I}}_\omega \mathbf{K}^{\mathrm{I}-1}_{\omega\gamma} \right)^{-1} \tag{8.140}$$

$$\mathbf{K}^*_{\omega\gamma} = \left(\mathbf{K}^{\mathrm{I}-1}_\gamma \mathbf{K}^{\mathrm{I}}_{\omega\gamma} \mathbf{K}^{\mathrm{I}-1}_\omega - \mathbf{K}^{\mathrm{I}-1}_{\gamma\omega} \right)^{-1} \tag{8.141}$$

$$\mathbf{K}^*_{\gamma\omega} = \left(\mathbf{K}^{\mathrm{I}-1}_\omega \mathbf{K}^{\mathrm{I}}_{\gamma\omega} \mathbf{K}^{\mathrm{I}-1}_\gamma - \mathbf{K}^{\mathrm{I}-1}_{\omega\gamma} \right)^{-1} \tag{8.142}$$

$$\mathbf{K}^*_{\omega\omega} = \left(\mathbf{K}^{\mathrm{I}-1}_\omega - \mathbf{K}^{\mathrm{I}-1}_{\omega\gamma} \mathbf{K}^{\mathrm{I}}_\gamma \mathbf{K}^{\mathrm{I}-1}_{\gamma\omega} \right)^{-1} \tag{8.143}$$

These two closure problems are of the form of a flow in a fluid/porous system, with a volume force in the fluid phase for problem I', and in the porous phase for problem II'. Their solution is relatively easy to obtain numerically for a given structure. Once the height closure variables solved, the four permeabilites can be evaluated by solving the system composed of Eqs. (8.128) and (8.139). Note that the permeability tensors $\mathbf{K}^*_{ij}$, as they are defined above, are in a convenient form to be used in a pressure-driven Darcy equation [Lasseux et al., 1996]. Once again, in the present study, the form of the coupling permeability tensors, $\mathbf{K}^{\mathrm{I}}_{\gamma\omega}$ and $\mathbf{K}^{\mathrm{I}}_{\omega\gamma}$, is unusual due to the fact that we wish to retain the Brinkman correction in the macroscopic equations. Yet, by changing the notations such as $\mathbf{K}^{\mathrm{I}}_{ij} = \mathbf{K}_i\mathbf{K}^{-1}_{ij}$, it is straight forward to verify that Eqs. (8.140) to (8.143) are equivalent to Eqs. (2.7) of [Lasseux et al., 1996].

Only closure problem III remains to be treated, along with the evaluation of the h_i and Π_i. This problem is similar to the one derived in Soulaine et al. [2013], except for the Brinkman correction in the ω-region, and the continuity of the normal stress at $A_{\gamma\omega}$. Thus following these authors, we propose a change of variables in the form

$$\mathbf{B}_\gamma = \mathbf{B}^0_\gamma h_\gamma + \mathbf{B}^1_\gamma.\mathbf{\Pi}^{\mathrm{I}}_\gamma + \mathbf{B}^2_\gamma.\mathbf{\Pi}^{\mathrm{I}}_\omega \tag{8.144}$$

$$\mathbf{B}_\omega = -\mathbf{B}^0_\omega h_\omega + \mathbf{B}^1_\omega.\mathbf{\Pi}^{\mathrm{I}}_\gamma + \mathbf{B}^2_\omega.\mathbf{\Pi}^{\mathrm{I}}_\omega \tag{8.145}$$

$$b_\gamma = 1 + b^0_\gamma h_\gamma + \mathbf{b}^1_\gamma.\mathbf{\Pi}^{\mathrm{I}}_\gamma + \mathbf{b}^2_\gamma.\mathbf{\Pi}^{\mathrm{I}}_\omega \tag{8.146}$$

$$b_\omega = -b^0_\omega h_\omega + \mathbf{b}^1_\omega.\mathbf{\Pi}^{\mathrm{I}}_\gamma + \mathbf{b}^2_\omega.\mathbf{\Pi}^{\mathrm{I}}_\omega \tag{8.147}$$

Here the mass transfer between the two regions is represented by the $(b^0_i, \mathbf{B}^0_i)$. Remarkably, the closure variables $(\mathbf{b}^1_i, \mathbf{B}^1_i)$ and $(\mathbf{b}^2_i, \mathbf{B}^2_i)$ are solutions of closure problems I' and II'. Thus, only a problem for $(b^0_i, \mathbf{B}^0_i)$ has to be built

Problem III' :

$$\nabla.\mathbf{B}^0_\gamma = \varepsilon^{-1}_\gamma \quad \text{in the } \gamma\text{-phase} \tag{8.148}$$

$$0 = -\nabla b^0_\gamma + \nabla^2\mathbf{B}^0_\gamma \quad \text{in the } \gamma\text{-phase} \tag{8.149}$$

$$\nabla.\mathbf{B}^0_\omega = -\varepsilon^{-1}_\omega \quad \text{in the } \omega\text{-region} \tag{8.150}$$

$$0 = -\nabla b^0_\omega + \nabla^2\mathbf{B}^0_\omega - \varepsilon_\alpha\varepsilon_\beta\mathbf{K}^{\mathrm{II}-1}_\omega\mathbf{B}^0_\omega \quad \text{in the } \omega\text{-region} \tag{8.151}$$

$$\mathbf{B}^0_\gamma = \mathbf{B}^0_\omega \quad \text{at } A_{\gamma\omega} \tag{8.152}$$

$$\mathbf{n}_{\gamma\omega}.\left[-\mathbf{I}b^0_\gamma + (\nabla\mathbf{B}^0_\gamma + \nabla\mathbf{B}^{0\,T}_\gamma)\right] = \mathbf{n}_{\gamma\omega}.\left[-\mathbf{I}b^0_\omega + (\nabla\mathbf{B}^0_\omega + \nabla\mathbf{B}^{0\,T}_\omega)\right] \quad \text{at } A_{\gamma\omega} \tag{8.153}$$

$$\mathbf{B}^0_\gamma = 0 \quad \text{at } A_{\gamma\kappa} \tag{8.154}$$

$$\mathbf{B}^0_\omega = 0 \quad \text{at } A_{\omega\kappa} \tag{8.155}$$

$$\mathbf{B}^0_\gamma(\mathbf{x} + l_i) = \mathbf{B}^0_\gamma(\mathbf{x}) \qquad \mathbf{B}^0_\omega(\mathbf{x} + l_i) = \mathbf{B}^0_\omega(\mathbf{x}) \qquad i = 1, 2, 3 \tag{8.156}$$

$$b^0_\gamma(\mathbf{x} + l_i) = b^0_\gamma(\mathbf{x}) \qquad b^0_\omega(\mathbf{x} + l_i) = b^0_\omega(\mathbf{x}) \qquad i = 1, 2, 3 \tag{8.157}$$

Where Eq. (8.100) is used to eliminate the h_i. This problem is similar to a flow in a fluid/porous system, where source terms are present in the continuity equations. Again, some constraint has to be applied to the pressure-like variable in order to insure uniqueness of the

solution. But first, let us write the average of Eqs. (8.146) and (8.147), and making use of Eq. (8.103) we have

$$0 = 1 + \langle b^0_\gamma \rangle^\gamma h_\gamma + \langle \mathbf{b}^1_\gamma \rangle^\gamma . \mathbf{\Pi}^{\mathrm{I}}_\gamma + \langle \mathbf{b}^2_\gamma \rangle^\gamma . \mathbf{\Pi}^{\mathrm{I}}_\omega \tag{8.158}$$

$$0 = -\langle b^0_\omega \rangle^\omega h_\omega + \langle \mathbf{b}^1_\omega \rangle^\omega . \mathbf{\Pi}^{\mathrm{I}}_\gamma + \langle \mathbf{b}^2_\omega \rangle^\omega . \mathbf{\Pi}^{\mathrm{I}}_\omega \tag{8.159}$$

In order to guarantee uniqueness of the solution, it is enough to constrain the pressure-like variables in only one region of the system. Therefore, we choose to apply

$$\langle b^0_\omega \rangle^\omega = 0 \qquad \langle \mathbf{b}^1_\gamma \rangle^\gamma = 0 \qquad \langle \mathbf{b}^2_\gamma \rangle^\gamma = 0 \tag{8.160}$$

which gives the relation for the mass exchange coefficient

$$\langle b^0_\gamma \rangle^\gamma = -h_\gamma^{-1} = h_\omega^{-1} \tag{8.161}$$

At this point, only $\mathbf{\Pi}_\gamma$ and $\mathbf{\Pi}_\omega$ remain to be evaluated. Averaging Eqs. (8.144) and (8.145), and making use of Eq. (8.95), we get

$$0 = \langle \mathbf{B}^0_\gamma \rangle^\gamma h_\gamma + \langle \mathbf{B}^1_\gamma \rangle^\gamma . \mathbf{\Pi}^{\mathrm{I}}_\gamma + \langle \mathbf{B}^2_\gamma \rangle^\gamma . \mathbf{\Pi}^{\mathrm{I}}_\omega \tag{8.162}$$

$$0 = -\langle \mathbf{B}^0_\omega \rangle^\omega h_\omega + \langle \mathbf{B}^1_\omega \rangle^\omega . \mathbf{\Pi}^{\mathrm{I}}_\gamma + \langle \mathbf{B}^2_\omega \rangle^\omega . \mathbf{\Pi}^{\mathrm{I}}_\omega \tag{8.163}$$

Since, as remarked above, $(\mathbf{B}^1_\gamma, \mathbf{B}^1_\omega)$ and $(\mathbf{B}^2_\gamma, \mathbf{B}^2_\omega)$ are solution of closure problems I' and II' respectively, Eqs. (8.128) and (8.139) imply

$$\langle \mathbf{B}^1_\gamma \rangle^\gamma = -\varepsilon_\gamma^{-1} \mathbf{K}^*_{\gamma\gamma} \qquad \langle \mathbf{B}^1_\omega \rangle^\omega = -\varepsilon_\alpha^{-1} \varepsilon_\beta^{-1} \varepsilon_\omega^{-1} \mathbf{K}^*_{\omega\gamma} \tag{8.164}$$

$$\langle \mathbf{B}^2_\gamma \rangle^\gamma = -\varepsilon_\gamma^{-1} \mathbf{K}^*_{\gamma\omega} \qquad \langle \mathbf{B}^2_\omega \rangle^\omega = -\varepsilon_\alpha^{-1} \varepsilon_\beta^{-1} \varepsilon_\omega^{-1} \mathbf{K}^*_{\omega\omega} \tag{8.165}$$

And substituting this relations into Eqs. (8.162) and (8.163), we finally get

$$\langle \mathbf{B}^0_\gamma \rangle^\gamma h_\gamma = \varepsilon_\gamma^{-1} \mathbf{K}^*_{\gamma\gamma} . \mathbf{\Pi}^{\mathrm{I}}_\gamma + \varepsilon_\gamma^{-1} \mathbf{K}^*_{\gamma\omega} . \mathbf{\Pi}^{\mathrm{I}}_\omega \tag{8.166}$$

$$-\langle \mathbf{B}^0_\omega \rangle^\omega h_\omega = \varepsilon_\alpha^{-1} \varepsilon_\beta^{-1} \varepsilon_\omega^{-1} \mathbf{K}^*_{\omega\gamma} . \mathbf{\Pi}^{\mathrm{I}}_\gamma + \varepsilon_\alpha^{-1} \varepsilon_\beta^{-1} \varepsilon_\omega^{-1} \mathbf{K}^*_{\omega\omega} . \mathbf{\Pi}^{\mathrm{I}}_\omega \tag{8.167}$$

To sum up, the closed momentum transport (Eqs. (8.59) and (8.60)) and mass conservation (Eqs. (8.108) and (8.109)) equations at the bioreactor scale, make appear height effective parameters : two main permeability tensors ($\mathbf{K}^{\mathrm{I}}_\gamma$, $\mathbf{K}^{\mathrm{I}}_\omega$), four coupling tensors ($\mathbf{K}^{\mathrm{I}}_{\gamma\omega}$, $\mathbf{K}^{\mathrm{I}}_{\omega\gamma}$, $\mathbf{\Pi}^{\mathrm{I}}_\gamma$, $\mathbf{\Pi}^{\mathrm{I}}_\omega$), and two mass exchange coefficients (h_γ, h_ω). For a given periodic cell, the solution of closure problem I' and II' allows the evaluation of the $\mathbf{K}^{\mathrm{I}}_i$ and $\mathbf{K}^{\mathrm{I}}_{ij}$, through Eqs. (8.128) and (8.139) and with the definitions Eqs. (8.140) and (8.143). Then, the resolution of problem III' directly gives the values of h_γ and h_ω. Finally, coupling the solutions of the three closure problems I', II', and III", $\mathbf{\Pi}^{\mathrm{I}}_\gamma$ and $\mathbf{\Pi}^{\mathrm{I}}_\omega$ can be computed through Eqs. (8.166) and (8.167).

Numerical results

We aim to study the evolution of the effective parameters as a function of (i) the tissue volume fraction, (ii) the tissue effective permeability. To this purpose, the three closure problems described above are solved on two-dimensional periodic unit cells such as the one depicted in

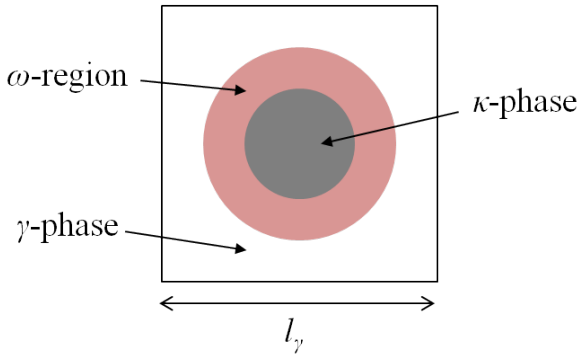

Figure 8.2 – Representation of a unit cell used to compute the effective transport properties of the bioreactor

figure Fig. 8.2. The volume fraction of the glass beads is kept constant at $\varepsilon_\kappa = 0.30$, while computations are done for the tissue volume fraction ranging from $\varepsilon_\omega = 0.01$ to 0.45. Four tissue permeabilities are examined $\mathbf{K}^{\mathrm{II}}_\omega / l^2_\gamma = 10^{-2}$, 10^{-4}, 10^{-6}, and 10^{-8} (corresponding to dimensional permeabilities of about $\mathbf{K}^{\mathrm{II}}_\omega = 10^{-8} m^2$, $10^{-10} m^2$, $10^{-12} m^2$, and $10^{-14} m^2$ respectively). In all the computations, the ECM porosity ε_α and volume fraction ε_β are kept equal to 0.9 and 0.6 respectively.

The main macroscopic permeabilities $\mathbf{K}^{\mathrm{I}}_\gamma$ and $\mathbf{K}^{\mathrm{I}}_\omega$, and the coupling macroscopic permeabilities $\mathbf{K}^{\mathrm{I}}_{\gamma\omega}$ and $\mathbf{K}^{\mathrm{I}}_{\omega\gamma}$, are plotted in Figs. 8.3 and 8.4 respectively, as a function of the tissue volume fraction ε_ω, for different values of the tissue effective permeability $\mathbf{K}^{\mathrm{II}}_\omega$. In all cases, the macroscopic permeabilities are sensitive to the tissue scale permeability $\mathbf{K}^{\mathrm{II}}_\omega$. As expected, the main effective permeability values are lower for a low tissue permeability $\mathbf{K}^{\mathrm{II}}_\omega$. Moreover, as the tissue volume fraction ε_ω tends to zero, the main permeability related to the γ-phase $\mathbf{K}^{\mathrm{I}}_\gamma$ tends to the same value, independently of $\mathbf{K}^{\mathrm{II}}_\omega$.

Concerning the coupling tensors, it has first to be noted that $\mathbf{K}^{\mathrm{I}}_{\gamma\omega}$ and $\mathbf{K}^{\mathrm{I}}_{\omega\gamma}$ have a similar behavior, and are of the same order of magnitude for a given tissue volume fraction ε_ω. Interestingly, the coupling coefficients are not monotonic, showing a maximal value for a critical tissue volume faction ε_ω. In order to understand this behavior, one has to keep in mind that the coupling coefficients $\mathbf{K}^{\mathrm{I}}_{ij}$ represent the interactions between the regions γ and ω, in terms of momentum transport. Consequently, in order to obtain high values of the $\mathbf{K}^{\mathrm{I}}_{ij}$, two conditions must be fulfilled : (i) that both fluid and porous regions exist (i.e. none of ε_ω nor ε_γ is negligible compared to the other), and (ii) that there is enough momentum in the system to be exchanged. This implies that, at very low tissue volume fractions, increasing the volume of tissue, enhances the ability of the system to exchange momentum. However, after a critical value of the tissue volume fraction, the porous region is large enough to weaken momentum in the overall system, decreasing the interactions between the two regions. As a result, the critical value of the tissue volume fraction is smaller when the tissue permeability $\mathbf{K}^{\mathrm{II}}_\omega$ is lower.

A similar mechanism is observed for the mass exchange coefficient in Fig. 8.5. However, the critical tissue volume fraction is more sensitive to the tissue permeability, and it seems that, for the lowest values of $\mathbf{K}^{\mathrm{II}}_\omega$, the critical volume fraction tends to zero, producing a monotone decrease of the mass exchange coefficient h_ω.

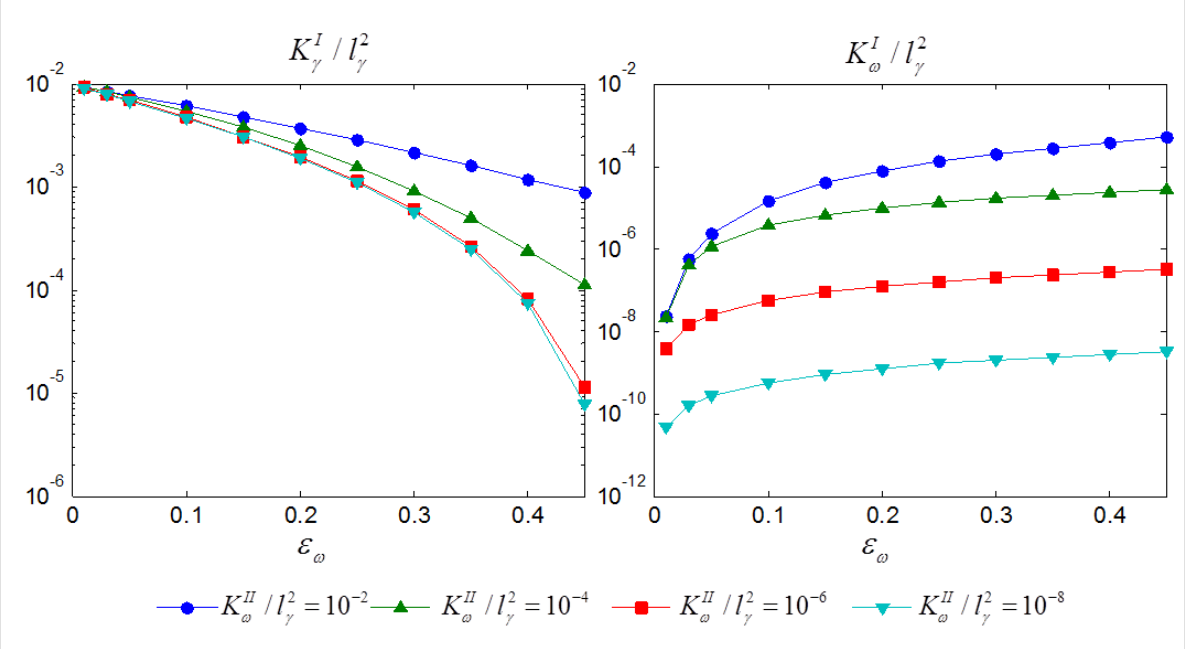

Figure 8.3 – Dimensionless main permeabilities as a function of the tissue volume fraction. ($\varepsilon_\kappa = 0.30$, $\varepsilon_\beta = 0.60$, $\varepsilon_\alpha = 0.90$)

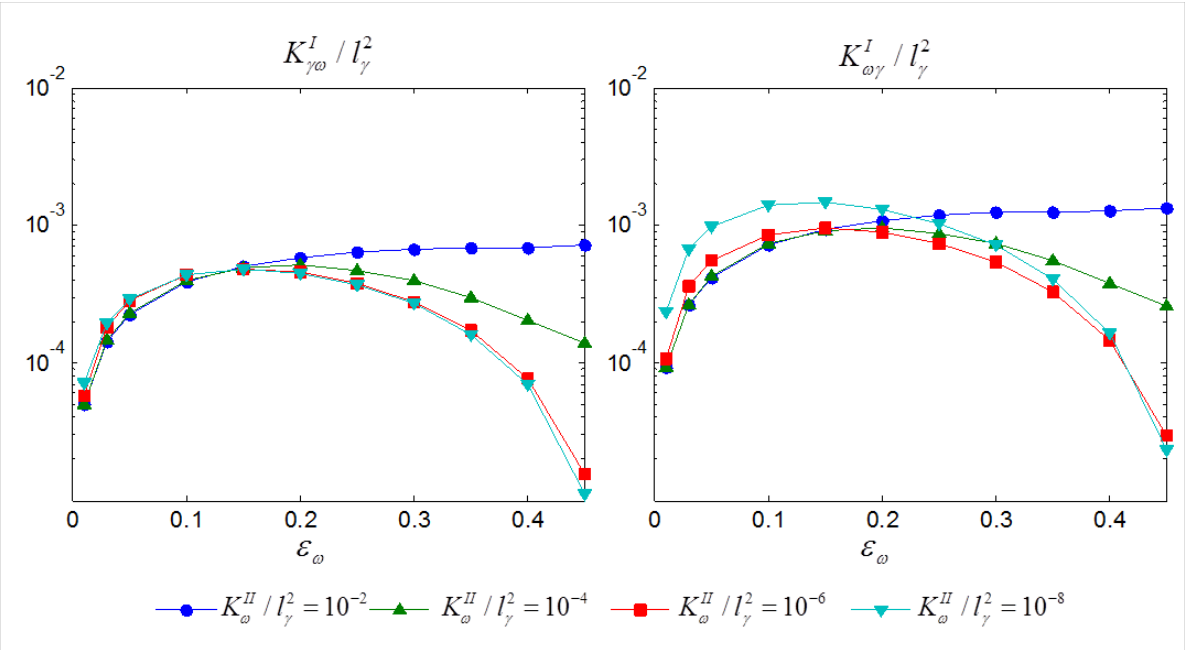

Figure 8.4 – Dimensionless coulping permeabilities as a function of the tissue volume fraction. ($\varepsilon_\kappa = 0.30$, $\varepsilon_\beta = 0.60$, $\varepsilon_\alpha = 0.90$)

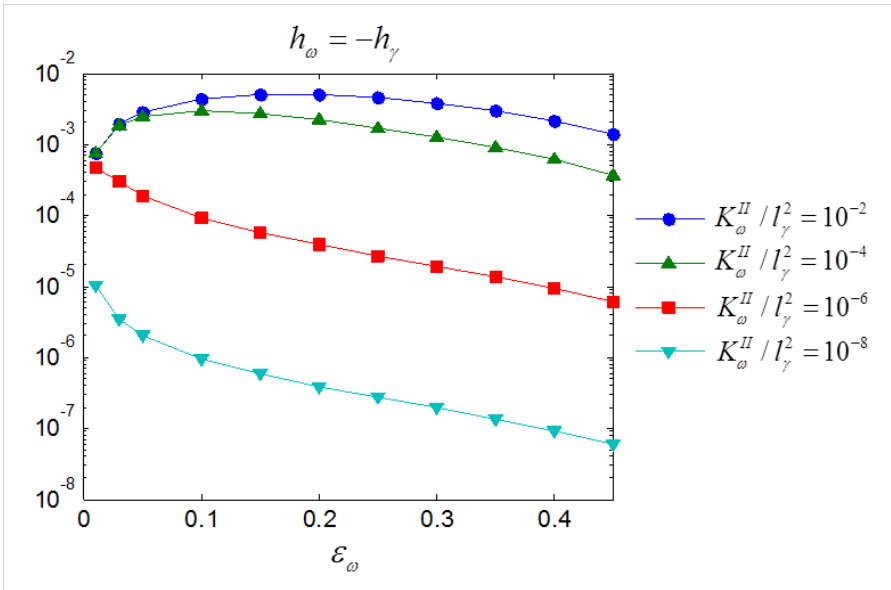

Figure 8.5 – Mass exchange coefficient as a function of the tissue volume fraction.
($\varepsilon_\kappa = 0.30$, $\varepsilon_\beta = 0.60$, $\varepsilon_\alpha = 0.90$)

The obtained values of the pressure driven exchange coefficients $\mathbf{\Pi}^{\mathrm{I}}_\gamma$ and $\mathbf{\Pi}^{\mathrm{I}}_\omega$ (not shown here), are of the order $\pm 10^{-9} l_\gamma$, independently of ε_ω. Yet, a strong dependence on the mesh size is noted, especially for extreme values of the tissue volume fraction, where numerical artifacts are the most likely to appear due to small geometrical elements.

The results presented above indicate that, in the macroscopic transport equations (Eqs. (8.59) and (8.60)), the coupling velocity terms may play a non-negligible role, depending on the geometry of the averaging volume. Yet, the evaluation of the order of magnitude of the effective properties in not enough to conclude on the relative importance of coupling terms in the macroscopic equation. Indeed, the effective properties are in factor of macroscopic quantities. Therefore, before to discard any term, the macroscopic field should be solved at level I, and the order of magnitude of the whole terms must be compared to each others. For instance, at low tissue permeability, $\langle \mathbf{v}_\omega \rangle^\omega$ is likely to be very small compared to $\langle \mathbf{v}_\gamma \rangle^\gamma$, even though the coupling tensors are of the same order of magnitude, $\mathbf{K}^{\mathrm{I}}_{\omega\gamma}$ may play a more important role than $\mathbf{K}^{\mathrm{I}}_{\gamma\omega}$.

8.3 Upscaling mass transport to the bioreactor scale

The mass transport problem at the tissue scale is composed of Eqs. (8.10), (8.13), (8.16), (8.17), (8.20) and (8.21). In this section, the tissue scale mass transport equations are homogenized, in order to derive the bioreactor scale mass conservation equations in non-equilibrium conditions. Finally the closure problem for the determination of the bioreactor effective parameters is developed.

8.3.1 Theoretical development

Similar systems as the one described here at the tissue scale have been studied in the literature [Lasseux et al., 2004; Golfier et al., 2009; Orgogozo et al., 2009, 2010]. In all these models, three phases are defined, a fluid-phase where diffusion and convection occur, a biomass region where diffusion and reaction are present, and a solid inert phase. Since mass transport occurs in two regions, the most general representation at the bioreactor scale should be composed of two mass transport equations per considered species [Wood, 2009; Davit et al., 2012]. For purpose of applicability, different set of approximations has led to the derivation of time non-local [Wood & Valdés-Parada, 2013] and local [Ahmadi et al., 1998; Cherblanc et al., 2003, 2007] two-equation models. The differential equations of these models include several effective parameters that can be computed through series of closure problems. Although two equation models are the most suitable to represent a wide range of conditions, the complexity of their development, resolution and interpretation has motivated the development of more accessible one-equation models.

Different assumptions can be made to reduce the macroscopic model into a one-equation model, and the most popular is the hypothesis of local mass equilibrium (see Sec. 7.3.1). The restrictions joined with this hypothesis have been derived in terms of length scale constraints [Quintard & Whitaker, 1998b; Wood & Whitaker, 1998; Wood et al., 2011], and in the particular case of a similar system to the one presented here, Golfier et al. [2009] verified its domain of validity by comparison with direct numerical simulations. The authors conclude that the one-equation local-mass-equilibrium model is valid for values of the Péclet (relative contribution of the convective transport over the diffusion) and Damköhler (relative contribution of the species consumption over the diffusion in the tissue) numbers under one.

In some specific cases, mass equilibrium may not be required to derive a one-equation model. Assuming either a reaction rate limited problem (RRLC), or a mass transfer limited consumption system (MTLC), Orgogozo et al. [2009, 2010] derive two different one-equation non-equilibrium models. In both cases, the results are compared with direct numerical simulations to asses the domain of validity. The RRLC model represents the case where the consumption of species is much faster than the diffusion, implying a homogeneous concentration field in the γ-phase. These conditions are generally met for values of the Péclet and Damköhler numbers over 1000. Alternatively, the MTLC model represents the case where the process is limited by mass transport between the two regions. This implies a null concentration in the ω-region, which may be obtained for Péclet numbers under 10, and Damköler numbers higher than 100. However it is important to note that for the two non-equilibrium models (RRLC and MTLC), the direct numerical simulations have been computed on a two-dimensional stratified system, far from the geometry of the current study. In both cases a macroscopic non-equilibrium one-equation model can be derived and the corresponding closure problem can be developed and solved in order to evaluate the effective diffusion-dispersion tensor.

Finally, based on a weighted concentration [Quintard et al., 2001] and a special decomposition Davit et al. [2010], a one-equation non-equilibrium model has been derived for time-asymptotic mass transport process in heterogeneous porous media. Direct numerical simulations show that the domain of validity of this model for a given configuration is relatively

insensitive to the Péclet and Damköhler numbers. However the main limitation is on the time dependency of the system. Indeed, this model fails to represent small time phenomena, restricting its validity to processes where the characteristic time of evolution of the transport process, is larger than the timescale associated with exchange between the two regions.

Returning to our system, the Péclet and Damköhler and Reynolds numbers can be evaluated in the case of the perfusion bioreactor

$$\left.\begin{array}{l} \|v_\gamma\| = 4\times10^{-3} m/s \\ l_\gamma = 1\times10^{-3} m \\ D_{A\alpha} = 3\times10^{-9} m^2/s \\ \mu_\alpha = 10^{-2} Pa.s \end{array}\right\} \begin{array}{l} \mathrm{Pe}_\gamma \simeq 10^3 \\ \mathrm{Re}_\gamma \simeq 10^1 \end{array} \left.\begin{array}{ll} k_A = 8\times10^{-6} g/(cm^3 s) & \\ \varepsilon_\sigma = 0.1 - 0.9 & \\ l_\omega = 10^{-5} - 10^{-3} m & \\ \alpha_0 = 0.1 - 1 & \\ K_A = 6\times10^{-5} g/cm^3 & \\ D_{A\omega} = 10^{-10} m^2/s & \end{array}\right\} \mathrm{Da}_\omega \simeq 10^{-2} - 10^4$$

The value of the Péclet number in the bioreactor indicates that neither the local mass equilibrium nor the MTLC models are suitable for the representation of mass transport in the γ-phase. The Damköhler number varies a lot depending on the possible values of the parameters. However l_ω is the main influencing parameter, and this suggests that Da_ω increases of several orders of magnitude during tissue growth. Under this circumstances the RRLC model may not be suitable neither. Nevertheless, since the bioreactor is perfused continuously with a culture medium whose concentrations vary very slowly in regard to cell consumption and growth, the problem falls into the time asymptotic regime, and the methodology presented in [Davit et al., 2010] may be applicable.Yet, this approach is based on the definiton of a weighted average, where the intrinsic average of the tissue concentration remain unknown. Since the tissue growth kinetic will be dependent on this variable, we choose, in the following section, to develop a non-equilibrium model of the type local two-equation.

Let us start the averaging process of the tissue scale mass transport Eqs. (8.10) and (8.13). Following similar steps than for the cellular scale (level III), one obtains

$$\begin{aligned} \frac{\partial\left(\varepsilon_\gamma\langle c_{A\gamma}\rangle^\gamma\right)}{\partial t} + \nabla.\left(\varepsilon_\gamma\langle \mathbf{v}_\gamma\rangle^\gamma\langle c_{A\gamma}\rangle^\gamma\right) = \nabla.\Big[D_{A\alpha}\mathbf{I}.\Big(\varepsilon_\gamma\nabla\langle c_{A\gamma}\rangle^\gamma + \sum_{i=\omega,\kappa}\frac{1}{\mathcal{V}_{\mathrm{II}}}\int_{A_{\gamma i}}\mathbf{n}_{\gamma i}\tilde{c}_{A\gamma}dA\Big)\Big] \\ + \sum_{i=\omega,\kappa}\frac{1}{\mathcal{V}_{\mathrm{II}}}\int_{A_{\gamma i}}\mathbf{n}_{\gamma i}.\left[\left(\mathbf{w}_{\gamma i}-\mathbf{v}_\gamma\right)c_{A\gamma} + D_{A\alpha}\nabla c_{A\gamma}\right]dA - \nabla.\langle\tilde{\mathbf{v}}_\gamma\tilde{c}_{A\gamma}\rangle \end{aligned} \tag{8.168}$$

$$\begin{aligned} \frac{\partial\left(\varepsilon_{\mathrm{III}}\varepsilon_\omega\langle c_{A\omega}\rangle^\omega\right)}{\partial t} + \nabla.\left(\varepsilon_\omega\langle \mathbf{v}_\omega\rangle^\omega\langle c_{A\omega}\rangle^\omega\right) = \\ \nabla.\Big[\mathbf{D}^{\mathrm{II}}_{A\omega}.\Big(\varepsilon_\omega\nabla\langle c_{A\omega}\rangle^\omega + \sum_{i=\gamma,\kappa}\frac{1}{\mathcal{V}_{\mathrm{II}}}\int_{A_{\omega i}}\mathbf{n}_{\omega i}\tilde{c}_{A\omega}dA\Big)\Big] \\ + \sum_{i=\gamma,\kappa}\frac{1}{\mathcal{V}_{\mathrm{II}}}\int_{A_{\omega i}}\mathbf{n}_{\omega i}.\left[\left(\varepsilon_{\mathrm{III}}\mathbf{w}_{\omega i}-\mathbf{v}_\omega\right)c_{A\omega} + \mathbf{D}^{\mathrm{II}}_{A\omega}.\nabla c_{A\omega}\right]dA - \nabla.\langle\tilde{\mathbf{v}}_\omega\tilde{c}_{A\omega}\rangle + \varepsilon_\omega\langle R_\omega\rangle^\omega \end{aligned} \tag{8.169}$$

Where Gray's spacial decomposition for the concentration has been introduced

$$c_{A\gamma} = \langle c_{A\gamma}\rangle^{\gamma} + \tilde{c}_{A\gamma} \qquad c_{A\omega} = \langle c_{A\omega}\rangle^{\omega} + \tilde{c}_{A\omega} \tag{8.170}$$

The second terms on the right hand sides of Eqs. (8.168) and (8.169) are interfacial flux, where convective and diffusive transport are included. The interfacial diffusive terms are further developed to obtain

$$\sum_{i=\omega,\kappa} \frac{1}{\mathcal{V}_{\text{II}}} \int_{A_{\gamma i}} \mathbf{n}_{\gamma i}.\left(D_{A\alpha}\nabla c_{A\gamma}\right) dA = - \nabla\varepsilon_{\gamma}.\left(D_{A\alpha}\nabla\langle c_{A\gamma}\rangle^{\gamma}\right) + \sum_{i=\omega,\kappa} \frac{1}{\mathcal{V}_{\text{II}}} \int_{A_{\gamma i}} \mathbf{n}_{\gamma i}.\left(D_{A\alpha}\nabla\tilde{c}_{A\gamma}\right) dA \tag{8.171}$$

$$\sum_{i=\gamma,\kappa} \frac{1}{\mathcal{V}_{\text{II}}} \int_{A_{\omega i}} \mathbf{n}_{\omega i}.\left(\mathbf{D}^{\text{II}}_{A\omega}.\nabla c_{A\omega}\right) dA = - \nabla\varepsilon_{\omega}.\left(\mathbf{D}^{\text{II}}_{A\omega}.\nabla\langle c_{A\omega}\rangle^{\omega}\right) + \sum_{i=\gamma,\kappa} \frac{1}{\mathcal{V}_{\text{II}}} \int_{A_{\omega i}} \mathbf{n}_{\omega i}.\left(\mathbf{D}^{\text{II}}_{A\omega}.\nabla\tilde{c}_{A\omega}\right) dA \tag{8.172}$$

Once again, the macroscopic properties of the bioreactor are supposed to evolve on a length scale much large than the length scale of the concentration deviations ($L \gg l_{\gamma}$ and $L \gg l_{\omega}$). This allows to neglect the gradient of the volume fractions, and Eqs. (8.168) and (8.169) takes the form

$$\begin{aligned}\frac{\partial\left(\varepsilon_{\gamma}\langle c_{A\gamma}\rangle^{\gamma}\right)}{\partial t} + \nabla.\left(\varepsilon_{\gamma}\langle\mathbf{v}_{\gamma}\rangle^{\gamma}\langle c_{A\gamma}\rangle^{\gamma}\right) &= \nabla.\Big[D_{A\alpha}\mathbf{I}.\Big(\varepsilon_{\gamma}\nabla\langle c_{A\gamma}\rangle^{\gamma} + \sum_{i=\omega,\kappa}\frac{1}{\mathcal{V}_{\text{II}}}\int_{A_{\gamma i}}\mathbf{n}_{\gamma i}\tilde{c}_{A\gamma}dA\Big)\Big] \\ &+ \sum_{i=\omega,\kappa}\frac{1}{\mathcal{V}_{\text{II}}}\int_{A_{\gamma i}}\mathbf{n}_{\gamma i}.\left[\left(\mathbf{w}_{\gamma i}-\mathbf{v}_{\gamma}\right)\tilde{c}_{A\gamma} + D_{A\alpha}\nabla\tilde{c}_{A\gamma}\right]dA \\ &+ \sum_{i=\omega,\kappa}\frac{1}{\mathcal{V}_{\text{II}}}\int_{A_{\gamma i}}\mathbf{n}_{\gamma i}.\left(\mathbf{w}_{\gamma i}-\mathbf{v}_{\gamma}\right)dA\langle c_{A\gamma}\rangle^{\gamma} - \nabla.\langle\tilde{\mathbf{v}}_{\gamma}\tilde{c}_{A\gamma}\rangle\end{aligned} \tag{8.173}$$

$$\begin{aligned}\frac{\partial\left(\varepsilon_{\text{III}}\varepsilon_{\omega}\langle c_{A\omega}\rangle^{\omega}\right)}{\partial t} + \nabla.\left(\varepsilon_{\omega}\langle\mathbf{v}_{\omega}\rangle^{\omega}\langle c_{A\omega}\rangle^{\omega}\right) &= \\ \nabla.\Big[\mathbf{D}^{\text{II}}_{A\omega}.\Big(\varepsilon_{\omega}\nabla\langle c_{A\omega}\rangle^{\omega} + \sum_{i=\gamma,\kappa}\frac{1}{\mathcal{V}_{\text{II}}}\int_{A_{\omega i}}\mathbf{n}_{\omega i}\tilde{c}_{A\omega}dA\Big)\Big] \\ + \sum_{i=\gamma,\kappa}\frac{1}{\mathcal{V}_{\text{II}}}\int_{A_{\omega i}}\mathbf{n}_{\omega i}.\left[\left(\varepsilon_{\text{III}}\mathbf{w}_{\omega i}-\mathbf{v}_{\omega}\right)\tilde{c}_{A\omega} + \mathbf{D}^{\text{II}}_{A\omega}.\nabla\tilde{c}_{A\omega}\right]dA \\ + \sum_{i=\gamma,\kappa}\frac{1}{\mathcal{V}_{\text{II}}}\int_{A_{\omega i}}\mathbf{n}_{\omega i}.\left(\varepsilon_{\text{III}}\mathbf{w}_{\omega i}-\mathbf{v}_{\omega}\right)dA\langle c_{A\omega}\rangle^{\omega} - \nabla.\langle\tilde{\mathbf{v}}_{\omega}\tilde{c}_{A\omega}\rangle + \varepsilon_{\omega}\langle R_{\omega}\rangle^{\omega}\end{aligned} \tag{8.174}$$

These are the non-closed macroscopic equations for mass transport at the bioreactor scale. A more compact form of the macroscopic equations can be obtain by applying the spacial averaging theorem to the average of the deviation gradient

$$\langle \nabla \tilde{c}_{A\gamma} \rangle = \nabla \langle \tilde{c}_{A\gamma} \rangle + \sum_{i=\omega,\kappa} \frac{1}{\mathcal{V}_{\text{II}}} \int_{A_{\gamma i}} \mathbf{n}_{\gamma i} \tilde{c}_{A\gamma} dA \tag{8.175}$$

It can be shown, by taking the average of Eq. (8.170), that the average of the concentration deviation is null. Thus the first term of the right hand side can be discarded, and the *non-closed macroscopic equations* read

$$\begin{aligned} \frac{\partial \left(\varepsilon_\gamma \langle c_{A\gamma} \rangle^\gamma\right)}{\partial t} + \nabla . \left(\varepsilon_\gamma \langle \mathbf{v}_\gamma \rangle^\gamma \langle c_{A\gamma} \rangle^\gamma\right) &= \nabla . \left[\varepsilon_\gamma D_{A\alpha} \mathbf{I} . \left(\nabla \langle c_{A\gamma} \rangle^\gamma + \langle \nabla \tilde{c}_{A\gamma} \rangle^\gamma\right)\right] \\ &+ \sum_{i=\omega,\kappa} \frac{1}{\mathcal{V}_{\text{II}}} \int_{A_{\gamma i}} \mathbf{n}_{\gamma i} . \left[\left(\mathbf{w}_{\gamma i} - \mathbf{v}_\gamma\right) \tilde{c}_{A\gamma} + D_{A\alpha} \nabla \tilde{c}_{A\gamma}\right] dA \\ &+ \sum_{i=\omega,\kappa} \frac{1}{\mathcal{V}_{\text{II}}} \int_{A_{\gamma i}} \mathbf{n}_{\gamma i} . \left(\mathbf{w}_{\gamma i} - \mathbf{v}_\gamma\right) dA \langle c_{A\gamma} \rangle^\gamma - \nabla . \langle \tilde{\mathbf{v}}_\gamma \tilde{c}_{A\gamma} \rangle \end{aligned} \tag{8.176}$$

$$\begin{aligned} \frac{\partial \left(\varepsilon_{\text{III}} \varepsilon_\omega \langle c_{A\omega} \rangle^\omega\right)}{\partial t} + \nabla . \left(\varepsilon_\omega \langle \mathbf{v}_\omega \rangle^\omega \langle c_{A\omega} \rangle^\omega\right) &= \nabla . \left[\varepsilon_\omega \mathbf{D}^{\text{II}}_{A\omega} . \left(\nabla \langle c_{A\omega} \rangle^\omega + \langle \nabla \tilde{c}_{A\omega} \rangle^\omega\right)\right] \\ &+ \sum_{i=\gamma,\kappa} \frac{1}{\mathcal{V}_{\text{II}}} \int_{A_{\omega i}} \mathbf{n}_{\omega i} . \left[\left(\varepsilon_{\text{III}} \mathbf{w}_{\omega i} - \mathbf{v}_\omega\right) \tilde{c}_{A\omega} + \mathbf{D}^{\text{II}}_{A\omega} . \nabla \tilde{c}_{A\omega}\right] dA \\ &+ \sum_{i=\gamma,\kappa} \frac{1}{\mathcal{V}_{\text{II}}} \int_{A_{\omega i}} \mathbf{n}_{\omega i} . \left(\varepsilon_{\text{III}} \mathbf{w}_{\omega i} - \mathbf{v}_\omega\right) dA \langle c_{A\omega} \rangle^\omega - \nabla . \langle \tilde{\mathbf{v}}_\omega \tilde{c}_{A\omega} \rangle + \varepsilon_\omega \langle R_\omega \rangle^\omega \end{aligned} \tag{8.177}$$

According to Eqs. (8.3) and (8.6), the reaction rate can be expressed in term of the tissue concentration as

$$R_\omega = -\varepsilon_\sigma k_A \frac{c_{A\omega}}{c_{A\omega} + \alpha_0 K_A} \tag{8.178}$$

The treatment of such non-linear kinetic in homogenization methods, is still an active research area. There are two common ways to deal with such a term. Either the reaction rate is suppose to not influence the closure problem, or conditions leading to the linearisation of Eq. (8.178) are hypothesized. The first approach has been followed at the cellular scale (Sec. 7.3.1). In the present section, we choose to maintain the reaction kinetic in the closure problem, and we suppose that the half saturation constant $\alpha_0 K_A$ is much higher than the local concentration $c_{A\omega}$. This leads to a linear reaction kinetic of the form

$$R_\omega = -\varepsilon_\sigma \frac{k_A}{\alpha_0 K_A} c_{A\omega} \tag{8.179}$$

which superficial average is

$$\langle R_\omega \rangle^\omega = -\varepsilon_\sigma \frac{k_A}{\alpha_0 K_A} \langle c_{A\omega} \rangle^\omega \tag{8.180}$$

The macroscopic equations (Eqs. (8.176) and (8.177)) are dependent on average and deviation concentrations only. In order to close these equations, we need to build a problem for the deviations. But let us first expand the left hand side such as

$$\frac{\partial\left(\varepsilon_\gamma\langle c_{A\gamma}\rangle^\gamma\right)}{\partial t}+\nabla.\left(\varepsilon_\gamma\langle\mathbf{v}_\gamma\rangle^\gamma\langle c_{A\gamma}\rangle^\gamma\right)=\varepsilon_\gamma\frac{\partial\langle c_{A\gamma}\rangle^\gamma}{\partial t}+\varepsilon_\gamma\nabla.\left(\langle\mathbf{v}_\gamma\rangle^\gamma\langle c_{A\gamma}\rangle^\gamma\right)+\langle c_{A\gamma}\rangle^\gamma\frac{\partial\varepsilon_\gamma}{\partial t}+\langle\mathbf{v}_\gamma\rangle^\gamma\langle c_{A\gamma}\rangle^\gamma\nabla\varepsilon_\gamma \quad (8.181)$$

The two last terms on the right hand side can be treated using the averaging theorems, leading to

$$\frac{\partial\left(\varepsilon_\gamma\langle c_{A\gamma}\rangle^\gamma\right)}{\partial t}+\nabla.\left(\varepsilon_\gamma\langle\mathbf{v}_\gamma\rangle^\gamma\langle c_{A\gamma}\rangle^\gamma\right)=\varepsilon_\gamma\frac{\partial\langle c_{A\gamma}\rangle^\gamma}{\partial t}+\varepsilon_\gamma\nabla.\left(\langle\mathbf{v}_\gamma\rangle^\gamma\langle c_{A\gamma}\rangle^\gamma\right)+\sum_{i=\omega,\kappa}\frac{1}{\mathcal{V}_{\mathrm{II}}}\int_{A_{\gamma i}}\mathbf{n}_{\gamma i}.\left(\mathbf{w}_{\gamma i}-\langle\mathbf{v}_\gamma\rangle^\gamma\right)dA\langle c_{A\gamma}\rangle^\gamma \quad (8.182)$$

Now introducing this relation into Eq. (8.176), dividing by ε_γ, and subtracting to the local transport equation Eq. (8.13), we get

$$\begin{aligned}\frac{\partial\tilde{c}_{A\gamma}}{\partial t}+\mathbf{v}_\gamma.\nabla\tilde{c}_{A\gamma}+\tilde{\mathbf{v}}_\gamma.\nabla\langle c_{A\gamma}\rangle^\gamma=\nabla.\left(D_{A\alpha}\nabla\tilde{c}_{A\gamma}\right)-D_{A\alpha}\langle\nabla\tilde{c}_{A\gamma}\rangle^\gamma\\+\sum_{i=\omega,\kappa}\frac{1}{V_\gamma}\int_{A_{\gamma i}}\mathbf{n}_{\gamma i}.\left(\mathbf{w}_{\gamma i}-\langle\mathbf{v}_\gamma\rangle^\gamma\right)dA\langle c_{A\gamma}\rangle^\gamma-\sum_{i=\omega,\kappa}\frac{1}{V_\gamma}\int_{A_{\gamma i}}\mathbf{n}_{\gamma i}.\left(\mathbf{w}_{\gamma i}-\mathbf{v}_\gamma\right)dA\langle c_{A\gamma}\rangle^\gamma\\-\sum_{i=\omega,\kappa}\frac{1}{V_\gamma}\int_{A_{\gamma i}}\mathbf{n}_{\gamma i}.\left[\left(\mathbf{w}_{\gamma i}-\mathbf{v}_\gamma\right)\tilde{c}_{A\gamma}+D_{A\alpha}\nabla\tilde{c}_{A\gamma}\right]dA+\varepsilon_\gamma^{-1}\nabla.\langle\tilde{\mathbf{v}}_\gamma\tilde{c}_{A\gamma}\rangle\end{aligned} \quad (8.183)$$

And similarly, for the ω-region we have

$$\begin{aligned}\frac{\partial\varepsilon_{\mathrm{III}}\tilde{c}_{A\omega}}{\partial t}+\mathbf{v}_\omega.\nabla\tilde{c}_{A\omega}+\tilde{\mathbf{v}}_\omega.\nabla\langle c_{A\omega}\rangle^\omega=\nabla.\left(\mathbf{D}^{\mathrm{II}}_{A\omega}.\nabla\tilde{c}_{A\omega}\right)-\mathbf{D}^{\mathrm{II}}_{A\omega}.\langle\nabla\tilde{c}_{A\omega}\rangle^\omega\\+\sum_{i=\gamma,\kappa}\frac{1}{V_\omega}\int_{A_{\omega i}}\mathbf{n}_{\omega i}.\left(\varepsilon_{\mathrm{III}}\mathbf{w}_{\omega i}-\langle\mathbf{v}_\omega\rangle^\omega\right)dA\langle c_{A\omega}\rangle^\omega-\sum_{i=\gamma,\kappa}\frac{1}{V_\omega}\int_{A_{\omega i}}\mathbf{n}_{\omega i}.\left(\varepsilon_{\mathrm{III}}\mathbf{w}_{\omega i}-\mathbf{v}_\omega\right)dA\langle c_{A\omega}\rangle^\omega\\-\sum_{i=\gamma,\kappa}\frac{1}{V_\omega}\int_{A_{\omega i}}\mathbf{n}_{\omega i}.\left[\left(\varepsilon_{\mathrm{III}}\mathbf{w}_{\omega i}-\mathbf{v}_\omega\right)\tilde{c}_{A\omega}+\mathbf{D}^{\mathrm{II}}_{A\omega}.\nabla\tilde{c}_{A\omega}\right]dA+\nabla.\langle\tilde{\mathbf{v}}_\omega\tilde{c}_{A\omega}\rangle+R_\omega-\langle R_\omega\rangle^\omega\end{aligned} \quad (8.184)$$

Also these equations may appear complex at first sight, they can be simplified on the basis of a comparison of the order of magnitude of the different terms. But before to do that, let us rearrange the interfacial macroscopic convective terms such as

$$\sum_{i=\omega,\kappa}\frac{1}{V_\gamma}\int_{A_{\gamma i}}\mathbf{n}_{\gamma i}.\left(\mathbf{w}_{\gamma i}-\langle\mathbf{v}_\gamma\rangle^\gamma\right)dA\langle c_{A\gamma}\rangle^\gamma-\sum_{i=\omega,\kappa}\frac{1}{V_\gamma}\int_{A_{\gamma i}}\mathbf{n}_{\gamma i}.\left(\mathbf{w}_{\gamma i}-\mathbf{v}_\gamma\right)dA\langle c_{A\gamma}\rangle^\gamma=\sum_{i=\omega,\kappa}\frac{1}{V_\gamma}\int_{A_{\gamma i}}\mathbf{n}_{\gamma i}.\tilde{\mathbf{v}}_\gamma dA\langle c_{A\gamma}\rangle^\gamma \quad (8.185)$$

The divergence theorem is then applied leading to

$$\sum_{i=\omega,\kappa}\frac{1}{V_\gamma}\int_{A_{\gamma i}}\mathbf{n}_{\gamma i}.\left(\mathbf{w}_{\gamma i}-\langle\mathbf{v}_\gamma\rangle^\gamma\right)dA\langle c_{A\gamma}\rangle^\gamma-\sum_{i=\omega,\kappa}\frac{1}{V_\gamma}\int_{A_{\gamma i}}\mathbf{n}_{\gamma i}.\left(\mathbf{w}_{\gamma i}-\mathbf{v}_\gamma\right)dA\langle c_{A\gamma}\rangle^\gamma=\frac{1}{V_\gamma}\int_{\mathcal{V}_{\text{II}}}\nabla.\tilde{\mathbf{v}}_\gamma dV\langle c_{A\gamma}\rangle^\gamma \quad (8.186)$$

In the case where the deviation of the velocity is divergence free, this term is null. However, in the present study this condition is not satisfied due to the production tissue in the averaging volume. Nevertheless, the deviation problem for the momentum problem has been developed in the previous section, and introducing Eq. (8.41) in the above equation yields

$$\sum_{i=\omega,\kappa}\frac{1}{V_\gamma}\int_{A_{\gamma i}}\mathbf{n}_{\gamma i}.\left(\mathbf{w}_{\gamma i}-\langle\mathbf{v}_\gamma\rangle^\gamma\right)dA\langle c_{A\gamma}\rangle^\gamma-\sum_{i=\omega,\kappa}\frac{1}{V_\gamma}\int_{A_{\gamma i}}\mathbf{n}_{\gamma i}.\left(\mathbf{w}_{\gamma i}-\mathbf{v}_\gamma\right)dA\langle c_{A\gamma}\rangle^\gamma=-\frac{\dot{m}_\gamma}{\varepsilon_\gamma^2\rho_\alpha}\langle c_{A\gamma}\rangle^\gamma \quad (8.187)$$

Where the mass exchange rate, being a macroscopic quantity, has been removed from the volume integral. The same procedure can be followed for the ω-region equation.

Returning to Eqs. (8.183) and (8.184), based on the length scale constraints $L\gg(l_\gamma,l_\omega)$, and supposing the deviation problem to be quasi-static, the simplified deviation problem takes the form

$$\mathbf{v}_\gamma.\nabla\tilde{c}_{A\gamma}+\tilde{\mathbf{v}}_\gamma.\nabla\langle c_{A\gamma}\rangle^\gamma=\nabla.\left(D_{A\alpha}\nabla\tilde{c}_{A\gamma}\right)-\frac{\dot{m}_\gamma}{\varepsilon_\gamma^2\rho_\alpha}\langle c_{A\gamma}\rangle^\gamma-\sum_{i=\omega,\kappa}\frac{1}{V_\gamma}\int_{A_{\gamma i}}\mathbf{n}_{\gamma i}.\left[\left(\mathbf{w}_{\gamma i}-\mathbf{v}_\gamma\right)\tilde{c}_{A\gamma}+D_{A\alpha}\nabla\tilde{c}_{A\gamma}\right]dA \quad \text{in the } \gamma\text{-phase} \quad (8.188)$$

$$\mathbf{v}_\omega.\nabla\tilde{c}_{A\omega}+\tilde{\mathbf{v}}_\omega.\nabla\langle c_{A\omega}\rangle^\omega=\nabla.\left(\mathbf{D}^{\text{II}}_{A\omega}.\nabla\tilde{c}_{A\omega}\right)-\frac{\dot{m}_\omega}{\varepsilon_\omega^2\rho_\alpha}\langle c_{A\omega}\rangle^\omega$$
$$-\sum_{i=\gamma,\kappa}\frac{1}{V_\omega}\int_{A_{\omega i}}\mathbf{n}_{\omega i}.\left[\left(\varepsilon_{\text{III}}\mathbf{w}_{\omega i}-\mathbf{v}_\omega\right)\tilde{c}_{A\omega}+\mathbf{D}^{\text{II}}_{A\omega}.\nabla\tilde{c}_{A\omega}\right]dA-\varepsilon_\sigma\frac{k_A}{\alpha_0 K_A}\tilde{c}_{A\omega} \quad \text{in the } \omega\text{-region} \quad (8.189)$$

$$-\mathbf{n}_{\gamma\kappa}.\left(D_{A\alpha}\nabla\tilde{c}_{A\gamma}\right)=\mathbf{n}_{\gamma\kappa}.\left(D_{A\alpha}\nabla\langle c_{A\gamma}\rangle^\gamma\right) \quad \text{at } A_{\gamma\kappa} \quad (8.190)$$

$$-\mathbf{n}_{\omega\kappa}.\left(\mathbf{D}^{\text{II}}_{A\omega}.\nabla\tilde{c}_{A\omega}\right)=\mathbf{n}_{\omega\kappa}.\left(\mathbf{D}^{\text{II}}_{A\omega}.\nabla\langle c_{A\omega}\rangle^\omega\right) \quad \text{at } A_{\omega\kappa} \quad (8.191)$$

$$\tilde{c}_{A\gamma}=\tilde{c}_{A\omega}-\left(\langle c_{A\gamma}\rangle^\gamma-\langle c_{A\omega}\rangle^\omega\right) \quad \text{at } A_{\gamma\omega} \quad (8.192)$$

$$-\mathbf{n}_{\gamma\omega}.\left(D_{A\alpha}\nabla\tilde{c}_{A\gamma}+D_{A\alpha}\nabla\langle c_{A\gamma}\rangle^\gamma\right)=-\mathbf{n}_{\gamma\omega}.\left(\mathbf{D}^{\text{II}}_{A\omega}.\nabla\tilde{c}_{A\omega}+\mathbf{D}^{\text{II}}_{A\omega}.\nabla\langle c_{A\omega}\rangle^\omega\right) \quad \text{at } A_{\gamma\omega} \quad (8.193)$$

Note that the convective terms in Eq. (8.193) are discarded due to the continuity of the concentration and velocity at $A_{\gamma\omega}$.

In the system described above, the mass exchange rates $\dot{m}_\gamma$ and $\dot{m}_\omega$ appear in the deviation problem. They represent, through Eqs. (8.23) and (8.24), the contribution of tissue production to the deviation of the concentrations. However, retaining this terms would necessitate to solve the closure problem in its transient form. This is a difficulty that has not been settled yet, and that is out of the scope of this study. Therefore, it will be assumed that the mass exchange rates do not influence the deviation problem. Note that this does not mean that the macroscopic problem will be independent of the mass exchange rates, as it will be seen lower.

Three source terms are present in the deviation problem Eqs. (8.188) to (8.193), indicating that the deviations can be link to the averages quantities as

$$\tilde{c}_{A\gamma} = \mathbf{d}_{\gamma\gamma}.\nabla\langle c_{A\gamma}\rangle^\gamma + \mathbf{d}_{\gamma\omega}.\nabla\langle c_{A\omega}\rangle^\omega + s_\gamma\left(\langle c_{A\gamma}\rangle^\gamma - \langle c_{A\omega}\rangle^\omega\right) \tag{8.194}$$

$$\tilde{c}_{A\omega} = \mathbf{d}_{\omega\gamma}.\nabla\langle c_{A\gamma}\rangle^\gamma + \mathbf{d}_{\omega\omega}.\nabla\langle c_{A\omega}\rangle^\omega + s_\omega\left(\langle c_{A\gamma}\rangle^\gamma - \langle c_{A\omega}\rangle^\omega\right) \tag{8.195}$$

where the closure variables $\mathbf{d}_{ij}$ are mapping vectors from the region j to the region i, and s_i are scalars ($i, j = \gamma, \omega$). Introducing this representations of the deviations into the macroscopic equations, the *closed mass transport equations* at the bioreactor scale is obtained.

$$\begin{aligned}\frac{\partial\left(\varepsilon_\gamma\langle c_{A\gamma}\rangle^\gamma\right)}{\partial t} + \nabla.\left(\varepsilon_\gamma\langle\mathbf{v}_\gamma\rangle^\gamma\langle c_{A\gamma}\rangle^\gamma\right) = \\ \nabla.\left(\mathbf{D}^{\mathrm{I}}_{\gamma\gamma}.\nabla\langle c_{A\gamma}\rangle^\gamma\right) + \nabla.\left(\mathbf{D}^{\mathrm{I}}_{\gamma\omega}.\nabla\langle c_{A\omega}\rangle^\omega\right) + \nabla.\left(\mathbf{d}^{\mathrm{I}}_\gamma\left(\langle c_{A\gamma}\rangle^\gamma - \langle c_{A\omega}\rangle^\omega\right)\right) \\ + \mathbf{u}^{\mathrm{I}}_{\gamma\gamma}.\nabla\langle c_{A\gamma}\rangle^\gamma + \mathbf{u}^{\mathrm{I}}_{\gamma\omega}.\nabla\langle c_{A\omega}\rangle^\omega + \alpha^{\mathrm{I}}_\gamma\left(\langle c_{A\gamma}\rangle^\gamma - \langle c_{A\omega}\rangle^\omega\right) + \frac{\dot{m}_\gamma}{\rho_\alpha}\langle c_{A\gamma}\rangle^\gamma\end{aligned} \tag{8.196}$$

$$\begin{aligned}\frac{\partial\left(\varepsilon_{\mathrm{III}}\varepsilon_\omega\langle c_{A\omega}\rangle^\omega\right)}{\partial t} + \nabla.\left(\varepsilon_\omega\langle\mathbf{v}_\omega\rangle^\omega\langle c_{A\omega}\rangle^\omega\right) = \\ \nabla.\left(\mathbf{D}^{\mathrm{I}}_{\omega\gamma}.\nabla\langle c_{A\gamma}\rangle^\gamma\right) + \nabla.\left(\mathbf{D}^{\mathrm{I}}_{\omega\omega}.\nabla\langle c_{A\omega}\rangle^\omega\right) + \nabla.\left(\mathbf{d}^{\mathrm{I}}_\omega\left(\langle c_{A\gamma}\rangle^\gamma - \langle c_{A\omega}\rangle^\omega\right)\right) \\ + \mathbf{u}^{\mathrm{I}}_{\omega\gamma}.\nabla\langle c_{A\gamma}\rangle^\gamma + \mathbf{u}^{\mathrm{I}}_{\omega\omega}.\nabla\langle c_{A\omega}\rangle^\omega + \alpha^{\mathrm{I}}_\omega\left(\langle c_{A\gamma}\rangle^\gamma - \langle c_{A\omega}\rangle^\omega\right) + \frac{\dot{m}_\omega}{\rho_\alpha}\langle c_{A\omega}\rangle^\omega - \varepsilon_\omega\varepsilon_\sigma\frac{k_A}{\alpha_0 K_A}\langle c_{A\omega}\rangle^\omega\end{aligned} \tag{8.197}$$

Where all the tissue scale variables are included within the effective parameters, defined as

$$\mathbf{D}^{\mathrm{I}}_{\gamma\gamma} = \varepsilon_\gamma\left[D_{A\alpha}\left(\mathbf{I} + \langle\nabla\mathbf{d}_{\gamma\gamma}\rangle^\gamma\right) - \langle\tilde{\mathbf{v}}_\gamma\mathbf{d}_{\gamma\gamma}\rangle^\gamma\right] \tag{8.198}$$

$$\mathbf{D}^{\mathrm{I}}_{\gamma\omega} = \varepsilon_\gamma\left[D_{A\alpha}\langle\nabla\mathbf{d}_{\gamma\omega}\rangle^\gamma - \langle\tilde{\mathbf{v}}_\gamma\mathbf{d}_{\gamma\omega}\rangle^\gamma\right] \tag{8.199}$$

$$\mathbf{d}^{\mathrm{I}}_\gamma = \varepsilon_\gamma\left[D_{A\alpha}\langle\nabla s_\gamma\rangle^\gamma - \langle\tilde{\mathbf{v}}_\gamma s_\gamma\rangle^\gamma\right] \tag{8.200}$$

$$\mathbf{u}^{\mathrm{I}}_{\gamma\gamma} = \sum_{i=\omega,\kappa}\frac{1}{\mathcal{V}_{\mathrm{II}}}\int_{A_{\gamma i}}\mathbf{n}_{\gamma i}.\left[\left(\mathbf{w}_{\gamma i} - \mathbf{v}_\gamma\right)\mathbf{d}_{\gamma\gamma} + D_{A\alpha}\nabla\mathbf{d}_{\gamma\gamma}\right]dA \tag{8.201}$$

$$\mathbf{u}^{\mathrm{I}}_{\gamma\omega} = \frac{1}{\mathcal{V}_{\mathrm{II}}}\int_{A_{\gamma\omega}}\mathbf{n}_{\gamma\omega}.\left[\left(\mathbf{w}_{\gamma\omega} - \mathbf{v}_\gamma\right)\mathbf{d}_{\gamma\omega} + D_{A\alpha}\nabla\mathbf{d}_{\gamma\omega}\right]dA \tag{8.202}$$

$$\alpha^{\mathrm{I}}_\gamma = \frac{1}{\mathcal{V}_{\mathrm{II}}}\int_{A_{\gamma\omega}}\mathbf{n}_{\gamma\omega}.\left[\left(\mathbf{w}_{\gamma\omega} - \mathbf{v}_\gamma\right)s_\gamma + D_{A\alpha}\nabla s_\gamma\right]dA \tag{8.203}$$

and

$$\mathbf{D}^{\mathrm{I}}_{\omega\gamma} = \varepsilon_\omega \left[\mathbf{D}^{\mathrm{II}}_{A\omega}.\langle\nabla\mathbf{d}_{\omega\gamma}\rangle^\omega - \langle\tilde{\mathbf{v}}_\omega\mathbf{d}_{\omega\gamma}\rangle^\omega\right] \tag{8.204}$$

$$\mathbf{D}^{\mathrm{I}}_{\omega\omega} = \varepsilon_\omega \left[\mathbf{D}^{\mathrm{II}}_{A\omega}.\left(\mathbf{I} + \langle\nabla\mathbf{d}_{\omega\omega}\rangle^\omega\right) - \langle\tilde{\mathbf{v}}_\omega\mathbf{d}_{\omega\omega}\rangle^\omega\right] \tag{8.205}$$

$$\mathbf{d}^{\mathrm{I}}_{\omega} = \varepsilon_\omega \left[\mathbf{D}^{\mathrm{II}}_{A\omega}.\langle\nabla s_\omega\rangle^\omega - \langle\tilde{\mathbf{v}}_\omega s_\omega\rangle^\omega\right] \tag{8.206}$$

$$\mathbf{u}^{\mathrm{I}}_{\omega\gamma} = \frac{1}{\mathcal{V}_{\mathrm{II}}}\int_{A_{\omega\gamma}} \mathbf{n}_{\omega\gamma}.\left[\left(\varepsilon_{\mathrm{III}}\mathbf{w}_{\omega\gamma} - \mathbf{v}_\omega\right)\mathbf{d}_{\omega\gamma} + \mathbf{D}^{\mathrm{II}}_{A\omega}.\nabla\mathbf{d}_{\omega\gamma}\right] dA \tag{8.207}$$

$$\mathbf{u}^{\mathrm{I}}_{\omega\omega} = \sum_{i=\gamma,\kappa}\frac{1}{\mathcal{V}_{\mathrm{II}}}\int_{A_{\omega i}} \mathbf{n}_{\omega i}.\left[\left(\varepsilon_{\mathrm{III}}\mathbf{w}_{\omega i} - \mathbf{v}_\omega\right)\mathbf{d}_{\omega\omega} + \mathbf{D}^{\mathrm{II}}_{A\omega}.\nabla\mathbf{d}_{\omega\omega}\right] dA \tag{8.208}$$

$$\alpha^{\mathrm{I}}_{\omega} = \frac{1}{\mathcal{V}_{\mathrm{II}}}\int_{A_{\omega\gamma}} \mathbf{n}_{\omega\gamma}.\left[\left(\varepsilon_{\mathrm{III}}\mathbf{w}_{\omega\gamma} - \mathbf{v}_\omega\right)s_\omega + \mathbf{D}^{\mathrm{II}}_{A\omega}.\nabla s_\omega\right] dA \tag{8.209}$$

In the closed macroscopic equations, the mass exchange rates have been introduced by making use of Eqs. (8.25) and (8.26). Moreover, in Eq. (8.197), it has been supposed that ρ_ω is equivalent to $\varepsilon_{\mathrm{III}}\rho_\alpha$. This hypothesis is not a strong assumption (see Eqs. (8.4) and (8.5)), and is consistent with the development in Sec. 7.1.

Compared to the averaged equation developed under the hypothesis of local mass equilibrium Eq. (7.95), the above macroscopic equations present several additional terms and effective properties. First, coupling diffusion-dispersion tensors $\mathbf{D}^{\mathrm{I}}_{ij}$ represent the influence of the diffusive flux in the j-region, on the transport in the i-region. Secondly, terms involving velocity like vectors $\mathbf{d}^{\mathrm{I}}_i$ and $\mathbf{u}^{\mathrm{I}}_{ij}$, act as non-conventional convection in the macroscopic equations. Also these terms are usually neglected at high Péclet numbers [Quintard & Whitaker, 1994a], their importance in the macroscopic mass transport for a given geometry remain to be evaluated. Thirdly, interfacial mass transfer is taken into account through the terms involving the α^{I}_i. Finally, terms involving the mass exchange rates $\dot{m}_i$ represent the influence of tissue growth on the mass transport process. The values of $\dot{m}_\gamma$ and $\dot{m}_\omega$ are provided by Eqs. (8.106) and (8.107) respectively, through the solution of the momentum transport closure problems.

The presence of all these additional effective parameters, is supposed to improve the representation of mass transport at the bioreactor scale, compared to more classical models encountered in the bio-engineering literature. The counterpart is that all the effective parameters should be computed for a given geometry, and for a given velocity field. This can be done by solving the closure problems related to the six closure variables.

Problem I (in $\nabla\langle c_{A\gamma}\rangle^\gamma$) :

$$\mathbf{v}_\gamma.\nabla\mathbf{d}_{\gamma\gamma} + \tilde{\mathbf{v}}_\gamma = \nabla.\left(D_{A\alpha}\nabla\mathbf{d}_{\gamma\gamma}\right) - \varepsilon_\gamma^{-1}\mathbf{u}^{\mathrm{I}}_{\gamma\gamma} \quad \text{in the } \gamma\text{-phase} \tag{8.210}$$

$$\mathbf{v}_\omega.\nabla\mathbf{d}_{\omega\gamma} = \nabla.\left(\mathbf{D}^{\mathrm{II}}_{A\omega}.\nabla\mathbf{d}_{\omega\gamma}\right) - \varepsilon_\omega^{-1}\mathbf{u}^{\mathrm{I}}_{\omega\gamma} - \varepsilon_\sigma\frac{k_A}{\alpha_0 K_A}\mathbf{d}_{\omega\gamma} \quad \text{in the } \omega\text{-region} \tag{8.211}$$

$$-\mathbf{n}_{\gamma\kappa}.\left(D_{A\alpha}\nabla\mathbf{d}_{\gamma\gamma}\right) = \mathbf{n}_{\gamma\kappa}.\left(D_{A\alpha}\mathbf{I}\right) \qquad \text{at } A_{\gamma\kappa} \tag{8.212}$$

$$-\mathbf{n}_{\omega\kappa}.\left(\mathbf{D}^{\mathrm{II}}_{A\omega}.\nabla\mathbf{d}_{\omega\gamma}\right) = 0 \qquad \text{at } A_{\omega\kappa} \tag{8.213}$$

$$\mathbf{d}_{\gamma\gamma} = \mathbf{d}_{\omega\gamma} \qquad \text{at } A_{\gamma\omega} \tag{8.214}$$

$$-\mathbf{n}_{\gamma\omega}.\left(D_{A\alpha}\nabla\mathbf{d}_{\gamma\gamma}\right)-\mathbf{n}_{\gamma\omega}.\left(D_{A\alpha}\mathbf{I}\right)=-\mathbf{n}_{\gamma\omega}.\left(\mathbf{D}^{\mathrm{II}}_{A\omega}.\nabla\mathbf{d}_{\omega\gamma}\right)\qquad\text{at } A_{\gamma\omega}\tag{8.215}$$

$$\mathbf{d}_{\gamma\gamma}(\mathbf{x}+l_i)=\mathbf{d}_{\gamma\gamma}(\mathbf{x})\qquad\mathbf{d}_{\omega\gamma}(\mathbf{x}+l_i)=\mathbf{d}_{\omega\gamma}(\mathbf{x})\qquad i=1,2,3\tag{8.216}$$

$$\langle\mathbf{d}_{\gamma\gamma}\rangle^{\gamma}=0\qquad\langle\mathbf{d}_{\omega\gamma}\rangle^{\omega}=0\tag{8.217}$$

Problem II (in $\nabla\langle c_{A\gamma}\rangle^{\gamma}$) :

$$\mathbf{v}_{\gamma}.\nabla\mathbf{d}_{\gamma\omega}=\nabla.\left(D_{A\alpha}\nabla\mathbf{d}_{\gamma\omega}\right)-\varepsilon_{\gamma}^{-1}\mathbf{u}^{\mathrm{I}}_{\gamma\omega}\quad\text{in the }\gamma\text{-phase}\tag{8.218}$$

$$\mathbf{v}_{\omega}.\nabla\mathbf{d}_{\omega\omega}+\tilde{\mathbf{v}}_{\omega}=\nabla.\left(\mathbf{D}^{\mathrm{II}}_{A\omega}.\nabla\mathbf{d}_{\omega\omega}\right)-\varepsilon_{\omega}^{-1}\mathbf{u}^{\mathrm{I}}_{\omega\omega}-\varepsilon_{\sigma}\frac{k_A}{\alpha_0 K_A}\mathbf{d}_{\omega\omega}\quad\text{in the }\omega\text{-region}\tag{8.219}$$

$$-\mathbf{n}_{\gamma\kappa}.\left(D_{A\alpha}\nabla\mathbf{d}_{\gamma\omega}\right)=0\qquad\text{at } A_{\gamma\kappa}\tag{8.220}$$

$$-\mathbf{n}_{\omega\kappa}.\left(\mathbf{D}^{\mathrm{II}}_{A\omega}.\nabla\mathbf{d}_{\omega\omega}\right)=\mathbf{n}_{\omega\kappa}.\mathbf{D}^{\mathrm{II}}_{A\omega}\qquad\text{at } A_{\omega\kappa}\tag{8.221}$$

$$\mathbf{d}_{\gamma\omega}=\mathbf{d}_{\omega\omega}\qquad\text{at } A_{\gamma\omega}\tag{8.222}$$

$$-\mathbf{n}_{\gamma\omega}.\left(D_{A\alpha}\nabla\mathbf{d}_{\gamma\omega}\right)=-\mathbf{n}_{\gamma\omega}.\left(\mathbf{D}^{\mathrm{II}}_{A\omega}.\nabla\mathbf{d}_{\omega\omega}\right)-\mathbf{n}_{\gamma\omega}.\mathbf{D}^{\mathrm{II}}_{A\omega}\qquad\text{at } A_{\gamma\omega}\tag{8.223}$$

$$\mathbf{d}_{\gamma\omega}(\mathbf{x}+l_i)=\mathbf{d}_{\gamma\omega}(\mathbf{x})\qquad\mathbf{d}_{\omega\omega}(\mathbf{x}+l_i)=\mathbf{d}_{\omega\omega}(\mathbf{x})\qquad i=1,2,3\tag{8.224}$$

$$\langle\mathbf{d}_{\gamma\omega}\rangle^{\gamma}=0\qquad\langle\mathbf{d}_{\omega\omega}\rangle^{\omega}=0\tag{8.225}$$

Problem III (in $\langle c_{A\gamma}\rangle^{\gamma}-\langle c_{A\omega}\rangle^{\omega}$) :

$$\mathbf{v}_{\gamma}.\nabla s_{\gamma}=\nabla.\left(D_{A\alpha}\nabla s_{\gamma}\right)-\varepsilon_{\gamma}^{-1}\alpha^{\mathrm{I}}_{\gamma}\quad\text{in the }\gamma\text{-phase}\tag{8.226}$$

$$\mathbf{v}_{\omega}.\nabla s_{\omega}=\nabla.\left(\mathbf{D}^{\mathrm{II}}_{A\omega}.\nabla s_{\omega}\right)-\varepsilon_{\omega}^{-1}\alpha^{\mathrm{I}}_{\omega}-\varepsilon_{\sigma}\frac{k_A}{\alpha_0 K_A}s_{\omega}\quad\text{in the }\omega\text{-region}\tag{8.227}$$

$$-\mathbf{n}_{\gamma\kappa}.\left(D_{A\alpha}\nabla s_{\gamma}\right)=0\qquad\text{at } A_{\gamma\kappa}\tag{8.228}$$

$$-\mathbf{n}_{\omega\kappa}.\left(\mathbf{D}^{\mathrm{II}}_{A\omega}.\nabla s_{\omega}\right)=0\qquad\text{at } A_{\omega\kappa}\tag{8.229}$$

$$s_{\gamma}=s_{\omega}-1\qquad\text{at } A_{\gamma\omega}\tag{8.230}$$

$$-\mathbf{n}_{\gamma\omega}.\left(D_{A\alpha}\nabla s_{\gamma}\right)=-\mathbf{n}_{\gamma\omega}.\left(\mathbf{D}^{\mathrm{II}}_{A\omega}.\nabla s_{\omega}\right)\tag{8.231}$$

$$s_{\gamma}(\mathbf{x}+l_i)=s_{\gamma}(\mathbf{x})\qquad s_{\omega}(\mathbf{x}+l_i)=s_{\omega}(\mathbf{x})\qquad i=1,2,3\tag{8.232}$$

$$\langle s_{\gamma}\rangle^{\gamma}=0\qquad\langle s_{\omega}\rangle^{\omega}=0\tag{8.233}$$

Keeping in mind that the fluid velocity satisfies a continuity condition at $A_{\gamma\omega}$, and a no slip condition at the interfaces with the solid, the following relations are obtained

$$\mathbf{u}^{\mathrm{I}}_{\gamma\gamma}=-\mathbf{u}^{\mathrm{I}}_{\omega\gamma}\tag{8.234}$$

$$\mathbf{u}^{\mathrm{I}}_{\gamma\omega}=-\mathbf{u}^{\mathrm{I}}_{\omega\omega}\tag{8.235}$$

$$\alpha^{\mathrm{I}}_{\gamma}=-\alpha^{\mathrm{I}}_{\omega}\tag{8.236}$$

It should be noted that, in the development of the above closure problems, the coupling between the closure variables associated with different orders of derivative has been neglected. Although this is an usual simplification in the context of the volume averaging method [Ahmadi et al., 1998; Cherblanc et al., 2003], its consequences regarding mass transport should be examined more closely in further work [Davit et al., 2010].

The solution of the three closure problems, allows the evaluation of the 12 effective parameters. The resolution of this problem, and the resulting effective parameters are presented below.

8.3.2 Computation of the effective parameters

A change of variable has been proposed by Cherblanc et al. [2003] to transform the three integro-differential problem, into five differential problems. Yet, given the macroscopic nature of the source terms, we choose to solve the closure problem in the current form. In this section, we wish to study the influence of the flow intensity and of the tissue volume fraction on the 12 effective parameters. In the following results, the volume fraction of the solid, the tissue permeability and the ratio between the diffusive coefficient have constant values of $\varepsilon_\kappa = 0.30$, $K^{\mathrm{II}}_\omega / l^2_\omega = 10^{-4}$, $D^{\mathrm{II}}_{A\omega} / D_{A\alpha} = 0.5$. Moreover, as a first hypothesis, the reaction is supposed to not influence the closure problem, so the Damhköker number ($\mathrm{Da}_\omega = k_A \varepsilon_\sigma l^2_\omega / (\alpha_0 K_A D_{A\omega})$) is null. Note that this last assumption is not a limitation of the model, and further computational study should include the effects of the reaction.

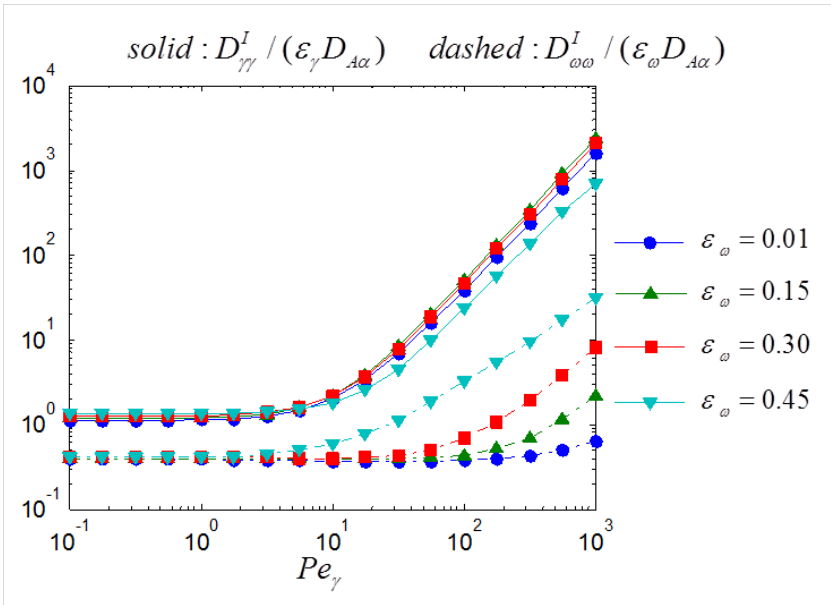

Figure 8.6 – Main longitudinal diffusion-dispersion coefficients ($\varepsilon_\kappa = 0.30$, $K^{\mathrm{II}}_\omega / l^2_\omega = 10^{-4}$, $D^{\mathrm{II}}_{A\omega} / D_{A\alpha} = 0.5$, $Da = 0$)

The main bioreactor diffusion-dispersion tensors are plotted in Fig. 8.6 as a function of the Péclet number ($\mathrm{Pe}_\gamma = \|v_\gamma\| l_\gamma / D_{A\alpha}$), for different values of the tissue volume fraction. For both coefficients, a classical diffusive regime is observed at low values of the Péclet number, while dispersion occurs at larger values. Only the dispersive part of the ω-region coefficient is significantly influenced by the tissue volume fraction.

The coupling effective diffusion-dispersion coefficients are shown in Fig. 8.7. We numerically find that the two coupling tensors are equal in the studied range of parameters. For values of the Péclet number lower than 50, $D^{\mathrm{I}}_{\gamma\omega}$ and $D^{\mathrm{I}}_{\omega\gamma}$ are null, while for higher values, dispersion effects influences the coupling coefficient. The interfacial mass transfer coefficients α^{I}_i depicted in Fig. 8.7, are shown to have values of the order of 10^1, slightly increasing as the values of the Péclet number gets larger. A higher sensitivity to the Péclet number is found for a large tissue volume fraction ε_ω.

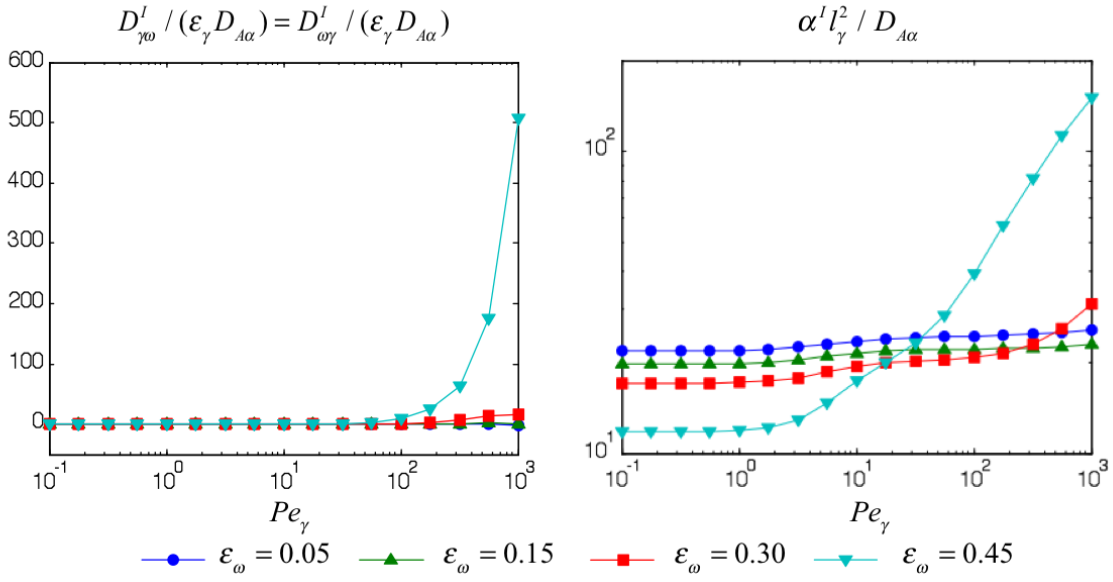

Figure 8.7 – Coupling longitudinal diffusion-dispersion coefficients ($\varepsilon_\kappa = 0.30$, $K^{\mathrm{II}}_\omega / l^2_\omega = 10^{-4}$, $D^{\mathrm{II}}_{A\omega} / D_{A\alpha} = 0.5$, $Da = 0$)

The velocity-like effective coefficients $\mathbf{d}^{\mathrm{I}}_i$, $\mathbf{u}^{\mathrm{I}}_{ij}$ have been computed in the same conditions, and have shown to follow a monotonic behavior in regard to the tissue volume fraction (Figs. 8.8 and 8.9). Moreover, they are of the same order of magnitude as the coupling tensors. It should be noted that the coefficients related to the ω-region concentrations are extremely sensitive to the tissue permeability K^{II}_ω. Further numerical investigations are currently in progress, in order to evaluate the respective influence of the effective terms. However, this necessitates to also solve the macroscopic model Eqs. (8.196) and (8.197), such as the whole terms including the various effective parameters can be compared. Additional numerical investigation is needed to compute the influence of the reactive term on the effective variables and on the macroscopic model.

Momentum and mass transport have been upscaled all along Part II, from the ECM (level IV) to the bioreactor scale (level I). It has been shown that the transport properties at the lower scales, can influence greatly the higher scales effective parameters. The result of the successive upscalings is a non-equilibrium multiple equation model for momentum and mass transport at the bioreactor scale (four macroscopic equations for momentum transport, and two for mass transport). Several effective parameters have been identified, and can be computed through the resolution of a series of closure problems. In the remaining part of the thesis, a macroscopic resolution of the model is proposed, where a tissue production kinetic is introduced. But before to do that, cell and tissue growth are studied in the perfusion bioreactor from an experimental point of view.

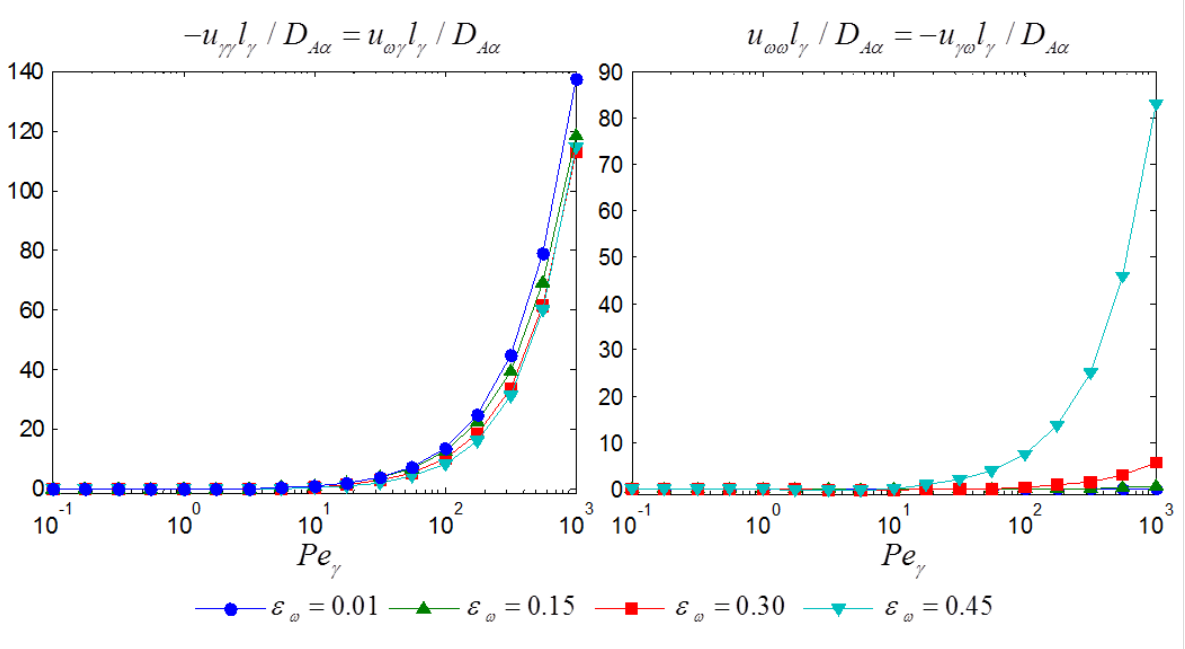

Figure 8.8 – Velocity-like coefficients ($\varepsilon_\kappa = 0.30$, $K_\omega^{\mathrm{II}}/l_\omega^2 = 10^{-4}$, $D_{A\omega}^{\mathrm{II}}/D_{A\alpha} = 0.5$, $Da = 0$)

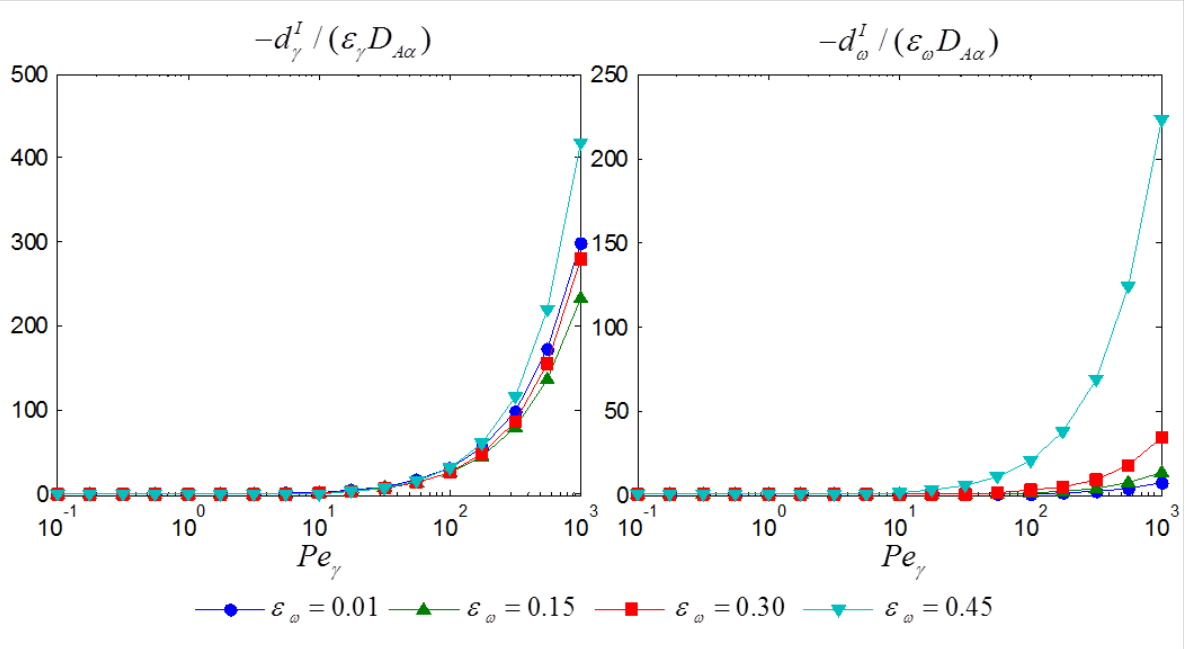

Figure 8.9 – Velocity-like coupling coefficients ($\varepsilon_\kappa = 0.30$, $K_\omega^{\mathrm{II}}/l_\omega^2 = 10^{-4}$, $D_{A\omega}^{\mathrm{II}}/D_{A\alpha} = 0.5$, $Da = 0$)

Part III

Cell Growth in a Perfusion Bioreactor : Relating Experimental and Multiscale Models

CHAPTER 9

EXPERIMENTAL MODEL OF THE PERFUSION BIOREACTOR

A VARIETY OF BIOREACTORS and their working principles has been presented in Chap. 2. Most of them have been developed in an attempt to prove the capacity of a specific design to enhance cell proliferation, differentiation and production of extracellular matrix. Yet, very few studies are devoted to quantify the spacialisation of cell proliferation within the bioreactor.

Based on the system developed in David et al. [2011], we propose in the present chapter, an experimental approach to quantify in space and time, the influence of culture medium flow rate on cell proliferation within a porous media. To that purpose, cells are cultured into a perfusion bioreactor, on a scaffold constituted of a stack of impermeable glass beads. After various time of culture, the formed constructs are fixed and embedded. Thanks to a combination of histological techniques and image analysis, the quantification of biomass production as a function of time is assessed.

9.1 Presentation of the experimental model

The double porosity bioreactor [David et al., 2011] has been designed in order to overcome limitations related to bone tissue engineering. Its principal aim is to produce osteoconductive substitutes in clinically relevant volumes. The main characteristics and results related to this system are summarized in Sec. 2.3. Briefly, a perfusion bioreactor has been designed, where micro-porous coral scaffolds (3mm size) are stacked in a perfusion chamber. Mouse embryos cells (C3H10T1/2-GFP) are cultured in the bioreactor up to 21 days. Cell proliferation is first quantified for different time of culture, then histological analysis are performed to asses the presence of cells in different regions of the bioreactor.

One of the main obstacle of evaluating the influence of perfusion on cell proliferation in such a bioreactor, is the complicated geometry in which the cells evolve. Even though experimental quantification of cell proliferation around and inside the coral cubes can be

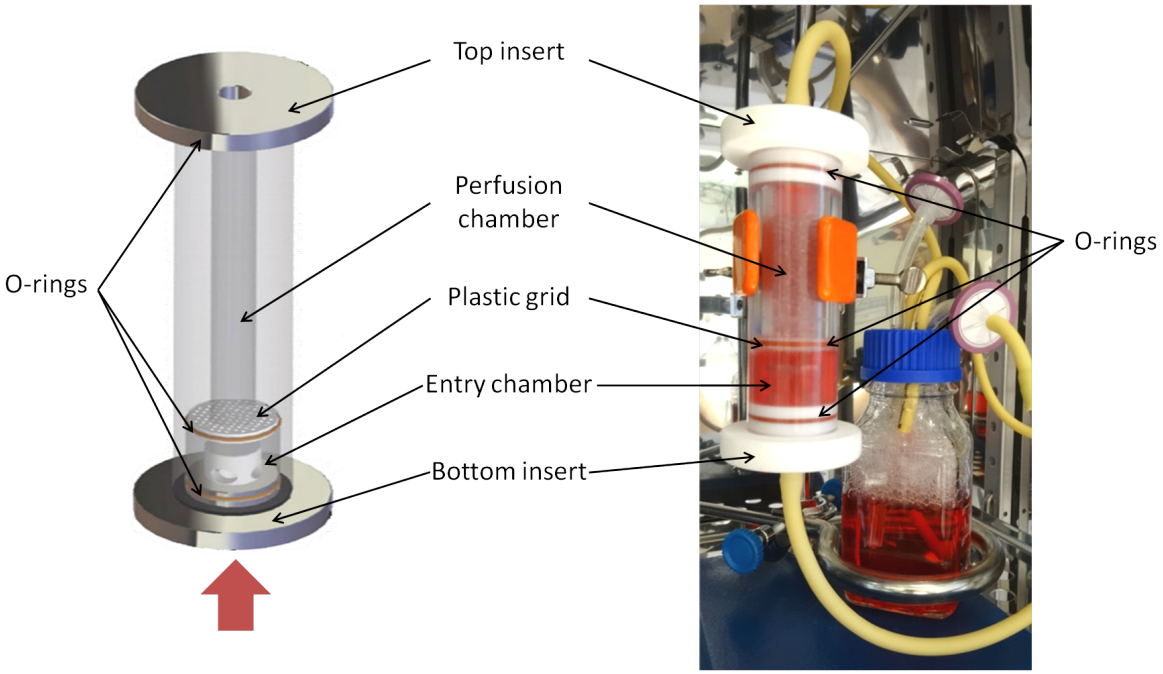

Figure 9.1 – The different components of the bioreactor

performed (but to what cost!), the complexity of the physical processes in such environment limits the relevance of the possible interpretations. Moreover, if one wishes to discuss the results in regard to a mathematical model, simplification assumption are needed on both, experimental and modeling approaches.

As a first step in the study of the bioreactor presented in [David et al., 2011], we choose to simplify the double porosity (the microscopic coral cube porosity, and the macroscopic porosity made by the stack of cubes) to a simple porosity. This is done by substituting the 3mm size coral cubes by 2mm diameter glass beads. The advantages of using a stack of glass beads as the scaffold are multiple. First, porous mediums composed of spheres are well characterized in the literature in terms of architecture and transport properties [Brinkman, 1947; Zick & Homsy, 1982; Warren & Stepanek, 2008]. Second, glass in known for its excellent biocompatibility, and adherent mammalian cells attach and spread very well on glass supports. Finally, it facilitates the comparison with experimental and modeling studies on biological porous media, based on similar geomoetry [Orgogozo et al., 2009; Golfier et al., 2009; Davit et al., 2010, 2011; Wood et al., 2011]. Here, mouse fibroblast cells (NIH/3T3, ATCC) are used. This choice is motivated by their known mechanosensibility [Korin et al., 2007], rapid division time, and simple cultivation procedure. Moreover, this cell type is often used in microfluidic systems [Steward Jr. et al., 2010; Zhang et al., 2011; Topman et al., 2012], facilitating comparisons with current experiments in such conditions [Chabanon et al., 2012].

Before presenting the experimental protocols, let us describe the experimental setup. Except when stated otherwise, all the material is purchased from Dominic Dutscher. The different components of the bioreactor are represented in Fig. 9.1. They include the bioreactor

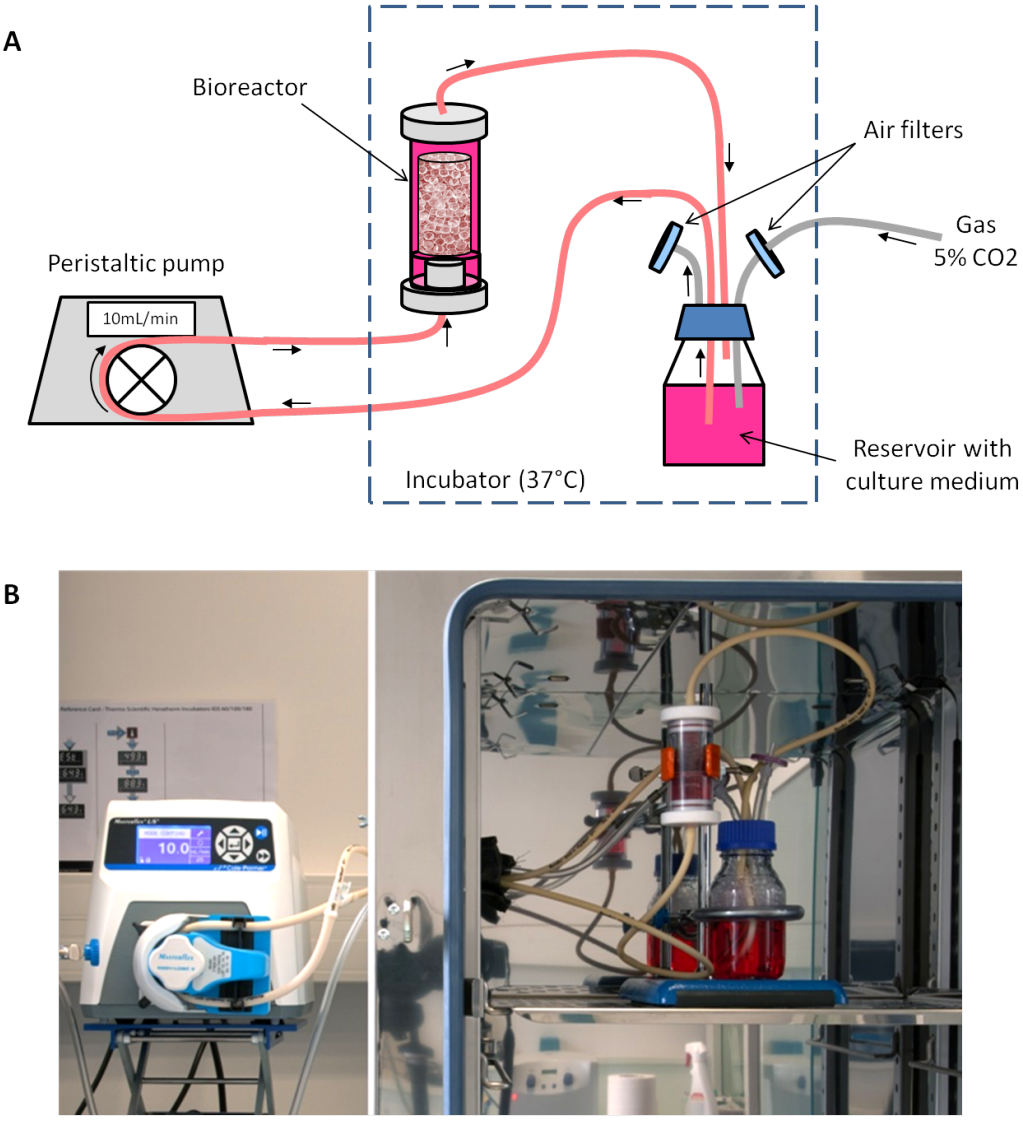

Figure 9.2 – Schematic representation (A), and photography (B) of the bioreactor experimental set up

chamber made of Polycarbonate (PC, Abaqueplast), divided by a circular plastic grid between the entry chamber (33mm length, 26mm inside diameter) and the perfusion chamber (50mm length, 14.2mm inside diameter) . This grid, also made of PC and pierced with multiple holes (1mm diameter), maintains the construct in the perfusion chamber, and helps assess a laminar flow of culture medium within the perfusion chamber. Two inserts made of Polytetrafluoroethylene (PTFE, Abaqueplast) close the chamber at the bottom and top. The different pieces are assembled tightly together thanks to silicon o-rings (Sefat, 22.1×1.6mm). In order to be able to remove the construct from the bioreactor without damaging it, a glass tube (Preciverre, 50mm length, 14mm outside diameter, 12mm inside diameter) is placed inside the perfusion chamber. The external diameter of the tube fits the internal diameter of the chamber, so all the perfusion takes place in the tube.

As shown in Fig. 9.2, culture medium flows through a closed loop from a reservoir to a persistaltic pump (Cole-Parmer, Masterflex L/S), to the bioreactor and back to the reservoir. The loop is constituted of silicon tubing (Pharm-Med, L/S16 for the main loop and L/S25 for the pump) connected to the bioreactor with screwed plastic connectors (Cole-Parmer). The culture medium is contained in a 250mL steril glass reservoir with a customized cap. The reservoir cap is pierced of four holes (5.3mm diameter), two for the culture medium silicon tubing, two for the gas tubing (Saint-Gobain, Tygon R3606). A constant supply of 5%CO_2 gas flows into the reservoir to maintain the culture medium pH. In order to keep sterile conditions, disposable air filters (30mm diameter, 0.45µm pores) are fixed with plastic luer lock (Cole-Parmer M 4.8mm) at the gas entrance and exit.

9.2 Material and methods

The experimental procedure follows three main steps. First, cells are cultured in perfusion and static conditions. Second, the samples are prepared for histological analysis, sliced and stained. Finally, an image analysis procedure allows the quantification of two indicators, the cell growth indicator (CGI), and the tissue growth indicator (TGI). In the present section, the corresponding experimental protocols are detailed.

9.2.1 Cell culture in the bioreactor

All experiments are carried in sterile conditions under a laminar flow hood. All material in contact with culture medium and cells, has been previously sterilized as follows. Except for the bioreactor chamber and grid, the whole perfusion loop is assembled, and sterilized in an autoclave (Advantage Lab AL02-01, 18min, 105°C, 220kPa). Due to the poor resistance of PC in thermal fatigue, the bioreactor chambre as well as the grid and its o-ring cannot follow standard autoclave sterilization cycles. Instead, this components are sterilized with a bleach bath of 1 hour. They are then rinsed abundantly through three successive bath in sterile distilled water. The glass tubes and glass beads are sterilized in an autoclave.

The cells used in all the experiments are fibroblasts NIH/3T3 (ATCC), routinely cultured in DMEM Glutamax (Gibco, Life Technologies) supplemented with 10% Fetal Calf Serum (Pan-Biotech) and 1% Penicillin Streptomycin (Pan-Biotech), at pH 7.4 and under standard cell culture conditions (37°C, 5% CO2). NIH/3T3 cells are passaged three times a week at 70% confluence, following standardized accepted protocols.

For each experiment, three samples are prepared, one cultured under perfusion within the bioreactor, one cultured in static conditions (static control), and one to asses the initial seeding conditions (T0 control). Three sterile plastic tubes (Falcon 15mL) are filled with 4.5mL of sterile glass beads (2mm diameter) each. Then 2.5mL of fibronectin solution is added (10µg/ml), and let 1 hour at 37°C. Then the solution is aspirated with a pipette, and 2mL of cell suspension (10^6 cell/ml) is added. The tubes are gently agitated in order to homogenized the mixture of glass beads and cells. The tubes are then let overnight in a CO_2

incubator (Termo Scientific, Series 8000DH) to allow the cells to sediment and attach to the beads.

Perfused Tube After sterilization, the bioreactor chamber is fixed to a clamp on a stand, and the grid is carefully inserted in the entry chamber, before to be abundantly rinsed with 70° ethanol. A sterile glass tube is inserted in the perfusion chamber before to be filled with the seeded glass beads prepared the day before. Then the chamber is closed by introducing the bottom and top insert, each being already connected to the reservoir cap through the tubing. The cap is mounted to a reservoir filled with 250mL culture medium (DMEM Glutamax + 10% Fetal Calf Serum +1% Penicillin Streptomycin), and the air filters are finally fixed to the air tubes. At this point, the bioreactor loop is closed and can be removed from the laminar flow hood without risks of contamination. The whole loop (seeded bioreactor, reservoir and tubing) are disposed in an incubator (Thermo Scientific, Heratherm). A hole in the side of the incubator allows a part of the tubing to be connected to the peristaltic pump located outside. This incubator does not provide a controlled CO_2 atmosphere, thus the reservoir is connected with a gas tube where a continuum flow of gas mixture at 5%CO_2 is perfused at 15mL/min. Once the set up is in place, the peristaltic pump is activated at 10mL/min, and the bioreactor is filled slowly with culture medium from bottom to top. Some delicate vibrations of the bioreactor may be needed to remove possible air bubbles trapped in the construct. Culture under perfusion are carried for 1, 2 or 3 weeks. The culture medium is changed twice a week by stopping the pump, clamping the loop so the bioreactor stays filled with culture medium, moving the entire loop under a laminar flow hood, and replacing reservoir with a new one filled with 200mL fresh culture medium. The system is then put back into the incubator, and the pump is reactivated, the whole procedure taking a couple of minute.

Static Tube For static culture, a sterile PTFE support is used to maintain vertical, a sterile glass tube in a 40mL straight container (Gosselin, TP30). The seeded glass beads are poured in the tube, and 35mL of fresh culture medium is added in the container. The container is closed, and put in a CO_2 incubator for 1, 2 or 3 weeks. The cap of the container is kept slightly open in order to allow gas exchange with the incubator atmosphere. Culture medium is changed twice a week by aspirating the old culture medium, and poring fresh one.

Tube T0 The seeded glass beads are directly poured in a glass tube. The construct is maintained in the glass tube by a pierced aluminum sheet at the bottom extremity of the tube. Then the tube is placed in a bath of formaldehyde to fix and conserve the biomass during the cultivation period of the perfused and static tubes.

At the end of the cultures, the perfused and static tubes are removed from the bioreactor and container respectively, and together with the T0 tube, they follow a series of bath in order to fix and to embed the biomass. This procedure is delicate since any movement of the beads may damage the structure of the construct. In order to facilitate the manipulations, the bottom of the tubes are covered by aluminum sheet, which are maintained with Parafilm. Small holes are produced in the aluminum sheet with a needle point, allowing the liquid of the different bath to flow through the construct. The tubes are then disposed inside 10mL syringes (Terumo) whose piston has been removed (and used as caps to close the syringes). This way, without having to manipulate the tubes, liquid can be poured by above, and the syringe can be emptied by opening the bottom exit of the syringe.

9.2.2 Histological protocol

Fixation Quickly after ending the cultures, the samples are placed into the syringes, and let in a bath of formalin (4% formaldehyde (Sigma-Aldrich) in phosphate buffered saline (Pan-Biotech)) at room temperature overnight. Formalin is a chemical fixative which allows to preserve the cells and tissue from degradation, and maintains the structure of the construct.

Dehydration The aim of histology is to solidify the studied biological sample, in order to be able to cut thin slices, and to observe the structure of the sample. This necessitates that the water contained in the biological tissue is replaced by the solidifying product. Therefore, the samples are dehydrated following a series of ethanol bath of increasing concentration :

- $1\times$15min in 70° ethanol
- $1\times$15min in 80° ethanol
- $1\times$15min in 90° ethanol
- $1\times$15min in 96° ethanol
- $3\times$15min in absolute ethanol

Embedding Once the samples are dehydrated, the embedding process can start. The Osteo-Bed Embedding kit (Sigma-Aldrich) is used here. This product has been originally developed for undecalcified bone specimens, and is also suitable for the study of soft tissue structures and immunohistochemistry. The formulation is based on methyl methacrylate (MMA), and is delivered in the form of a solution of Osteo-Bed Resin, and a catalyst powder. Two solutions are prepared from this components : the Osteo-Bed infiltration solution (1.4g of catalyst for 100mL of Osteo-Bed resin), and the Osteo-Bed embedding solution (3.5g of catalyst for 100mL of Osteo-Bed resin). The embedding procedure consists in a series of bath of this different solutions, where the time of impregnation must be adapted to the samples. Here is the protocol followed for the bioreactor constructs :

- 3 bathes of Osteo-Bed Resin solution, of 12 to 24 hours each, at room temperature
- 1 bath of Osteo-Bed infiltration solution, of 8 hours at room temperature
- 1 bath of Osteo-Bed embedding solution, of 1 week at 32°C

The Osteo-Bed solutions are photosensitive products, and all the manipulations are carried by limiting as much as possible direct light exposure. Due to the exothermic nature of the polymerization process, the last bath must be kept in a thermostatic bath at 32°C (Julabo F34-ED) to avoid the formation of bubbles.

Slicing Once the polymerization process is over, the glass tube surrounding the construct can be removed by breaking it in pieces. At this point, the construct is a polymerized cylinder of approximately 40mm length and 12mm diameter. Three marks are made at 5, 15 and 25mm from the bottom of the construct, respectively. This helps identify the bottom, middle and upper part of the bioreactor in order to relate proliferation to the position from its entrance. Using a precision sectioning saw (Buehler, IsoMet Low Speed Saw), three transverse slices are obtained at each mark, leading to a total of nine slices per construct. Between two cuts,

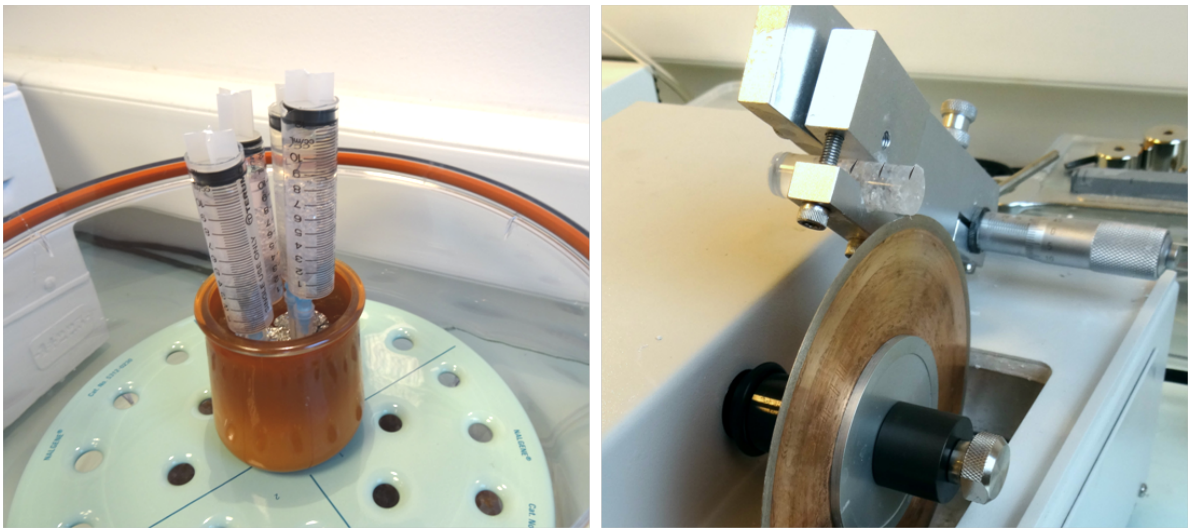

Figure 9.3 – Photography of syringes containing tubes of constructs in Osteo-Bed solution (left), and of a construct sample being sliced (right).

the edge of the sample is glued (Loctite, SuperGlue 3 Precision) to a clean microscope slide. Thanks to a micrometer gauge, the thickness of the cut slices are set to 300µm. The rotation speed is adjusted to graduation 7, and the time required to cut one slice is of the order of five minutes, depending on the wear of the blade (Buehler, IsoMet Diamond Wafering blade 5×0.014in). Once the slices are cut, the surface needs to be polished with grinding paper P4000 (Buehler, Microcut Silicon Carbide) on a rotating polisher for about 2min. At this stage, microscopic observations allows to clearly distinct the glass beads from the embedding polymer. However a staining procedure is required in order to observe the cells.

Staining A large variety of staining methods exists to study the structure of all kind of biological tissues [Bancroft & Gamble, 2008]. Here we need a reliable, rapid and simple method which is capable of staining the cells embedded in MMA polymer. Stevenel Blue has been shown to answer this prerequisites [Maniatopoulos et al., 1985], and can be prepared from solutions of methylene blue (Sigma-Aldrich, 1g/75mL) and potassium permanganate (Sigma-Aldrich, 1.5g/75mL). A glass container filled with Stevenel's blue is preheated and maintained at 60°C in a water bath. The construct slices are then immersed in the colorant solution at 60°C for 10min, then rinsed with tap water. The slices are then passed under compressed air to remove the excess of water, and let to dry at room temperature for a couple of hours, allowing the stabilization of the coloration.

9.2.3 Image analysis

The colored slices are observed with an upright optical microscope (Optika B350), equipped with a numerical camera (Optikam PRO5) and an acquisition software (Optika vision pro). In order to reconstruct numerically an entire slice of the construct, approximately twenty photos are taken for each slide (microscope parameters : objective ×4, frosted glass filter, maximum luminosity ; software parameters : exposure 0.1325, gain 1, gamma 0.32, satura-

tion 1, contrast 1, RGB 2.75 2 3). After reducing their size by 40% with the software ImageJ [Schneider et al., 2012], the photographs are numerically merged using the image processing software Adobe Photoshop CS4.

At this point, the presence of cellularized regions can be qualitatively observed for different culture time and location within the bioreactor (Fig. 9.5). Cells appear in blue, while the glass beads are recognizable by their shape and texture. Yet some quantification procedure must be established in order for the experimental approach to be useful. Therefore we will define two indicators related to cell and tissue growth. First, the number of blue pixels are supposed representative of the surface of the slide occupied by cells. Thus we define the cell growth indicator (CGI) as the ratio of the surface occupied by blue pixels to the surface of the slice. Second, it can be noted that even though all the cells are not in contact, they still form a continuous region. Although we do not have experimental proof of the presence of extracellular matrix (ECM) between the cells, we suppose the surface occupied by this continuous regions to be representative of the tissue. Based on this idea, we define a second indicator, termed as tissue growth indicator (TGI). In order to evaluate the CGI and TGI, we need to measure the total surface of the construct (S_{tot}), the surface occupied by the blue pixels (S_{pix}), and the surface occupied by the continuous blue regions (S_{reg}). With this notations, the two indicators are defined as

$$\begin{cases} \text{Cell Growth Indicator :} & CGI = S_{\text{pix}}/S_{\text{tot}} \\ \text{Tissue Growth Indicator :} & TGI = S_{\text{reg}}/S_{\text{tot}} \end{cases} \tag{9.1}$$

Additionally, the surface occupied by the glass beads (S_{beads}) will also be measured.

The photograph of each slice is processed using ImageJ software. First the surface of the total slice S_{tot} is measured, and the outside is deleted. Secondly, the glass beads are manually colored in green (RGB 0 250 0) using the circle tool. Then the color image is split in three gray scale images, one for each RGB channel. The values of the gray scales range between 1 (black) to 255 (white). Most of the background artifacts are contained in the Blue channel, while the cells appear only in the Red and Green channels. On the Blue channel, the glass beads have now a value of 255, and applying a threshold at 254 allows to isolate the surface occupied by the beads, and to measure S_{beads}. Thirdly, adding up the Red and Green channels, most of the cells appear on a white background. Some remaining artifacts may be removed by adjusting the threshold (between 200 and 220) to fit the comparison with the original colored photograph. Remaining artifacts may be removed by hands with geometrical tools, and the surface occupied by the blue pixels S_{pix} can be measured. Only the surface occupied by the continuous cell regions remains to be measured. The two images of the isolated cells, and the isolated beads are added. At this point we have a binary image where the cells and the beads are in black. Before to select the continuous blue regions, a set of criteria must be defined in order to insure reproductibility. Here we chose regions with relatively homogeneous cell distribution, and where the distance between cells is inferior to 10 cell diameters. These regions are filled in black using the geometrical tools combined with "erosion", "dilatation" and "fill holes" tools for binary images. Finally, subtracting the beads, S_{reg} can be evaluated.

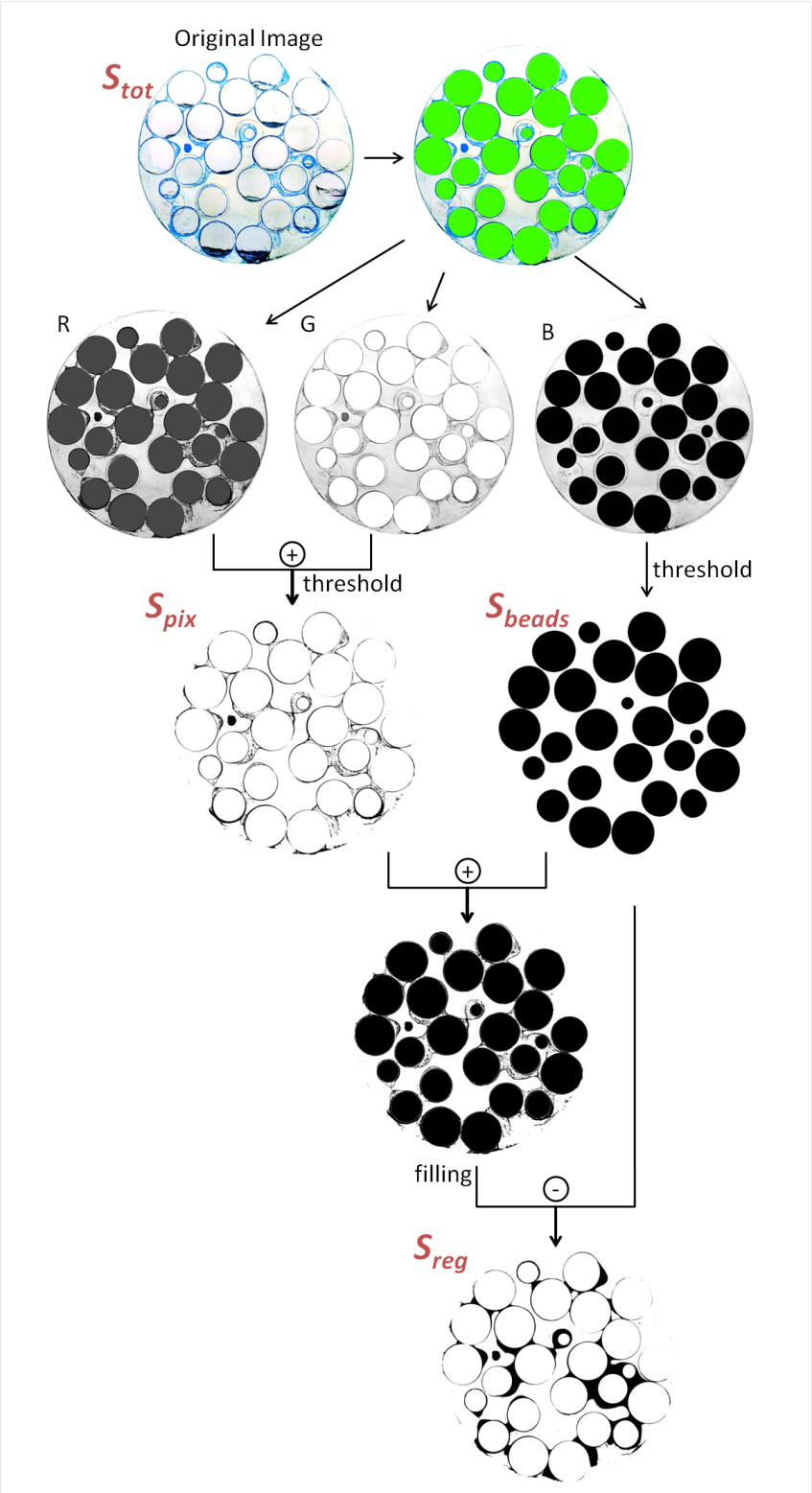

Figure 9.4 – Scheme of the image processing steps leading to the different surface measurement

9.3 Observations of cell proliferation

For each duration of culture (1, 2 and 3 weeks), three independent experiments have been carried, each experiment producing three constructs (a perfused, a static and a T0). Each of the 27 resulting constructs have been prepared following the above histology protocols, yielding to more than 200 slides to analyze.

9.3.1 Results

Representative reconstructed slices at different times of cultivation are showed in Fig. 9.5. The glass beads are recognizable by the clear circles. Their different diameters are due to the different plan of cut of the spheres. The slice taken from a T0 construct (24 hours post seeding) shows only the glass beads, with some very thin lines of blue on their surface. The thickness of this blue lines are too small to distinct attached cells from residual stain infiltrated between the glass and MMA polymer. After three weeks of culture in static conditions, no visible cell proliferation is observed compared to T0. In contrast, slices obtained from constructs perfused for 1 week, show some thicker blue lines around the beads. In some slides, small regions are uniformly colored in blue, revealing the presence of multilayered cell structures. At two and three weeks of perfusion, large continuous blue regions indicate the formation of complex three-dimensional cell structures. In perfusion culture conditions, the apparent continuity of this cell populated regions, indicates that they constitute a tissue. Although there is here a lack of experimental evidence that cells in this regions are surrounded by extracellular matrix (ECM), the term "tissue" will be used to refer to this continuous regions. When the tissue regions reach a certain thickness, a decrease in cell density is observed at their center, while denser cell layers remain close to the boundary with culture medium. At three weeks of perfusion, large strips of dense tissue appear disconnected from the beads.

In an attempt to quantify cell proliferation in perfused culture conditions, the above observations suggest that indicators based on surface measurements may be relevant. Therefore two surface fraction indicators have been defined (see Eq. (9.1)), the cell growth indicator (CGI), and the tissue growth indicator (TGI). The evolution of the CGI and TGI as a function of time is shown in Fig. 9.6. Consistently with direct observations (Fig. 9.5), constructs cultured in static conditions do not show any evolution in cell nor tissue growth indicators. On the other hand, after three weeks of perfusion, an increase of a factor 20 to 30 is observed for the two indicators, compared to initial and static constructs. The dependency in time of the CGI and TGI follows a similar non-linear behavior.

Interestingly, the two indicators appear to be sensitive to the position in the bioreactor. In order to underline this phenomena, in Fig. 9.7, the CGI and TGI are plotted as a function of the distance to the perfusion chamber entrance. At short culture times, the cell and tissue growth indicators show a slight decrease with the distance to the chamber entrance. This effect is accentuated after 2 weeks of cultivation, where the CGI and TGI are higher at 5mm than at 15 and 25mm from the entrance of the chamber. No significant difference is observed between 15 and 25mm at 2 weeks of perfusion. It has to be noted that at 3 weeks of perfusion,

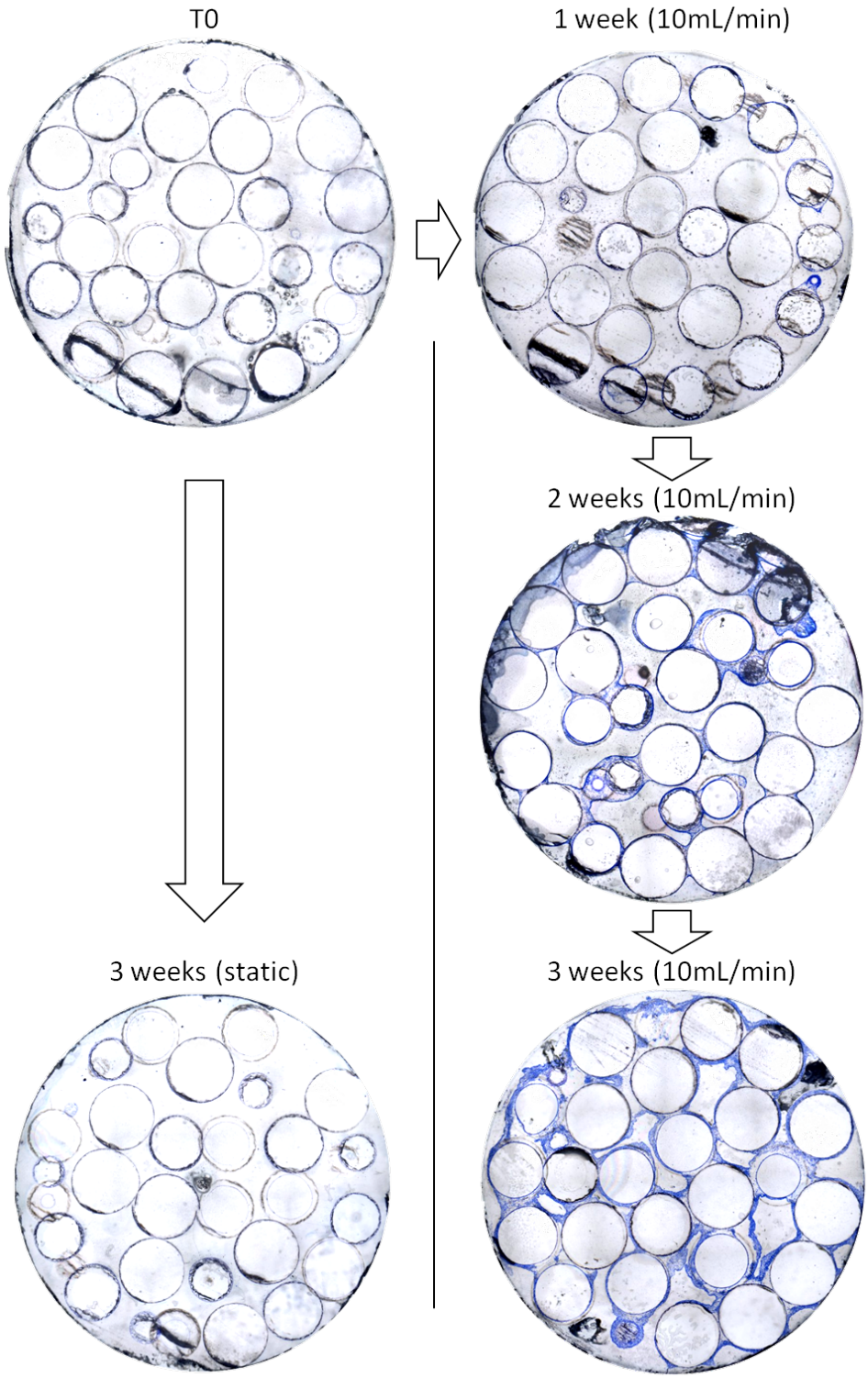

Figure 9.5 – Representative photographs of stained slices at different culture time. Cells are colored with Stevenel's Blue. All slices are taken at 15mm from the chamber entrance. (Diameter of a slice = 12mm)

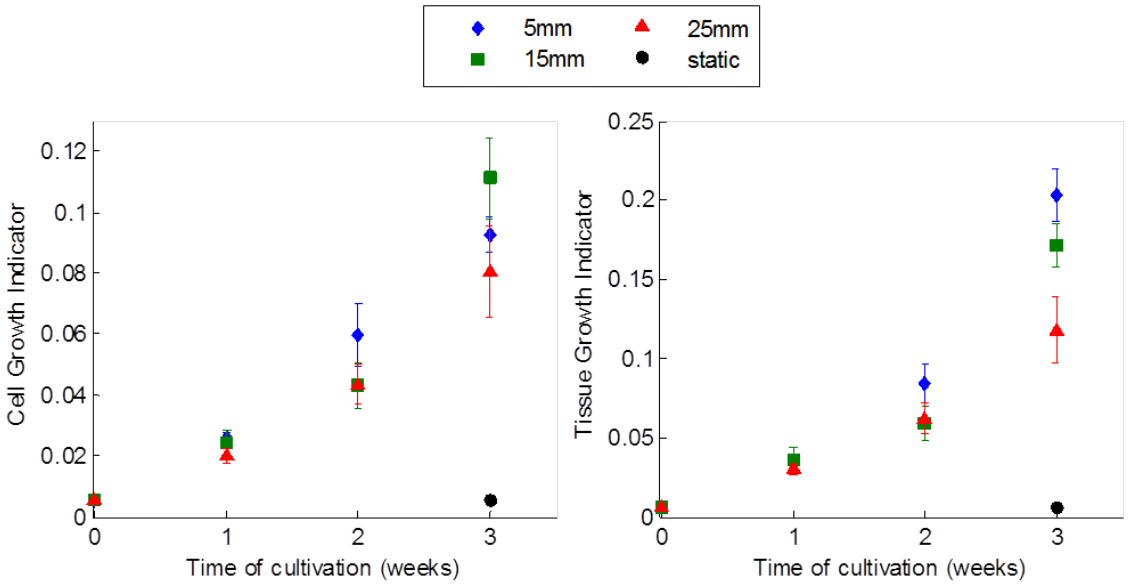

Figure 9.6 – Mean CGI (left) and TGI (right) as a function of time. Bar length represents standard deviations.

the CGI and TGI behave differently. While the TGI decreases continuously with distance to the entrance, the CGI is lower at 5mm than 15mm.

The CGI and TGI are measures related to the surface fractions of cells and tissues within a slice. Their values must be analyzed in regard to the space available for cell and tissue growth, thus the surface fraction of glass beads has to be studied. Fig. 9.8 displays the mean surface fraction of the glass beads ($S_{\text{beads}}/S_{\text{tot}}$) as a function of the position in the perfusion chamber. No significant variation of the beads surface fraction is observed between the different zones of study. The overall mean and standard deviations of the beads surface fraction are 0.55 and 0.03 respectively. This results indicate that, at 5mm and more from the bottom of the tube, the glass bead stack is homogeneous. In other words, the lower boundary does not effect significantly the arrangement of beads after 5mm.

9.3.2 Discussion

The two indicators (CGI and TGI) defined by Eq. (9.1) are surface fractions related to cell and tissue growth. Although they do not allow a quantification of the cell number nor precise tissue surface (at least not without a calibration experimental campaign), they can be used to evaluate the evolution of these parameters with time and space. The determination procedures of the CGI and TGI have specific weak points. The CGI is more sensible to variations of luminosity due to small differences in the thickness of the slices (imprecision of the saw, amount of glue). On the other side, the continuous region is not always well defined, and the determination of the TGI is more operator dependent. Yet, we expect the uncertainties related to both of this measures, to be smaller than the variability between the different samples.

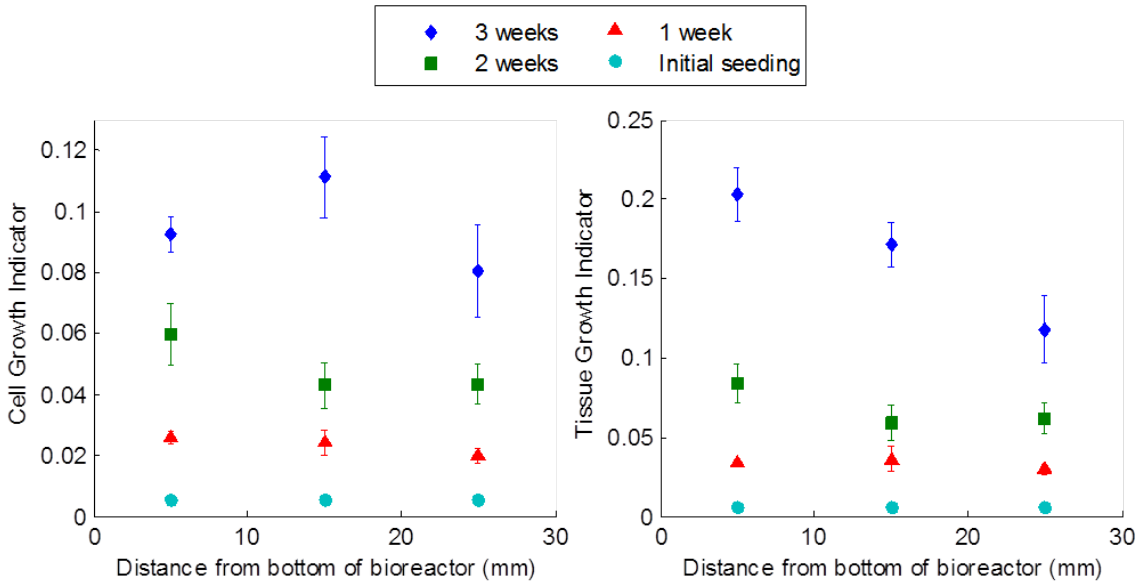

Figure 9.7 – Mean CGI (left) and TGI (right) as a function of the distance to the perfusion chamber entrance. Bar length represents standard deviations. Only perfused and T0 samples are represented here.

As indicated in Fig. 9.7, at two weeks of cultivation, both CGI and TGI are higher in the closest region to the perfusion chamber entrance. This behavior is strongly confirmed for the tissue at three weeks, where there is almost a factor 2 between the TGI at 25mm and 5mm from the entrance. Two explanations are possible, either the seeding procedure induces an initial gradient of cell density along the bioreactor, either the transport conditions in the lower part of the bioreactor are more favorable to cell and tissue growth. Although the results at T0 and 1 week tend to show an homogeneous initial distribution of cells, the determination of the CGI and TGI may not be sensitive enough to reveal variations for such small values. The influence of the seeding procedure could be tested by modifying the seeding protocol, yet for a question of time, this is let for future work. However the influence of the transport properties on cell proliferation and tissue formation, can be studied through the model built in Part II. This approach is developed bellow in Chap. 10.

In Fig. 9.7, the disconnection between the behavior of the two indicators at 3 weeks of perfusion, implies a change in cell density within the tissue. This is consistent with the observed zones of lower cell density in Fig. 9.5. It is possible to hypothesize that, when the tissue is growing thicker, cells migrate to the outer part in order to have access to higher concentration of nutrient and oxygen. This would explain the presence of the high density layer of cells surrounding the tissue, leading to the formation of the zones of tissue far from the beads after 3 weeks of perfusion. This hypothesis could be tested by assessing the presence or absence of ECM in poorly cell populated regions. To that purpose staining experiments with different collagen dyes (Eosin, Picro-fuchsin, Methyl blue) have been carried. Since MMA polymer is poorly permeable to most stains, this coloration tests have been combined to various deplasticizing protocols (acetone, Osteobed Embedding solvent). Unfortunately, at the current time, none of this tests has led to conclusive results.

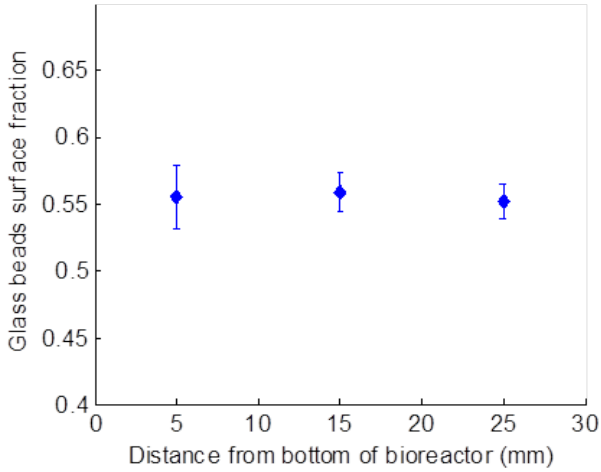

Figure 9.8 – Mean surface fraction of the glass beads as a function of distance to the chamber entrance. Bar length represents standard deviations.

At 3 weeks of perfusion, the lower part of the bioreactor is occupied at more than 20% by tissue. Since the surface fraction of the glass beads is about 55%, the surface by which the culture medium flows has been reduced from 45 to 25% of the tube's surface. As the tissue grows, the volume by which the culture medium flows is reduced, increasing its velocity. This leads to a competition between the tissue expansion, and the forces exerted by the culture medium on the tissue. The reduction in cell proliferation indicated by Fig. 9.6 at 5mm, as well as the irregular shapes of tissue at 3 weeks of perfusion in Fig. 9.5, suggest that the balance point between tissue growth and hydrodynamic forces has been reached.

In this study, the observations and measurements of the indicators are made from planar cuts of the constructs, and the three-dimensional structure of the construct can only be guessed. 3D imaging would be of valuable help to understand the formation of the observed complicated structure of tissue, and to asses the relevance of CGI and TGI. This could be done by preparing several adjacent slices in the histological process, and reconstructing the 3D structure after a digitization and segmentation of the slices. However, the thickness of the saw blade (about 700µm) reduces the resolution of this approach to about 1mm, and the time required to prepare and reconstruct a relevant volume of sample is highly discouraging. Another possibility would be the use of X-ray microtomography [Porter et al., 2007; Davit et al., 2011; Voronov et al., 2013]. But even though this technology is getting more easily available, it still necessitates heavy procedures as well as highly qualified manpower. Moreover biological phases and water (or culture medium) have similar X-ray attenuation, and contrasting agents are often required, complicating the experimental procedure. Lastly X-rays are damageable for cells, and this technique is considered as destructive (yet probably less than histology).

The above results give information about cell and tissue growth kinetics, as well as the dependency on their position in the chamber. Yet, a full interpretation of this results, based only on the experimental observation, remain limited. The use of modeling and computa-

tional tools may be of valuable help in this task. In the remaining of this document, the multiscale model previously developed is solved at the bioreactor scale, and the comparison of the experimental and modeling results is discussed.

CHAPTER 10

MACROSCOPIC MODEL OF THE PERFUSION BIOREACTOR

THE EXPERIMENTAL STUDY presented in the previous chapter, gives insight on cell and tissue growth kinetic within a perfusion bioreactor. Yet, the underlying mechanisms driving the production of biomass, are difficult to analyze based on experimental observations only. Here, we aim to take advantage of the model developed in Part II, in order to improve the understanding of the transport phenomena leading to the production of tissue in the bioreactor.

In Chaps. 6 to 8, a theoretical framework has been derived, where mass and momentum transport have been successively upscaled from the ECM, up to the bioreactor scale. The obtained macroscopic model, composed of Eqs. (8.59), (8.60), (8.108), (8.109), (8.196) and (8.197), must be solved at the bioreactor scale, in order to obtain the time and space evolution of the intrinsic averages of (i) the culture medium velocities, (ii) the concentration of a limiting nutritive species, such as glucose, and (iii) the tissue volume fraction. But before to be able to solve this system, two tasks remain to be dealt with. First, a kinetic for the production of biological tissue must be incorporated in the model. Second, the multiple effective parameters appearing in the macroscopic transport equations must be computed for realistic parameters and geometries, representing bioreactor culture conditions comparable to those in Chap. 9. These two points are the subject of Secs. 10.1 and 10.2 respectively. Finally, the resolution the macroscopic model will be presented in Sec. 10.3.

10.1 Tissue growth model

In this section, a tissue growth model, based on cell and ECM production kinetics, is proposed. The equation describing the evolution of the tissue density Eq. (8.24), has actually already been derived through successive upscalings presented in Part II. Here, the tissue production kinetic is introduced, which has the advantage of naturally including the biomass production, within the theoretical framework developed for transport at the bioreactor scale.

Let us recall the mass conservation equation at the bioreactor scale Eq. (8.24)

$$\underbrace{\frac{\partial}{\partial t}\left(\varepsilon_\omega \langle \rho_\omega \rangle^\omega\right)}_{\substack{\text{tissue density} \\ \text{accumulation}}} + \underbrace{\nabla.\left(\rho_\alpha \varepsilon_\omega \langle \mathbf{v}_\omega \rangle^\omega\right)}_{\substack{\text{culture medium} \\ \text{mass convective flux}}} = \underbrace{\dot{m}_\omega}_{\substack{\text{interfacial mass} \\ \text{exchange rate}}} + \underbrace{\varepsilon_\omega \langle Q_\omega \rangle^\omega}_{\substack{\text{tissue} \\ \text{production rate}}} \tag{10.1}$$

This equation has to be solved along with the rest of the macroscopic model for momentum transport. Here, the interfacitial mass exchange rate can be expressed by Eq. (8.107), and only the tissue production rate remain to be defined. To start with, using the definition Eq. (8.7), the tissue production rate can be expressed as the sum of the cell and ECM tissue production rate

$$\varepsilon_\omega \langle Q_\omega \rangle^\omega = \varepsilon_\omega \langle \varepsilon_\beta \langle Q_\beta \rangle^\beta + \varepsilon_\sigma \langle Q_\sigma \rangle^\sigma \rangle^\omega \tag{10.2}$$

Several models have been proposed in the literature to relate the cell growth rate to the biochemical [Chung et al., 2007] or biohysical [Sacco et al., 2010] environment. However there has been much fewer attempts to describe the production of ECM [Nikolaev et al., 2010].

Here Q_β and Q_σ have been formulated as point reaction at the cellular scale. Although this is mathematically correct, there is no real physical meaning behind this. For instance, the production of cell mass does not come from one point in the cytoplasm, but from the interaction of multiple and complex mechanisms, distributed in the whole cell. Moreover the production of ECM is insured by the cells, and should be dependent on quantities related to cells, instead of variables in the β-region. Following this idea, here, Q_β and Q_σ will not be defined at the cellular scale, but in their average form $\langle Q_\beta \rangle^\beta$ and $\langle Q_\sigma \rangle^\sigma$. This allows to use parameters that are representative of a population of cells, without having to introduce, for example, stochastic parameters that would represent cell cycle or biological variability.

We start by the cell growth rate, and propose to use a modified Contois kinetic [Galban & Locke, 1999a; Chung et al., 2007; Sacco et al., 2010]

$$\langle Q_\sigma \rangle^\sigma = \left(\frac{k_m(\tau) \langle c_{A\sigma} \rangle^\sigma}{\langle c_{A\sigma} \rangle^\sigma + \varepsilon_\sigma \rho_\sigma k_s \alpha_0^{-1}} - k_d \right) \left(\varepsilon_\beta \rho_\beta + \varepsilon_\sigma \rho_\sigma \right) \tag{10.3}$$

where $k_m(\tau)$ is the maximum growth rate, that here depends on the average shear stress τ. k_s is the saturation constant, and k_d is the cell death rate coefficient. This kinetic is actually very similar to a Michaelis-Menten reaction rate, and its average form can be easily derived from the point equation. This equation depends on nutrient average concentration in the σ-region, and cell density in order to represent cell inhibition. Since the local mass equilibrium is supposed at the cellular scale, we have $\{c_A\} = \alpha_0 \langle c_{A\sigma} \rangle^\sigma$. And using the notation correspondence $c_{A\omega} = \{c_A\}$, the cell growth rate can be written

$$\langle Q_\sigma \rangle^\sigma = \left(\frac{k_m(\tau) c_{A\omega}}{c_{A\omega} + \varepsilon_\sigma \rho_\sigma k_s} - k_d \right) \rho_\omega \tag{10.4}$$

Let us now focus on the ECM production rate. Several hypothesis can be made concerning the form of $\langle Q_\beta \rangle^\beta$. For instance, it could be supposed that the production of ECM is only

dependent on the cell number, or that it follows a simple Contois kinetic without cell density inhibition. In the present study, for seek of simplicity, the production of ECM is supposed to be proportional to the production rate of cell material. Hence we have

$$\langle Q_\beta \rangle^\beta = \xi \langle Q_\sigma \rangle^\sigma \tag{10.5}$$

where ξ is a proportional constant, larger or equal to one. If ξ is larger than one, the tissue expands by producing more ECM than cells, which is a characteristic of certain types of connective tissues. The total tissue production rate takes the form

$$\varepsilon_\omega \langle Q_\omega \rangle^\omega = \varepsilon_\omega \left\langle \left(\varepsilon_\beta \xi + \varepsilon_\sigma\right) \left(\frac{k_m(\tau) c_{A\omega}}{c_{A\omega} + \varepsilon_\sigma \rho_\sigma k_s} - k_d \right) \rho_\omega \right\rangle^\omega \tag{10.6}$$

and when introduced back into Eq. (10.1), the general expression of the tissue mass conservation equation is obtain

$$\frac{\partial}{\partial t} \left(\varepsilon_\omega \langle \rho_\omega \rangle^\omega\right) + \nabla . \left(\rho_\alpha \varepsilon_\omega \langle \mathbf{v}_\omega \rangle^\omega\right) = \dot{m}_\omega + \varepsilon_\omega \left\langle \left(\varepsilon_\beta \xi + \varepsilon_\sigma\right) \left(\frac{k_m(\tau) c_{A\omega}}{c_{A\omega} + \varepsilon_\sigma \rho_\sigma k_s} - k_d \right) \rho_\omega \right\rangle^\omega \tag{10.7}$$

At this point, the bioreactor scale quantities are explicitly linked to cellular scale growth parameters.

The use of the tissue mass conservation Eq. (10.7) in its current form, is quite complicated, and some assumptions have to be made in order to make its resolution possible. As a first hypothesis, ξ is supposed very close to one. This means that the time variations of ε_β and ε_σ can be neglected, and thus, by definition (Eq. (8.4)), that the time variations of $\langle \rho_\omega \rangle^\omega$ are null. Additionally, when the cell distribution in the tissue is supposed homogeneous, we obtain $\langle \rho_\omega \rangle^\omega = \rho_\omega$ constant in space. If one is willing to accept this simplifications, the tissue mass conservation equation takes the form

$$\rho_\omega \frac{\partial \varepsilon_\omega}{\partial t} + \nabla . \left(\rho_\alpha \varepsilon_\omega \langle \mathbf{v}_\omega \rangle^\omega\right) = \dot{m}_\omega + \varepsilon_\omega \rho_\omega \left(\varepsilon_\beta \xi + \varepsilon_\sigma\right) \left\langle \frac{k_m(\tau) c_{A\omega}}{c_{A\omega} + \varepsilon_\sigma \rho_\sigma k_s} - k_d \right\rangle^\omega \tag{10.8}$$

Finally, one can notice that the production term under the superficial average is similar to a Michaelis-Menten reaction kinetic. Following Wood & Whitaker [2000], it can be shown that, under the length scale constraints of this study, and for k_s and k_d constant within the tissue, the tissue production rate is expressed as

$$\rho_\omega \frac{\partial \varepsilon_\omega}{\partial t} + \nabla . \left(\rho_\alpha \varepsilon_\omega \langle \mathbf{v}_\omega \rangle^\omega\right) = \dot{m}_\omega + \varepsilon_\omega \rho_\omega \left(\varepsilon_\beta \xi + \varepsilon_\sigma\right) \left(\frac{\langle k_m(\tau) \rangle^\omega \langle c_{A\omega} \rangle^\omega}{\langle c_{A\omega} \rangle^\omega + \varepsilon_\sigma \rho_\sigma k_s} - k_d \right) \tag{10.9}$$

The mass exchange term can be further expressed using Eq. (8.107) and the solution of the closure problem for momentum transport at the bioreactor scale. Eq. (10.9) involves only macroscopic variables, and can be solved in complement with the rest of the macroscopic system describing mass transport at the bioreactor scale. The resolution of the macroscopic problem is discussed in Sec. 10.3.

10.2 Realistic effective transport parameters

The bioreactor scale transport equations derived in Chap. 8 necessitate the knowledge of the effective parameters values. Fortunately, the computations of this parameters is possible by solving the corresponding closure problems on representative unit cells. In this section, we discuss a methodology to compute realistic bioreactor effective parameters. Nevertheless, the macroscopic properties depends on the lower scales effective transport properties, and we start by computing the tissue effective transport parameters.

10.2.1 Tissue effective parameters

Secs. 7.2.2 and 7.3.2 revealed the importance of the ECM transport parameters on the effective tissue permeability $\mathbf{K}_{\omega}^{\mathrm{II}}$ and diffusion-dispersion tensor $\mathbf{D}_{A\omega}^{\mathrm{II}}$. However these computations have been carried for bi-dimensional in-line arrays of cylinders. In this section, more realistic tridimensional geometries are modeled to represent the cellular scale (level III). Using parameters from the literature we estimate $\mathbf{K}_{\omega}^{\mathrm{II}}$ and $\mathbf{D}_{A\omega}^{\mathrm{II}}$ and compare them with experimental measurements from bibliography.

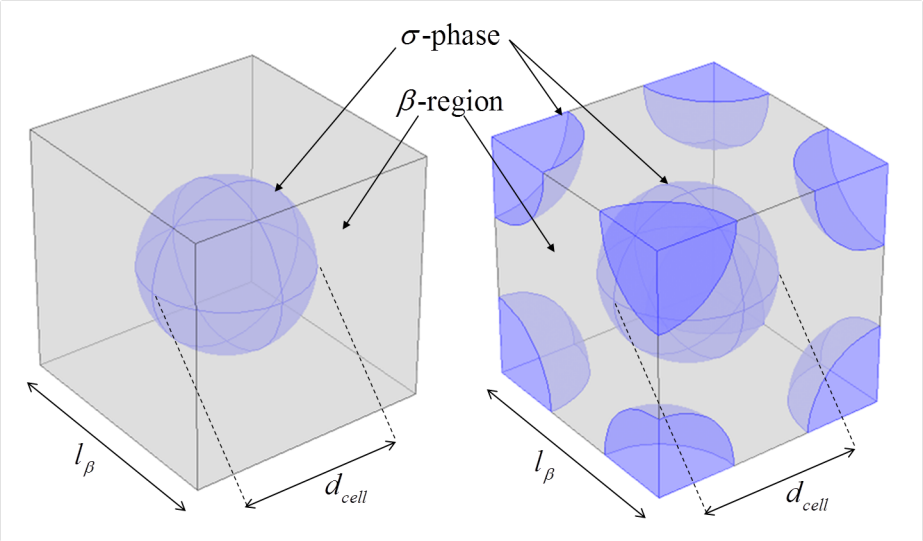

Figure 10.1 – Three-dimensional periodic unit cells for the cellular scale (level III). Simple Cubic (left) and Centered Cubic (right) arrangement of cells.

The cells are modeled by spheres embedded in a porous matrix. The arrangement of the spheres is either simple cubic (SC) or centered cubic (CC) (Fig. 10.1). The values of the parameters used in the model are taken either from the sources reported in Tab. 6.1, or from the resolution at the ECM scale (Secs. 6.2.1 and 6.2.2), and are summarized in Tab. 10.1.

The tissue permeability is computed by solving Eqs. (7.61) to (7.67) on the tridimensional unit cells (Fig. 10.1). The cell diameter is taken constant ($d_{\mathrm{cell}} = 10 \times 10^{-6} m$) and the ECM volume fraction ε_β is varied between 0.5 and 0.95. Following the results presented in

Description	Parameter	Value used in the model
ECM fibers diameter	d_{fib}	$10^{-7}m$
Cell diameter	d_{cell}	$10^{-5}m$
Scale IV unit cell length	l_α	$10 \times d_{\text{fib}} = 10^{-6}$
ECM permeability	K_β^{III}	$10^{-2} \times l_\alpha^2$
		$= 10^{-4} \times d_{\text{cell}}^2$
		$= 10^{-14}m^2$
ECM fluid volume fraction	ε_α	0.90
Culture medium dynamic viscosity	μ_α	$10^{-4}Pa.s$
Glucose diffusion coefficient in culture medium	$D_{A\alpha}$	$6 \times 10^{-10}m^2/s$

Table 10.1 – Values used for the computation of the tissue effective transport parameters

Sec. 6.2.1, for a fiber diameter of $d_{\text{fiber}} = 100 \times 10^{-9}m$ and a ratio between the ECM unit cell and the fiber diameter of $l_\alpha/d_{\text{fiber}} = 10$, the ECM permeability K_β^{III} is of the order of $10^{-2} \times l_\alpha^2$ with a corresponding ECM porosity of 0.90. The results are presented in Fig. 10.2 in term of dimensionless and dimensional permeability. Contrary to the previous results on permeability, in Fig. 10.2 the tissue permeability is adimensionalized by the square of the cell diameter (instead of the square of the unit cell length). This has two practical advantages. First, it can be assumed that the cellular volume fraction in the tissue depends mostly on the number of cells, and not on the diameter of the cells. Thus varying l_β and keeping d_{cell} constant seems more appropriate. Second, the dimensionless ECM permeability related to the cell diameter $K_\beta^{\text{III}}/d_{\text{cell}}^2$ should be a constant, and this also motivates to take d_{cell} as the relevant length scale.

The computed tissue permeability K_ω^{II} is of 3 to $9 \times 10^{-15}m^2$. These values are in good agreement with the reported permeabilities found in the literature [Levick, 1987; Swartz & Fleury, 2007; Fournier, 2011; Tarbell & Shi, 2013]. One can observe that the tissue permeability is mainly controlled by the ECM permeability, and this explains the very weak influence of the disposition of the cells on the tissue permeability. As reported in Sec. 6.2.1, when the ECM volume fraction becomes close to one (little number of cells in the tissue), K_ω^{II} tends to the ECM permeability.

10.2.2 Bioreactor effective parameters

Bioreactor effective parameters are computed on representative unit cells at the tissue scale. One of the main difficulty of this study, is the evolving nature of the tissue architecture, leading to different bioreactor effective parameters depending on the state of culture. The tissue volume fraction has been experimentally measured in Chap. 9, and its value ranges between zero and 0.25 depending on the cultivation time. Additionally, the glass bead volume fraction has been shown to be approximately 0.55.

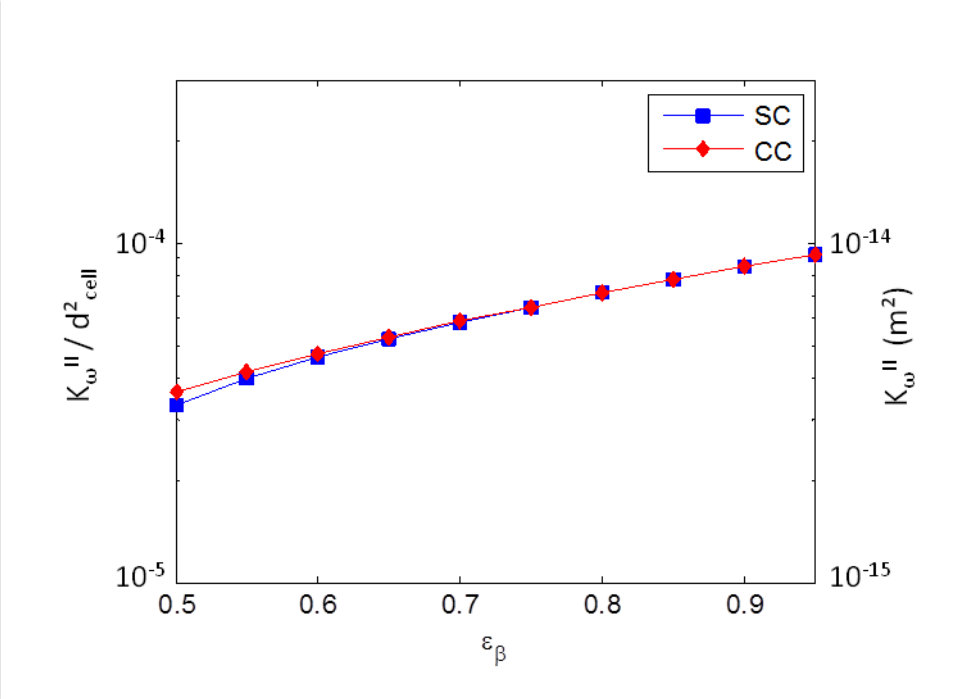

Figure 10.2 – Tissue permeability for CS ans CC arrangement of cells.

Under this considerations, a three-dimensional unit cell for the computation of realistic bioreactor properties is proposed (see Fig. 10.3). The glass beads are represented by a simple cubic array of spheres, which volume fraction set to $\varepsilon_\kappa = 0.5$. The tissue region is described by a layer of constant thickness, covering the totality of the spheres. The value of the tissue volume fraction can vary by adjusting the thickness of the tissue layer.

Unfortunately, for computational cost reasons, the resolution of the closure problems on the unit cell described above has not been proceeded yet. This will be the subject of future work.

10.3 Resolution at the bioreactor scale

Although at the present time, the macroscopic model has not been solved yet, the main features of its resolution process are discussed in this section.

Let us recall the results of the bioreactor scale transport model developed in Part II. Starting with the momentum problem, the macroscopic transport equations in the superficial form are

$$\rho_\alpha \varepsilon_\gamma^{-1} \frac{\partial \langle \mathbf{v}_\gamma \rangle}{\partial t} = -\nabla \langle p_\gamma \rangle^\gamma + \rho_\alpha \mathbf{g} + \mu_\alpha \varepsilon_\gamma^{-1} \nabla^2 \langle \mathbf{v}_\gamma \rangle - \frac{\mu_\alpha}{\mathbf{K}_\gamma^{\mathrm{I}}} \langle \mathbf{v}_\gamma \rangle + \frac{\mu_\alpha}{\mathbf{K}_{\gamma\omega}^{\mathrm{I}}} \langle \mathbf{v}_\omega \rangle + \mathbf{\Pi}_\gamma^{\mathrm{I}} \left(\langle p_\gamma \rangle^\gamma - \langle p_\omega \rangle^\omega \right) \quad (10.10)$$

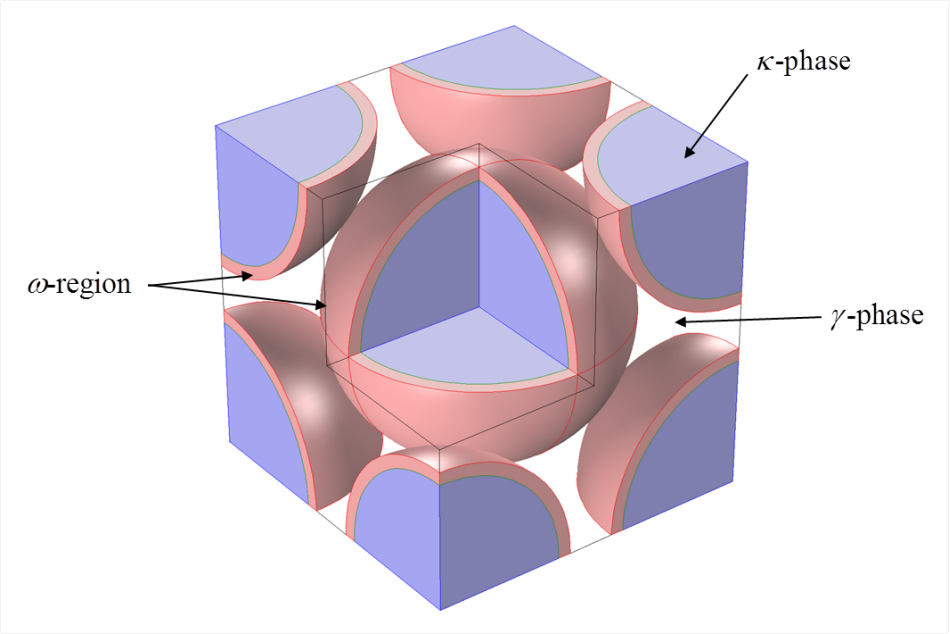

Figure 10.3 – Example of three-dimensional unit cell used to compute realistic bioreactor effective properties. Blue and pink regions represent the glass beads and the tissue respectively.

$$\rho_\alpha \varepsilon_\alpha^{-1}\varepsilon_\beta^{-1}\varepsilon_\omega^{-1}\frac{\partial \langle \mathbf{v}_\omega \rangle}{\partial t} = -\nabla \langle p_\omega \rangle^\omega + \rho_\alpha \mathbf{g} + \mu_\alpha \varepsilon_\alpha^{-1}\varepsilon_\beta^{-1}\varepsilon_\omega^{-1}\nabla^2 \langle \mathbf{v}_\omega \rangle - \frac{\mu_\alpha}{\mathbf{K}_\omega^{\mathrm{I}}}\langle \mathbf{v}_\omega \rangle + \frac{\mu_\alpha}{\mathbf{K}_{\omega\gamma}^{\mathrm{I}}}\langle \mathbf{v}_\gamma \rangle + \mathbf{\Pi}_\omega^{\mathrm{I}}\left(\langle p_\gamma \rangle^\gamma - \langle p_\omega \rangle^\omega\right) \quad (10.11)$$

Here the variables are $\langle \mathbf{v}_\gamma \rangle$, $\langle \mathbf{v}_\omega \rangle$, $\langle p_\gamma \rangle^\gamma$, $\langle p_\omega \rangle^\omega$, and ε_ω. These equations have to be completed with the mass conservation equations

$$\frac{\partial}{\partial t}\left(\varepsilon_\alpha \rho_\alpha\right) + \nabla.\left(\rho_\alpha \langle \mathbf{v}_\gamma \rangle\right) = -\rho_\alpha \frac{h_\gamma}{\mu_\alpha}\left(\langle p_\gamma \rangle^\gamma - \langle p_\omega \rangle^\omega\right) \quad (10.12)$$

$$\frac{\partial}{\partial t}\left(\varepsilon_\omega \rho_\omega\right) + \nabla.\left(\rho_\alpha \langle \mathbf{v}_\omega \rangle\right) = -\rho_\alpha \frac{h_\omega}{\mu_\alpha \varepsilon_\alpha^{-1}\varepsilon_\beta^{-1}}\left(\langle p_\gamma \rangle^\gamma - \langle p_\omega \rangle^\omega\right) + \varepsilon_\omega \rho_\omega\left(\varepsilon_\beta \xi + \varepsilon_\sigma\right)\left(\frac{\langle k_m(\tau) \rangle^\omega \langle c_{A\omega} \rangle^\omega}{\langle c_{A\omega} \rangle^\omega + \varepsilon_\sigma \rho_\sigma k_s} - k_d\right) \quad (10.13)$$

Where the tissue production rate has been introduced. One can see in Eq. (10.13), a coupling of the momentum problem with the problem for mass transport. And the macroscopic

concentration fields of $\langle c_{A\gamma}\rangle^{\gamma}$ and $\langle c_{A\omega}\rangle^{\omega}$ are obtained from

$$\begin{aligned}\frac{\partial\left(\varepsilon_{\gamma}\langle c_{A\gamma}\rangle^{\gamma}\right)}{\partial t}+\nabla.\left(\varepsilon_{\gamma}\langle\mathbf{v}_{\gamma}\rangle^{\gamma}\langle c_{A\gamma}\rangle^{\gamma}\right)=\\ \nabla.\left(\mathbf{D}^{\mathrm{I}}_{\gamma\gamma}.\nabla\langle c_{A\gamma}\rangle^{\gamma}\right)+\nabla.\left(\mathbf{D}^{\mathrm{I}}_{\gamma\omega}.\nabla\langle c_{A\omega}\rangle^{\omega}\right)+\nabla.\left(\mathbf{d}^{\mathrm{I}}_{\gamma}\left(\langle c_{A\gamma}\rangle^{\gamma}-\langle c_{A\omega}\rangle^{\omega}\right)\right)\\ +\mathbf{u}^{\mathrm{I}}_{\gamma\gamma}.\nabla\langle c_{A\gamma}\rangle^{\gamma}+\mathbf{u}^{\mathrm{I}}_{\gamma\omega}.\nabla\langle c_{A\omega}\rangle^{\omega}+\alpha^{\mathrm{I}}_{\gamma}\left(\langle c_{A\gamma}\rangle^{\gamma}-\langle c_{A\omega}\rangle^{\omega}\right)\\ -\frac{h_{\gamma}}{\mu_{\alpha}}\left(\langle p_{\gamma}\rangle^{\gamma}-\langle p_{\omega}\rangle^{\omega}\right)\langle c_{A\gamma}\rangle^{\gamma}\end{aligned}\tag{10.14}$$

$$\begin{aligned}\frac{\partial\left(\varepsilon_{\mathrm{III}}\varepsilon_{\omega}\langle c_{A\omega}\rangle^{\omega}\right)}{\partial t}+\nabla.\left(\varepsilon_{\omega}\langle\mathbf{v}_{\omega}\rangle^{\omega}\langle c_{A\omega}\rangle^{\omega}\right)=\\ \nabla.\left(\mathbf{D}^{\mathrm{I}}_{\omega\gamma}.\nabla\langle c_{A\gamma}\rangle^{\gamma}\right)+\nabla.\left(\mathbf{D}^{\mathrm{I}}_{\omega\omega}.\nabla\langle c_{A\omega}\rangle^{\omega}\right)+\nabla.\left(\mathbf{d}^{\mathrm{I}}_{\omega}\left(\langle c_{A\gamma}\rangle^{\gamma}-\langle c_{A\omega}\rangle^{\omega}\right)\right)\\ +\mathbf{u}^{\mathrm{I}}_{\omega\gamma}.\nabla\langle c_{A\gamma}\rangle^{\gamma}+\mathbf{u}^{\mathrm{I}}_{\omega\omega}.\nabla\langle c_{A\omega}\rangle^{\omega}+\alpha^{\mathrm{I}}_{\omega}\left(\langle c_{A\gamma}\rangle^{\gamma}-\langle c_{A\omega}\rangle^{\omega}\right)\\ -\frac{h_{\omega}}{\mu_{\alpha}\varepsilon_{\alpha}^{-1}\varepsilon_{\beta}^{-1}}\left(\langle p_{\gamma}\rangle^{\gamma}-\langle p_{\omega}\rangle^{\omega}\right)\langle c_{A\omega}\rangle^{\omega}-\varepsilon_{\omega}\varepsilon_{\sigma}\frac{k_{A}}{\alpha_{0}K_{A}}\langle c_{A\omega}\rangle^{\omega}\end{aligned}\tag{10.15}$$

Compared to more usual transport problems, the numerous additional terms may appear discouraging. However preliminary macroscopic computations can be proceeded (for instance in static conditions for a given distribution of tissue), so that the order of magnitude of the different terms are evaluated. This may allow to simplify the problem by neglecting very small terms (most likely the terms involving $\mathbf{\Pi}^{\mathrm{I}}_{i}$, h_i, $\mathbf{d}^{\mathrm{I}}_{i}$, $\mathbf{u}^{\mathrm{I}}_{ij}$ and α^{I}_{i}).

Then, the simplified system should be solved in transient conditions. At the macroscopic scale, the bioreactor is a one dimensional domain representing the position in the length of the perfusion chamber. Various culture conditions can be modeled, in particular, the effect of initial seeding (initial conditions for ε_{ω}) on the final distribution of tissue should be studied, in order to help the interpretation of the experimental results of Chap. 9.

General Conclusions

The main goal of this thesis, is to gain insight on the relations between transport phenomena and tissue production, within a perfusion bioreactor for bone tissue engineering [David et al., 2011]. To this purpose, a combined modeling and experimental approach has been followed.

A theoretical framework based on the volume averaging method with closure has been developed, in order to investigate transport phenomena occurring in the perfusion bioreactor. Three successive upscalings have been operated, from the extracellular matrix (ECM) scale, up to the bioreactor scale. At each scale, the effective transport properties have been evaluated by solving the corresponding closure problem. The interscale dependencies arising from the encountered hierarchical structures have been studied. Finally, a bioreactor scale model for mass and momentum transport has been obtained, where the relevant informations contained at the lower scale were retained. The construction of this model allowed the incorporation of a tissue growth rate, which parameters were related to the cell and ECM production.

In complement, an experimental model of the bioreactor has been proposed, where cells were grown on spherical and impermeable glass beads, under culture medium perfusion. A methodology based on histology and image analysis has been developed, in order to quantify, through the definition of two indicators, the evolution of cell and tissue in space and time.

Although the resolution of the macroscopic model could not be done in the time of this thesis, a methodology has been proposed to compute the evolution of the tissue volume fraction, and its influence on mass and momentum transport. The results of such simulations should help the interpretation of the experimental results, and provide informations on the production of tissue in a perfusion bioreactor.

Perspectives

Concerning the experimental approach, the validity and precision of the two growth indicators defined in Chap. 9 should be examined. This necessitate the comparison with results of the cell/tissue volume fractions obtained with other methods, such as X-ray microtomography, multiphoton microscopy, or bioliminescence imaging. Additionally, the influence of more culture parameters should be investigated. For instance, as shown along this study, the transport properties of the bioreactor are non-linearly dependent on the Péclet Number. Therefore the intensity of the culture medium flow is expected to play a critical role in the production of biomass. An experimental parametric study of the bioreactor input flow rate

should be carried experimentally, so that the results on tissue growth, can be related to the computed bioreactor transport properties. It would also be interesting to modify the cultured cell line, to observer different cell growth and ECM production kinetics. Another important aspect yet to be studied, is the importance of the mechanical stimuli induced by the culture medium flow. In the current experimental setup, the contribution of such biophysical stimuli on cellular activity cannot be assessed. The quantification of the influence shear stress on cell proliferation is a challenging experimental task. The use of microfluidic systems seems a promising approach, and current investigations are carried in that direction [Chabanon et al., 2012; David et al., 2014].

Regarding the model built from successive upscaling in Part II, several improvements can be proposed. Indeed, in this thesis, the mass transport model is very general, facilitating the coherence of the whole theory. However, more specific transport mechanisms should be taken into account in order improve the representation of the biophysical and biochemical processes. In particular, the description at the cellular scale can be greatly refined. To start with, the choice of local mass equilibrium between the ECM and the cellular region can be questioned. Unfortunately, few experimental clues on the validity of such assumption are available, and this hypothesis should be checked for each transported species considered. Then, the variety of existing membrane transport mechanism would necessitate a specific modeling work for each considered transported species. Additionally, interactions between biomolecules should be treated, implying to take into account multispecies transport. Moreover, transport within the cell region has not been described here. There are interesting work perspectives in the representation of the structure and transport mechanisms in the intracellular space [Kühn et al., 2011]. Finally, the dispersive effects within the ECM have not been included in the present analysis. Although these phenomena are not likely to occur in low permeability ECM, a number of experimental study make use of high permeability collagen gel, where dispersive effects at the cellular scale could influence cell activity.

In the present thesis, two-equation non-equilibrium models have been developed for the description of transport phenomena at the tissue scale. This choice has been motivated by the necessity to have access to the tissue intrinsic averages, which are required in the tissue production rate. On one hand, this type of model allows to capture more details of the transport phenomena taking place within the bioreactor. In particular, although a deeper investigation of the coupling effective tensor is required, their non monotonic behavior may play an important role in the regulation of tissue growth. On the other hand, the improved representations related to these models, comes with an increased level of complexity, which hinder their applicability. A possible simplification may be obtained by the use of one-equation non-equilibrium models such as those presented in App. C and [Davit et al., 2010]. In that cases, the tissue production rate should be dependent on the weighted averages of the concentration and velocity. The validity of this "simpler" one-equation bioreactor model, would have to be assessed by comparison of the macroscopic solution, with the two-equation model.

NOMENCLATURE

General notations

A_{ij}	interfacial area between the i and j phase(s)/region(s)
CGI	Cell growth indicator
ε_i	volume fraction of the i-phase/region
$\mathbf{g}$	gravitational acceleration
$\mathbf{I}$	unit tensor
l_i	length scale associated with the i-phase/region
L_ψ	length scale associated with average of ψ
$\mathbf{n}_{ij}$	normal vector oriented from the i toward the j phase/region
$\langle \psi_i \rangle$	superficial average of ψ_i
$\langle \psi_i \rangle^\beta$	intrinsic average of ψ_i
ψ_i	a local quantity associated with the i-phase/region
Pe_i	Péclet number in the i phase/region
$\tilde{\psi}_i$	spacial deviation of ψ_i
r_0	length scale associated with the averaging volume
t	time variable
t_ψ	time scale associated with variation of ψ
TGI	Tissue growth indicator
V_i	volume of the i-phase/region within the averaging volume
$\mathbf{w}_{ij}$	velocity of the interface between the i and j phase(s)/region(s)

Notations defined at scale IV

α	phase indicator of the interstitial fluid phase defined at scale IV
$\mathbf{B}_\alpha$	closure variable associated with the velocity in α-phase
$\mathbf{b}_\alpha$	closure variable associated with the pressure in α-phase
$c_{A\alpha}$	local concentration of the substrate A in the α-phase
$\mathbf{d}_\alpha$	closure variable associated with the concentration in α-phase

$D_{A\alpha}$ diffusion coefficient of the substrate A in the α-phase
η phase indicator of the ECM fibrous structure phase defined at scale IV
p_β local pressure in the α-phase
Q_η production rate of collagen fibers
μ_α dynamic viscosity of the α-phase
ρ_α density of the α-phase
$\mathbf{v}_\alpha$ local fluid velocity in the α-phase
$\mathcal{V}_{\text{IV}}$ averaging volume associated with scale IV

Notations defined at scale III

α_0 equilibrium coefficient
$\alpha_{1,2,3,4}$ membrane transport parameters
β phase indicator of the ECM region defined at scale III
$\mathbf{B}_\beta$ closure variable associated with the velocity in β-region
$\mathbf{b}_\beta$ closure variable associated with the pressure in β-region
$c_{A\beta}$ $(= \langle c_{A\alpha} \rangle)$ local concentration of the substrate A in the β-region
$c_{A\sigma}$ local concentration of the substrate A in the σ-phase
$\mathbf{d}_\beta$ closure variable associated with the concentration in β-region
$\mathbf{d}_\sigma$ closure variable associated with the concentration in σ-phase
$\mathbf{D}^{\text{III}}_{A\beta}$ dispersion tensor of substrate A in the β-region
$D_{\sigma\beta}$ relative diffusivity between the σ-phase and the β-region
$D_{A\sigma}$ diffusion coefficient of the substrate A in the σ-phase
E_0 surface concentration of transporter proteins
Γ see Eq. (7.92)
γ_β relative membrane transport parameter
$\mathbf{K}^{\text{III}}_\beta$ permeability tensor of the β-region
ξ proportional constant betwen ECM and tissue growth rates
K_A half saturation constant of intracellular reaction
k_A specific degradation rate of substrate A
k_d cell death rate
$k_m(\tau)$ maximum cell growth rate (depending on the average shear stress τ)
k_s saturation constant related to cell growth rate
p_β $(= \langle p_\alpha \rangle^\alpha)$ local pressure in the β-region
Q_β $(= \langle Q_\eta \rangle)$ average production rate of ECM (β-region)
Q_σ production rate of the σ-phase
ρ_β $(= \varepsilon_\alpha \rho_\alpha + \varepsilon_\beta \rho_\beta)$ total density of the β-region
ρ_σ density of the σ-phase
R_σ consumption of species A in the σ-phase

σ phase indicator of the intracellular phase defined at scale III
$\mathbf{v}_\beta$ ($= \langle \mathbf{v}_\alpha \rangle$) local fluid velocity in the β-region
$\mathcal{V}_{\text{III}}$ averaging volume associated with scale III

Notations defined at scale II

$\mathbf{B}_{ij}$ velocity-like closure variable (2nd order tensor)
$\mathbf{b}_{ij}$ pressure-like closure variable (1st order tensor)
$\mathbf{B}_i$ velocity-like closure variable (1st order tensor)
b_i pressure-like closure variable (scalar)
$\{c_A\}$ local mass equilibrium average of the cell scale concentrations
$c_{A\gamma}$ local concentration of substrate A in the γ-phase
$c_{A\omega}$ ($= \{c_A\}$) local concentration of the substrate A in the ω-region
$\mathbf{D}^{\text{II}}_{A\omega}$ effective dispersion tensor of substrate A in the ω-region
$\mathbf{d}_{ij}$ concentration-like closure variable (1st order tensor)
s_i concentration-like closure variable (scalar)
γ phase indicator of the culture medium phase defined at scale II
κ phase indicator of the glass bead phase defined at scale II
$\mathbf{K}^\star_\beta$ intermediate permeability tensor related to the structure of the β-region
$\mathbf{K}^{\text{II}}_\omega$ effective permeability tensor of the ω-region
$\dot{m}_i$ interfacial mass exchange rates between the i-phase/region and the other
p_γ local pressure in the γ-phase
p_ω ($= \langle p_\beta \rangle^\beta$) local pressure in the ω-region
Q_ω ($= \langle Q_\beta + Q_\sigma \rangle$) average production rate of tissue (ω-region)
ρ_ω ($= \varepsilon_\beta \rho_\beta + \varepsilon_\sigma \rho_\sigma$) total density of the ω-region
ε_{III} ($= \alpha_0^{-1} \varepsilon_\sigma + \varepsilon_\alpha \varepsilon_\beta$)
R_ω (average consumption of substrate A in the ω-region
$\mathbf{v}_\gamma$ local fluid velocity in the γ-phase
$\mathbf{v}_\omega$ ($= \langle \mathbf{v}_{A\beta} \rangle$) local fluid velocity in the ω-region
$\mathcal{V}_{\text{II}}$ averaging volume associated with scale II
ω phase indicator of the tissue region defined at scale II

Notations defined at scale I

α^{I}_i interfacial mas transfer effective coefficient
$\mathbf{D}^{\text{I}}_{ii}$ main effective diffusion-dispersion tensor related to the i-phase/region
$\mathbf{D}^{\text{I}}_{ij}$ coupling effective diffusion-dispersion tensor
$\mathbf{d}^{\text{I}}_i$ velocity like effective coefficient
h_i mass exchange coefficients

$\mathbf{K}_{\omega}^{\mathrm{I}\star}$ intermediate effective permeability arising from the structure of the ω-region
$\mathbf{K}_{i}^{\mathrm{I}}$ main effective permeability tensor related to the i-phase/region
$\mathbf{K}_{ij}^{\mathrm{I}}$ coupling effective permeability tensor
$\mathbf{\Pi}_{i}^{\mathrm{I}}$ pressure related effective tensor
$\mathbf{u}_{ij}^{\mathrm{I}}$ velocity like effective coefficient
χ_{ij} interface exchange velocity-like coefficients

Part IV

Appendices

APPENDIX A

VOLUME AVERAGING FROM LEVEL IV TO III

A.1 Averaging momentum transport in the α-phase

Local conservation equations valid in the α-phase are described by Eqs. (6.2) to (6.5). The volume averaging method is first applied on momentum transport by averaging the conservation Eq. (6.2). Considering ρ_α and μ_α constant, the superficial average of the momentum transport in the α-phase is

$$\rho_\alpha \left\langle \frac{\partial \mathbf{v}_\alpha}{\partial t} \right\rangle = -\left\langle \nabla p_\alpha \right\rangle + \mu_\alpha \left\langle \nabla^2 \mathbf{v}_\alpha \right\rangle \tag{A.1}$$

In order to interchange spatial integration and time differentiation in the left hand side of Eq. (A.1) , the *general transport theorem* [Howes & Whitaker, 1985; Whitaker, 1999] is applied along with the no-slip condition Eq. (6.4)

$$\left\langle \frac{\partial \mathbf{v}_\alpha}{\partial t} \right\rangle = \frac{\partial \langle \mathbf{v}_\alpha \rangle}{\partial t} \tag{A.2}$$

The pressure term of Eq. (A.1) can be treated so to interchange spatial differentiation and integration using *the spatial averaging theorem* [Howes & Whitaker, 1985; Whitaker, 1999]

$$\left\langle \nabla p_\alpha \right\rangle = \varepsilon_\alpha \nabla \left\langle p_\alpha \right\rangle^\alpha + \left\langle p_\alpha \right\rangle^\alpha \nabla \varepsilon_\alpha + \frac{1}{\mathcal{V}_{\mathrm{IV}}} \int_{A_{\alpha\eta}} \mathbf{n}_{\alpha\eta} p_\alpha dA \tag{A.3}$$

In order to treat the local pressure in the area integral, Gray's spacial decomposition [Gray, 1975] of the pressure is used

$$p_\alpha = \left\langle p_\alpha \right\rangle^\alpha + \tilde{p}_\alpha \tag{A.4}$$

leading to

$$\left\langle \nabla p_\alpha \right\rangle = \varepsilon_\alpha \nabla \left\langle p_\alpha \right\rangle^\alpha + \left\langle p_\alpha \right\rangle^\alpha \nabla \varepsilon_\alpha + \frac{1}{\mathcal{V}_{\mathrm{IV}}} \int_{A_{\alpha\eta}} \mathbf{n}_{\alpha\eta} \left\langle p_\alpha \right\rangle^\alpha dA + \frac{1}{\mathcal{V}_{\mathrm{IV}}} \int_{A_{\alpha\eta}} \mathbf{n}_{\alpha\eta} \tilde{p}_\alpha dA \tag{A.5}$$

Using Taylor's expansion around the centroid of $\mathcal{V}_{\text{IV}}$ and the geometrical theorems [Quintard & Whitaker, 1994b], we get rid of the non-local term

$$\langle \nabla p_\alpha \rangle = \varepsilon_\alpha \nabla \langle p_\alpha \rangle^\alpha + \frac{1}{\mathcal{V}_{\text{IV}}} \int_{A_{\alpha\eta}} \mathbf{n}_{\alpha\eta} \tilde{p}_\alpha dA \tag{A.6}$$

with the length scale constraints

$$l_\alpha << r_0 \tag{A.7}$$

$$r_0^2 << L_{\varepsilon_\alpha} L_{p1} \tag{A.8}$$

where L_{p1} is the characteristic length scale on which the pressure gradient vary in the α-phase.

We now focus on the viscosity term in Eq. (A.1). Applying twice the spacial averaging theorem and making use of the no-slip condition Eq. (6.4) we get

$$\left\langle \nabla^2 \mathbf{v}_\alpha \right\rangle = \nabla^2 \langle \mathbf{v}_\alpha \rangle + \frac{1}{\mathcal{V}_{\text{IV}}} \int_{A_{\alpha\eta}} \mathbf{n}_{\alpha\eta} . \nabla \mathbf{v}_\alpha dA \tag{A.9}$$

The spacial decomposition of the velocity

$$\mathbf{v}_\alpha = \langle \mathbf{v}_\alpha \rangle^\alpha + \tilde{\mathbf{v}}_\alpha \tag{A.10}$$

allows to write Eq. (A.9) in the form

$$\begin{aligned} \left\langle \nabla^2 \mathbf{v}_\alpha \right\rangle = \varepsilon_\alpha \nabla^2 \langle \mathbf{v}_\alpha \rangle^\alpha + \langle \mathbf{v}_\alpha \rangle^\alpha . \nabla^2 \varepsilon_\alpha + 2 \nabla \varepsilon_\alpha . \nabla \langle \mathbf{v}_\alpha \rangle^\alpha \\ + \frac{1}{\mathcal{V}_{\text{IV}}} \int_{A_{\alpha\eta}} \mathbf{n}_{\alpha\eta} . \nabla \langle \mathbf{v}_\alpha \rangle^\alpha dA + \frac{1}{\mathcal{V}_{\text{IV}}} \int_{A_{\alpha\eta}} \mathbf{n}_{\alpha\eta} . \nabla \tilde{\mathbf{v}}_\alpha dA \end{aligned} \tag{A.11}$$

Once again we can eliminate the non local term represented by the fourth term of the right hand side of Eq. (A.11) using Taylor's expansion around the centroid of $\mathcal{V}_{\text{IV}}$ and the geometrical theorems [Quintard & Whitaker, 1994b]

$$\left\langle \nabla^2 \mathbf{v}_\alpha \right\rangle = \varepsilon_\alpha \nabla^2 \langle \mathbf{v}_\alpha \rangle^\alpha + \langle \mathbf{v}_\alpha \rangle^\alpha . \nabla^2 \varepsilon_\alpha + \nabla \varepsilon_\alpha . \nabla \langle \mathbf{v}_\alpha \rangle^\alpha + \frac{1}{\mathcal{V}_{\text{IV}}} \int_{A_{\alpha\eta}} \mathbf{n}_{\alpha\eta} . \nabla \tilde{\mathbf{v}}_\alpha dA \tag{A.12}$$

with the length scale restrictions

$$l_\alpha << r_0 \tag{A.13}$$

$$r_0^2 << L_\varepsilon L_{v2} \tag{A.14}$$

where L_{v2} is the characteristic length scale on which the laplacian of $\mathbf{v}_\alpha$ vary.

We now study the order of magnitude of the three first terms of the right hand side of Eq. (A.12)

$$\varepsilon_\alpha \nabla^2 \langle \mathbf{v}_\alpha \rangle^\alpha = O\left(\varepsilon_\alpha \frac{\langle \mathbf{v}_\alpha \rangle^\alpha}{L_{v1}} \right) \tag{A.15}$$

$$\langle \mathbf{v}_\alpha \rangle^\alpha . \nabla^2 \varepsilon_\alpha = O\left(\varepsilon_\alpha \frac{\langle \mathbf{v}_\alpha \rangle^\alpha}{L_{\varepsilon 1}} \right) \tag{A.16}$$

$$\nabla \varepsilon_\alpha . \nabla \langle \mathbf{v}_\alpha \rangle^\alpha = O\left(\varepsilon_\alpha \frac{\langle \mathbf{v}_\alpha \rangle^\alpha}{L_\varepsilon L_v} \right) \tag{A.17}$$

and conclude that the following simplifications

$$\nabla\varepsilon_\alpha.\nabla\left\langle \mathbf{v}_\alpha\right\rangle^\alpha << \varepsilon_\alpha\nabla^2\left\langle \mathbf{v}_\alpha\right\rangle^\alpha \tag{A.18}$$

$$\left\langle \mathbf{v}_\alpha\right\rangle^\alpha.\nabla^2\varepsilon_\alpha << \varepsilon_\alpha\nabla^2\left\langle \mathbf{v}_\alpha\right\rangle^\alpha \tag{A.19}$$

are valid if the next length scale constraints are met

$$L_{v1} << L_\varepsilon L_v \tag{A.20}$$

$$L_{v1} << L_{\varepsilon 1} \tag{A.21}$$

The viscosity term can then be simplified to the form

$$\left\langle\nabla^2\mathbf{v}_\alpha\right\rangle = \varepsilon_\alpha\nabla^2\left\langle \mathbf{v}_\alpha\right\rangle^\alpha + \frac{1}{\mathcal{V}_{\text{IV}}}\int_{A_{\alpha\eta}}\mathbf{n}_{\alpha\eta}.\nabla\tilde{\mathbf{v}}_\alpha dA \tag{A.22}$$

Thus, combining Eqs. (A.2), (A.6) and (A.22) into Eq. (A.1), and keeping the length scale constraints Eqs. (A.7), (A.8), (A.13) and (A.14) valid, we obtain the *unclosed averaged equation for momentum transport in the α-phase*

$$\rho_\alpha\varepsilon_\alpha^{-1}\frac{\partial\left(\varepsilon_\alpha\langle\mathbf{v}_\alpha\rangle^\alpha\right)}{\partial t} = -\nabla\left\langle p_\alpha\right\rangle^\alpha + \mu_\alpha\nabla^2\left\langle \mathbf{v}_\alpha\right\rangle^\alpha + \frac{1}{V_\alpha}\int_{A_{\alpha\eta}}\mathbf{n}_{\alpha\eta}.\left(-\mathbf{I}\tilde{p}_\alpha + \mu_\alpha\nabla\tilde{\mathbf{v}}_\alpha\right)dA \tag{A.23}$$

We now average the continuity Eq. (6.1)

$$\left\langle\nabla.\mathbf{v}_\alpha\right\rangle = 0 \tag{A.24}$$

Applying the spacial averaging theorem, and using the no-slip boundary condition Eq. (6.4), Eq. (A.24) simplifies to

$$\nabla.\left\langle \mathbf{v}_\alpha\right\rangle^\alpha = 0 \tag{A.25}$$

A.2 Averaging mass transport in the α-phase

The mass conservation equation in the α-phase (Eq. (6.3)) is averaged

$$\left\langle\frac{\partial c_{A\alpha}}{\partial t}\right\rangle + \left\langle\nabla.\left(\mathbf{v}_\alpha c_{A\alpha}\right)\right\rangle = \left\langle\nabla.\left(D_{A\alpha}\nabla c_{A\alpha}\right)\right\rangle \tag{A.26}$$

The intersitial medium diffusion coefficient $D_{A\alpha}$ is assumed to be constant in space, and by applying twice the spatial averaging theorem, and once the general transport theorem, Eq. (A.26) can be written

$$\frac{\partial\left(\varepsilon_\alpha\left\langle c_{A\alpha}\right\rangle^\alpha\right)}{\partial t} + \left\langle\nabla.\left(\mathbf{v}_\alpha c_{A\alpha}\right)\right\rangle = \nabla.\left[D_{A\alpha}\left(\varepsilon_\alpha\nabla\left\langle c_{A\alpha}\right\rangle^\alpha + \left\langle c_{A\alpha}\right\rangle^\alpha\nabla\varepsilon_\alpha + \frac{1}{\mathcal{V}_{\text{IV}}}\int_{A_{\alpha\eta}}\mathbf{n}_{\alpha\eta}c_{A\alpha}dA\right)\right] \tag{A.27}$$

where the integral of the interfacial flux is eliminated due to the boundary condition Eq. (6.5). In order to eliminate $c_{A\alpha}$ from the surface integrals, Gray's spatial decomposition [Gray, 1975] is used

$$c_{A\alpha} = \langle c_{A\alpha} \rangle^{\alpha} + \tilde{c}_{A\alpha} \tag{A.28}$$

where $\tilde{c}_{A\alpha}$ is the spatial deviation of species concentration in the α-phase. It follows that the interfacial integral term in Eq. (A.27) can be written as

$$\frac{1}{\mathcal{V}_{\text{IV}}} \int_{A_{\alpha\eta}} \mathbf{n}_{\alpha\eta} c_{A\alpha} dA = \frac{1}{\mathcal{V}_{\text{IV}}} \int_{A_{\alpha\eta}} \mathbf{n}_{\alpha\eta} \langle c_{A\alpha} \rangle^{\alpha} dA + \frac{1}{\mathcal{V}_{\text{IV}}} \int_{A_{\alpha\eta}} \mathbf{n}_{\alpha\eta} \tilde{c}_{A\alpha} dA \tag{A.29}$$

The intrinsic average is removed from the area integral using Taylor series about the centroid of the averaging volume $\mathcal{V}$, and applying the geometrical theorems [Quintard & Whitaker, 1994b] we get

$$\frac{\partial \left(\varepsilon_{\alpha} \langle c_{A\alpha} \rangle^{\alpha} \right)}{\partial t} + \langle \nabla . \left(\mathbf{v}_{\alpha} c_{A\alpha} \right) \rangle = \nabla . \left[D_{A\alpha} \left(\varepsilon_{\alpha} \nabla \langle c_{A\alpha} \rangle^{\alpha} + \frac{1}{\mathcal{V}_{\text{IV}}} \int_{A_{\alpha\eta}} \mathbf{n}_{\alpha\eta} \tilde{c}_{A\alpha} dA \right) \right] \tag{A.30}$$

with the length scale constraints

$$l_{\alpha} << r_0 \tag{A.31}$$

$$r_0^2 << L_{\varepsilon_{\alpha}} L_{c_{\alpha 1}} \tag{A.32}$$

The convective term remains to be treated. Applying the spacial averaging theorem and using Gray decomposition for the velocity and the species concentration, the convective term can be developed as

$$\langle \nabla . \left(\mathbf{v}_{\alpha} c_{A\alpha} \right) \rangle = \nabla . \left\langle \varepsilon_{\alpha} \langle \mathbf{v}_{\alpha} \rangle^{\alpha} \langle c_{A\alpha} \rangle^{\alpha} + \langle \mathbf{v}_{\alpha} \rangle^{\alpha} \tilde{c}_{A\alpha} + \tilde{\mathbf{v}}_{\alpha} \langle c_{A\alpha} \rangle^{\alpha} + \tilde{\mathbf{v}}_{\alpha} \tilde{c}_{A\alpha} \right\rangle \tag{A.33}$$

We suppose that the variations of the averaged quantities can be ignored within the averaging volume. It follows that the averages can be removed from the volume integrals, and the averages of the deviations can be neglected (see [Whitaker, 1999, chap. 3.2] for more details). Eq. (A.33) is simplified as

$$\langle \nabla . \left(\mathbf{v}_{\alpha} c_{A\alpha} \right) \rangle = \nabla . \left(\varepsilon_{\alpha} \langle \mathbf{v}_{\alpha} \rangle^{\alpha} \langle c_{A\alpha} \rangle^{\alpha} + \langle \tilde{\mathbf{v}}_{\alpha} \tilde{c}_{A\alpha} \rangle \right) \tag{A.34}$$

Applying this result in Eq. (A.30), we obtain the *the unclosed averaged equation for mass transport in the α-phase*:

$$\frac{\partial \left(\varepsilon_{\alpha} \langle c_{A\alpha} \rangle^{\alpha} \right)}{\partial t} + \varepsilon_{\alpha} \langle \mathbf{v}_{\alpha} \rangle^{\alpha} . \nabla \langle c_{A\alpha} \rangle^{\alpha} = \nabla . \left[D_{A\alpha} \left(\varepsilon_{\alpha} \nabla \langle c_{A\alpha} \rangle^{\alpha} + \frac{1}{\mathcal{V}_{\text{IV}}} \int_{A_{\alpha\eta}} \mathbf{n}_{\alpha\eta} \tilde{c}_{A\alpha} dA \right) \right] - \nabla . \langle \tilde{\mathbf{v}}_{\alpha} \tilde{c}_{\alpha} \rangle \tag{A.35}$$

A.3 Closure

The deviation problem for momentum conservation is deduced by subtracting Eq. (A.23) to Eq. (6.2), and after some algebra

$$0 = -\nabla\tilde{p}_\alpha + \mu_\alpha\nabla^2\tilde{\mathbf{v}}_\alpha - \frac{1}{V_\alpha}\int_{A_{\alpha\eta}} \mathbf{n}_{\alpha\eta}.\left(-\mathbf{I}\tilde{p}_\alpha + \mu_\alpha\nabla\tilde{\mathbf{v}}_\alpha\right) dA \tag{A.36}$$

Here the closure problem is considered to be quasi-steady by imposing the constraint

$$\frac{\mu_\alpha}{\rho_\alpha}\frac{t_v}{l_\alpha^2} >> 1 \tag{A.37}$$

where t_v is the characteristic time for changes in the α-phase velocity. Note that assuming the closure problem to be quasi-steady does not mean the averaged problem to be quasi-steady.

The deviation problem for the continuity equation is obtained by subtracting Eq. (A.25) to Eq. (6.1)

$$\nabla.\tilde{\mathbf{v}}_\alpha = 0 \tag{A.38}$$

The deviation problem for the no-slip condition given by Eq. (6.4) is directly obtain from the spatial decomposition

$$\tilde{\mathbf{v}}_\alpha = -\langle\mathbf{v}_\alpha\rangle^\alpha \qquad \text{at } A_{\alpha\eta} \tag{A.39}$$

This equality plays a important role for the closure since it is the only source term in the momentum transport problem. Given the form of the source, a linear relation between the deviation and the average is proposed

$$\tilde{\mathbf{v}}_\alpha = \mathbf{B}_\alpha.\langle\mathbf{v}_\alpha\rangle^\alpha \tag{A.40}$$

$$\tilde{p}_\alpha = \mu_\alpha\mathbf{b}_\alpha.\langle\mathbf{v}_\alpha\rangle^\alpha \tag{A.41}$$

where $\mathbf{B}_\alpha$ and $\mathbf{b}_\alpha$ are the closure variables. Substituting these forms of the deviations in Eq. (A.23) we obtain the *closed averaged equation for momentum transport in the α-phase*:

$$\rho_\alpha\varepsilon_\alpha^{-1}\frac{\partial\left(\varepsilon_\alpha\langle\mathbf{v}_\alpha\rangle^\alpha\right)}{\partial t} = -\nabla\left\langle p_\alpha\right\rangle^\alpha + \mu_\alpha\nabla^2\left\langle\mathbf{v}_\alpha\right\rangle^\alpha - \frac{\mu_\alpha}{\mathbf{K}_\alpha^{\mathrm{III}}}\varepsilon_\alpha\langle\mathbf{v}_\alpha\rangle^\alpha \tag{A.42}$$

where $\mathbf{K}_\alpha^{\mathrm{III}}$ is the permeability tensor defined as

$$\varepsilon_\alpha\mathbf{K}_\alpha^{\mathrm{III}-1} = \frac{1}{V_\alpha}\int_{A_{\alpha\eta}}\mathbf{n}_{\alpha\eta}.(-\mathbf{I}\mathbf{b}_\alpha + \nabla\mathbf{B}_\alpha)dA \tag{A.43}$$

The permeability can be evaluated when solving the closure variable defined through the deviation problem

$$0 = -\nabla\mathbf{b}_\alpha + \nabla^2\mathbf{B}_\alpha + \varepsilon_\alpha\mathbf{K}_\alpha^{\mathrm{III}-1} \tag{A.44}$$

$$\nabla.\mathbf{B}_\alpha = 0 \tag{A.45}$$

$$\mathbf{B}_\alpha = -\mathbf{I} \quad \text{at } A_{\alpha\eta} \tag{A.46}$$

$$\langle\mathbf{B}_\alpha\rangle^\alpha = 0 \tag{A.47}$$

$$\mathbf{B}_\alpha(\mathbf{x}+l_i) = \mathbf{B}_\alpha(\mathbf{x}) \qquad i = 1,2,3 \tag{A.48}$$

Following the same methodology, the deviation problem for mass transport in the α-phase is derived

$$\tilde{\mathbf{v}}_\alpha.\nabla\langle c_{A\alpha}\rangle^\alpha + \mathbf{v}_\alpha.\nabla\tilde{c}_{A\alpha} = \nabla.\left(D_{A\alpha}\nabla\tilde{c}_{A\alpha}\right) - \frac{1}{V_\alpha}\int_{A_{\alpha\eta}} \mathbf{n}_{\alpha\eta}.\left(D_{A\alpha}\nabla\tilde{c}_{A\alpha}\right)dA + \varepsilon_\alpha^{-1}\nabla.\langle\tilde{\mathbf{v}}_\alpha\tilde{c}_{A\alpha}\rangle \quad \text{(A.49)}$$

Comparing the orders of magnitude

$$\mathbf{v}_\alpha.\nabla\tilde{c}_{A\alpha} = O\left(\langle v_\alpha\rangle\frac{\tilde{c}_{A\alpha}}{l_\alpha}\right) \quad \text{(A.50)}$$

$$\varepsilon_\alpha^{-1}\nabla.\langle\tilde{\mathbf{v}}_\alpha\tilde{c}_{A\alpha}\rangle = O\left(\langle v_\alpha\rangle\frac{\tilde{c}_{A\alpha}}{L}\right) \quad \text{(A.51)}$$

the last term of Eq. (A.49) can be neglected on the basis of length scale separation.

The simplified deviation problem for mass transport in the α-phase can then be written, using the weighted average concentration

$$\tilde{\mathbf{v}}_\alpha.\nabla\langle c_{A\alpha}\rangle^\alpha + \mathbf{v}_\alpha.\nabla\tilde{c}_{A\alpha} = \nabla.\left(D_{A\alpha}\nabla\tilde{c}_{A\alpha}\right) - \frac{1}{V_\alpha}\int_{A_{\alpha\eta}} \mathbf{n}_{\alpha\eta}.\left(D_{A\alpha}\nabla\tilde{c}_{A\alpha}\right)dA \quad \text{(A.52)}$$

Using the spacial decomposition in the boundary condition Eq. (6.5) we obtain

$$-\mathbf{n}_{\alpha\eta}.D_{A\alpha}\nabla\tilde{c}_{A\alpha} = \mathbf{n}_{\alpha\eta}.D_{A\alpha}\nabla\langle c_{A\alpha}\rangle^\alpha \quad \text{(A.53)}$$

Considering the form of the source terms in the mass transport deviation problem, the closure variable is defined trough the relation between the deviation and the gradient of the averaged concentration

$$\tilde{c}_{A\alpha} = \mathbf{d}_\alpha.\nabla\langle c_{A\alpha}\rangle^\alpha \quad \text{(A.54)}$$

and the closed averaged equation for mass transport in the α-phase can then be written in the form

$$\frac{\partial\left(\varepsilon_\alpha\langle c_{A\alpha}\rangle^\alpha\right)}{\partial t} + \varepsilon_\alpha\langle\mathbf{v}_\alpha\rangle^\alpha.\nabla\langle c_{A\alpha}\rangle^\alpha = \nabla.\left(\mathbf{D}_{A\alpha}^{\mathrm{III}}.\nabla\langle c_{A\alpha}\rangle^\alpha\right) \quad \text{(A.55)}$$

where the diffusion/dispersion tensor is defined as

$$\mathbf{D}_{A\alpha}^{\mathrm{III}} = D_{A\alpha}\left(\varepsilon_\alpha\mathbf{I} + \frac{1}{\mathcal{V}}\int_{A_{\alpha\eta}}\mathbf{n}_{\alpha\eta}\mathbf{d}_\alpha dA\right) + \langle\tilde{\mathbf{v}}_\alpha\mathbf{d}_\alpha\rangle \quad \text{(A.56)}$$

and the closure variable $\mathbf{d}_\alpha$ is the solution of the closure problem

$$\tilde{\mathbf{v}}_\alpha + \mathbf{v}_\alpha.\nabla\mathbf{d}_\alpha = D_{A\alpha}\nabla^2\mathbf{d}_\alpha - \frac{D_{A\alpha}}{V_\alpha}\int_{A_{\alpha\eta}}\mathbf{n}_{\alpha\eta}.\nabla\mathbf{d}_\alpha dA \quad \text{(A.57)}$$

$$-\mathbf{n}_{\alpha\eta}.\nabla\mathbf{d}_\alpha = \mathbf{n}_{\alpha\eta} \quad \text{(A.58)}$$

$$\langle\mathbf{d}_\alpha\rangle = 0 \quad \text{(A.59)}$$

$$\mathbf{d}_\alpha(\mathbf{x}+l_i) = \mathbf{d}_\alpha(\mathbf{x}) \qquad i=1,2,3 \quad \text{(A.60)}$$

APPENDIX **B**

DISPERSION IN BI-DISPERSE HIERARCHICAL POROUS MEDIA

Transport phenomena in porous systems often involve "multi-porous" configurations where, for instance, the solid matrix can also be porous, the pores at the different scales (micro- and macro-pores) being saturated by the same fluid. Another example concerns porous structures where the impermeable solid macro-structure is embedded in a finer saturated porous medium, itself eventually embedded in another finer porous structure and so on (see figure B.1). In other words, the pores at a given scale are filled by a finer porous medium whose structure is not necessarily the same than the structure at the upper scale.

This type of *hierarchical* porous media has been characterized using several terminologies depending on the number of scales and on the associated porous morphologies. For example, two-scale porous structures composed of spherical solid particules are described as "binary mixture" [Mota et al., 2001], "multisized" porous media [MacDonald et al., 1991; Dias et al., 2008; Morad & Khalili, 2009], "bimodal" distribution of particles [Guyon et al., 1987; Vahedi Tafreshi et al., 2009] or "bidisperse" [Moutsopoulos & Koch, 1999; Moutsopoulos et al., 2009]. This latter terminology has been widely used to describe transfer phenomena in catalyst pellets where the porous architecture is represented by micro- and macro-pore network, the terminology "bidisperse" being in that case, the dispersion of the pore size instead of the grain size [Burghardt et al., 1988; Petropoulos et al., 1991; Silva & Rodrigues, 1996].

Although these multiscale porous structures are present in a large variety of applications (packed-bed reactors, sandy soils,...), few attempts have been performed in order to propose averaged models taking into account the hierarchical dependence on the geometry and the physics at the different scales of the system. Part of the studies have been devoted to the determination of the permeability. Modified expression of the Kozeny-Carman relationship have been obtained for porous structures composed by multi-sized spherical particles [MacDonald et al., 1991; Mota et al., 2001; Dias et al., 2008; Moutsopoulos et al., 2009] or for bimodal fibrous porous media [Vahedi Tafreshi et al., 2009; Markicevic & Djilali, 2006]. A bidiperse porous medium composed by two types of spheres has been considered using ensemble average Moutsopoulos & Koch [1999]. It was found that the small grains have higher influence

on the permeability, while large grains have stronger effect on dispersion. The contribution from the mass transfer boundary layer to the effective dispersion at the larger scale was emphasized. In this study, the theory for moderate and highly permeable media were developed separately.

On the contrary, the objective of the present study is to derive a general macroscopic model for momentum and solute dispersion in a three-scale hierarchical porous structure (many intermediate scales could have been incorporated in the analysis). Two upscaling are successively performed using the volume averaging method Whitaker [1999] and the effective transport properties (permeability, diffusion-dispersion coefficient) at the different scales are determined by numerically solving the associated closure problems. Note that similar analysis have been performed in the context of large-scale averaging of heterogeneous porous media for momentum [Quintard & Whitaker, 1996b,a, 1998a] and solute transport [Quintard & Whitaker, 1998b; Ahmadi et al., 1998; Quintard et al., 2001; Cherblanc et al., 2003]. However, as previously said, hierarchical porous structures considered in the present study differ from the heterogeneous one in the cited references since they are characterized by impermeable solid matrix embedded in finer porous regions. Therefore, momentum is governed by Darcy-Brinkman equation within the pores of the finer porous region where no slip condition is adopted at the solid/porous interface. Nevertheless, the analysis for solute dispersion presents similarities which are detailed in appendix. Numerical results show the influence of the micro- and meso-scale phenomena on permeability and dispersion coefficients at the macroscale.

B.1 Upscaling analysis

B.1.1 Mesoscopic Model

The hierarchical multiscale porous structure under consideration is represented Figure B.1. At the microscopic scale (level III) the porous structure is composed by a rigid and inert solid matrix (κ-phase) saturated by a newtonian fluid (α-phase). The porous medium is assummed to be homogeneous and physical properties of both the fluid and solid phases are constant. In addition, the flow is supposed to be laminar and incompressible. Therefore, conservation equations for momentum and species transport at scale III take the classical form

$$\nabla.\mathbf{v}_\alpha = 0 \tag{B.1}$$

$$\rho_\alpha \frac{\partial \mathbf{v}_\alpha}{\partial t} = -\nabla p_\alpha + \rho_\alpha \mathbf{g} + \mu_\alpha \nabla^2 \mathbf{v}_\alpha \tag{B.2}$$

$$\mathbf{v}_\alpha = 0 \quad \text{at } A_{\alpha\kappa} \tag{B.3}$$

$$\frac{\partial c_{A\alpha}}{\partial t} + \mathbf{v}_\alpha.\nabla c_{A\alpha} = \nabla.\left(\mathcal{D}_A \nabla c_{A\alpha}\right) \tag{B.4}$$

$$-\mathbf{n}_{\alpha\kappa}.\left(\mathcal{D}_{A\alpha}\nabla c_{A\alpha}\right) = 0 \quad \text{at } A_{\alpha\kappa} \tag{B.5}$$

where $\mathbf{v}_\alpha$, p_α and $c_{A\alpha}$ are the velocity, pressure and concentration in the α-phase, respectively. ρ_α, μ_α and $\mathcal{D}_{A\alpha}$ are the density, the dynamic viscosity and the molecular diffusivity coefficient

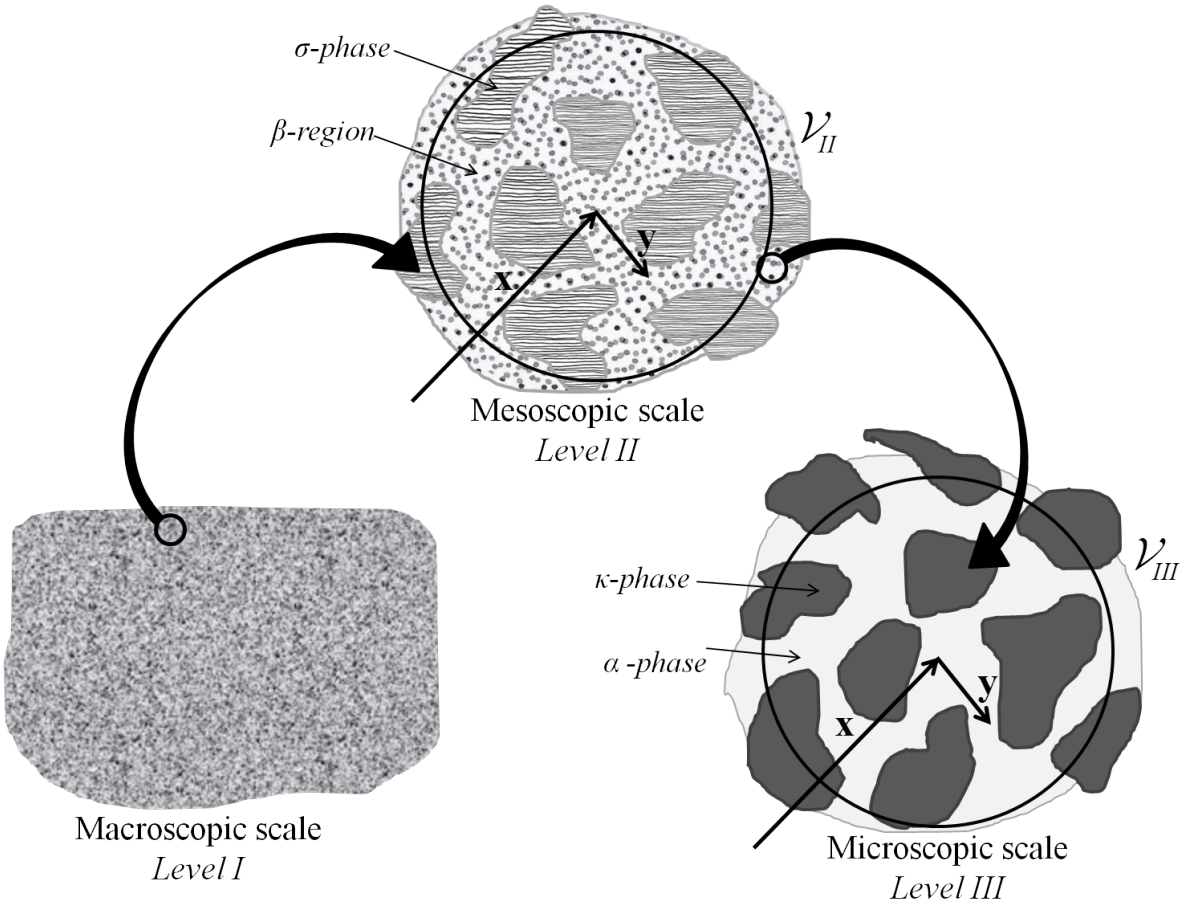

Figure B.1 – Representation of the hierarchical porous medium

of the α-phase while $\mathbf{g}$ is the gravity. Equations (B.3) and (B.5) represent the no-slip and no-species flux boundary conditions at the fluid-solid interface $A_{\alpha\kappa}$, respectively where $\mathbf{n}_{\alpha\kappa}$ is the unit normal vector oriented from the α-phase toward the κ-phase.

Averaging this above problem using the volume averaging method Whitaker [1999] has been extensively detailed in the litterature Whitaker [1986a]; Quintard & Whitaker [1994a]; Whitaker [1999]; Bousquet-Melou et al. [2002]; Neculae et al. [2002] and for conciseness, only the resulting mesoscopic model at scale II is presented below

$$\nabla.\langle \mathbf{v}_\alpha \rangle_\beta = 0 \tag{B.6}$$

$$\rho_\alpha \varepsilon_\alpha^{-1} \frac{\partial \langle \mathbf{v}_\alpha \rangle_\beta}{\partial t} = -\nabla \langle p_\alpha \rangle_\beta^\alpha - \frac{\mu_\alpha}{\mathbf{K}_\alpha^*} \langle \mathbf{v}_\alpha \rangle_\beta + \mu_\alpha \varepsilon_\alpha^{-1} \nabla^2 \langle \mathbf{v}_\alpha \rangle_\beta + \rho_\alpha \mathbf{g} \tag{B.7}$$

$$\frac{\partial \left(\varepsilon_\alpha \langle c_{A\alpha} \rangle_\beta^\alpha \right)}{\partial t} + \langle \mathbf{v}_\alpha \rangle_\beta . \nabla \langle c_{A\alpha} \rangle_\beta^\alpha = \nabla . \left(\mathbf{D}_{A\alpha}^* . \nabla \langle c_{A\alpha} \rangle_\beta^\alpha \right) \tag{B.8}$$

where $\langle \mathbf{v}_\alpha \rangle_\beta$ is the superficial averaged velocity defined by

$$\langle \mathbf{v}_\alpha \rangle_\beta = \frac{1}{\mathcal{V}_{III}} \int_{\mathcal{V}^\alpha} \mathbf{v}_\alpha \, dV \tag{B.9}$$

while $\langle p_\alpha \rangle_\beta^\alpha$ and $\langle c_{A\alpha} \rangle_\beta^\alpha$ are the intrinsic averaged pressure and concentration given by

$$\langle p_\alpha \rangle_\beta^\alpha = \frac{1}{\mathcal{V}_\alpha} \int_{\mathcal{V}_\alpha} \mathbf{p}_\alpha \, dV \tag{B.10}$$

$$\langle c_{A\alpha} \rangle_\beta^\alpha = \frac{1}{\mathcal{V}_\alpha} \int_{\mathcal{V}_\alpha} \mathbf{c}_\alpha \, dV \tag{B.11}$$

Note that the subscript β is used to remember that the different variables are defined in the β-region. $\mathbf{K}_\alpha^*$ and $\mathbf{D}_{A\alpha}^*$ are the permeability and the diffusion-dispersion tensors of the region β at scale II, respectively. They are defined by

$$\varepsilon_\alpha \mathbf{K}_\alpha^{*-1} = -\frac{1}{\mathcal{V}_\alpha} \int_{A_{\alpha\kappa}} \mathbf{n}_{\alpha\kappa}. \left(-\mathbf{b}_\alpha + \nabla \mathbf{B}_\alpha\right) dA \tag{B.12}$$

$$\mathbf{D}_{A\alpha}^{*-1} = \mathcal{D}_{A\alpha} \left(\varepsilon_\alpha \mathbf{I} + \frac{1}{\mathcal{V}_{\text{III}}} \int_{A_{\alpha\kappa}} \mathbf{n}_{\alpha\kappa} \mathbf{d}_\alpha dA \right) - \langle \tilde{\mathbf{v}}_\alpha \mathbf{d}_\alpha \rangle \tag{B.13}$$

where $\mathbf{B}_\alpha$, $\mathbf{b}_\alpha$ and $\mathbf{d}_\alpha$ are the associated closure variables solution of the two following quasi-steady closure problems

$$0 = -\nabla \mathbf{b}_\alpha + \nabla^2 \mathbf{B}_\alpha + \varepsilon_\alpha \mathbf{K}_{\alpha,\beta}^{-1} \tag{B.14}$$

$$\nabla . \mathbf{B}_\alpha = 0 \tag{B.15}$$

$$\mathbf{B}_\alpha = -\mathbf{I} \qquad \text{at } A_{\alpha\kappa} \tag{B.16}$$

$$\mathbf{B}_\alpha(\mathbf{x}) = \mathbf{B}_\alpha(\mathbf{x} + l_i) \qquad i = 1, 2, 3 \tag{B.17}$$

$$\mathbf{b}_\alpha(\mathbf{x}) = \mathbf{b}_\alpha(\mathbf{x} + l_i) \qquad i = 1, 2, 3 \tag{B.18}$$

$$\langle \mathbf{B}_\alpha \rangle^\alpha = 0 \tag{B.19}$$

$$\tilde{\mathbf{v}}_\alpha + \mathbf{v}_\alpha . \nabla \mathbf{d}_\alpha = \mathcal{D}_{A\alpha} \nabla^2 \mathbf{d}_\alpha \tag{B.20}$$

$$-\mathbf{n}_{\alpha\kappa} . \nabla \mathbf{d}_\alpha = \mathbf{n}_{\alpha\kappa} \qquad \text{at } A_{\alpha\kappa} \tag{B.21}$$

$$\mathbf{d}_\alpha(\mathbf{x}) = \mathbf{d}_\alpha(\mathbf{x} + l_i) \qquad i = 1, 2, 3 \tag{B.22}$$

$$\langle \mathbf{d}_\alpha \rangle^\alpha = 0 \tag{B.23}$$

It si worth recalling that these problems have been derived on the framework of spacial and time scale separations [Goyeau et al., 1999]. In order to determine the effective transport properties at scale II, these closure problems are solved numerically using Comsol Multiphysics Software. The numerical validation of the determination of the permeability, not reported here, has been performed by comparing the numerical results with the analytical solution provided by Zick and Homsy Zick & Homsy [1982] for cubic periodic array of spheres.

In the following, the analysis is performed using two bi-dimensional periodic inline and staggered cylinder unit cells (Fig. B.2). First, at the mesoscopic scale, the permeability given by Eq. (B.12) is computed for different porosity values and the dimensionless longitudinal component of $\mathbf{K}_\alpha^*$ is plotted in Fig. B.3. Then, the diffusion-dispersion tensor defined by Eq. (B.13) is computed for different solutal Péclet numbers and for three porosity values ($\varepsilon_\alpha = 0.55$, 0.75 and 0.95). The longitudinal diffusion-dispersion coefficient plotted in Fig.

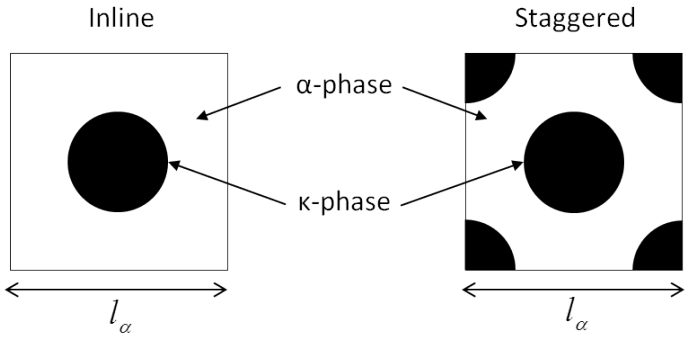

Figure B.2 – Geometries of the periodic unit cell at scale III

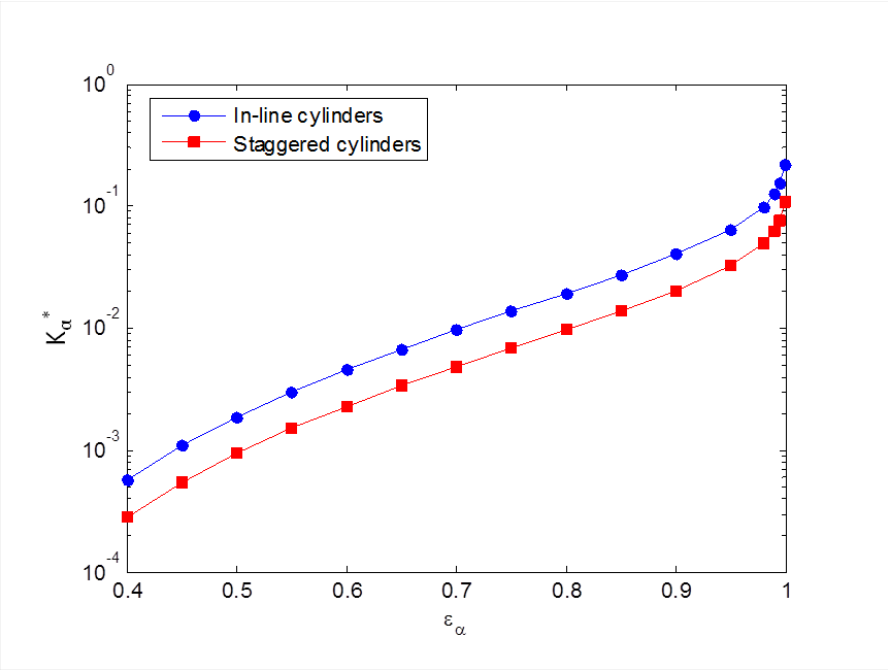

Figure B.3 – Longitudinal dimensionless permeability for in-line and staggered cylinders.

B.4 shows mainly two classical regions where the diffusion dominates for small or moderate Péclet numbers while dispersion process strongly dominates at high Péclet numbers. Note that the transition between the two regimes depends on the arrangement of the microstructure. Indeed, this transition takes place at a larger range of Péclet for the staggered configuration and the longitudinal coefficient is found to be of one order of magnitude smaller than for the in-line structure. This is mainly due to the fact that, in this latter case, dispersion mainly occurs in the direction of the flow while transverse dispersion is found to be important for the more tortuous staggered structure Neculae et al. [2002].
Although classical, this preliminary upscaling is very important since it gives us the local information in the β-region at scale II. In order to simplify the notations, the following nomen-

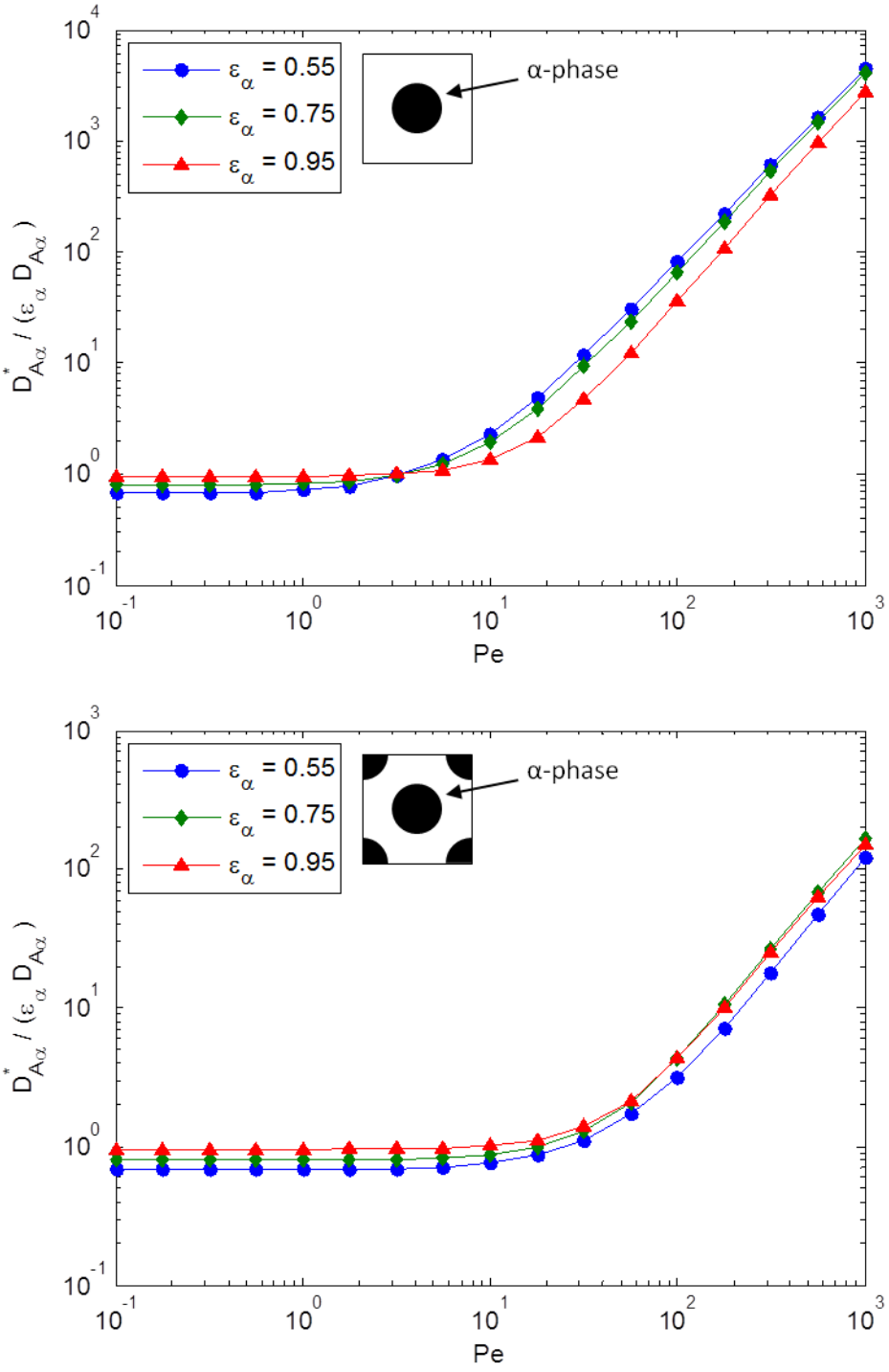

Figure B.4 – Longitudinal diffusion-dispersion for in-line cylinders (left), staggered cylinders (right)

clature is adopted before performing the second upscaling

$$\mathbf{v}_\beta = \langle \mathbf{v}_\alpha \rangle_\beta \tag{B.24}$$

$$p_\beta = \langle p_\alpha \rangle_\beta^\alpha \tag{B.25}$$

$$c_{A\beta} = \langle c_{A\alpha} \rangle_\beta \tag{B.26}$$

Therefore, transport equations (B.6) to (B.8) become:

$$\nabla.\mathbf{v}_\beta = 0 \quad \text{in the } \beta\text{-region} \tag{B.27}$$

$$\rho_\alpha \varepsilon_\alpha^{-1} \frac{\partial \mathbf{v}_\beta}{\partial t} = -\nabla p_\beta - \frac{\mu_\alpha}{\mathbf{K}_\alpha^*} \mathbf{v}_\beta + \mu_\alpha \varepsilon_\alpha^{-1} \nabla^2 \mathbf{v}_\beta + \rho_\alpha \mathbf{g} \quad \text{in the } \beta\text{-region} \tag{B.28}$$

$$\varepsilon_\alpha \frac{\partial c_{A\beta}}{\partial t} + \mathbf{v}_\beta.\nabla c_{A\beta} = \nabla.\left(\mathbf{D}_{A\alpha}^*.\nabla c_{A\beta}\right) \quad \text{in the } \beta\text{-region} \tag{B.29}$$

It is worth recalling that the effective dispersion tensor $\mathbf{D}_{A\alpha}^*$ depends on the cell Péclet number defined by

$$Pe_\alpha = \frac{\| v_\alpha \| l_\alpha}{\mathcal{D}_\alpha} \tag{B.30}$$

with

$$\| v_\alpha \| = \left(\langle \mathbf{v}_\alpha \rangle^\alpha . \langle \mathbf{v}_\alpha \rangle^\alpha \right)^{1/2} \tag{B.31}$$

and using the new nomenclature gives

$$\| v_\alpha \| = \left(\mathbf{v}_\beta . \mathbf{v}_\beta \right)^{1/2} \tag{B.32}$$

This clearly indicates that $\mathbf{D}_{A\alpha}^*$, is dependent on the local mesoscopic velocity field. Consequences on the derivation of the macroscopic solute transport at the are detailled in section B.1.2 Before, let us define the boundary conditions at the porous/solid interface $A_{\beta\sigma}$. Strictly speaking, boundary conditions at the interface between a porous layer and an homogeneous plain region (fluid or solid) should result from upscaling the local transport phenomena in this interfacial region. This has been the object of intense research activity for transport modeling at a fluid-porous interface through the so-called Beavers and Joseph's problem [Beavers & Joseph, 1967; Ochoa et al., 1986; Goyeau et al., 2003; Valdés-Parada et al., 2013] but the equivalent for transport phenomena between a fluid and a solid is still missing. In the present analysis, since momentum transport is governed by the Darcy-Brinkman equation and due to the fact that the larger solid spheres are impermeable, a no-slip condition and a null diffusive flux are considered at $A_{\beta\sigma}$

$$\mathbf{v}_\beta = 0 \quad \text{at } A_{\beta\sigma} \tag{B.33}$$

$$\mathbf{n}_{\beta\sigma}.\left(\mathbf{D}_{A\alpha}^*.\nabla c_{A\beta}\right) = 0 \quad \text{at } A_{\beta\sigma} \tag{B.34}$$

Eqs. (B.27) to (B.34) represent the local system at the mesoscopic scale (scale II). In order to derive macroscopic transport equations (scale I), the volume averaging method is applied once more. Note that the form of the system at scale II is similar than the one at scale III. The main differences are due to the presence of the Darcy term in Eq. (B.28) and to the non-constant diffusion-dispersion tensor in Eq. (B.29).

B.1.2 Macroscopic model

Momentum transport

Applying the averaging procedure to Eq. (B.28) leads to the following non-closed macroscopic equation

$$\rho_\alpha \varepsilon_\alpha^{-1} \frac{\partial \left(\varepsilon_\beta \langle \mathbf{v}_\beta \rangle^\beta\right)}{\partial t} = -\varepsilon_\beta \nabla \langle p_\beta \rangle^\beta - \frac{\mu_\alpha}{\mathbf{K}_\alpha^*} \varepsilon_\beta \langle \mathbf{v}_\beta \rangle^\beta + \mu_\alpha \varepsilon_\alpha^{-1} \varepsilon_\beta \nabla^2 \langle \mathbf{v}_\beta \rangle^\beta + \varepsilon_\beta \rho_\alpha \mathbf{g} + \frac{1}{\mathcal{V}_{\text{II}}} \int_{A_{\beta\sigma}} \mathbf{n}_{\beta\sigma}. \left(-\mathbf{I}\tilde{p}_\beta + \mu_\alpha \varepsilon_\alpha^{-1} \nabla \tilde{\mathbf{v}}_\beta\right) dA \quad \text{(B.35)}$$

where $\tilde{\mathbf{v}}_\beta$ and $\tilde{p}_\beta$ are the spacial deviations of the velocity and the pressure [Gray, 1975], respectively. It is worth mentioning that Eq. (B.35) is valid under the following length scale constraints [Whitaker, 1999]

$$l_\beta << r_0 \quad \text{(B.36)}$$
$$r_0^2 << L_\varepsilon L_{p1} \quad \text{(B.37)}$$
$$r_0^2 << L_\varepsilon L_{v1} \quad \text{(B.38)}$$
$$r_0^2 << L_\varepsilon L_{v2} \quad \text{(B.39)}$$

where l_β is the mesoscopic pore length scale, r_0 being the size of the averaging volume $\mathcal{V}_{\text{II}}$. L_{p1}, L_{v1} and L_{v2} represent the characteristic length scales for the macroscopic pressure gradient, velocity gradient and velocity laplacian, respectively. In order to close equation (B.35), deviations fields $\tilde{\mathbf{v}}_\beta$ and $\tilde{p}_\beta$ are determined through associated deviation problem which is obtained by subtracting the non-closed macroscopic equations to the local ones where the spatial decomposition has been previously introduced. This leads to the following deviation problem

$$\nabla.\tilde{\mathbf{v}}_\beta = 0 \qquad \text{in the } \beta\text{-region} \quad \text{(B.40)}$$

$$0 = -\nabla \tilde{p}_\beta - \frac{\mu_\alpha}{\mathbf{K}_\alpha^*} \tilde{\mathbf{v}}_\beta + \mu_\alpha \varepsilon_\alpha^{-1} \nabla^2 \tilde{\mathbf{v}}_\beta - \frac{1}{V_\beta} \int_{A_{\beta\sigma}} \mathbf{n}_{\beta\sigma}. \left(-\mathbf{I}\tilde{p}_\beta + \mu_\alpha \varepsilon_\alpha^{-1} \nabla \tilde{\mathbf{v}}_\beta\right) dA \qquad \text{in the } \beta\text{-region} \quad \text{(B.41)}$$

$$\tilde{\mathbf{v}}_\beta = -\langle \mathbf{v}_\beta \rangle^\beta \qquad \text{at } A_{\beta\sigma} \quad \text{(B.42)}$$

The only source term in this deviation problem is given by the boundary condition (B.42) whose form suggests us to writte the deviations under the form

$$\tilde{\mathbf{v}}_\beta = \mathbf{B}_\beta.\langle \mathbf{v}_\beta \rangle^\beta \quad \text{(B.43)}$$
$$\tilde{p}_\beta = \mu_\alpha \varepsilon_\alpha^{-1} \mathbf{b}_\beta.\langle \mathbf{v}_\beta \rangle^\beta \quad \text{(B.44)}$$

where $\mathbf{b}_\beta$ and $\mathbf{B}_\beta$ represent the closure variables. Substituting the above expressions in the non-closed averaged momentum equation (B.35) gives

$$\rho_\alpha \varepsilon_\alpha^{-1} \varepsilon_\beta^{-1} \frac{\partial \left(\varepsilon_\beta \langle \mathbf{v}_\beta \rangle^\beta\right)}{\partial t} = -\nabla \langle p_\beta \rangle^\beta + \mu_\alpha \varepsilon_\alpha^{-1} \nabla^2 \langle \mathbf{v}_\beta \rangle^\beta + \rho_\alpha \mathbf{g} - \mu_\alpha \varepsilon_\alpha^{-1} \left[\frac{\varepsilon_\alpha}{\mathbf{K}_\alpha^*} - \frac{1}{V_\beta} \int_{A_{\beta\sigma}} \mathbf{n}_{\beta\sigma}. \left(-\mathbf{I}\mathbf{b}_\beta + \nabla \mathbf{B}_\beta\right) dA\right] \langle \mathbf{v}_\beta \rangle^\beta \quad \text{(B.45)}$$

In addition, if we define

$$\varepsilon_\alpha \varepsilon_\beta \mathbf{K}_\beta^{*-1} = -\frac{1}{V_\beta} \int_{A_{\beta\sigma}} \mathbf{n}_{\beta\sigma}.\left(-\mathbf{I}\mathbf{b}_\beta + \nabla \mathbf{B}_\beta\right) dA \tag{B.46}$$

the term in braces in Eq.(B.45) can be written such as

$$\varepsilon_\beta \mathbf{K}_{\text{eff}}^{*-1} = \varepsilon_\alpha \mathbf{K}_\alpha^{*-1} + \varepsilon_\beta \mathbf{K}_\beta^{*-1} \tag{B.47}$$

where $\mathbf{K}_{\text{eff}}$ represents the permeability tensor at the macroscopic scale (level I). It explicitly involves two contributions : the permeability arising from the microscale ($\mathbf{K}_\alpha^*$) and the drag at the mesoscale ($\mathbf{K}_\beta^*$). Using expression (B.47) in equation (B.45) leads to the averaged momentum equation under the following "Darcy-Brinkman" form [Brinkman, 1947]

$$\rho_\alpha \varepsilon_\alpha^{-1} \varepsilon_\beta^{-1} \frac{\partial \left(\varepsilon_\beta \langle \mathbf{v}_\beta \rangle^\beta\right)}{\partial t} = -\nabla \langle p_\beta \rangle^\beta - \frac{\mu_\alpha}{\mathbf{K}_{\text{eff}}} \varepsilon_\beta \langle \mathbf{v}_\beta \rangle^\beta + \mu_\alpha \varepsilon_\alpha^{-1} \nabla^2 \langle \mathbf{v}_\beta \rangle^\beta + \rho_\alpha \mathbf{g} \tag{B.48}$$

The determination of the macroscopic permeability must be performed in two steps: first $\mathbf{K}_\alpha^*$ is obtained solving the classical closure problem (Eqs. 6.18-6.27) on a representative periodic unit cell, while in a second step $\mathbf{K}_\beta^*$ is determined by solving the following new closure problem

$$0 = -\nabla \mathbf{b}_\beta - \varepsilon_\alpha \mathbf{K}_\alpha^{*-1} \mathbf{B}_\beta + \nabla^2 \mathbf{B}_\beta + \varepsilon_\beta \mathbf{K}_\beta^{*-1} \tag{B.49}$$

$$\nabla.\mathbf{B}_\beta = 0 \tag{B.50}$$

$$\mathbf{B}_\beta = -\mathbf{I} \quad \text{at } A_{\beta\sigma} \tag{B.51}$$

$$\mathbf{B}_\beta(\mathbf{x}) = \mathbf{B}_\beta(\mathbf{x} + l_i) \qquad i = 1, 2, 3 \tag{B.52}$$

$$\mathbf{b}_\beta(\mathbf{x}) = \mathbf{b}_\beta(\mathbf{x} + l_i) \qquad i = 1, 2, 3 \tag{B.53}$$

$$\langle \mathbf{B}_\beta \rangle^\beta = 0 \tag{B.54}$$

Note that this mesoscopic closure problem explicity involves the microscopic drag contribution through $\mathbf{K}_\alpha^*$.

Numerical results illustrating this hierarchical contribution are presented in figures B.5. The effective permeability at scale I, $\mathbf{K}_{\text{eff}}$ (solid lines) and the permeability at scale II, $\mathbf{K}_\beta$ (dashed lines) are plotted for different permeabilty values at the microscale III and for three ratio of the characteristic cell sizes. First, it can be seen that the permeability at the lowest scale $\mathbf{K}_\alpha$, strongly influence the macroscopic permeability coefficient, especially for large porosity values ε_β where $\mathbf{K}_{\text{eff}}$ tends to $\mathbf{K}_\alpha$. On the other hand, we verify that $\mathbf{K}_{\text{eff}}$ logically tends toward $\mathbf{K}_\beta$ for small ε_β values and obviously for ε_α close to one (fluid behavior). Note that these observations are verified whatever the ratio l_β / l_α.

Mass transport

Let us now focus our attention on the derivation of the macroscopic mass transport model and the determination of the associated effectif multiscale dispersion coefficient. The local mass transport at scale II is governed by equations Eqs. (B.29) and (B.33). Eq. (B.29)

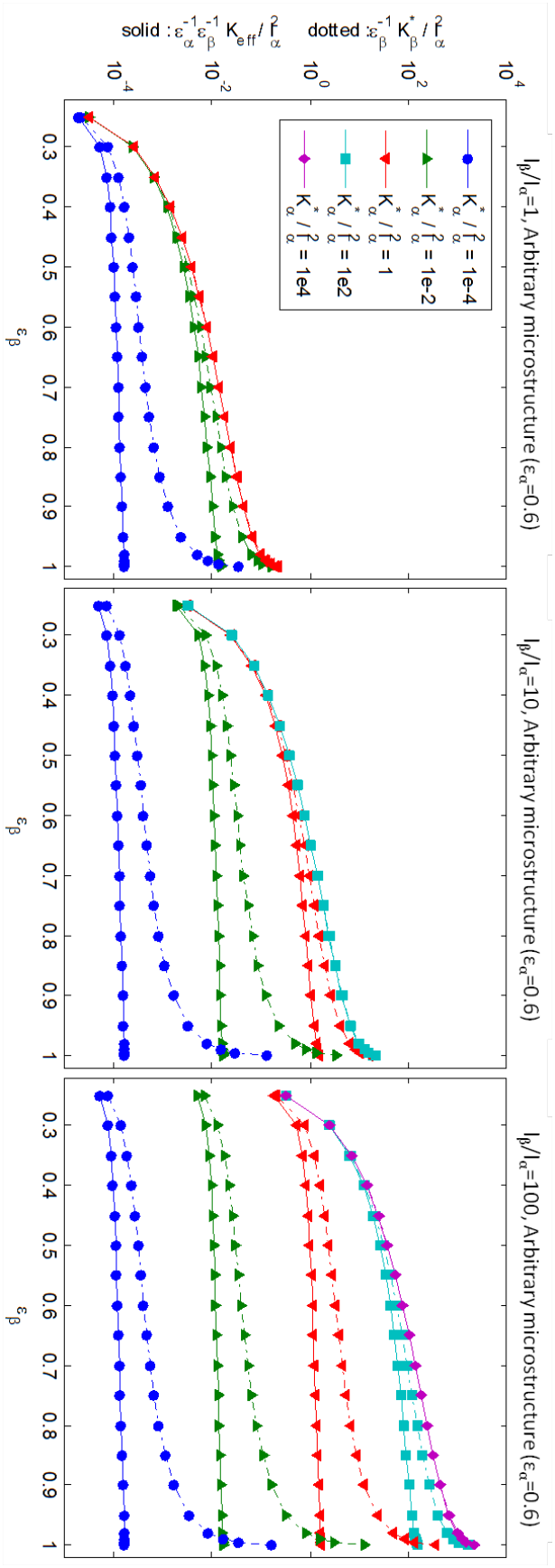

Figure B.5 – Effective permeability at scale I

looks familiar and therefore the derivation of a macroscopic form at scale I using the volume averaging method seems to be easy. However, the difficulty here lies in diffusive term whose effective diffusion-dispersion coefficient $\mathbf{D}^*_{A\alpha}$ depends on the local velocity field $\mathbf{v}_\beta$. This difficulty has been treated in the context of heterogeous porous media by Quintard & Whitaker [1998b] considering the spatial decomposition of the diffusion-dispersion effective coefficient. Following this idea, we propose the following spatial decomposition

$$\mathbf{D}^*_{A\alpha} = \langle \mathbf{D}^*_{A\alpha} \rangle^\beta + \tilde{\mathbf{D}}^*_{A\alpha} \tag{B.55}$$

For conciseness, only the main steps of the derivation are reported in this section, all the details being provided in Appendix B.3.1. Using also the spatial decomposition for concentration and velocity fields leads to the non-closed macroscopic mass transport equation

$$\begin{aligned} &\varepsilon_\alpha \frac{\partial \left(\varepsilon_\beta \langle c_{A\beta} \rangle^\beta \right)}{\partial t} + \varepsilon_\beta \langle \mathbf{v}_\beta \rangle^\beta . \nabla \langle c_{A\beta} \rangle^\beta = \\ &\nabla . \left[\langle \mathbf{D}^*_{A\alpha} \rangle^\beta . \left(\varepsilon_\beta \nabla \langle c_{A\beta} \rangle^\beta + \frac{1}{\mathcal{V}_{\text{II}}} \int_{A_{\beta\sigma}} \mathbf{n}_{\beta\sigma} \tilde{c}_{A\beta} dA \right) - \langle \tilde{\mathbf{v}}_\beta \tilde{c}_{A\beta} \rangle \right] + \nabla . \left\langle \tilde{\mathbf{D}}^*_{A\alpha} . \nabla \tilde{c}_{A\beta} \right\rangle \end{aligned} \tag{B.56}$$

where the right hand side corresponds to the multi-scale contributions to the diffusion-dispersion phenomena.The first term involving the tensor $\langle \mathbf{D}^*_{A\alpha} \rangle^\beta$ represents the averaged diffusion-dispersion at scale II while the second one is an additional dispersion contribution due to the dependence of $\mathbf{D}^*_{A\alpha}$ with the velocity field. The deviation problem is obtained by subtracting Eq. (B.56) from Eq. (B.29) where spatial decompositions have been previously introduced. Considering that scale separation and quasi stationarity are satisfied, the associated deviation problem takes the form

$$\tilde{\mathbf{v}}_\beta . \nabla \langle c_{A\beta} \rangle^\beta + \mathbf{v}_\beta . \nabla \tilde{c}_{A\beta} = \nabla . \left(\mathbf{D}^*_{A\alpha} . \nabla \tilde{c}_{A\beta} \right) + \nabla . \left(\tilde{\mathbf{D}}^*_{A\alpha} . \nabla \langle c_{A\beta} \rangle^\beta \right) \tag{B.57}$$

$$-\mathbf{n}_{\beta\sigma} . \left(\mathbf{D}^*_{A\alpha} . \nabla \tilde{c}_{A\beta} \right) = \mathbf{n}_{\beta\sigma} . \left(\mathbf{D}^*_{A\alpha} . \nabla \langle c_{A\beta} \rangle^\beta \right) \quad \text{at } A_{\beta\sigma} \tag{B.58}$$

The originality of this deviation problem lies in the presence of the averaged dispersion tensor (instead of the molecular diffusivity in a classical case) and in the last term of the right hand side of Eq. (B.57). In addition, from the boundary condition Eq. (B.58), it clearly appears that the two diffusive terms in Eq. (B.57) are of the same order of magnitude. Under these circumstances, the form of the macroscopic source terms in Eqs. (B.57) and (B.58) suggests that the deviation concentration $\tilde{c}_{A\beta}$ migh be related to the averaged values as

$$\tilde{c}_{A\beta} = \mathbf{d}_\beta . \nabla \langle c_{A\beta} \rangle^\beta + \phi_\beta \nabla^2 \langle c_{A\beta} \rangle^\beta \tag{B.59}$$

where ϕ_β and $\mathbf{d}_\beta$ are the closure variables. The introduction of expression (B.59) in Eqs. (B.57) and (B.58) would lead to two closure problems, one coresponding to the first order derivative of $\langle c_{A\beta} \rangle^\beta$ (for $\mathbf{d}_\beta$), the second one being of the third order derivative. By experience, it is known that expansion at the first order is sufficient to obtain an accurate determination of the effective transport properties Under these considerations, expression (B.59) reduces to

$$\tilde{c}_{A\beta} = \mathbf{d}_\beta . \nabla \langle c_{A\beta} \rangle^\beta \tag{B.60}$$

giving rise to the closure problem

$$\tilde{\mathbf{v}}_\beta + \mathbf{v}_\beta.\nabla\mathbf{d}_\beta = \nabla.\left(\mathbf{D}^*_{A\alpha}.\nabla\mathbf{d}_\beta\right) + \nabla.\tilde{\mathbf{D}}^*_{A\alpha} \tag{B.61}$$

$$-\mathbf{n}_{\beta\sigma}.\left(\mathbf{D}^*_{A\alpha}.\nabla\mathbf{d}_\beta\right) = \mathbf{n}_{\beta\sigma}.\mathbf{D}^*_{A\alpha} \qquad \text{at } A_{\beta\sigma} \tag{B.62}$$

$$\mathbf{d}_\beta(\mathbf{x}) = \mathbf{d}_\beta(\mathbf{x}+l_i) \qquad l_i = 1,2,3 \tag{B.63}$$

$$\langle\mathbf{d}_\beta\rangle^\beta = 0 \tag{B.64}$$

Note that a similar form including the aditionnal dispersion term has been obtained for solute transport in heterogeneous porous media [Quintard & Whitaker, 1998b; Ahmadi et al., 1998] but in their case, the source term involving $\tilde{\mathbf{D}}^*_{A\alpha}$ has been neglected since the velocity field was obtained from Darcy's law. In the present analysis, momentum transport is governed by the Darcy-Brinkman equation (Eq. (B.28)) giving rise to a non-constant diffusion-dispersion coefficient whose deviations can be significant. Finally, substituting Eq. (B.60) in Eq. (B.56) gives the closed form of the macroscopic conservation equation for mass transport

$$\varepsilon_\alpha \frac{\partial\left(\varepsilon_\beta\langle c_{A\beta}\rangle^\beta\right)}{\partial t} + \varepsilon_\beta\langle\mathbf{v}_\beta\rangle^\beta.\nabla\langle c_{A\beta}\rangle^\beta = \nabla.\left(\mathbf{D}_{\text{eff}}.\nabla\langle c_{A\beta}\rangle^\beta\right) \tag{B.65}$$

where the macroscopic diffusion-dispersion tensor is given by

$$\mathbf{D}_{\text{eff}} = \langle\mathbf{D}^*_{A\alpha}\rangle^\beta.\left(\varepsilon_\beta\mathbf{I} + \frac{1}{\mathcal{V}_{\text{II}}}\int_{A_{\beta\sigma}}\mathbf{n}_{\beta\sigma}\mathbf{d}_\beta dA\right) - \langle\tilde{\mathbf{v}}_\beta\mathbf{d}_\beta\rangle + \left\langle\tilde{\mathbf{D}}^*_{A\alpha}.\nabla\mathbf{d}_\beta\right\rangle \tag{B.66}$$

In this expression, let us recall that the $\mathbf{D}^*_{A\alpha}$ is an effective tensor resulting from the micro-mesoscopic upscaling. The first three terms in expression (B.66) represent the mesoscopic contribution to the macroscopic effective diffusion-dispersion coefficient while the last term is a diffusive contribution due to the deviation of the mesoscopic diffusion-dispersion tensor.

Numerical solutions of the closure problem given by equations (B.61)-(B.62) are obtained for the same hierarchical bidisperse porous structures previously used for the permeability. First, the longitudinal component of the effective diffusion-dispersion coefficient for in-line bidisperse structure is represented in figure B.6. It is observed that whatever the ratio l_β/l_α, the decrease of the average properties (ε_α and $\mathbf{K}_\alpha$) at scale III increases the tortuosity effect in the diffusive regime (small Péclet numbers) but also gives rise to a more intense dispersion regime ($Pe \geq 10$). We can observe in figure B.7 that the transition between the diffusive and the dispersive regimes takes place at larger Péclet numbers ($Pe \sim 10$) for staggered structure than for In-line structures where $Pe \sim 1$. Figure B.8 compares the different terms of the effective diffusion-dispersion coefficient given by Eq. (B.66) for $l_\beta/l_\alpha = 10$. As expected, it is shown that both the dimensionless mesoscopic contribution $< \tilde{\mathbf{v}}_\beta\mathbf{d}_\beta >$ and macroscopic dispersion term $< \tilde{\mathbf{D}}^*_{A\alpha}.\nabla\mathbf{d}_\beta >$ strongly depend on the Péclet number. Indeed, a diffusive regime is found for small or moderate Péclat numbers while a dispersive behavior is illustrated for high Péclet numbers. In addition, the ratio between these two terms shows that the mesoscopic contribution is about one order of magnitude smaller than the macroscopic dispersion for small Péclet number but this difference becomes smaller at large Péclet number especially with the increase of porosity and permeability at the mesoscopic scale. Note that

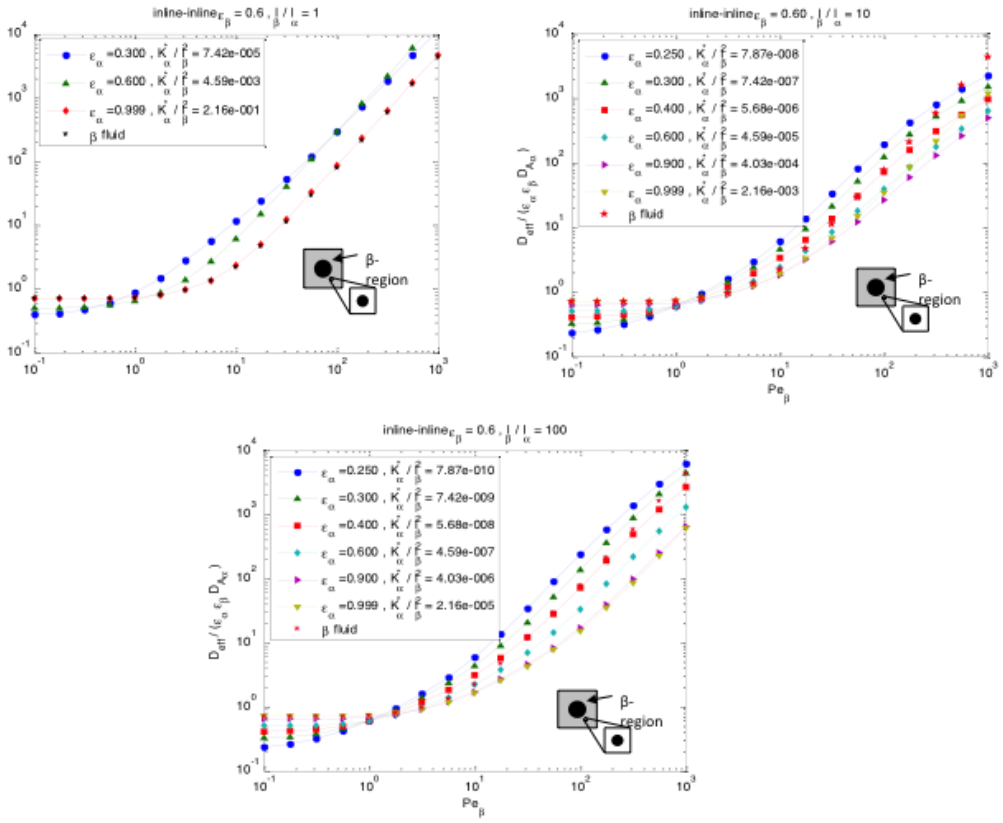

Figure B.6 – Longitudinal diffusion-dispersion coefficient for a bidisperse in-line cylinders configuration

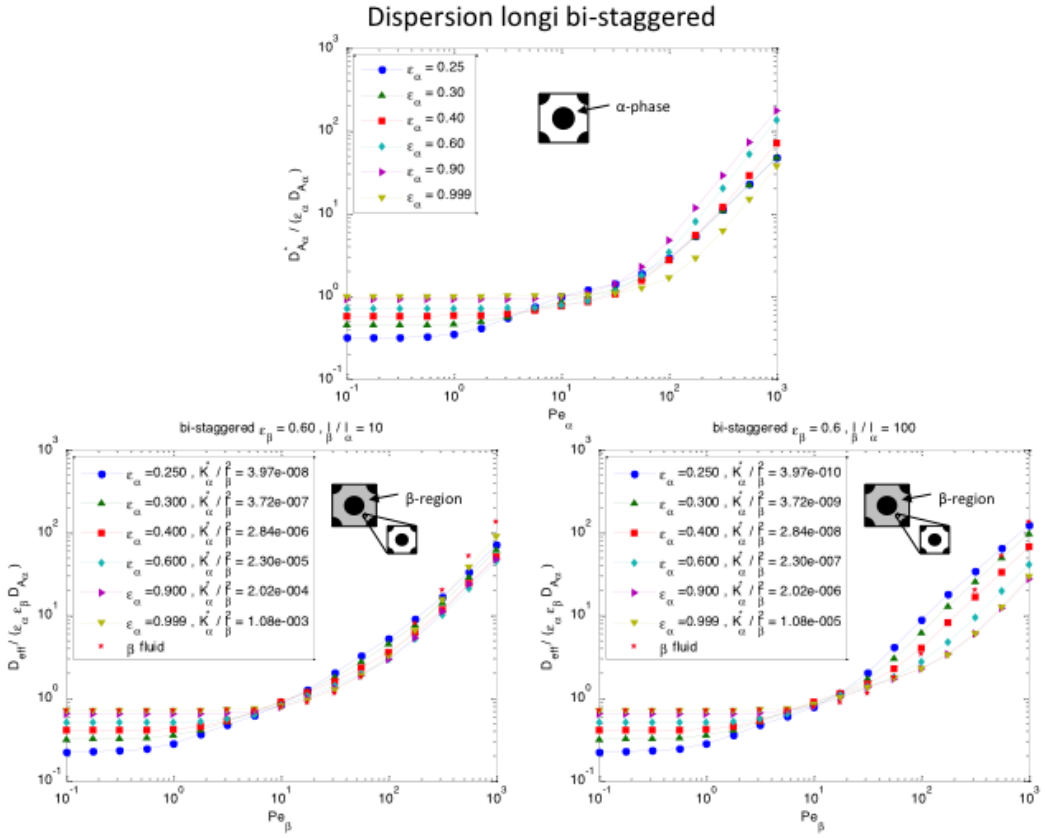

Figure B.7 – Longitudinal diffusion-dispersion coefficient for a bidisperse staggered cylinders configuration

this behaviour is in agreement with Moutsopoulos & Koch [1999] but our analysis provides a more general and explicit formulation able to quantify the influence of the finest porous structure in a such a bidisperse configuration.

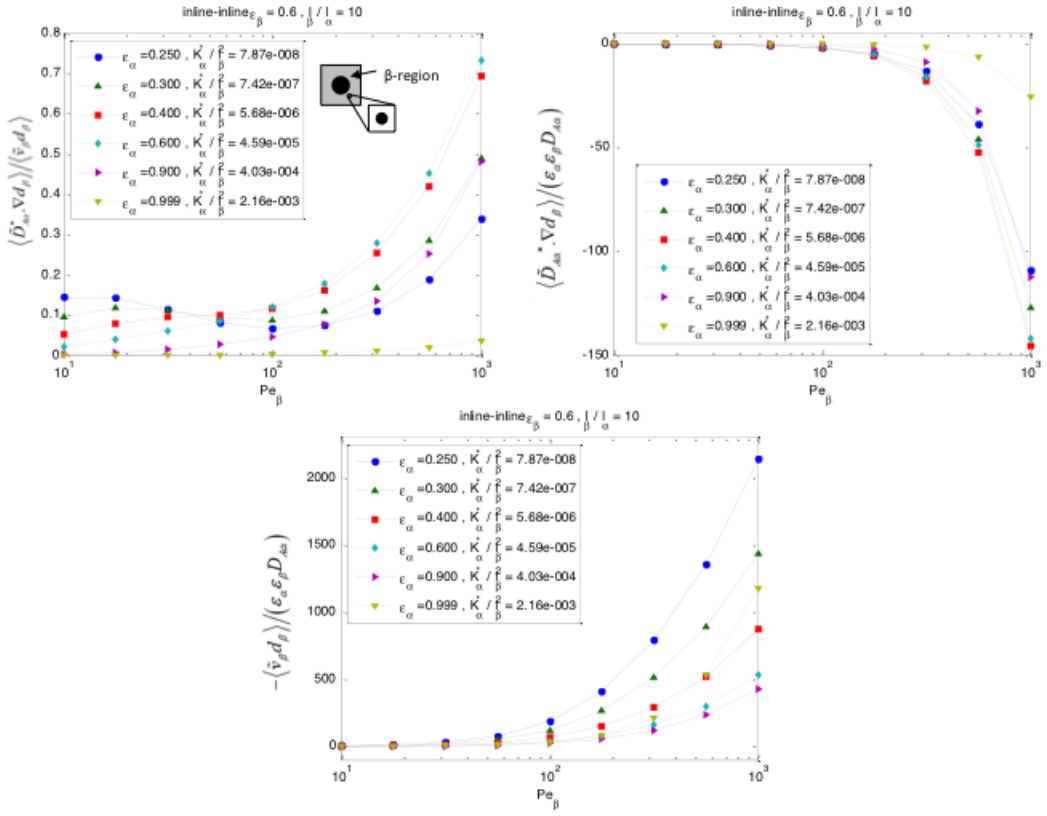

Figure B.8 – Comparison of the different terms of the effective diffusion-dispersion coefficient given by (B.66) for $l_\beta/l_\alpha = 10$.

For $l_\beta/l_\alpha = 100$, the macroscopic dispersion term (last term in (B.66)) strongly dominates the others contributions whatever the mesocopic porosity and permeabilty values (Figure B.9). This behaviour is in agreement with Moutsopoulos & Koch [1999] but our analysis provides

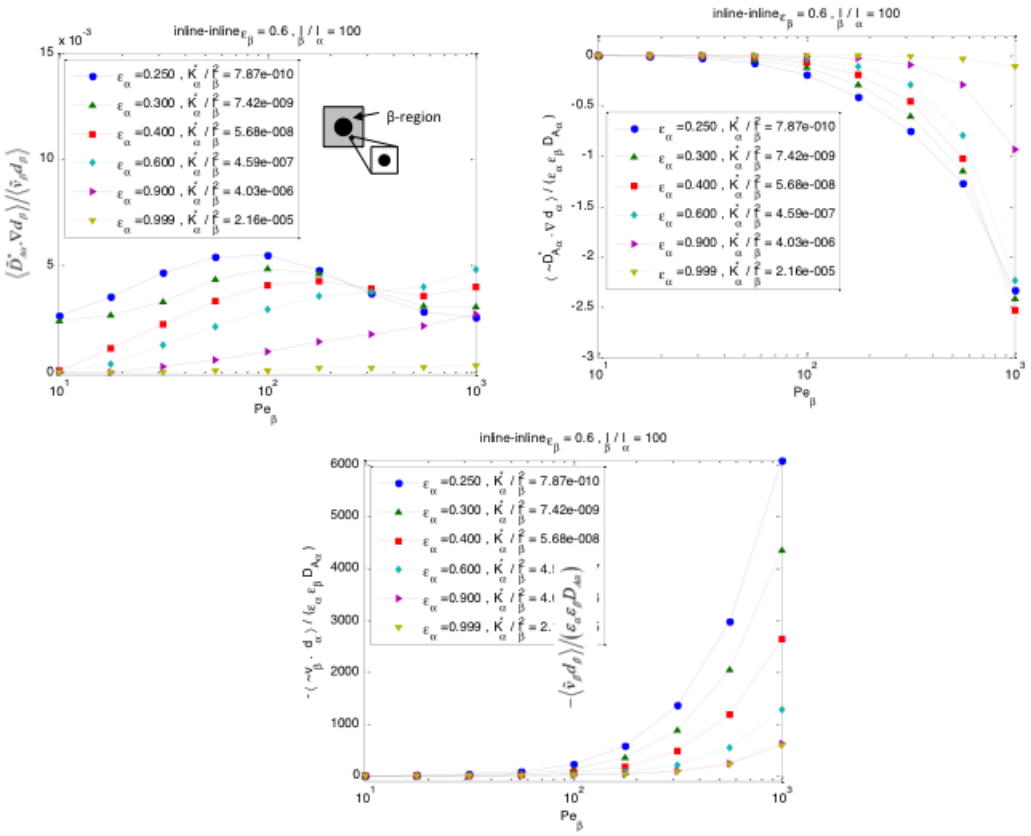

Figure B.9 – Comparison of the different terms of the effective diffusion-dispersion coefficient given by (B.66) for $l_\beta/l_\alpha = 100$.

a more general and explicit formulations in order to quantify the influence of the finest porous structures on the effective diffusion-dispersion coefficient.

B.2 Conclusion

A general macroscopic model for momentum and solute dispersion in a hierarchical bidisperse porous structures has been developed using the volume averaging methyyod. The closure problems associated to the macroscopic effective transport properties have been derived and solved numerically. The results illustrate the influence of the mesoscopic scale on the macroscopic ones. Momentum is governed by Darcy-Brinkman equation within the pores of the finer porous region where no slip condition is adopted at the solid/porous interface.

Nevertheless, the analysis for solute dispersion presents similarities which are detailed in appendix B3. Numerical results show the influence of the micro- and meso-scale phenomena on permeability and dispersion coefficients at the macroscale.

B.3 Appendix

B.3.1 Derivation of the macroscopic solute transport equation

The macroscopic solute transport equation is derived by averaging the mesoscopic equation (Eq. B.29) with the associated boundary condition (Eq. (B.34)). The difficulty here lies in the fact that the diffusion-dispersion tensor $\mathbf{D}^*_{A\alpha}$ depends on the velocity field. Let us focus our attention on the averaging the right hand side of Eq. B.29. Applying the averaging theorems gives

$$\langle \nabla . \left(\mathbf{D}^*_{A\alpha} . \nabla c_{A\beta} \right) \rangle = \nabla . \langle \mathbf{D}^*_{A\alpha} . \nabla c_{A\beta} \rangle + \frac{1}{\mathcal{V}_{\text{II}}} \int_{A_{\beta\sigma}} \mathbf{n}_{\beta\sigma} . \left(\mathbf{D}^*_{A\alpha} . \nabla c_{A\beta} \right) dA \tag{B.67}$$

where the area integral is discarded due to the boundary condition (Eq. (B.34)). Following Quintard & Whitaker [1998b], the tensor $\mathbf{D}^*_{A\alpha}$ can be decomposed under the form

$$\mathbf{D}^*_{A\alpha} = \langle \mathbf{D}^*_{A\alpha} \rangle^\beta + \tilde{\mathbf{D}}^*_{A\alpha} \tag{B.68}$$

and also using the spacial decomposition for the concentration $c_{A\beta}$ gives

$$\langle \mathbf{D}^*_{A\alpha} . \nabla c_{A\beta} \rangle = \left\langle \langle \mathbf{D}^*_{A\alpha} \rangle^\beta . \nabla \langle c_{A\beta} \rangle^\beta + \langle \mathbf{D}^*_{A\alpha} \rangle^\beta . \nabla \tilde{c}_{A\beta} + \tilde{\mathbf{D}}^*_{A\alpha} . \nabla \langle c_{A\beta} \rangle^\beta + \tilde{\mathbf{D}}^*_{A\alpha} . \nabla \tilde{c}_{A\beta} \right\rangle \tag{B.69}$$

Here, due to scale separation, it can be shown that averaged quantities used in the spacial decomposition are close to averaged quantities defined at the centroid of the averaging volume . Under these circumstances, variation of the averaged quantities can be neglected and the above expression takes the form

$$\langle \mathbf{D}^*_{A\alpha} . \nabla c_{A\beta} \rangle = \langle \mathbf{D}^*_{A\alpha} \rangle^\beta . \left\langle \nabla \langle c_{A\beta} \rangle^\beta \right\rangle + \langle \mathbf{D}^*_{A\alpha} \rangle^\beta . \langle \nabla \tilde{c}_{A\beta} \rangle + \left\langle \tilde{\mathbf{D}}^*_{A\alpha} . \nabla \langle c_{A\beta} \rangle^\beta \right\rangle + \left\langle \tilde{\mathbf{D}}^*_{A\alpha} . \nabla \tilde{c}_{A\beta} \right\rangle \tag{B.70}$$

Let us first consider the third term of Eq. (B.70). Using the spacial averaging theorem in the form

$$\nabla \langle c_{A\beta} \rangle^\beta = \langle \nabla c_{A\beta} \rangle^\beta - \frac{1}{V_\beta} \int_{\beta\sigma} \mathbf{n}_{\beta\sigma} c_{A\beta} dA \tag{B.71}$$

allows us to write

$$\left\langle \tilde{\mathbf{D}}^*_{A\alpha} . \nabla \langle c_{A\beta} \rangle^\beta \right\rangle = \left\langle \tilde{\mathbf{D}}^*_{A\alpha} . \langle \nabla c_{A\beta} \rangle^\beta - \tilde{\mathbf{D}}^*_{A\alpha} . \frac{1}{V_\beta} \int_{A_{\beta\sigma}} \mathbf{n}_{\beta\sigma} c_{A\beta} dA \right\rangle \tag{B.72}$$

which can also be written under the form

$$\left\langle \tilde{\mathbf{D}}^*_{A\alpha} . \nabla \langle c_{A\beta} \rangle^\beta \right\rangle = \langle \tilde{\mathbf{D}}^*_{A\alpha} \rangle . \langle \nabla c_{A\beta} \rangle^\beta - \langle \tilde{\mathbf{D}}^*_{A\alpha} \rangle . \frac{1}{V_\beta} \int_{A_{\beta\sigma}} \mathbf{n}_{\beta\sigma} c_{A\beta} dA \tag{B.73}$$

However, since

$$\langle \tilde{\mathbf{D}}^*_{A\alpha} \rangle = 0 \tag{B.74}$$

Eq. (B.70) simplifies under the form

$$\langle \mathbf{D}^*_{A\alpha}.\nabla c_{A\beta} \rangle = \langle \mathbf{D}^*_{A\alpha} \rangle^\beta . \left\langle \nabla \langle c_{A\beta} \rangle^\beta \right\rangle + \langle \mathbf{D}^*_{A\alpha} \rangle^\beta . \langle \nabla \tilde{c}_{A\beta} \rangle + \left\langle \tilde{\mathbf{D}}^*_{A\alpha}.\nabla \tilde{c}_{A\beta} \right\rangle \tag{B.75}$$

Let us consider now the first term of the right hand side of Eq. (B.75). Using the spacial averaging theorem gives

$$\langle \mathbf{D}^*_{A\alpha} \rangle^\beta . \left\langle \nabla \langle c_{A\beta} \rangle^\beta \right\rangle = \langle \mathbf{D}^*_{A\alpha} \rangle^\beta . \left[\nabla \left(\varepsilon_\beta \langle c_{A\beta} \rangle^\beta \right) + \frac{1}{\mathcal{V}_{\text{II}}} \int_{A_{\beta\sigma}} \mathbf{n}_{\beta\sigma} \langle c_{A\beta} \rangle^\beta dA \right] \tag{B.76}$$

Again, due to scale separation, the above expression tbecomes

$$\langle \mathbf{D}^*_{A\alpha} \rangle^\beta . \left\langle \nabla \langle c_{A\beta} \rangle^\beta \right\rangle = \varepsilon_\beta \langle \mathbf{D}^*_{A\alpha} \rangle^\beta . \nabla \langle c_{A\beta} \rangle^\beta \tag{B.77}$$

The second term of Eq. (B.75)

$$\langle \mathbf{D}^*_{A\alpha} \rangle^\beta . \langle \nabla \tilde{c}_{A\beta} \rangle = \langle \mathbf{D}^*_{A\alpha} \rangle^\beta . \left[\nabla \langle \tilde{c}_{A\beta} \rangle + \frac{1}{\mathcal{V}_{\text{II}}} \int_{A_{\beta\sigma}} \mathbf{n}_{\beta\sigma} \tilde{c}_{A\beta} dA \right] \tag{B.78}$$

and discarding the average of the deviation, Eq. (B.75) finaly reduces to

$$\langle \mathbf{D}^*_{A\alpha}.\nabla c_{A\beta} \rangle = \langle \mathbf{D}^*_{A\alpha} \rangle^\beta . \left(\varepsilon_\beta \nabla \langle c_{A\beta} \rangle^\beta + \frac{1}{\mathcal{V}_{\text{II}}} \int_{A_{\beta\sigma}} \mathbf{n}_{\beta\sigma} \tilde{c}_{A\beta} dA \right) + \left\langle \tilde{\mathbf{D}}^*_{A\alpha}.\nabla \tilde{c}_{A\beta} \right\rangle \tag{B.79}$$

Finallly, the unclosed averaged equation for solute transport takes the form

$$\begin{aligned} &\varepsilon_\alpha \frac{\partial \left(\varepsilon_\beta \left\langle c_{A\beta} \right\rangle^\beta \right)}{\partial t} + \varepsilon_\beta \left\langle \mathbf{v}_\beta \right\rangle^\beta . \nabla \left\langle c_{A\beta} \right\rangle^\beta = \\ &\nabla . \left[\langle \mathbf{D}^*_{A\alpha} \rangle^\beta . \left(\varepsilon_\beta \nabla \langle c_{A\beta} \rangle^\beta + \frac{1}{\mathcal{V}_{\text{II}}} \int_{A_{\beta\sigma}} \mathbf{n}_{\beta\sigma} \tilde{c}_{A\beta} dA \right) \right] + \nabla . \left\langle \tilde{\mathbf{D}}^*_{A\alpha}.\nabla \tilde{c}_{A\beta} \right\rangle - \nabla . \langle \tilde{\mathbf{v}}_\beta \tilde{c}_{A\beta} \rangle \end{aligned} \tag{B.80}$$

B.3.2 Deviation problem

The deviation equation is obtained by subtracting the non-closed Eq. (B.80) from the local one (Eq. B.4) where the spatial decompositions have been previously introduced. After few simplifications, the concentration deviation equation takes the form

$$\begin{aligned} \tilde{\mathbf{v}}_\beta.\nabla \langle c_{A\beta} \rangle^\beta + \mathbf{v}_\beta.\nabla \tilde{c}_{A\beta} = \nabla . \left(\mathbf{D}^*_{A\alpha}.\nabla \tilde{c}_{A\beta} \right) + \nabla . \left(\tilde{\mathbf{D}}^*_{A\alpha}.\nabla \langle c_{A\beta} \rangle^\beta \right) \\ - \nabla . \left(\langle \mathbf{D}^*_{A\alpha} \rangle^\beta . \frac{1}{V_\beta} \int_{A_{\beta\sigma}} \mathbf{n}_{\beta\sigma} \tilde{c}_{A\beta} dA \right) - \varepsilon_\beta^{-1} \nabla . \langle \tilde{\mathbf{D}}^*_{A\alpha}.\nabla \tilde{c}_{A\beta} \rangle \end{aligned} \tag{B.81}$$

An estimate of the order of magnitude of the different terms of the above deviation equation is preformed in order to simplify the problem. Using the boundary condition (B.34) gives

$$-\mathbf{n}_{\beta\sigma}.\left(\langle\mathbf{D}^*_{A\alpha}\rangle^{\beta}.\nabla c_{A\beta}\right)=\mathbf{n}_{\beta\sigma}.\left(\tilde{\mathbf{D}}^*_{A\alpha}.\nabla c_{A\beta}\right)\quad\text{at } A_{\beta\sigma} \tag{B.82}$$

where we can deduce that $\langle\mathbf{D}^*_{A\alpha}\rangle^{\beta}$ and $\tilde{\mathbf{D}}^*_{A\alpha}$ are of the same order of magnitude. Moreover, on the basis of these estimates estimate

$$\nabla.\left(\mathbf{D}^*_{A\alpha}.\nabla\tilde{c}_{A\beta}\right)=\mathcal{O}\left(\frac{\langle\mathbf{D}^*_{A\alpha}\rangle^{\beta}\tilde{c}_{A\beta}}{l_\beta^2}\right) \tag{B.83}$$

$$\nabla.\left(\langle\mathbf{D}^*_{A\alpha}\rangle^{\beta}.\frac{1}{V_\beta}\int_{A_{\beta\sigma}}\mathbf{n}_{\beta\sigma}\tilde{c}_{A\beta}dA\right)=\mathcal{O}\left(\frac{\varepsilon_\beta^{-1}\langle\mathbf{D}^*_{A\alpha}\rangle^{\beta}\tilde{c}_{A\beta}}{l_\beta L_{\text{II}}}\right) \tag{B.84}$$

$$\varepsilon_\beta^{-1}\nabla.\langle\tilde{\mathbf{D}}^*_{A\alpha}.\nabla\tilde{c}_{A\beta}\rangle=\mathcal{O}\left(\frac{\langle\mathbf{D}^*_{A\alpha}\rangle^{\beta}\tilde{c}_{A\beta}}{l_\beta L_{\text{II}}}\right) \tag{B.85}$$

the two last terms of Eq. (B.81) can be discarded and therefore the deviation problem for mass transport takes the form

$$\tilde{\mathbf{v}}_\beta.\nabla\langle c_{A\beta}\rangle^{\beta}+\mathbf{v}_\beta.\nabla\tilde{c}_{A\beta}=\nabla.\left(\mathbf{D}^*_{A\alpha}.\nabla\tilde{c}_{A\beta}\right)+\nabla.\left(\tilde{\mathbf{D}}^*_{A\alpha}.\nabla\langle c_{A\beta}\rangle^{\beta}\right) \tag{B.86}$$

$$-\mathbf{n}_{\beta\sigma}.\left(\mathbf{D}^*_{A\alpha}.\nabla\tilde{c}_{A\beta}\right)=\mathbf{n}_{\beta\sigma}.\left(\mathbf{D}^*_{A\alpha}.\nabla\langle c_{A\beta}\rangle^{\beta}\right)\quad\text{at } A_{\beta\sigma} \tag{B.87}$$

APPENDIX C

ONE EQUATION MODEL OF MOMENTUM TRANSPORT IN THE BIOREACTOR

In the following development, we propose the derivation of a one-equation non-equilibrium model based on weighted averages. This model is the first to our knowledge to result in a simple one-equation momentum transport in mechanical non-equilibrium conditions. The simplicity of its form, and the unique closure problem needed to evaluate the effective permeability, makes easier its use in, for instance, biotechnological application.

The fundamental idea of the one-equation non-equilibrium model, is that even though the velocity and pressure are very different in the two regions, it is still possible to describe the overall momentum transport in terms of special averages defined as

$$(\varepsilon_\gamma + \varepsilon_\omega) \langle \mathbf{v} \rangle^{\gamma\omega} = \varepsilon_\gamma \langle \mathbf{v}_\gamma \rangle^\gamma + \varepsilon_\omega \varepsilon_\alpha^{-1} \varepsilon_\beta^{-1} \langle \mathbf{v}_\omega \rangle^\omega \tag{C.1}$$

$$(\varepsilon_\gamma + \varepsilon_\omega) \langle p \rangle^{\gamma\omega} = \varepsilon_\gamma \langle p_\gamma \rangle^\gamma + \varepsilon_\omega \langle p_\omega \rangle^\omega \tag{C.2}$$

In itself, this kind of average is not new since it has already been used in three-phase mass equilibrium [Lasseux et al., 2004; Golfier et al., 2009] and non-equilibrium systems [Davit et al., 2010]. However it has never been exploited in momentum transport, and some discussions about its physical meaning may be useful.

The sum of the γ and ω-regions may be seen as a composite $\gamma\omega$-region where momentum (and mass) transport occurs. In this spirit, $\langle \mathbf{v} \rangle^{\gamma\omega}$ and $\langle p \rangle^{\gamma\omega}$ should be regarded as special "intrinsic averages" within the $\gamma\omega$-region. This is the reason why in Eqs. (C.1) and (C.2), the term $\varepsilon_\gamma + \varepsilon_\omega$ is kept on the left hand side to remind that $(\varepsilon_\gamma + \varepsilon_\omega) \langle \mathbf{v} \rangle^{\gamma\omega}$ and $(\varepsilon_\gamma + \varepsilon_\omega) \langle p \rangle^{\gamma\omega}$ are equivalent to "superficial" averages. Moreover, one has to recall that, as defined in Eq. (8.1), $\mathbf{v}_\omega$ is a superficial average of the velocity at the cellular scale. Since for the definition of the weighted average, we seek the intrinsic average in the ω-region , we need to divide $\mathbf{v}_\omega$ by $\varepsilon_\alpha \varepsilon_\beta$. Note that this is not necessary for the pressure because p_ω is already an intrinsic pressure.

Along with these definitions, and following Davit et al. [2010] a special decomposition is

proposed of the form

$$\mathbf{v}_\gamma = \langle \mathbf{v} \rangle^{\gamma\omega} + \hat{\mathbf{v}}_\gamma \quad ; \quad \mathbf{v}_\omega = \varepsilon_\alpha \varepsilon_\beta \langle \mathbf{v} \rangle^{\gamma\omega} + \hat{\mathbf{v}}_\omega \tag{C.3}$$

$$p_\gamma = \langle p \rangle^{\gamma\omega} + \hat{p}_\gamma \quad ; \quad p_\omega = \langle p \rangle^{\gamma\omega} + \hat{p}_\omega \tag{C.4}$$

where $\hat{\mathbf{v}}_\gamma$, $\hat{\mathbf{v}}_\omega$, $\hat{p}_\gamma$ and $\hat{p}_\omega$ are special deviations to the weighted average. Note the presence of $\varepsilon_\alpha \varepsilon_\beta$ in $\mathbf{v}_\omega$. When Gray's spacial decomposition is also introduced in the γ and ω-regions

$$\mathbf{v}_\gamma = \langle \mathbf{v}_\gamma \rangle^{\gamma} + \tilde{\mathbf{v}}_\gamma \quad ; \quad \mathbf{v}_\omega = \langle \mathbf{v}_\omega \rangle^{\omega} + \tilde{\mathbf{v}}_\omega \tag{C.5}$$

$$p_\gamma = \langle p_\gamma \rangle^{\gamma} + \tilde{p}_\gamma \quad ; \quad p_\omega = \langle p_\omega \rangle^{\omega} + \tilde{p}_\omega \tag{C.6}$$

It is easy to show that the special deviations are linked to the classic spacial deviations through

$$\hat{\mathbf{v}}_\gamma = \langle \hat{\mathbf{v}}_\gamma \rangle^{\gamma} + \tilde{\mathbf{v}}_\gamma \quad ; \quad \hat{\mathbf{v}}_\omega = \langle \hat{\mathbf{v}}_\omega \rangle^{\omega} + \tilde{\mathbf{v}}_\omega \tag{C.7}$$

$$\hat{p}_\gamma = \langle \hat{p}_\gamma \rangle^{\gamma} + \tilde{p}_\gamma \quad ; \quad \hat{p}_\omega = \langle \hat{p}_\omega \rangle^{\omega} + \tilde{p}_\omega \tag{C.8}$$

Now that the weighted average and its special deviations are defined, we are ready to start the up-scaling of momentum transport from the tissue to the bioreactor scale. Following the main steps of the volume averaging method presented in Sec. 7.2.1, the non-closed momentum equation in the γ and ω-regions are written

$$\begin{aligned} \rho_\alpha \frac{\partial(\varepsilon_\gamma \langle \mathbf{v}_\gamma \rangle^\gamma)}{\partial t} - \rho_\alpha \frac{1}{\mathcal{V}_{\text{II}}} \int_{A_{\gamma\omega}} \mathbf{n}_{\gamma\omega} . \left(\mathbf{w}_{\gamma\omega} \mathbf{v}_\gamma\right) dA = \\ - \varepsilon_\gamma \nabla \langle p_\gamma \rangle^\gamma + \rho_\alpha \varepsilon_\gamma \mathbf{g} + \mu_\alpha \varepsilon_\gamma \nabla^2 \langle \mathbf{v}_\gamma \rangle^\gamma \\ + \frac{1}{\mathcal{V}_{\text{II}}} \int_{A_{\gamma\omega}} \mathbf{n}_{\gamma\omega} . \left(-\tilde{p}_\gamma + \mu_\alpha \nabla \tilde{\mathbf{v}}_\gamma\right) dA + \frac{1}{\mathcal{V}_{\text{II}}} \int_{A_{\gamma\kappa}} \mathbf{n}_{\gamma\kappa} . \left(-\tilde{p}_\gamma + \mu_\alpha \nabla \tilde{\mathbf{v}}_\gamma\right) dA \end{aligned} \tag{C.9}$$

$$\begin{aligned} \rho_\alpha \varepsilon_\alpha^{-1} \varepsilon_\beta^{-1} \frac{\partial(\varepsilon_\omega \langle \mathbf{v}_\omega \rangle^\omega)}{\partial t} - \rho_\alpha \varepsilon_\alpha^{-1} \varepsilon_\beta^{-1} \frac{1}{\mathcal{V}_{\text{II}}} \int_{A_{\omega\gamma}} \mathbf{n}_{\omega\gamma} . \left(\mathbf{w}_{\gamma\omega} \mathbf{v}_\omega\right) dA \\ - \varepsilon_\omega \nabla \langle p_\omega \rangle^\omega + \mu_\alpha \varepsilon_\alpha^{-1} \varepsilon_\beta^{-1} \varepsilon_\omega \nabla^2 \langle \mathbf{v}_\omega \rangle^\omega - \frac{\mu_\alpha}{\mathbf{K}_\omega^{\text{III}}} \varepsilon_\omega \langle \mathbf{v}_\omega \rangle^\omega \\ + \frac{1}{\mathcal{V}_{\text{II}}} \int_{A_{\omega\gamma}} \mathbf{n}_{\omega\gamma} . \left(-\tilde{p}_\omega \mathbf{I} + \mu_\alpha \varepsilon_\alpha^{-1} \varepsilon_\beta^{-1} \nabla \tilde{\mathbf{v}}_\omega\right) dA \\ + \frac{1}{\mathcal{V}_{\text{II}}} \int_{A_{\omega\kappa}} \mathbf{n}_{\omega\kappa} . \left(-\tilde{p}_\omega \mathbf{I} + \mu_\alpha \varepsilon_\alpha^{-1} \varepsilon_\beta^{-1} \nabla \tilde{\mathbf{v}}_\omega\right) dA \end{aligned} \tag{C.10}$$

where $\mathbf{w}_{\gamma\omega}$ is the velocity of the interface between the γ and ω regions, $\mathbf{n}_{ij}$ is the unit normal vector pointing from the i to the j-region, A_{ij} is the surface between the i and j regions, and $\mathcal{V}_{\text{II}}$ is the averaging volume at the tissue scale (level II). In Eqs. (C.9) and (C.10), the only differences with the previous chapters are the multiple surface integrals due to the three-phase system, and the convective term at $A_{\gamma\omega}$ which cannot be discarded due to the velocity continuity. In order to treat these terms, the surface integral on the left hand side of Eq. (C.9)

is developed using the special decompositions for the fluid velocity

$$\frac{1}{\mathcal{V}_{\text{II}}}\int_{A_{\gamma\omega}}\mathbf{n}_{\gamma\omega}.\mathbf{w}_{\gamma\omega}.\mathbf{v}_{\gamma}dA+\frac{1}{\mathcal{V}_{\text{II}}}\int_{A_{\gamma\kappa}}\mathbf{n}_{\gamma\kappa}.\mathbf{w}_{\gamma\kappa}.\mathbf{v}_{\gamma}dA=$$
$$\frac{1}{\mathcal{V}_{\text{II}}}\int_{A_{\gamma\omega}}\mathbf{n}_{\gamma\omega}.\mathbf{w}_{\gamma\omega}.\langle\mathbf{v}\rangle^{\gamma\omega}dA+\frac{1}{\mathcal{V}_{\text{II}}}\int_{A_{\gamma\kappa}}\mathbf{n}_{\gamma\kappa}.\mathbf{w}_{\gamma\kappa}.\langle\mathbf{v}\rangle^{\gamma\omega}dA$$
$$+\frac{1}{\mathcal{V}_{\text{II}}}\int_{A_{\gamma\omega}}\mathbf{n}_{\gamma\omega}.\mathbf{w}_{\gamma\omega}.\hat{\mathbf{v}}_{\gamma}dA+\frac{1}{\mathcal{V}_{\text{II}}}\int_{A_{\gamma\kappa}}\mathbf{n}_{\gamma\kappa}.\mathbf{w}_{\gamma\kappa}.\hat{\mathbf{v}}_{\gamma}dA \quad \text{(C.11)}$$

The weighted averages can be removed from the integrals, and using the general transport theorem, the interfacial convective terms are written

$$\frac{1}{\mathcal{V}_{\text{II}}}\int_{A_{\gamma\omega}}\mathbf{n}_{\gamma\omega}.\mathbf{w}_{\gamma\omega}.\mathbf{v}_{\gamma}dA+\frac{1}{\mathcal{V}_{\text{II}}}\int_{A_{\gamma\kappa}}\mathbf{n}_{\gamma\kappa}.\mathbf{w}_{\gamma\kappa}.\mathbf{v}_{\gamma}dA=$$
$$\frac{\partial\varepsilon_{\gamma}}{\partial t}\langle\mathbf{v}\rangle^{\gamma\omega}+\frac{1}{\mathcal{V}_{\text{II}}}\int_{A_{\gamma\omega}}\mathbf{n}_{\gamma\omega}.\mathbf{w}_{\gamma\omega}.\hat{\mathbf{v}}_{\gamma}dA+\frac{1}{\mathcal{V}_{\text{II}}}\int_{A_{\gamma\kappa}}\mathbf{n}_{\gamma\kappa}.\mathbf{w}_{\gamma\kappa}.\hat{\mathbf{v}}_{\gamma}dA \quad \text{(C.12)}$$

The same development is done with the ω-region, and the non-closed region average equations reads

$$\rho_{\alpha}\frac{\partial(\varepsilon_{\gamma}\langle\mathbf{v}_{\gamma}\rangle^{\gamma})}{\partial t}-\rho_{\alpha}\frac{\partial\varepsilon_{\gamma}}{\partial t}\langle\mathbf{v}\rangle^{\gamma\omega}-\rho_{\alpha}\frac{1}{\mathcal{V}_{\text{II}}}\int_{A_{\gamma\omega}}\mathbf{n}_{\gamma\omega}.\mathbf{w}_{\gamma\omega}.\hat{\mathbf{v}}_{\gamma}dA=$$
$$-\varepsilon_{\gamma}\nabla\langle p_{\gamma}\rangle^{\gamma}+\rho_{\alpha}\varepsilon_{\gamma}\mathbf{g}+\mu_{\alpha}\varepsilon_{\gamma}\nabla^{2}\langle\mathbf{v}_{\gamma}\rangle^{\gamma}$$
$$+\frac{1}{\mathcal{V}_{\text{II}}}\int_{A_{\gamma\omega}}\mathbf{n}_{\gamma\omega}.\left(-\tilde{p}_{\gamma}+\mu_{\alpha}\nabla\tilde{\mathbf{v}}_{\gamma}\right)dA+\frac{1}{\mathcal{V}_{\text{II}}}\int_{A_{\gamma\kappa}}\mathbf{n}_{\gamma\kappa}.\left(-\tilde{p}_{\gamma}+\mu_{\alpha}\nabla\tilde{\mathbf{v}}_{\gamma}\right)dA \quad \text{(C.13)}$$

$$\rho_{\alpha}\varepsilon_{\alpha}^{-1}\varepsilon_{\beta}^{-1}\frac{\partial(\varepsilon_{\omega}\langle\mathbf{v}_{\omega}\rangle^{\omega})}{\partial t}-\rho_{\alpha}\frac{\partial\varepsilon_{\omega}}{\partial t}\langle\mathbf{v}\rangle^{\gamma\omega}-\rho_{\alpha}\varepsilon_{\alpha}^{-1}\varepsilon_{\beta}^{-1}\frac{1}{\mathcal{V}_{\text{II}}}\int_{A_{\omega\gamma}}\mathbf{n}_{\omega\gamma}.\mathbf{w}_{\omega\gamma}.\hat{\mathbf{v}}_{\omega}dA=$$
$$-\varepsilon_{\omega}\nabla\langle p_{\omega}\rangle^{\omega}-\frac{\mu_{\alpha}}{\mathbf{K}_{\omega}^{\text{II}}}\varepsilon_{\omega}\langle\mathbf{v}_{\omega}\rangle^{\omega}+\rho_{\alpha}\varepsilon_{\omega}\mathbf{g}+\mu_{\alpha}\varepsilon_{\alpha}^{-1}\varepsilon_{\beta}^{-1}\varepsilon_{\omega}\nabla^{2}\langle\mathbf{v}_{\omega}\rangle^{\omega}$$
$$+\frac{1}{\mathcal{V}_{\text{II}}}\int_{A_{\omega\gamma}}\mathbf{n}_{\omega\gamma}.\left(-\tilde{p}_{\omega}+\mu_{\alpha}\varepsilon_{\alpha}^{-1}\varepsilon_{\beta}^{-1}\nabla\tilde{\mathbf{v}}_{\omega}\right)dA+\frac{1}{\mathcal{V}_{\text{II}}}\int_{A_{\omega\kappa}}\mathbf{n}_{\omega\kappa}.\left(-\tilde{p}_{\omega}+\mu_{\alpha}\varepsilon_{\alpha}^{-1}\varepsilon_{\beta}^{-1}\nabla\tilde{\mathbf{v}}_{\omega}\right)dA \quad \text{(C.14)}$$

At this point we have two average equations for momentum transport at the bioreactor scale (level I). If the transport properties concerning the flow in the two regions are close enough, it would be possible to hypothesis mechanical equilibrium [Quintard & Whitaker, 1998a] the same way mass equilibrium has been supposed for mass transport at the cellular scale (Sec. 7.3.1). However in our case the transport equations in the two regions are different (Stokes in the γ-region, Darcy-Brinkman in the ω-region), and the fluid velocity is much higher in the culture medium region than in the tissue. Therefore it is not possible to assume mechanical equilibrium here, and if one wish to develop a two-equation non-equilibrium model, Eqs. (C.13) and (C.14) should be used as the basis for the macroscopic equations

(where Gray's decomposition are used in the convective terms instead of the special decomposition). However in the present work, a one equation non-equilibrium model is desired, and adding up Eqs. (C.9) and (C.10) the weighted averages appear in a unique macroscopic equation

$$\rho_\alpha \frac{\partial}{\partial t}\left[\left(\varepsilon_\gamma+\varepsilon_\omega\right)\langle\mathbf{v}\rangle^{\gamma\omega}\right]-\rho_\alpha\frac{\partial}{\partial t}\left(\varepsilon_\gamma+\varepsilon_\omega\right)\langle\mathbf{v}\rangle^{\gamma\omega}= \\ -\left(\varepsilon_\gamma+\varepsilon_\omega\right)\nabla\langle p\rangle^{\gamma\omega}+\left(\varepsilon_\gamma+\varepsilon_\omega\right)\mu_\alpha\nabla^2\langle\mathbf{v}\rangle^{\gamma\omega}-\frac{\mu_\alpha}{\mathbf{K}_\omega^{\mathrm{III}}}\varepsilon_\omega\langle\mathbf{v}_\omega\rangle^{\omega}+\rho_\alpha\left(\varepsilon_\gamma+\varepsilon_\omega\right)\mathbf{g} \\ +\sum_{i=\omega,\kappa}\frac{1}{\mathcal{V}_{\mathrm{II}}}\int_{A_{\gamma i}}\mathbf{n}_{\gamma i}.\left(-\tilde{p}_\gamma\mathbf{I}+\mu_\alpha\nabla\tilde{\mathbf{v}}_\gamma\right)dA+\sum_{i=\gamma,\kappa}\frac{1}{\mathcal{V}_{\mathrm{II}}}\int_{A_{\omega i}}\mathbf{n}_{\omega i}.\left(-\tilde{p}_\omega\mathbf{I}+\mu_\alpha\varepsilon_\alpha^{-1}\varepsilon_\omega^{-1}\nabla\tilde{\mathbf{v}}_\omega\right)dA \\ +\rho_\alpha\frac{1}{\mathcal{V}_{\mathrm{II}}}\int_{A_{\gamma\omega}}\mathbf{n}_{\gamma\omega}.\mathbf{w}_{\gamma\omega}\left(\hat{\mathbf{v}}_\gamma-\varepsilon_\alpha^{-1}\varepsilon_\beta^{-1}\hat{\mathbf{v}}_\omega\right)dA \quad \text{(C.15)}$$

The porous medium constituted by the solid glass beads is rigid and has time invariant properties, implying that the quantity $\varepsilon_\gamma+\varepsilon_\omega=1-\varepsilon_\kappa$ is constant in time (space independence can also be easily accepted, at least in the longitudinal direction of the bioreactor). The second term on the left hand size can thus be discarded, and dividing by $\varepsilon_\gamma+\varepsilon_\omega$ we have

$$\frac{\rho_\alpha}{\varepsilon_\gamma+\varepsilon_\omega}\frac{\partial}{\partial t}\left[\left(\varepsilon_\gamma+\varepsilon_\omega\right)\langle\mathbf{v}\rangle^{\gamma\omega}\right]=-\nabla\langle p\rangle^{\gamma\omega}+\mu_\alpha\nabla^2\langle\mathbf{v}\rangle^{\gamma\omega}-\frac{\varepsilon_\omega}{\varepsilon_\gamma+\varepsilon_\omega}\frac{\mu_\alpha}{\mathbf{K}_\omega^{\mathrm{III}}}\langle\mathbf{v}_\omega\rangle^{\omega} \\ +\frac{\varepsilon_\gamma}{\varepsilon_\gamma+\varepsilon_\omega}\sum_{i=\omega,\kappa}\frac{1}{V_\gamma}\int_{A_{\gamma i}}\mathbf{n}_{\gamma i}.\left(-\tilde{p}_\gamma\mathbf{I}+\mu_\alpha\nabla\tilde{\mathbf{v}}_\gamma\right)dA \\ +\frac{\varepsilon_\omega}{\varepsilon_\gamma+\varepsilon_\omega}\sum_{i=\gamma,\kappa}\frac{1}{V_\omega}\int_{A_{\omega i}}\mathbf{n}_{\omega i}.\left(-\tilde{p}_\omega\mathbf{I}+\mu_\alpha\varepsilon_\alpha^{-1}\varepsilon_\omega^{-1}\nabla\tilde{\mathbf{v}}_\omega\right)dA \\ +\frac{\rho_\alpha}{\varepsilon_\gamma+\varepsilon_\omega}\frac{1}{\mathcal{V}_{\mathrm{II}}}\int_{A_{\gamma\omega}}\mathbf{n}_{\gamma\omega}.\mathbf{w}_{\gamma\omega}\left(\hat{\mathbf{v}}_\gamma-\varepsilon_\alpha^{-1}\varepsilon_\beta^{-1}\hat{\mathbf{v}}_\omega\right)dA \quad \text{(C.16)}$$

Note that spacial decomposition are still present in this equation. In order to eliminate these terms, the relations between the two kind of deviations Eq. (C.7) are introduced in the

integral terms and we have

$$\varepsilon_\gamma \sum_{i=\omega,\kappa} \frac{1}{V_\gamma} \int_{A_{\gamma i}} \mathbf{n}_{\gamma i}.\left(-\tilde{p}_\gamma \mathbf{I} + \mu_\alpha \nabla \tilde{\mathbf{v}}_\gamma\right) dA$$
$$+ \varepsilon_\omega \sum_{i=\gamma,\kappa} \frac{1}{V_\omega} \int_{A_{\omega i}} \mathbf{n}_{\omega i}.\left(-\tilde{p}_\omega \mathbf{I} + \mu_\alpha \varepsilon_\alpha^{-1} \varepsilon_\omega^{-1} \nabla \tilde{\mathbf{v}}_\omega\right) dA =$$
$$+ \varepsilon_\gamma \sum_{i=\omega,\kappa} \frac{1}{V_\gamma} \int_{A_{\gamma i}} \mathbf{n}_{\gamma i}.\left(-\hat{p}_\gamma \mathbf{I} + \mu_\alpha \nabla \hat{\mathbf{v}}_\gamma\right) dA$$
$$+ \varepsilon_\omega \sum_{i=\gamma,\kappa} \frac{1}{V_\omega} \int_{A_{\omega i}} \mathbf{n}_{\omega i}.\left(-\hat{p}_\omega \mathbf{I} + \mu_\alpha \varepsilon_\alpha^{-1} \varepsilon_\omega^{-1} \nabla \hat{\mathbf{v}}_\omega\right) dA$$
$$- \varepsilon_\gamma \sum_{i=\omega,\kappa} \frac{1}{V_\gamma} \int_{A_{\gamma i}} \mathbf{n}_{\gamma i}.\left(-\langle \hat{p}_\gamma \rangle^\gamma \mathbf{I} + \mu_\alpha \nabla \langle \hat{\mathbf{v}}_\gamma \rangle^\gamma\right) dA$$
$$- \varepsilon_\omega \sum_{i=\gamma,\kappa} \frac{1}{V_\omega} \int_{A_{\omega i}} \mathbf{n}_{\omega i}.\left(-\langle \hat{p}_\omega \rangle^\omega \mathbf{I} + \mu_\alpha \varepsilon_\alpha^{-1} \varepsilon_\omega^{-1} \nabla \langle \hat{\mathbf{v}}_\omega \rangle^\omega\right) dA \quad \text{(C.17)}$$

Once again, under the classical length scale constraints, the averages can be removed from the integral, ans using the geometrical theorem we have

$$\varepsilon_\gamma \sum_{i=\omega,\kappa} \frac{1}{V_\gamma} \int_{A_{\gamma i}} \mathbf{n}_{\gamma i}.\left(-\tilde{p}_\gamma \mathbf{I} + \mu_\alpha \nabla \tilde{\mathbf{v}}_\gamma\right) dA$$
$$+ \varepsilon_\omega \sum_{i=\gamma,\kappa} \frac{1}{V_\omega} \int_{A_{\omega i}} \mathbf{n}_{\omega i}.\left(-\tilde{p}_\omega \mathbf{I} + \mu_\alpha \varepsilon_\alpha^{-1} \varepsilon_\omega^{-1} \nabla \tilde{\mathbf{v}}_\omega\right) dA =$$
$$+ \varepsilon_\gamma \sum_{i=\omega,\kappa} \frac{1}{V_\gamma} \int_{A_{\gamma i}} \mathbf{n}_{\gamma i}.\left(-\hat{p}_\gamma \mathbf{I} + \mu_\alpha \nabla \hat{\mathbf{v}}_\gamma\right) dA$$
$$+ \varepsilon_\omega \sum_{i=\gamma,\kappa} \frac{1}{V_\omega} \int_{A_{\omega i}} \mathbf{n}_{\omega i}.\left(-\hat{p}_\omega \mathbf{I} + \mu_\alpha \varepsilon_\alpha^{-1} \varepsilon_\omega^{-1} \nabla \hat{\mathbf{v}}_\omega\right) dA$$
$$+ \varepsilon_\gamma \nabla \varepsilon_\gamma.\left(-\langle \hat{p}_\gamma \rangle^\gamma \mathbf{I} + \mu_\alpha \nabla \langle \hat{\mathbf{v}}_\gamma \rangle^\gamma\right) + \varepsilon_\omega \nabla \varepsilon_\omega.\left(-\langle \hat{p}_\omega \rangle^\omega \mathbf{I} + \mu_\alpha \varepsilon_\alpha^{-1} \varepsilon_\omega^{-1} \nabla \langle \hat{\mathbf{v}}_\omega \rangle^\omega\right) \quad \text{(C.18)}$$

If the porous medium constituted by the glass beads and the tissue is homogeneous, the gradient of the volume fractions can be neglected, and the weighted average equation can be expressed as

$$\frac{\rho_\alpha}{\varepsilon_\gamma + \varepsilon_\omega} \frac{\partial}{\partial t} \left[(\varepsilon_\gamma + \varepsilon_\omega) \langle \mathbf{v} \rangle^{\gamma\omega}\right] = -\nabla \langle p \rangle^{\gamma\omega} + \mu_\alpha \nabla^2 \langle \mathbf{v} \rangle^{\gamma\omega} - \frac{\varepsilon_\omega}{\varepsilon_\gamma + \varepsilon_\omega} \frac{\mu_\alpha}{\mathbf{K}_\omega^{\text{III}}} \langle \mathbf{v}_\omega \rangle^\omega + \rho_\alpha \mathbf{g}$$
$$+ \frac{\varepsilon_\gamma}{\varepsilon_\gamma + \varepsilon_\omega} \sum_{i=\omega,\kappa} \frac{1}{V_\gamma} \int_{A_{\gamma i}} \mathbf{n}_{\gamma i}.\left(-\hat{p}_\gamma \mathbf{I} + \mu_\alpha \nabla \hat{\mathbf{v}}_\gamma\right) dA$$
$$+ \frac{\varepsilon_\omega}{\varepsilon_\gamma + \varepsilon_\omega} \sum_{i=\gamma,\kappa} \frac{1}{V_\omega} \int_{A_{\omega i}} \mathbf{n}_{\omega i}.\left(-\hat{p}_\omega \mathbf{I} + \mu_\alpha \varepsilon_\alpha^{-1} \varepsilon_\omega^{-1} \nabla \hat{\mathbf{v}}_\omega\right) dA$$
$$+ \frac{\rho_\alpha}{\varepsilon_\gamma + \varepsilon_\omega} \frac{1}{\mathcal{V}_{\text{II}}} \int_{A_{\gamma\omega}} \mathbf{n}_{\gamma\omega}.\mathbf{w}_{\gamma\omega} \left(\hat{\mathbf{v}}_\gamma - \varepsilon_\alpha^{-1} \varepsilon_\beta^{-1} \hat{\mathbf{v}}_\omega\right) dA \quad \text{(C.19)}$$

This is the *non-closed averaged equation* for momentum transport at the bioreactor scale, and this form is consistent with Eq. (7.25) developed for a flow in a single porous region. Here, the $\varepsilon_\alpha^{-1}\varepsilon_\beta^{-1}$ are included within the definition of $\langle \mathbf{v} \rangle^{\gamma\omega}$, and we have an additional term on the right hand side which represents mass exchange at $A_{\gamma\omega}$.

Eq. (C.19) still includes tissue scale variables, and we now need to develop a problem for the special deviations in order to close the problem. This is done by subtracting Eq. (C.19) to Eqs. (8.9) and (8.12)

$$\begin{aligned}\rho_\alpha \frac{\partial \hat{\mathbf{v}}_\gamma}{\partial t} = &-\nabla \hat{p}_\gamma + \mu_\alpha \nabla^2 \hat{\mathbf{v}}_\gamma + \mu_\alpha \frac{\varepsilon_\omega}{\varepsilon_\gamma + \varepsilon_\omega} \frac{1}{\mathbf{K}_\omega^{\text{II}}} \left(\langle \hat{\mathbf{v}}_\omega \rangle^\omega + \varepsilon_\alpha \varepsilon_\beta \langle \mathbf{v} \rangle^{\gamma\omega} \right) \\ &- \frac{\varepsilon_\gamma}{\varepsilon_\gamma + \varepsilon_\omega} \sum_{i=\omega,\kappa} \frac{1}{V_\gamma} \int_{A_{\gamma i}} \mathbf{n}_{\gamma i}. \left(-\hat{p}_\gamma \mathbf{I} + \mu_\alpha \nabla \hat{\mathbf{v}}_\gamma \right) dA \\ &- \frac{\varepsilon_\omega}{\varepsilon_\gamma + \varepsilon_\omega} \sum_{i=\gamma,\kappa} \frac{1}{V_\omega} \int_{A_{\omega i}} \mathbf{n}_{\omega i}. \left(-\hat{p}_\omega \mathbf{I} + \mu_\alpha \varepsilon_\alpha^{-1} \varepsilon_\beta^{-1} \nabla \hat{\mathbf{v}}_\omega \right) dA \\ &- \frac{1}{\varepsilon_\gamma + \varepsilon_\omega} \rho_\alpha \frac{1}{\mathcal{V}_{\text{II}}} \int_{A_{\gamma\omega}} \mathbf{n}_{\gamma\omega}.\mathbf{w}_{\gamma\omega} \left(\hat{\mathbf{v}}_\gamma - \varepsilon_\alpha^{-1} \varepsilon_\beta^{-1} \hat{\mathbf{v}}_\omega \right) dA \quad \text{in the } \gamma\text{-region} \end{aligned} \tag{C.20}$$

$$\begin{aligned}\rho_\alpha \varepsilon_\alpha^{-1} \varepsilon_\beta^{-1} \frac{\partial \hat{\mathbf{v}}_\omega}{\partial t} = &-\nabla \hat{p}_\omega + \mu_\alpha \varepsilon_\alpha^{-1} \varepsilon_\beta^{-1} \nabla^2 \hat{\mathbf{v}}_\omega - \frac{\mu_\alpha}{\mathbf{K}_\omega^{\text{II}}} \left(\hat{\mathbf{v}}_\omega + \langle \mathbf{v} \rangle^{\gamma\omega} \right) \\ &+ \mu_\alpha \frac{\varepsilon_\omega}{\varepsilon_\gamma + \varepsilon_\omega} \frac{1}{\mathbf{K}_\omega^{\text{II}}} \left(\langle \hat{\mathbf{v}}_\omega \rangle^\omega + \varepsilon_\alpha \varepsilon_\beta \langle \mathbf{v} \rangle^{\gamma\omega} \right) \\ &- \frac{\varepsilon_\gamma}{\varepsilon_\gamma + \varepsilon_\omega} \sum_{i=\omega,\kappa} \frac{1}{V_\gamma} \int_{A_{\gamma i}} \mathbf{n}_{\gamma i}. \left(-\hat{p}_\gamma \mathbf{I} + \mu_\alpha \nabla \hat{\mathbf{v}}_\gamma \right) dA \\ &- \frac{\varepsilon_\omega}{\varepsilon_\gamma + \varepsilon_\omega} \sum_{i=\gamma,\kappa} \frac{1}{V_\omega} \int_{A_{\omega i}} \mathbf{n}_{\omega i}. \left(-\hat{p}_\omega \mathbf{I} + \mu_\alpha \varepsilon_\alpha^{-1} \varepsilon_\beta^{-1} \nabla \hat{\mathbf{v}}_\omega \right) dA \\ &- \frac{1}{\varepsilon_\gamma + \varepsilon_\omega} \rho_\alpha \frac{1}{\mathcal{V}_{\text{II}}} \int_{A_{\gamma\omega}} \mathbf{n}_{\gamma\omega}.\mathbf{w}_{\gamma\omega} \left(\hat{\mathbf{v}}_\gamma - \varepsilon_\alpha^{-1} \varepsilon_\beta^{-1} \hat{\mathbf{v}}_\omega \right) dA \quad \text{in the } \omega\text{-region} \end{aligned} \tag{C.21}$$

To this point, these equations appear quite complex, however an examination of the order of magnitude of the different terms leads to a simplified form of the deviation problem. Before to do that, one needs to evaluate the order of magnitude of the special velocity deviations, and this is done by applying the special decompositions to the boundary conditions Eqs. (8.14) and (8.15), resulting in

$$\hat{\mathbf{v}}_\gamma = O\left(\langle \mathbf{v} \rangle^{\gamma\omega} \right) \quad ; \quad \hat{\mathbf{v}}_\omega = O\left(\varepsilon_\alpha \varepsilon_\beta \langle \mathbf{v} \rangle^{\gamma\omega} \right) \tag{C.22}$$

Now the orders of magnitude of the accumulation, viscous diffusion, and mass exchange terms of Eqs. (C.20) and (C.21) can be evaluated as follows

$$\rho_\alpha \frac{\partial \hat{\mathbf{v}}_\gamma}{\partial t} = O\left(\rho_\alpha \frac{\langle \mathbf{v} \rangle^{\gamma\omega}}{t_{v\gamma}} \right) \quad ; \quad \rho_\alpha \varepsilon_\alpha^{-1} \varepsilon_\beta^{-1} \frac{\partial \hat{\mathbf{v}}_\omega}{\partial t} = O\left(\frac{\langle \mathbf{v} \rangle^{\gamma\omega}}{t_{v\omega}} \right) \tag{C.23}$$

$$\mu_\alpha \nabla^2 \hat{\mathbf{v}}_\gamma = O\left(\frac{\mu_\alpha \langle \mathbf{v} \rangle^{\gamma\omega}}{l_\gamma^2}\right) \quad ; \quad \mu_\alpha \varepsilon_\alpha^{-1} \varepsilon_\beta^{-1} \nabla^2 \hat{\mathbf{v}}_\omega = O\left(\frac{\mu_\alpha \langle \mathbf{v} \rangle^{\gamma\omega}}{l_\omega^2}\right) \tag{C.24}$$

$$\frac{1}{\varepsilon_\gamma + \varepsilon_\omega} \rho_\alpha \frac{1}{\mathcal{V}_{\text{II}}} \int_{A_{\gamma\omega}} \mathbf{n}_{\gamma\omega}.\mathbf{w}_{\gamma\omega} \left(\hat{\mathbf{v}}_\gamma - \varepsilon_\alpha^{-1} \varepsilon_\beta^{-1} \hat{\mathbf{v}}_\omega\right) dA = O\left(\rho_\alpha \frac{1}{l_\gamma} \frac{l_\gamma}{t_{\mathbf{w}}} \langle \mathbf{v} \rangle^{\gamma\omega} \ , \ \rho_\alpha \frac{1}{l_\omega} \frac{l_\omega}{t_{\mathbf{w}}} \langle \mathbf{v} \rangle^{\gamma\omega}\right) \tag{C.25}$$

One sees that if the time scale associated with the velocity of the tissue interface is much larger than the time scale associated with the deviations of the velocities in the γ and ω-regions respectively ($t_{\mathbf{w}} \gg (t_{v\gamma}, t_{v\omega})$), the mass exchange terms in Eqs. (C.20) and (C.21) can be discarded. Moreover the deviation problem can be supposed stationary when the length scale constraints $\rho_\alpha / t_{v\gamma} \ll \mu_\alpha / l_\gamma^2$ and $\rho_\alpha / t_{v\omega} \ll \mu_\alpha / l_\omega^2$ are satisfied. These hypothesis have been made in the previous developments of Chaps. 6 and 7, and if they are also accepted here, the *deviation problem for momentum transport at the tissue scale* takes the form

$$\nabla.\hat{\mathbf{v}}_\gamma = 0 \quad \text{in the } \gamma\text{-region} \tag{C.26}$$

$$\begin{aligned} 0 = &-\nabla \hat{p}_\gamma + \mu_\alpha \nabla^2 \hat{\mathbf{v}}_\gamma + \mu_\alpha \frac{\varepsilon_\omega}{\varepsilon_\gamma + \varepsilon_\omega} \frac{1}{\mathbf{K}_\omega^{\text{II}}} \left(\langle \hat{\mathbf{v}}_\omega \rangle^\omega + \varepsilon_\alpha \varepsilon_\beta \langle \mathbf{v} \rangle^{\gamma\omega}\right) \\ &- \frac{\varepsilon_\gamma}{\varepsilon_\gamma + \varepsilon_\omega} \sum_{i=\omega,\kappa} \frac{1}{V_\gamma} \int_{A_{\gamma i}} \mathbf{n}_{\gamma i}. \left(-\hat{p}_\gamma \mathbf{I} + \mu_\alpha \nabla \hat{\mathbf{v}}_\gamma\right) dA \\ &- \frac{\varepsilon_\omega}{\varepsilon_\gamma + \varepsilon_\omega} \sum_{i=\gamma,\kappa} \frac{1}{V_\omega} \int_{A_{\omega i}} \mathbf{n}_{\omega i}. \left(-\hat{p}_\omega \mathbf{I} + \mu_\alpha \varepsilon_\alpha^{-1} \varepsilon_\beta^{-1} \nabla \hat{\mathbf{v}}_\omega\right) dA \quad \text{in the } \gamma\text{-region} \end{aligned} \tag{C.27}$$

$$\nabla.\hat{\mathbf{v}}_\omega = 0 \quad \text{in the } \omega\text{-region} \tag{C.28}$$

$$\begin{aligned} 0 = &-\nabla \hat{p}_\omega + \mu_\alpha \varepsilon_\alpha^{-1} \varepsilon_\beta^{-1} \nabla^2 \hat{\mathbf{v}}_\omega - \frac{\mu_\alpha}{\mathbf{K}_\omega^{\text{II}}} \left(\hat{\mathbf{v}}_\omega + \langle \mathbf{v} \rangle^{\gamma\omega}\right) \\ &+ \mu_\alpha \frac{\varepsilon_\omega}{\varepsilon_\gamma + \varepsilon_\omega} \frac{1}{\mathbf{K}_\omega^{\text{II}}} \left(\langle \hat{\mathbf{v}}_\omega \rangle^\omega + \varepsilon_\alpha \varepsilon_\beta \langle \mathbf{v} \rangle^{\gamma\omega}\right) \\ &- \frac{\varepsilon_\gamma}{\varepsilon_\gamma + \varepsilon_\omega} \sum_{i=\omega,\kappa} \frac{1}{V_\gamma} \int_{A_{\gamma i}} \mathbf{n}_{\gamma i}. \left(-\hat{p}_\gamma \mathbf{I} + \mu_\alpha \nabla \hat{\mathbf{v}}_\gamma\right) dA \\ &- \frac{\varepsilon_\omega}{\varepsilon_\gamma + \varepsilon_\omega} \sum_{i=\gamma,\kappa} \frac{1}{V_\omega} \int_{A_{\omega i}} \mathbf{n}_{\omega i}. \left(-\hat{p}_\omega \mathbf{I} + \mu_\alpha \varepsilon_\alpha^{-1} \varepsilon_\beta^{-1} \nabla \hat{\mathbf{v}}_\omega\right) dA \quad \text{in the } \omega\text{-region} \end{aligned} \tag{C.29}$$

$$\hat{\mathbf{v}}_\gamma = -\langle \mathbf{v} \rangle^{\gamma\omega} \quad \text{at } A_{\gamma\kappa} \tag{C.30}$$

$$\hat{\mathbf{v}}_\omega = -\varepsilon_\alpha \varepsilon_\beta \langle \mathbf{v} \rangle^{\gamma\omega} \quad \text{at } A_{\omega\kappa} \tag{C.31}$$

$$\hat{\mathbf{v}}_\gamma - \hat{\mathbf{v}}_\omega = -\left(1 - \varepsilon_\alpha \varepsilon_\beta\right) \langle \mathbf{v} \rangle^{\gamma\omega} \quad \text{at } A_{\gamma\omega} \tag{C.32}$$

$$\mathbf{n}_{\gamma\omega}. \left[-\hat{p}_\gamma \mathbf{I} + \mu_\alpha \left(\nabla \hat{\mathbf{v}}_\gamma + \nabla \hat{\mathbf{v}}_\gamma^T\right)\right] = \mathbf{n}_{\gamma\omega}. \left[-\hat{p}_\omega \mathbf{I} + \mu_\alpha \varepsilon_\alpha^{-1} \varepsilon_\beta^{-1} \left(\nabla \hat{\mathbf{v}}_\omega + \nabla \hat{\mathbf{v}}_\omega^T\right)\right] \quad \text{at } A_{\gamma\omega} \tag{C.33}$$

$$\varepsilon_\gamma \langle \hat{\mathbf{v}}_\gamma \rangle^\gamma + \varepsilon_\omega \varepsilon_\alpha^{-1} \varepsilon_\beta^{-1} \langle \hat{\mathbf{v}}_\omega \rangle^\omega = 0 \tag{C.34}$$

In the development of boundary condition Eq. (C.33), the length scale separation $l_\gamma \ll L_\gamma$ has been used to neglect the gradient of the velocity deviations in regard to the gradient of the velocity averages. Note that due to the definition of the special deviation Eq. (C.3), the usual condition on the average of the deviations is different here. Instead, we have Eq. (C.34).

The deviation problem defined by Eqs. (C.26) to (C.34) involves only source terms in $\langle \mathbf{v} \rangle^{\gamma\omega}$ This motivates the following relations between the special deviations and the weighted average

$$\left\{ \begin{array}{l} \hat{\mathbf{v}}_\gamma = \mathbf{B}_\gamma . \langle \mathbf{v} \rangle^{\gamma\omega} \\ \hat{p}_\gamma = \mu_\alpha \mathbf{b}_\gamma . \langle \mathbf{v} \rangle^{\gamma\omega} \end{array} \right. ; \left\{ \begin{array}{l} \hat{\mathbf{v}}_\omega = \varepsilon_\alpha \varepsilon_\beta \mathbf{B}_\omega . \langle \mathbf{v} \rangle^{\gamma\omega} \\ \hat{p}_\omega = \mu_\alpha \mathbf{b}_\omega . \langle \mathbf{v} \rangle^{\gamma\omega} \end{array} \right. \tag{C.35}$$

When comparing with the definition of the closure variables Eqs. (7.42) and (7.43) proposed in Sec. 7.2.1, one could expect to have $\varepsilon_\alpha^{-1}\varepsilon_\beta^{-1}$ in the definition of $\hat{p}_\omega$ instead of having $\varepsilon_\alpha \varepsilon_\beta$ in $\hat{\mathbf{v}}_\omega$. In fact, as highlighted before, $\varepsilon_\alpha^{-1}\varepsilon_\beta^{-1}$ is already contained in the definition of the weighted average Eq. (C.1). And this is also why $\hat{\mathbf{v}}_\omega$ needs to be compensated with $\varepsilon_\alpha \varepsilon_\beta$.

Introducing the closure variables in Eq. (C.19), the macroscopic equation for momentum transport is closed and takes the form

$$\begin{aligned} \frac{\rho_\alpha}{\varepsilon_\gamma + \varepsilon_\omega} \frac{\partial}{\partial t} \left[(\varepsilon_\gamma + \varepsilon_\omega) \langle \mathbf{v} \rangle^{\gamma\omega} \right] &= -\nabla \langle p \rangle^{\gamma\omega} + \mu_\alpha \nabla^2 \langle \mathbf{v} \rangle^{\gamma\omega} + \rho_\alpha \mathbf{g} \\ - \mu_\alpha \Bigg[\frac{\varepsilon_\omega}{\varepsilon_\gamma + \varepsilon_\omega} \frac{\varepsilon_\alpha \varepsilon_\beta}{\mathbf{K}_\omega^{\mathrm{II}}} \left(\langle \mathbf{B}_\omega \rangle^\omega + \mathbf{I} \right) - \frac{\varepsilon_\gamma}{\varepsilon_\gamma + \varepsilon_\omega} \sum_{i=\omega,\kappa} \frac{1}{V_\gamma} \int_{A_{\gamma i}} \mathbf{n}_{\gamma i} . \left(-\mathbf{b}_\gamma \mathbf{I} + \nabla \mathbf{B}_\gamma \right) dA \\ - \frac{\varepsilon_\omega}{\varepsilon_\gamma + \varepsilon_\omega} \sum_{i=\gamma,\kappa} \frac{1}{V_\omega} \int_{A_{\omega i}} \mathbf{n}_{\omega i} . \left(-\mathbf{b}_\omega \mathbf{I} + \nabla \mathbf{B}_\omega \right) dA \Bigg] \langle \mathbf{v} \rangle^{\gamma\omega} \end{aligned} \tag{C.36}$$

By analogy with Sec. 7.2.1, it is possible to define three permeability tensors

$$\varepsilon_\alpha \varepsilon_\beta \mathbf{K}_{\gamma\omega}^{\star -1} = \frac{\varepsilon_\omega}{\varepsilon_\gamma + \varepsilon_\omega} \frac{\varepsilon_\alpha \varepsilon_\beta}{\mathbf{K}_\omega^{\mathrm{II}}} \left(\langle \mathbf{B}_\omega \rangle^\omega + \mathbf{I} \right) \tag{C.37}$$

$$\varepsilon_\gamma \mathbf{K}_\gamma^{\star -1} = -\frac{\varepsilon_\gamma}{\varepsilon_\gamma + \varepsilon_\omega} \sum_{i=\omega,\kappa} \frac{1}{V_\gamma} \int_{A_{\gamma i}} \mathbf{n}_{\gamma i} . \left(-\mathbf{b}_\gamma \mathbf{I} + \nabla \mathbf{B}_\gamma \right) dA \tag{C.38}$$

and

$$\varepsilon_\omega \mathbf{K}_\omega^{\star -1} = -\frac{\varepsilon_\omega}{\varepsilon_\gamma + \varepsilon_\omega} \sum_{i=\gamma,\kappa} \frac{1}{V_\omega} \int_{A_{\omega i}} \mathbf{n}_{\omega i} . \left(-\mathbf{b}_\omega \mathbf{I} + \nabla \mathbf{B}_\omega \right) dA \tag{C.39}$$

The two permeabilities $\mathbf{K}_\gamma^\star$ and $\mathbf{K}_\omega^\star$ have a relatively classic form, and respectively represent the contribution of the γ and ω-region geometry to the bioreactor effective permeability. Yet, by showing a dependence in $\langle \mathbf{B}_\omega \rangle^\omega$, the first tensor $\mathbf{K}_{\gamma\omega}^\star$ appears slightly different from the result obtained in Sec. 7.2.1. Note that when the spacial (instead of the special) deviations are used, $\langle \mathbf{B}_\omega \rangle^\omega = 0$, and a more usual participation of the ω-region permeability is recovered. Anyway, $\mathbf{K}_{\gamma\omega}^\star$ represents the contribution of the ω-region permeability to the overall effective permeability.

The bioreactor effective permeability tensor is a combination of the above tensors, and can be written

$$(\varepsilon_\gamma + \varepsilon_\omega)\,\mathbf{K}_{\text{eff}}^{\text{I}-1} = \varepsilon_\alpha\varepsilon_\beta\mathbf{K}_{\gamma\omega}^{\star-1} + \varepsilon_\gamma\mathbf{K}_{\gamma}^{\star-1} + \varepsilon_\omega\mathbf{K}_{\omega}^{\star-1} \tag{C.40}$$

so that the *closed macroscopic equation* for momentum transport in the bioreactor is

$$\rho_\alpha(\varepsilon_\gamma + \varepsilon_\omega)^{-1}\frac{\partial}{\partial t}\left[(\varepsilon_\gamma + \varepsilon_\omega)\langle\mathbf{v}\rangle^{\gamma\omega}\right] = \\ -\nabla\langle p\rangle^{\gamma\omega} - \frac{\mu_\alpha}{\mathbf{K}_{\text{eff}}^{\text{I}}}\left(\varepsilon_\gamma + \varepsilon_\omega\right)\langle\mathbf{v}\rangle^{\gamma\omega} + \mu_\alpha\nabla^2\langle\mathbf{v}\rangle^{\gamma\omega} + \rho_\alpha\mathbf{g} \tag{C.41}$$

This equation is a Darcy-Brinkman equation for the weighted velocity and pressure. Once again, it is important to keep in mind that the porosity of the tissue is included in $\langle\mathbf{v}\rangle^{\gamma\omega}$. The superficial form of the bioreactor momentum transport equation can be obtained by defining a *superficial weighted velocity*

$$\langle\mathbf{v}\rangle = (\varepsilon_\gamma + \varepsilon_\omega)\langle\mathbf{v}\rangle^{\gamma\omega} \tag{C.42}$$

so that we have

$$\rho_\alpha(\varepsilon_\gamma + \varepsilon_\omega)^{-1}\frac{\partial}{\partial t}\langle\mathbf{v}\rangle = -\nabla\langle p\rangle^{\gamma\omega} - \frac{\mu_\alpha}{\mathbf{K}_{\text{eff}}^{\text{I}}}\langle\mathbf{v}\rangle + \mu_\alpha(\varepsilon_\gamma + \varepsilon_\omega)^{-1}\nabla^2\langle\mathbf{v}\rangle + \rho_\alpha\mathbf{g} \tag{C.43}$$

Here the effective viscosity is $\mu_\alpha\left(\varepsilon_\gamma + \varepsilon_\omega\right)^{-1}$.

The effective permeability tensor remains to be evaluated, and this is done by introducing the closure variables in the deviation problem. This leads to a *closure problem* for the fluid-porous-solid system of the form

$$\nabla.\mathbf{B}_\gamma = 0 \quad \text{in the } \gamma\text{-region} \tag{C.44}$$

$$0 = -\nabla\mathbf{b}_\gamma + \nabla^2\mathbf{B}_\gamma + (\varepsilon_\gamma + \varepsilon_\omega)\,\mathbf{K}_{\text{eff}}^{\text{I}-1} \quad \text{in the } \gamma\text{-region} \tag{C.45}$$

$$\nabla.\mathbf{B}_\omega = 0 \quad \text{in the } \omega\text{-region} \tag{C.46}$$

$$0 = -\nabla\mathbf{b}_\omega + \nabla^2\mathbf{B}_\omega - \varepsilon_\alpha\varepsilon_\beta\mathbf{K}_{\omega}^{\text{II}-1}\left(\mathbf{B}_\omega + \mathbf{I}\right) + (\varepsilon_\gamma + \varepsilon_\omega)\,\mathbf{K}_{\text{eff}}^{\text{I}-1} \quad \text{in the } \omega\text{-region} \tag{C.47}$$

$$\mathbf{B}_\gamma = -\mathbf{I} \quad \text{at } A_{\gamma\kappa} \tag{C.48}$$

$$\mathbf{B}_\omega = -\mathbf{I} \quad \text{at } A_{\omega\kappa} \tag{C.49}$$

$$\mathbf{B}_\gamma - \varepsilon_\alpha\varepsilon_\beta\mathbf{B}_\omega = -\left(1 - \varepsilon_\alpha\varepsilon_\beta\right)\mathbf{I} \quad \text{at } A_{\gamma\omega} \tag{C.50}$$

$$\mathbf{n}_{\gamma\omega}.\left[-\mathbf{b}_\gamma\mathbf{I} + \left(\nabla\mathbf{B}_\gamma + \nabla\mathbf{B}_\gamma^T\right)\right] = \mathbf{n}_{\gamma\omega}.\left[-\mathbf{b}_\omega\mathbf{I} + \left(\nabla\mathbf{B}_\omega + \nabla\mathbf{B}_\omega^T\right)\right] \quad \text{at } A_{\gamma\omega} \tag{C.51}$$

$$\mathbf{B}_\gamma(\mathbf{x} + l_i) = \mathbf{B}_\gamma(\mathbf{x}) \quad ; \quad \mathbf{b}_\gamma(\mathbf{x} + l_i) = \mathbf{b}_\gamma(\mathbf{x}) \quad i = 1, 2, 3 \tag{C.52}$$

$$\mathbf{B}_\omega(\mathbf{x} + l_i) = \mathbf{B}_\omega(\mathbf{x}) \quad ; \quad \mathbf{b}_\omega(\mathbf{x} + l_i) = \mathbf{b}_\omega(\mathbf{x}) \quad i = 1, 2, 3 \tag{C.53}$$

$$\varepsilon_\gamma\langle\mathbf{B}_\gamma\rangle^\gamma + \varepsilon_\omega\langle\mathbf{B}_\omega\rangle^\omega = 0 \tag{C.54}$$

This closure problem has to be solved in a representative volume, and for homogeneous porous media, a periodic unit cell is suitable. Thus periodic conditions have been added to the closure problem (Eqs. (C.52) and (C.53)).

Although this problem is an integro-differentional problem, it can be written in the form of an incompressible Brinkman flow. In order to simplify its numerical resolution, a first variable change is proposed

$$\begin{cases} \mathbf{B}_\gamma^\sharp = \mathbf{B}_\gamma + \mathbf{I} \\ \mathbf{B}_\omega^\sharp = \mathbf{B}_\omega + \mathbf{I} \end{cases} \tag{C.55}$$

so the closure problem reads

$$\nabla.\mathbf{B}_\gamma^\sharp = 0 \quad \text{in the } \gamma\text{-region} \tag{C.56}$$

$$0 = -\nabla\mathbf{b}_\gamma + \nabla^2\mathbf{B}_\gamma^\sharp + (\varepsilon_\gamma + \varepsilon_\omega)\,\mathbf{K}_{\text{eff}}^{\text{I}-1} \quad \text{in the } \gamma\text{-region} \tag{C.57}$$

$$\nabla.\mathbf{B}_\omega^\sharp = 0 \quad \text{in the } \omega\text{-region} \tag{C.58}$$

$$0 = -\nabla\mathbf{b}_\omega + \nabla^2\mathbf{B}_\omega^\sharp - \mathbf{K}_\omega^{\text{II}-1}\mathbf{B}_\omega^\sharp + (\varepsilon_\gamma + \varepsilon_\omega)\,\mathbf{K}_{\text{eff}}^{\text{I}-1} \quad \text{in the } \omega\text{-region} \tag{C.59}$$

$$\mathbf{B}_\gamma^\sharp = 0 \quad \text{at } A_{\gamma\kappa} \tag{C.60}$$

$$\mathbf{B}_\omega^\sharp = 0 \quad \text{at } A_{\omega\kappa} \tag{C.61}$$

$$\mathbf{B}_\gamma^\sharp - \varepsilon_\alpha\varepsilon_\beta\mathbf{B}_\omega^\sharp = 0 \quad \text{at } A_{\gamma\omega} \tag{C.62}$$

$$\mathbf{n}_{\gamma\omega}.\left[-\mathbf{b}_\gamma\mathbf{I} + \left(\nabla\mathbf{B}_\gamma^\sharp + \nabla\mathbf{B}_\gamma^{\sharp T}\right)\right] = \mathbf{n}_{\gamma\omega}.\left[-\mathbf{b}_\omega\mathbf{I} + \left(\nabla\mathbf{B}_\omega^\sharp + \nabla\mathbf{B}_\omega^{\sharp T}\right)\right] \quad \text{at } A_{\gamma\omega} \tag{C.63}$$

$$\mathbf{B}_\gamma^\sharp(\mathbf{x} + l_i) = \mathbf{B}_\gamma^\sharp(\mathbf{x}) \quad ; \quad \mathbf{b}_\gamma(\mathbf{x} + l_i) = \mathbf{b}_\gamma(\mathbf{x}) \quad i = 1, 2, 3 \tag{C.64}$$

$$\mathbf{B}_\omega^\sharp(\mathbf{x} + l_i) = \mathbf{B}_\omega^\sharp(\mathbf{x}) \quad ; \quad \mathbf{b}_\omega(\mathbf{x} + l_i) = \mathbf{b}_\omega(\mathbf{x}) \quad i = 1, 2, 3 \tag{C.65}$$

$$\varepsilon_\gamma\langle\mathbf{B}_\gamma^\sharp\rangle^\gamma + \varepsilon_\omega\langle\mathbf{B}_\omega^\sharp\rangle^\omega = (\varepsilon_\gamma + \varepsilon_\omega)\,\mathbf{I} \tag{C.66}$$

And finally with a last variable change

$$\begin{cases} \mathbf{B}'_\gamma = (\varepsilon_\gamma + \varepsilon_\omega)^{-1}\,\mathbf{B}_\gamma^\sharp\mathbf{K}_{\text{eff}} \\ \mathbf{B}'_\omega = (\varepsilon_\gamma + \varepsilon_\omega)^{-1}\,\mathbf{B}_\omega^\sharp\mathbf{K}_{\text{eff}} \end{cases} ; \quad \begin{cases} \mathbf{b}'_\gamma = (\varepsilon_\gamma + \varepsilon_\omega)^{-1}\,\mathbf{b}_\gamma\mathbf{K}_{\text{eff}} \\ \mathbf{b}'_\omega = (\varepsilon_\gamma + \varepsilon_\omega)^{-1}\,\mathbf{b}_\omega\mathbf{K}_{\text{eff}} \end{cases} \tag{C.67}$$

the closure problem can be set in the form of an incompressible Brinkman's flow

$$\nabla.\mathbf{B}'_\gamma = 0 \quad \text{in the } \gamma\text{-region} \tag{C.68}$$

$$0 = -\nabla\mathbf{b}'_\gamma + \nabla^2\mathbf{B}'_\gamma + \mathbf{I} \quad \text{in the } \gamma\text{-region} \tag{C.69}$$

$$\nabla.\mathbf{B}'_\omega = 0 \quad \text{in the } \omega\text{-region} \tag{C.70}$$

$$0 = -\nabla\mathbf{b}'_\omega + \nabla^2\mathbf{B}'_\omega - \mathbf{K}_\omega^{\text{II}-1}\mathbf{B}'_\omega + \mathbf{I} \quad \text{in the } \omega\text{-region} \tag{C.71}$$

$$\mathbf{B}'_\gamma = 0 \quad \text{at } A_{\gamma\kappa} \tag{C.72}$$

$$\mathbf{B}'_\omega = 0 \quad \text{at } A_{\omega\kappa} \tag{C.73}$$

$$\mathbf{B}'_\gamma - \varepsilon_\alpha\varepsilon_\beta\mathbf{B}'_\omega = 0 \quad \text{at } A_{\gamma\omega} \tag{C.74}$$

$$\mathbf{n}_{\gamma\omega}.\left[-\mathbf{b}'_\gamma\mathbf{I} + \left(\nabla\mathbf{B}'_\gamma + \nabla\mathbf{B}'^T_\gamma\right)\right] = \mathbf{n}_{\gamma\omega}.\left[-\mathbf{b}'_\omega\mathbf{I} + \left(\nabla\mathbf{B}'_\omega + \nabla\mathbf{B}'^T_\omega\right)\right] \quad \text{at } A_{\gamma\omega} \tag{C.75}$$

$$\mathbf{B}'_\gamma(\mathbf{x} + l_i) = \mathbf{B}'_\gamma(\mathbf{x}) \quad ; \quad \mathbf{b}'_\gamma(\mathbf{x} + l_i) = \mathbf{b}'_\gamma(\mathbf{x}) \quad i = 1, 2, 3 \tag{C.76}$$

$$\mathbf{B}'_\omega(\mathbf{x} + l_i) = \mathbf{B}'_\omega(\mathbf{x}) \quad ; \quad \mathbf{b}'_\omega(\mathbf{x} + l_i) = \mathbf{b}'_\omega(\mathbf{x}) \quad i = 1, 2, 3 \tag{C.77}$$

$$\varepsilon_\gamma\langle\mathbf{B}'_\gamma\rangle^\gamma + \varepsilon_\omega\langle\mathbf{B}'_\omega\rangle^\omega = \mathbf{K}_{\text{eff}} \tag{C.78}$$

BIBLIOGRAPHY

Aaron, R. K., Ciombor, D. M., Wang, S., & Simon, B. (2006). Clinical biophysics: the promotion of skeletal repair by physical forces. *Annals of the New York Academy of Sciences*, *1068*, 513–531. Cited on page(s) 25.

Acosta Santamaría, V. A., Malvè, M., Duizabo, A., Mena Tobar, A., Gallego Ferrer, G., García Aznar, J. M., Doblaré, M., & Ochoa, I. (2013). Computational methodology to determine fluid related parameters of non regular three-dimensional scaffolds. *Annals of Biomedical Engineering*, *41*, 2367–2380. Cited on page(s) 36, 37.

Ahmadi, A., Quintard, M., & Whitaker, S. (1998). Transport in chemically and mechanically heterogeneous porous media: V. two-equation model for solute transport with adsorption. *Advances in Water Resources*, *22*, 59–86. Cited on page(s) 82, 111, 119, 164, 174.

Altmann, B., Steinberg, T., Giselbrecht, S., Gottwald, E., Tomakidi, P., Bächle-Haas, M., & Kohal, R.-J. (2011). Promotion of osteoblast differentiation in 3d biomaterial micro-chip arrays comprising fibronectin-coated poly(methyl methacrylate) polycarbonate. *Biomaterials*, *32*, 8947–8956. Cited on page(s) 49.

Amaral Souto, H. P., & Moyne, C. (1997). Dispersion in two-dimensional periodic porous media. part II. dispersion tensor. *Physics of Fluids*, *9*, 2253–2263. Cited on page(s) 67.

Araujo, R. P., & McElwain, D. L. S. (2004). A history of the study of solid tumour growth: The contribution of mathematical modelling. *Bulletin of Mathematical Biology*, *66*, 1039–1091. Cited on page(s) 40.

Ashcroft, F. M. (1999). *Ion Channels and Disease*. Academic Press. Cited on page(s) 72, 73.

Baas, E., Kuiper, J. H., Yang, Y., Wood, M. A., & El Haj, A. J. (2010). In vitro bone growth responds to local mechanical strain in three-dimensional polymer scaffolds. *Journal of Biomechanics*, *43*, 733–739. Cited on page(s) 24.

Bancroft, G. N., Sikavitsas, V. I., van den Dolder, J., Sheffield, T. L., Ambrose, C. G., Jansen, J. A., & Mikos, A. G. (2002). Fluid flow increases mineralized matrix deposition in 3d perfusion culture of marrow stromal osteoblasts in a dose-dependent manner. *Proceedings of the National Academy of Sciences*, *99*, 12600 –12605. Cited on page(s) 20, 23.

Bancroft, J. D., & Gamble, M. (2008). *Theory and Practice of Histological Techniques*. (6th ed.). Churchill Livingstone: Elsevier Health Sciences. Cited on page(s) 131.

Beavers, G. S., & Joseph, D. D. (1967). Boundary conditions at a naturally permeable wall. *Journal of Fluid Mechanics*, *30*, 197–207. Cited on page(s) 93, 169.

Bodamyali, T., Bhatt, B., Hughes, F. J., Winrow, V. R., Kanczler, J. M., Simon, B., Abbott, J., Blake, D. R., & Stevens, C. R. (1998). Pulsed electromagnetic fields simultaneously induce osteogenesis and upregulate transcription of bone morphogenetic proteins 2 and 4 in rat osteoblastsin vitro. *Biochemical and Biophysical Research Communications*, *250*, 458–461. Cited on page(s) 25.

Boschetti, F., Raimondi, M. T., Migliavacca, F., & Dubini, G. (2006). Prediction of the micro-fluid dynamic environment imposed to three-dimensional engineered cell systems in bioreactors. *Journal of Biomechanics*, *39*, 418–425. Cited on page(s) 35, 36, 37, 38, 53.

Bose, S., Roy, M., & Bandyopadhyay, A. (2012). Recent advances in bone tissue engineering scaffolds. *Trends in Biotechnology*, *30*, 546–554. Cited on page(s) 15.

Botchwey, E. A., Dupree, M. A., Pollack, S. R., Levine, E. M., & Laurencin, C. T. (2003). Tissue engineered bone: Measurement of nutrient transport in three-dimensional matrices. *Journal of Biomedical Materials Research Part A*, *67A*, 357–367. Cited on page(s) 39, 53.

Botchwey, E. A., Pollack, S. R., Levine, E. M., & Laurencin, C. T. (2001). Bone tissue engineering in a rotating bioreactor using a microcarrier matrix system. *Journal of Biomedical Materials Research*, *55*, 242–253. Cited on page(s) 22.

Bousquet-Melou, P., Goyeau, B., Quintard, M., Fichot, F., & Gobin, D. (2002). Average momentum equation for interdendritic flow in a solidifying columnar mushy zone. *International Journal of Heat and Mass Transfer*, *45*, 3651–3665. Cited on page(s) 73, 165.

Brinkman, H. C. (1947). A calculation of the viscous force exerted by a flowing fluid on a dense swarm of particles. *Applied Scientific Research*, *1*, 27–34. Cited on page(s) 61, 71, 126, 171.

Buckwalter, J. A., Glimcher, M. J., Cooper, R. R., & Recker, R. (1995a). Bone biology. i: Structure, blood supply, cells, matrix, and mineralization. *Journal of bone and joint surgery. American volume*, *77*, 1256–1275. Cited on page(s) 8, 10.

Buckwalter, J. A., Glimcher, M. J., Cooper, R. R., & Recker, R. (1995b). Bone biology. II: Formation, form, modeling, remodeling, and regulation of cell function. *Journal of bone and joint surgery. American volume*, *77*, 1276–1289. Cited on page(s) 9.

Burghardt, A., Rogut, J., & Gotkowska, J. (1988). Diffusion coefficients in bidisperse porous structures. *Chemical Engineering Science*, *43*, 2463–2476. Cited on page(s) 163.

Byrne, H., & Drasdo, D. (2008). Individual-based and continuum models of growing cell populations: a comparison. *Journal of Mathematical Biology*, *58*, 657–687. Cited on page(s) 40, 41.

Bölgen, N., Yang, Y., Korkusuz, P., Güzel, E., El Haj, A. J., & Pişkin, E. (2008). Three-dimensional ingrowth of bone cells within biodegradable cryogel scaffolds in bioreactors at different regimes. *Tissue Engineering Part A*, *14*, 1743–1750. Cited on page(s) 25.

Calori, G., Mazza, E., Colombo, M., & Ripamonti, C. (2011). The use of bone-graft substitutes in large bone defects: Any specific needs? *Injury*, *42, Supplement 2*, S56–S63. Cited on page(s) 1, 10, 11, 12.

Cartmell, S. H., Porter, B. D., Garcia, A. J., & Guldberg, R. E. (2003). Effects of medium perfusion rate on cell-seeded three-dimensional bone constructs in vitro. *Tissue Engineering*, *9*, 1197–1203. Cited on page(s) 16, 20, 21, 23, 53.

Chabanon, M., Duval, H., Francais, O., Lepioufle, B., Perrin, E., Goyeau, B., & David, B. (2012). Discrete model combined with mimetic microfluidic chips to study cell growth in porous scaffold under flow conditions. *Computer Methods in Biomechanics and Biomedical Engineering*, *15*, 25–26. Cited on page(s) 49, 126, 150.

Chandesris, M., & Jamet, D. (2006). Boundary conditions at a planar fluid–porous interface for a poiseuille flow. *International Journal of Heat and Mass Transfer*, *49*, 2137–2150. Cited on page(s) 94.

Chary, S. R., & Jain, R. K. (1989). Direct measurement of interstitial convection and diffusion of albumin in normal and neoplastic tissues by fluorescence photobleaching. *Proceedings of the National Academy of Sciences*, *86*, 5385–5389. Cited on page(s) 58.

Cheng, G., Markenscoff, P., & Zygourakis, K. (2009). A 3d hybrid model for tissue growth: The interplay between cell population and mass transport dynamics. *Biophysical Journal*, *97*, 401–414. Cited on page(s) 42.

Cheng, G., Youssef, B. B., Markenscoff, P., & Zygourakis, K. (2006). Cell population dynamics modulate the rates of tissue growth processes. *Biophysical Journal*, *90*, 713–724. Cited on page(s) 42.

Cherblanc, F., Ahmadi, A., & Quintard, M. (2003). Two-medium description of dispersion in heterogeneous porous media: Calculation of macroscopic properties. *Water Resources Research*, *39*, 1154. Cited on page(s) 82, 111, 119, 120, 164.

Cherblanc, F., Ahmadi, A., & Quintard, M. (2007). Two-domain description of solute transport in heterogeneous porous media: Comparison between theoretical predictions and numerical experiments. *Advances in Water Resources*, *30*, 1127–1143. Cited on page(s) 111.

Chung, C., Lin, T.-H., Chen, S.-D., & Huang, H.-I. (2010). Hybrid cellular automaton modeling of nutrient modulated cell growth in tissue engineering constructs. *Journal of Theoretical Biology*, *262*, 267–278. Cited on page(s) 39, 42, 43, 53.

Chung, C. A., Chen, C. P., Lin, T. H., & Tseng, C. S. (2008). A compact computational model for cell construct development in perfusion culture. *Biotechnology and Bioengineering*, *99*, 1535–1541. Cited on page(s) 44.

Chung, C. A., Chen, C. W., Chen, C. P., & Tseng, C. S. (2007). Enhancement of cell growth in tissue-engineering constructs under direct perfusion: Modeling and simulation. *Biotechnology and Bioengineering*, *97*, 1603–1616. Cited on page(s) 44, 54, 71, 142.

Cioffi, M., Boschetti, F., Raimondi, M. T., & Dubini, G. (2006). Modeling evaluation of the fluid-dynamic microenvironment in tissue-engineered constructs: A micro-CT based model. *Biotechnology and Bioengineering*, *93*, 500–510. Cited on page(s) 35, 36, 37, 38.

Cioffi, M., Küffer, J., Ströbel, S., Dubini, G., Martin, I., & Wendt, D. (2008). Computational evaluation of oxygen and shear stress distributions in 3d perfusion culture systems: Macro-scale and micro-structured models. *Journal of Biomechanics*, *41*, 2918–2925. Cited on page(s) 37, 38, 39, 53.

Codling, E. A., Plank, M. J., & Benhamou, S. (2008). Random walk models in biology. *Journal of The Royal Society Interface*, *5*, 813–834. Cited on page(s) 40.

Coletti, F., Macchietto, S., & Elvassore, N. (2006). Mathematical modeling of three-dimensional cell cultures in perfusion bioreactors. *Industrial & Engineering Chemistry Research*, *45*, 8158–8169. Cited on page(s) 44.

Colnot, C. (2011). Cell sources for bone tissue engineering: Insights from basic science. *Tissue Engineering. Part B, Reviews*, *17*, 449–457. Cited on page(s) 16.

Contois, D. E. (1959). Kinetics of bacterial growth: Relationship between population density and specific growth rate of continuous cultures. *Journal of General Microbiology*, *21*, 40 –50. Cited on page(s) 40, 43.

Cowin, S. C. (2001). *Bone Mechanics Handbook, Second Edition*. Taylor & Francis. Cited on page(s) 8, 15.

Cowin, S. C. (2007). The significance of bone microstructure in mechanotransduction. *Journal of Biomechanics*, *40, Supplement 1*, S105–S109. Cited on page(s) 20.

Cushman, J. H., Bennethum, L. S., & Hu, B. X. (2002). A primer on upscaling tools for porous media. *Advances in Water Resources*, *25*, 1043–1067. Cited on page(s) 53.

Dafni, H., Israely, T., Bhujwalla, Z. M., Benjamin, L. E., & Neeman, M. (2002). Overexpression of vascular endothelial growth factor 165 drives peritumor interstitial convection and induces lymphatic drain magnetic resonance imaging, confocal microscopy, and histological tracking of triple-labeled albumin. *Cancer Research*, *62*, 6731–6739. Cited on page(s) 58.

Darcy, H. (1856). *Les fontaines publiques de la ville de Dijon*. Paris: Victor Dalmont. Cited on page(s) 77.

David, B., Bonnefont-Rousselot, D., Oudina, K., Degat, M.-C., Deschepper, M., Viateau, V., Bensidhoum, M., Oddou, C., & Petite, H. (2011). A perfusion bioreactor for engineering bone constructs: an in vitro and in vivo study. *Tissue Engineering Part C: Methods*, *17*, 505–516. Cited on page(s) 16, 19, 23, 24, 26, 33, 49, 53, 125, 126, 149.

David, B., Doré, E., Jaffrin, M. Y., & Legallais, C. (2004). Mass transfers in a fluidized bed bioreactor using alginate beads for a future bioartificial liver. *The International journal of artificial organs*, *27*, 284–293. Cited on page(s) 26.

David, B., Perrin, E., Lazaar, M., Chabanon, M., Le Pioufle, B., & Français, O. (2014). Reproducing topography and roughness of osteoconductive materials in a microfluidic device for bone tissue engineering. In *Proceedings of the 4th European Conference on Microfluidics*. Limerick, Ireland. Cited on page(s) 14, 150.

Davit, Y., Debenest, G., Wood, B. D., & Quintard, M. (2010). Modeling non-equilibrium mass transport in biologically reactive porous media. *Advances in Water Resources*, (pp. 1075–1093). Cited on page(s) 54, 83, 94, 95, 111, 112, 119, 126, 150, 183.

Davit, Y., Iltis, G., Debenest, G., Veran-Tissoires, S., Wildenschild, D., Gerino, M., & Quintard, M. (2011). Imaging biofilm in porous media using x-ray computed microtomography. *Journal of Microscopy*, *242*, 15–25. Cited on page(s) 126, 138.

Davit, Y., Wood, B. D., Debenest, G., & Quintard, M. (2012). Correspondence between one- and two-equation models for solute transport in two-region heterogeneous porous media. *Transport in Porous Media*, *95*, 213–238. Cited on page(s) 111.

Delaine-Smith, R. M., Sittichokechaiwut, A., & Reilly, G. C. (2014). Primary cilia respond to fluid shear stress and mediate flow-induced calcium deposition in osteoblasts. *FASEB journal: official publication of the Federation of American Societies for Experimental Biology*, *28*, 430–439. Cited on page(s) 20.

Deschepper, M., Oudina, K., David, B., Myrtil, V., Collet, C., Bensidhoum, M., Logeart-Avramoglou, D., & Petite, H. (2011). Survival and function of mesenchymal stem cells (MSCs) depend on glucose to overcome exposure to long-term, severe and continuous hypoxia. *Journal of Cellular and Molecular Medicine*, *15*, 1505–1514. Cited on page(s) 17.

d'Humieres, D. (1992). Generalized lattice-boltzmann equations. In *Rarefied gas dynamics- Theory and simulations* (pp. 450–458). Washington, DC: AIAA volume 159 of *Progress in Astronautics and Aeronautics*. (B.d. shizgal, d.p. weaver ed.). Cited on page(s) 37.

Dias, M. R., Fernandes, P. R., Guedes, J. M., & Hollister, S. J. (2012). Permeability analysis of scaffolds for bone tissue engineering. *Journal of Biomechanics*, *45*, 938–944. Cited on page(s) 34.

Dias, R. P., Fernandes, C. S., Teixeira, J. A., Mota, M., & Yelshin, A. (2008). Permeability analysis in bisized porous media: Wall effect between particles of different size. *Journal of Hydrology*, *349*, 470–474. Cited on page(s) 163.

Dimitriou, R., Tsiridis, E., & Giannoudis, P. V. (2005). Current concepts of molecular aspects of bone healing. *Injury*, *36*, 1392–1404. Cited on page(s) 11.

Dunn, J. C. Y., Chan, W.-Y., Cristini, V., Kim, J. S., Lowengrub, J., Singh, S., & Wu, B. M. (2006). Analysis of cell growth in three-dimensional scaffolds. *Tissue engineering*, *12*, 705–716. Cited on page(s) 44.

El Haj, A. J., & Cartmell, S. H. (2010). Bioreactors for bone tissue engineering. *Proceedings of the Institution of Mechanical Engineers. Part H, Journal of Engineering in Medicine*, *224*, 1523–1532. Cited on page(s) 25.

El Haj, A. J., Minter, S. L., Rawlinson, S. C. F., Suswillo, R., & Lanyon, L. E. (1990). Cellular responses to mechanical loading in vitro. *Journal of Bone and Mineral Research*, *5*, 923–932. Cited on page(s) 23, 24, 53.

Engler, A. J., Sen, S., Sweeney, H. L., & Discher, D. E. (2006). Matrix elasticity directs stem cell lineage specification. *Cell*, *126*, 677–689. Cited on page(s) 13.

Fleury, M. E., Boardman, K. C., & Swartz, M. A. (2006). Autologous morphogen gradients by subtle interstitial flow and matrix interactions. *Biophysical Journal*, *91*, 113–121. Cited on page(s) 53, 57.

Fournier, R. L. (2011). *Basic Transport Phenomena in Biomedical Engineering, Third Edition*. CRC Press. Cited on page(s) 58, 95, 145.

Freed, L. E., Marquis, J. C., Langer, R., & Vunjak-Novakovic, G. (1994). Kinetics of chondrocyte growth in cell-polymer implants. *Biotechnology and Bioengineering*, *43*, 597–604. Cited on page(s) 43, 53.

Freed, L. E., & Vunjak-Novakovic, G. (1995). Cultivation of cell–polymer tissue constructs in simulated microgravity. *Biotechnology and Bioengineering*, *46*, 306–313. Cited on page(s) 21.

Frohlich, M., Grayson, W. L., Wan, L. Q., Marolt, D., Drobnic, M., & Vunjak-Novakovic, G. (2008). Tissue engineered bone grafts: Biological requirements, tissue culture and clinical relevance. *Current stem cell research & therapy*, *3*, 254–264. Cited on page(s) 10, 11, 12, 15.

Galban, C. J., & Locke, B. R. (1997). Analysis of cell growth in a polymer scaffold using a moving boundary approach. *Biotechnology and Bioengineering*, *56*, 422–432. Cited on page(s) 43, 45.

Galban, C. J., & Locke, B. R. (1999a). Analysis of cell growth kinetics and substrate diffusion in a polymer scaffold. *Biotechnology and Bioengineering*, *65*, 121–132. Cited on page(s) 39, 43, 54, 142.

Galban, C. J., & Locke, B. R. (1999b). Effects of spatial variation of cells and nutrient and product concentrations coupled with product inhibition on cell growth in a polymer scaffold. *Biotechnology and Bioengineering*, *64*, 633–643. Cited on page(s) 39, 43, 54, 83.

Galbusera, F., Cioffi, M., & Raimondi, M. T. (2008). An in silico bioreactor for simulating laboratory experiments in tissue engineering. *Biomedical Microdevices*, *10*, 547–554. Cited on page(s) 39, 41.

Galbusera, F., Cioffi, M., Raimondi, M. T., & Pietrabissa, R. (2007). Computational modeling of combined cell population dynamics and oxygen transport in engineered tissue subject to interstitial perfusion. *Computer Methods in Biomechanics & Biomedical Engineering*, *10*, 279–287. Cited on page(s) 38, 39, 42.

Gao, Y., Zhang, X., Rama, P., Liu, Y., Chen, R., Ostadi, H., & Jiang, K. (2012). Calculating the anisotropic permeability of porous media using the lattice boltzmann method and x-ray computed tomography. *Transport in Porous Media*, *92*, 457–472. Cited on page(s) 38.

Garanich, J. S., Mathura, R. A., Shi, Z.-D., & Tarbell, J. M. (2007). Effects of fluid shear stress on adventitial fibroblast migration: implications for flow-mediated mechanisms of arterialization and intimal hyperplasia. *American Journal of Physiology - Heart and Circulatory Physiology*, *292*, H3128–H3135. Cited on page(s) 57.

Garijo, N., Manzano, R., Osta, R., & Perez, M. (2012). Stochastic cellular automata model of cell migration, proliferation and differentiation: Validation with in vitro cultures of muscle satellite cells. *Journal of Theoretical Biology*, *314*, 1–9. Cited on page(s) 42.

Giannoudis, P. V., Dinopoulos, H., & Tsiridis, E. (2005). Bone substitutes: An update. *Injury*, *36*, S20–S27. Cited on page(s) 11, 12.

Glowacki, J., Mizuno, S., & Greenberger, J. S. (1998). Perfusion enhances functions of bone marrow stromal cells in three-dimensional culture. *Cell Transplantation*, *7*, 319–326. Cited on page(s) 20.

Goldstein, A. S., Juarez, T. M., Helmke, C. D., Gustin, M. C., & Mikos, A. G. (2001). Effect of convection on osteoblastic cell growth and function in biodegradable polymer foam scaffolds. *Biomaterials*, *22*, 1279–1288. Cited on page(s) 20, 22, 33, 34, 35.

Golfier, F., Wood, B. D., Orgogozo, L., Quintard, M., & Buès, M. (2009). Biofilms in porous media: Development of macroscopic transport equations via volume averaging with closure for local mass equilibrium conditions. *Advances in Water Resources*, *32*, 463–485. Cited on page(s) 54, 72, 83, 84, 95, 111, 126, 183.

Goyeau, B., Benihaddadene, T., Gobin, D., & Quintard, M. (1997). Averaged momentum equation for flow through a nonhomogenenous porous structure. *Transport in Porous Media*, *28*, 19–50. Cited on page(s) 80.

Goyeau, B., Gobin, D., Benihaddadene, T., Gobin, D., & Quintard, M. (1999). Numerical calculation of the permeability in a dendritic mushy zone. *Metallurgical and Materials Transactions B*, *30*, 613–622. Cited on page(s) 62, 166.

Goyeau, B., Lhuillier, D., Gobin, D., & Velarde, M. (2003). Momentum transport at a fluid–porous interface. *International Journal of Heat and Mass Transfer*, *46*, 4071–4081. Cited on page(s) 45, 49, 94, 169.

Gray, W. G. (1975). A derivation of the equations for multi-phase transport. *Chemical Engineering Science*, *30*, 229–233. Cited on page(s) 74, 157, 160, 170.

Grayson, W., Bhumiratana, S., Grace Chao, P., Hung, C., & Vunjak-Novakovic, G. (2010). Spatial regulation of human mesenchymal stem cell differentiation in engineered osteochondral constructs: effects of pre-differentiation, soluble factors and medium perfusion. *Osteoarthritis and Cartilage*, *18*, 714–723. Cited on page(s) 20.

Grayson, W. L., Bhumiratana, S., Cannizzaro, C., Chao, P.-H. G., Lennon, D. P., Caplan, A. I., & Vunjak-Novakovic, G. (2008). Effects of initial seeding density and fluid perfusion rate on formation of tissue-engineered bone. *Tissue Engineering Part A*, *14*, 1809–1820. Cited on page(s) 17, 23, 53.

Grayson, W. L., Marolt, D., Bhumiratana, S., Frohlich, M., Guo, X. E., & Vunjak-Novakovic, G. (2011). Optimizing the medium perfusion rate in bone tissue engineering bioreactors. *Biotechnology and Bioengineering*, *108*, 1159–1170. Cited on page(s) 20, 23, 35, 53.

Guyon, E., Oger, L., & Plona, T. J. (1987). Transport properties in sintered porous media composed of two particle sizes. *Journal of Physics D: Applied Physics*, *20*, 1637. Cited on page(s) 163.

Hansmann, J., Groeber, F., Kahlig, A., Kleinhans, C., & Walles, H. (2013). Bioreactors in tissue engineering-principles, applications and commercial constraints. *Biotechnology Journal*, *8*, 298–307. Cited on page(s) 53.

Hendrikson, W. J., van Blitterswijk, C. A., Verdonschot, N., Moroni, L., & Rouwkema, J. (2014). Modeling mechanical signals on the surface of uCT and CAD based rapid prototype scaffold models to predict (early stage) tissue development. *Biotechnology and Bioengineering*, *111*, 1864–1875. Cited on page(s) 36.

Hoey, D. A., Downs, M. E., & Jacobs, C. R. (2012). The mechanics of the primary cilium: An intricate structure with complex function. *Journal of Biomechanics*, *45*, 17–26. Cited on page(s) 20.

Hoffmann, M., Kuska, J.-P., Zscharnack, M., Loeffler, M., & Galle, J. (2011). Spatial organization of mesenchymal stem cells in vitro - results from a new individual cell-based model with podia. *PLoS ONE*, *6*, e21960. Cited on page(s) 41.

Holt, G. E., Halpern, J. L., Dovan, T. T., Hamming, D., & Schwartz, H. S. (2005). Evolution of an in vivo bioreactor. *Journal of Orthopaedic Research*, *23*, 916–923. Cited on page(s) 25.

Horikawa, A., Okada, K., Sato, K., & Sato, M. (2000). Morphological changes in osteoblastic cells (MC3t3-e1) due to fluid shear stress: Cellular damage by prolonged application of fluid shear stress. *The Tohoku Journal of Experimental Medicine*, *191*, 127–137. Cited on page(s) 20.

Howes, F. A., & Whitaker, S. (1985). The spatial averaging theorem revisited. *Chemical Engineering Science*, *40*, 1387–1392. Cited on page(s) 60, 157.

Hung, C. T., Pollack, S. R., Reilly, T. M., & Brighton, C. T. (1995). Real-time calcium response of cultured bone cells to fluid flow. *Clinical Orthopaedics and Related Research*, *313*, 256–269. Cited on page(s) 20.

Hutmacher, D. W. (2000). Scaffolds in tissue engineering bone and cartilage. *Biomaterials*, *21*, 2529–2543. Cited on page(s) 13, 14, 15, 36.

Höfling, F., & Franosch, T. (2013). Anomalous transport in the crowded world of biological cells. *Reports on Progress in Physics*, *76*, 046602. Cited on page(s) 72.

Ignatius, A., Blessing, H., Liedert, A., Schmidt, C., Neidlinger-Wilke, C., Kaspar, D., Friemert, B., & Claes, L. (2005). Tissue engineering of bone: effects of mechanical strain on osteoblastic cells in type i collagen matrices. *Biomaterials*, *26*, 311–318. Cited on page(s) 25.

Ingber, D. E. (2006). Cellular mechanotransduction: putting all the pieces together again. *The FASEB Journal*, *20*, 811–827. Cited on page(s) 20.

Jaasma, M. J., & O'Brien, F. J. (2008). Mechanical stimulation of osteoblasts using steady and dynamic fluid flow. *Tissue Engineering Part A*, *14*, 1213–1223. Cited on page(s) 23.

Jacobs, C. R., Temiyasathit, S., & Castillo, A. B. (2010). Osteocyte mechanobiology and pericellular mechanics. *Annual Review of Biomedical Engineering*, *12*, 369–400. Cited on page(s) 20.

Jain, R. K. (1999). Transport of molecules, particles, and cells in solid tumors. *Annual Review of Biomedical Engineering*, *1*, 241–263. Cited on page(s) 58.

Janicki, P., & Schmidmaier, G. (2011). What should be the characteristics of the ideal bone graft substitute? combining scaffolds with growth factors and/or stem cells. *Injury*, *42, Supplement 2*, S77–S81. Cited on page(s) 12.

Janssen, F. W., Oostra, J., Oorschot, A. v., & van Blitterswijk, C. A. (2006). A perfusion bioreactor system capable of producing clinically relevant volumes of tissue-engineered bone: In vivo bone formation showing proof of concept. *Biomaterials*, *27*, 315–323. Cited on page(s) 23, 24, 53.

Jeong, D., Yun, A., & Kim, J. (2011). Mathematical model and numerical simulation of the cell growth in scaffolds. *Biomechanics and modeling in mechanobiology*, *11*, 677–88. Cited on page(s) 44.

Jones, G. W., & Chapman, S. J. (2012). Modeling growth in biological materials. *SIAM Review*, *54*, 52–118. Cited on page(s) 40.

Jungreuthmayer, C., Donahue, S. W., Jaasma, M. J., Al-Munajjed, A. A., Zanghellini, J., Kelly, D. J., & O'Brien, F. J. (2009a). A comparative study of shear stresses in collagen-glycosaminoglycan and calcium phosphate scaffolds in bone tissue-engineering bioreactors. *Tissue Engineering Part A*, *15*, 1141–1149. Cited on page(s) 20, 35, 37, 38, 53.

Jungreuthmayer, C., Jaasma, M., Al-Munajjed, A., Zanghellini, J., Kelly, D., & O'Brien, F. J. (2009b). Deformation simulation of cells seeded on a collagen-GAG scaffold in a flow perfusion bioreactor using a sequential 3d CFD-elastostatics model. *Medical Engineering & Physics*, *31*, 420–427. Cited on page(s) 21, 37, 41.

Kapellos, G. E., Alexiou, T. S., & Payatakes, A. C. (2012). A multiscale theoretical model for fluid flow in cellular biological media. *International Journal of Engineering Science*, *51*, 241–271. Cited on page(s) 94.

Khademhosseini, A., Langer, R., Borenstein, J., & Vacanti, J. P. (2006). Microscale technologies for tissue engineering and biology. *Proceedings of the National Academy of Sciences of the United States of America*, *103*, 2480–2487. Cited on page(s) 13.

Kneser, U., Schaefer, D. J., Polykandriotis, E., & Horch, R. E. (2006). Tissue engineering of bone: the reconstructive surgeon's point of view. *Journal of Cellular and Molecular Medicine*, *10*, 7–19. Cited on page(s) 7, 11, 12, 13, 15.

Kommareddy, K. P., Lange, C., Rumpler, M., Dunlop, J. W. C., Manjubala, I., Cui, J., Kratz, K., Lendlein, A., & Fratzl, P. (2010). Two stages in three-dimensional in vitro growth of tissue generated by osteoblastlike cells. *Biointerphases*, *5*, 45. Cited on page(s) 17.

Korin, N., Bransky, A., Dinnar, U., & Levenberg, S. (2007). A parametric study of human fibroblasts culture in a microchannel bioreactor. *Lab on a Chip*, *7*, 611. Cited on page(s) 49, 53, 126.

Kreke, M. R., & Goldstein, A. S. (2004). Hydrodynamic shear stimulates osteocalcin expression but not proliferation of bone marrow stromal cells. *Tissue Engineering*, *10*, 780–788. Cited on page(s) 49.

Kwon, R. Y., & Jacobs, C. R. (2007). Time-dependent deformations in bone cells exposed to fluid flow in vitro: investigating the role of cellular deformation in fluid flow-induced signaling. *Journal of Biomechanics*, *40*, 3162–3168. Cited on page(s) 20.

Kühn, T., Ihalainen, T. O., Hyväluoma, J., Dross, N., Willman, S. F., Langowski, J., Vihinen-Ranta, M., & Timonen, J. (2011). Protein diffusion in mammalian cell cytoplasm. *PLoS ONE*, *6*, e22962. Cited on page(s) 72, 150.

Laganà, M., & Raimondi, M. T. (2012). A miniaturized, optically accessible bioreactor for systematic 3d tissue engineering research. *Biomedical Microdevices*, *14*, 225–234. Cited on page(s) 49.

Lallemand, P., & Luo, L.-S. (2000). Theory of the lattice boltzmann method: Dispersion, dissipation, isotropy, galilean invariance, and stability. *Physical Review E*, *61*, 6546–6562. Cited on page(s) 37.

Langer, R., & Vacanti, J. P. (1993). Tissue engineering. *Science*, *260*, 920–926. Cited on page(s) 7.

Lappa, M. (2003). Organic tissues in rotating bioreactors: fluid mechanical aspects, dynamic growth models, and morphological evolution. *Biotechnology and Bioengineering*, *84*, 518–532. Cited on page(s) 45, 47.

Lasseux, D., Ahmadi, A., Cleis, X., & Garnier, J. (2004). A macroscopic model for species transport during in vitro tissue growth obtained by the volume averaging method. *Chemical Engineering Science*, *59*, 1949–1964. Cited on page(s) 39, 53, 54, 83, 95, 111, 183.

Lasseux, D., Arani, A. A. A., & Ahmadi, A. (2011). On the stationary macroscopic inertial effects for one phase flow in ordered and disordered porous media. *Physics of Fluids (1994-present)*, *23*, 073103. Cited on page(s) 93.

Lasseux, D., Quintard, M., & Whitaker, S. (1996). Determination of permeability tensors for two-phase flow in homogeneous porous media: Theory. *Transport in Porous Media*, *24*, 107–137. Cited on page(s) 94, 96, 101, 104, 106.

Leclerc, E., David, B., Griscom, L., Lepioufle, B., Fujii, T., Layrolle, P., & Legallais, C. (2006). Study of osteoblastic cells in a microfluidic environment. *Biomaterials*, *27*, 586–595. Cited on page(s) 20, 49, 57.

Lee, Y. (1994). *Computer-assisted analysis of endothelial cell migration and proliferation*. Ph.D. thesis Rice University Houston, Texas. Cited on page(s) 42.

Lee, Y., Kouvroukoglou, S., McIntire, L., & Zygourakis, K. (1995). A cellular automaton model for the proliferation of migrating contact-inhibited cells. *Biophysical Journal*, *69*, 1284–1298. Cited on page(s) 42.

Legallais, C., Doré, E., & Paullier, P. (2000). Design of a fluidized bed bioartificial liver. *Artificial Organs*, *24*, 519–525. Cited on page(s) 26.

Lemon, G., & King, J. R. (2007). Multiphase modelling of cell behaviour on artificial scaffolds: effects of nutrient depletion and spatially nonuniform porosity. *Mathematical Medicine and Biology*, *24*, 57–83. Cited on page(s) 44.

Lemon, G., King, J. R., Byrne, H. M., Jensen, O. E., & Shakesheff, K. M. (2006). Mathematical modelling of engineered tissue growth using a multiphase porous flow mixture theory. *Journal of Mathematical Biology*, *52*, 571–594. Cited on page(s) 44.

Levick, J. R. (1987). Flow through interstitium and other fibrous matrices. *Experimental Physiology*, *72*, 409–437. Cited on page(s) 58, 95, 145.

Lewis, M. C., MacArthur, B. D., Malda, J., Pettet, G., & Please, C. P. (2005). Heterogeneous proliferation within engineered cartilaginous tissue: the role of oxygen tension. *Biotechnology and Bioengineering*, *91*, 607–615. Cited on page(s) 44.

Luo, W., Xiong, W., Zhou, J., Fang, Z., Chen, W., Fan, Y., & Li, F. (2011). Laminar shear stress delivers cell cycle arrest and anti-apoptosis to mesenchymal stem cells. *Acta Biochimica et Biophysica Sinica*, *43*, 210–216. Cited on page(s) 57.

Ma, C., Kumar, R., Xu, X., & Mantalaris, A. (2006). A combined fluid dynamics, mass transport and cell growth model for a three-dimensional perfused biorector for tissue engineering of haematopoietic cells. *Biochemical Engineering Journal*, . Cited on page(s) 71.

MacDonald, M. J., Chu, C.-F., Guilloit, P. P., & Ng, K. M. (1991). A generalized blake-kozeny equation for multisized spherical particles. *AIChE Journal*, *37*, 1583–1588. Cited on page(s) 163.

Maes, F., Van Ransbeeck, P., Van Oosterwyck, H., & Verdonck, P. (2009). Modeling fluid flow through irregular scaffolds for perfusion bioreactors. *Biotechnology and Bioengineering*, *103*, 621–630. Cited on page(s) 36.

Malda, J., Rouwkema, J., Martens, D. E., le Comte, E. P., Kooy, F. K., Tramper, J., van Blitterswijk, C. A., & Riesle, J. (2004). Oxygen gradients in tissue-engineered pegt/pbt cartilaginous constructs: Measurement and modeling. *Biotechnology and Bioengineering*, *86*, 9–18. Cited on page(s) 17, 58.

Maniatopoulos, C., Rodriguez, A., Deporter, D., & Melcher, A. (1985). An improved method for preparing histological sections of metallic implants. *The International journal of oral & maxillofacial implants*, *1*, 31–37. Cited on page(s) 131.

Markicevic, B., & Djilali, N. (2006). Two-scale modeling in porous media: Relative permeability predictions. *Physics of Fluids*, *18*, 033101–033101–13. Cited on page(s) 163.

Martin, I., Smith, T., & Wendt, D. (2009). Bioreactor-based roadmap for the translation of tissue engineering strategies into clinical products. *Trends in Biotechnology*, *27*, 495–502. Cited on page(s) 30.

Martin, I., Wendt, D., & Heberer, M. (2004). The role of bioreactors in tissue engineering. *Trends in Biotechnology*, *22*, 80–86. Cited on page(s) 30.

Mastro, A. M., Babich, M. A., Taylor, W. D., & Keith, A. D. (1984). Diffusion of a small molecule in the cytoplasm of mammalian cells. *Proceedings of the National Academy of Sciences*, *81*, 3414–3418. Cited on page(s) 83.

Mauney, J. R., Sjostorm, S., Blumberg, J., Horan, R., O'Leary, J. P., Vunjak-Novakovic, G., Volloch, V., & Kaplan, D. L. (2004). Mechanical stimulation promotes osteogenic differentiation of human bone marrow stromal cells on 3-d partially demineralized bone scaffolds in vitro. *Calcified Tissue International*, *74*, 458–468. Cited on page(s) 24.

McCoy, R. J., & O'Brien, F. J. (2010). Influence of shear stress in perfusion bioreactor cultures for the development of three-dimensional bone tissue constructs: A review. *Tissue Engineering Part B: Reviews*, *16*, 587–601. Cited on page(s) 1, 20, 21, 53.

McGarry, J. G., Klein-Nulend, J., Mullender, M. G., & Prendergast, P. J. (2004). A comparison of strain and fluid shear stress in stimulating bone cell responses—a computational and experimental study. *The FASEB Journal*, . Cited on page(s) 20.

Meyer, U., Wiesmann, H. P., Kruse-Losler, B., Handschel, J., Stratmann, U., & Joos, U. (1999). Strain-related bone remodeling in distraction osteogenesis of the mandible. *Plastic and Reconstructive Surgery*, *103*, 800–807. Cited on page(s) 20, 53.

Morad, M. R., & Khalili, A. (2009). Transition layer thickness in a fluid-porous medium of multi-sized spherical beads. *Experiments in Fluids*, *46*, 323–330. Cited on page(s) 163.

Mota, M., Teixeira, J. A., Bowen, W. R., & Yelshin, A. (2001). Binary spherical particle mixed beds : porosity and permeability relationship measurement. *Transactions of the Filtration Society*, *1*, 101–106. Cited on page(s) 163.

Moutsopoulos, K. N., & Koch, D. L. (1999). Hydrodynamic and boundary-layer dispersion in bidisperse porous media. *Journal of Fluid Mechanics*, *385*, 359–379. Cited on page(s) 163, 177, 178.

Moutsopoulos, K. N., Papaspyros, I. N. E., & Tsihrintzis, V. A. (2009). Experimental investigation of inertial flow processes in porous media. *Journal of Hydrology*, *374*, 242–254. Cited on page(s) 163.

Mueller, S. M., Mizuno, S., Gerstenfeld, L. C., & Glowacki, J. (1999). Medium perfusion enhances osteogenesis by murine osteosarcoma cells in three-dimensional collagen sponges. *Journal of Bone and Mineral Research*, *14*, 2118–2126. Cited on page(s) 21.

Murphy, C. M., Haugh, M. G., & O'Brien, F. J. (2010). The effect of mean pore size on cell attachment, proliferation and migration in collagen–glycosaminoglycan scaffolds for bone tissue engineering. *Biomaterials*, *31*, 461–466. Cited on page(s) 13.

Muschler, G. F., Nakamoto, C., & Griffith, L. G. (2004). Engineering principles of clinical cell-based tissue engineering. *The Journal of Bone and Joint Surgery*, *86-A*, 1541–1558. Cited on page(s) 10, 13, 15, 16, 17, 20.

Mygind, T., Stiehler, M., Baatrup, A., Li, H., Zou, X., Flyvbjerg, A., Kassem, M., & Bunger, C. (2007). Mesenchymal stem cell ingrowth and differentiation on coralline hydroxyapatite scaffolds. *Biomaterials*, *28*, 1036–1047. Cited on page(s) 17, 21.

Nava, M. M., Raimondi, M. T., & Pietrabissa, R. (2013). A multiphysics 3d model of tissue growth under interstitial perfusion in a tissue-engineering bioreactor. *Biomechanics and Modeling in Mechanobiology*, *12*, 1169–1179. Cited on page(s) 45, 47.

Neale, G., & Nader, W. (1974). Practical significance of brinkman's extension of darcy's law: Coupled parallel flows within a channel and a bounding porous medium. *The Canadian Journal of Chemical Engineering*, *52*, 475–478. Cited on page(s) 93.

Neculae, A., Goyeau, B., Quintard, M., & Gobin, D. (2002). Passive dispersion in dendritic structures. *Materials Science and Engineering: A*, *323*, 367–376. Cited on page(s) 165, 167.

Neidlinger-Wilke, C., Wilke, H.-J., & Claes, L. (1994). Cyclic stretching of human osteoblasts affects proliferation and metabolism: A new experimental method and its application. *Journal of Orthopaedic Research*, *12*, 70–78. Cited on page(s) 25.

Ng, C. P., & Swartz, M. A. (2003). Fibroblast alignment under interstitial fluid flow using a novel 3-d tissue culture model. *American Journal of Physiology - Heart and Circulatory Physiology*, *284*, H1771–H1777. Cited on page(s) 57, 67, 82.

Ng, C. P., & Swartz, M. A. (2006). Mechanisms of interstitial flow-induced remodeling of fibroblast–collagen cultures. *Annals of Biomedical Engineering*, *34*, 446–454. Cited on page(s) 57, 67, 82.

Nield, D. A., & Bejan, A. (2006). *Convection in Porous Media*. Springer. Cited on page(s) 93.

Nikolaev, N. I., Obradovic, B., Versteeg, H. K., Lemon, G., & Williams, D. J. (2010). A validated model of GAG deposition, cell distribution, and growth of tissue engineered cartilage cultured in a rotating bioreactor. *Biotechnology and Bioengineering*, *105*, 842–853. Cited on page(s) 39, 71, 142.

Ochoa, J. A. (1988). *Diffusion and reaction in heterogeneous media*. Ph.D. thesis University of California Davis, California. Cited on page(s) 39.

Ochoa, J. A., Stroeve, P., & Whitaker, S. (1986). Diffusion and reaction in cellular media. *Chemical Engineering Science*, *41*, 2999–3013. Cited on page(s) 54, 82, 83, 84, 169.

Ochoa-Tapia, J. A., & Whitaker, S. (1995). Momentum transfer at the boundary between a porous medium and a homogeneous fluid-i. theoretical development. *International Journal of Heat and Mass Transfer*, *38*, 2635–2646. Cited on page(s) 93, 94.

O'Dea, R. D., Waters, S. L., & Byrne, H. M. (2008). A two-fluid model for tissue growth within a dynamic flow environment. *European Journal of Applied Mathematics*, *19*, 607–634. Cited on page(s) 44, 47.

O'Dea, R. D., Waters, S. L., & Byrne, H. M. (2010). A multiphase model for tissue construct growth in a perfusion bioreactor. *Mathematical Medicine and Biology*, *27*, 95–127. Cited on page(s) 44, 45, 47.

Olivier, V., Hivart, P., Descamps, M., & Hardouin, P. (2007). In vitro culture of large bone substitutes in a new bioreactor: importance of the flow direction. *Biomedical Materials*, *2*, 174–180. Cited on page(s) 16, 23.

Orgogozo, L., Golfier, F., & Buès, M. (2009). Upscaling of transport processes in porous media with biofilms in equilibrium and non-equilibrium conditions. *Applicable Analysis*, *88*, 1579–1588. Cited on page(s) 54, 72, 111, 126.

Orgogozo, L., Golfier, F., Buès, M., & Quintard, M. (2010). Upscaling of transport processes in porous media with biofilms in non-equilibrium conditions. *Advances in Water Resources*, *33*, 585–600. Cited on page(s) 54, 72, 111.

Osborne, J. M., O'Dea, R. D., Whiteley, J. P., Byrne, H. M., & Waters, S. L. (2010). The influence of bioreactor geometry and the mechanical environment on engineered tissues. *Journal of Biomechanical Engineering*, *132*, 051006–12. Cited on page(s) 44, 47.

Park, J. Y., Yoo, S. J., Patel, L., Lee, S. H., & Lee, S.-H. (2010). Cell morphological response to low shear stress in a two-dimensional culture microsystem with magnitudes comparable to interstitial shear stress. *Biorheology*, *47*, 165–178. Cited on page(s) 20, 49, 53, 57.

Pathi, P., Ma, T., & Locke, B. R. (2005). Role of nutrient supply on cell growth in bioreactor design for tissue engineering of hematopoietic cells. *Biotechnology and Bioengineering*, *89*, 743–758. Cited on page(s) 39, 54.

Pedersen, J. A., Boschetti, F., & Swartz, M. A. (2007). Effects of extracellular fiber architecture on cell membrane shear stress in a 3d fibrous matrix. *Journal of Biomechanics*, *40*, 1484–1492. Cited on page(s) 20, 53, 58.

Pedersen, J. A., Lichter, S., & Swartz, M. A. (2010). Cells in 3d matrices under interstitial flow: Effects of extracellular matrix alignment on cell shear stress and drag forces. *Journal of Biomechanics*, *43*, 900–905. Cited on page(s) 20, 53, 57, 58.

Petite, H., Viateau, V., Bensaid, W., Meunier, A., de Pollak, C., Bourguignon, M., Oudina, K., Sedel, L., & Guillemin, G. (2000). Tissue-engineered bone regeneration. *Nature Biotechnology*, *18*, 959–963. Cited on page(s) 1, 25.

Petropoulos, J. H., Petrou, J. K., & Liapis, A. I. (1991). Network model investigation of gas transport in bidisperse porous adsorbents. *Industrial & Engineering Chemistry Research*, *30*, 1281–1289. Cited on page(s) 163.

Pham, N. H., Voronov, R. S., VanGordon, S. B., Sikavitsas, V. I., & Papavassiliou, D. V. (2012). Predicting the stress distribution within scaffolds with ordered architecture. *Biorheology*, *49*, 235–247. Cited on page(s) 35, 37, 38.

Pierre, J., & Oddou, C. (2007). Engineered bone culture in a perfusion bioreactor: a 2d computational study of stationary mass and momentum transport. *Computer Methods in Biomechanics and Biomedical Engineering*, *10*, 429–438. Cited on page(s) 39.

Pioletti, D. P. (2013). Integration of mechanotransduction concepts in bone tissue engineering. *Computer Methods in Biomechanics and Biomedical Engineering*, *16*, 1050–1055. Cited on page(s) 15.

Plank, M. J., & Simpson, M. J. (2012). Models of collective cell behaviour with crowding effects: comparing lattice-based and lattice-free approaches. *Journal of The Royal Society Interface*, *9*, 2983–2996. Cited on page(s) 41.

Porter, B., Zauel, R., Stockman, H., Guldberg, R., & Fyhrie, D. (2005). 3-d computational modeling of media flow through scaffolds in a perfusion bioreactor. *Journal of Biomechanics*, *38*, 543–549. Cited on page(s) 37, 38.

Porter, B. D., Lin, A. S., Peister, A., Hutmacher, D., & Guldberg, R. E. (2007). Noninvasive image analysis of 3d construct mineralization in a perfusion bioreactor. *Biomaterials*, *28*, 2525–2533. Cited on page(s) 138.

Quarto, R., Mastrogiacomo, M., Cancedda, R., Kutepov, S. M., Mukhachev, V., Lavroukov, A., Kon, E., & Marcacci, M. (2001). Repair of large bone defects with the use of autologous bone marrow stromal cells. *New England Journal of Medicine*, *344*, 385–386. Cited on page(s) 1.

Quintard, M., Cherblanc, F., & Whitaker, S. (2001). Dispersion in heterogeneous porous media: One-equation non-equilibrium model. *Transport in Porous Media*, *44*, 181–203. Cited on page(s) 82, 111, 164.

Quintard, M., & Whitaker, S. (1994a). Convection, dispersion, and interfacial transport of contaminants: Homogeneous porous media. *Advances in Water Resources*, *17*, 221–239. Cited on page(s) 118, 165.

Quintard, M., & Whitaker, S. (1994b). Transport in ordered and disordered porous media II: Generalized volume averaging. *Transport in Porous Media*, *14*, 179–206. Cited on page(s) 61, 158, 160.

Quintard, M., & Whitaker, S. (1994c). Transport in ordered and disordered porous media III: Closure and comparison between theory and experiment. *Transport in Porous Media*, *15*, 31–49. Cited on page(s) 61.

Quintard, M., & Whitaker, S. (1996a). Transport in chemically and mechanically heterogeneous porous media : I. theoretical development of region-averaged equations for slightly compressible single-phase flow. *Advances in Water Resources*, *19*, 29–47. Cited on page(s) 76, 77, 96, 164.

Quintard, M., & Whitaker, S. (1996b). Transport in chemically and mechanically heterogeneous porous media: II. comparison with numerical experiments for slightly compressible single-phase flow. *Advances in Water Resources*, *19*, 49–60. Cited on page(s) 96, 164.

Quintard, M., & Whitaker, S. (1998a). Transport in chemically and mechanically heterogeneous porous media: III. large-scale mechanical equilibrium and the regional form of darcy's law. *Advances in Water Resources*, *21*, 617–629. Cited on page(s) 76, 95, 96, 98, 164, 185.

Quintard, M., & Whitaker, S. (1998b). Transport in chemically and mechanically heterogeneous porous media: IV. large-scale mass equilibrium for solute transport with adsorption. *Advances in Water Resources*, *22*, 33–57. Cited on page(s) 82, 111, 164, 173, 174, 179.

Raimondi, M. T., Moretti, M., Cioffi, M., Giordano, C., Boschetti, F., Laganà, K., & Pietrabissa, R. (2006). The effect of hydrodynamic shear on 3d engineered chondrocyte systems subject to direct perfusion. *Biorheology*, *43*, 215–222. Cited on page(s) 20, 37, 44, 53.

Rauh, J., Milan, F., Gunther, K. P., & Stiehler, M. (2011). Bioreactor systems for bone tissue engineering. *Tissue Engineering Part B: Reviews*, *17*, 263–280. Cited on page(s) 21, 22, 24.

Rutkowski, J. M., & Swartz, M. A. (2007). A driving force for change: interstitial flow as a morphoregulator. *Trends in Cell Biology*, *17*, 44–50. Cited on page(s) 59.

Sacco, R., Causin, P., Zunino, P., & Raimondi, M. T. (2010). A multiphysics/multiscale 2d numerical simulation of scaffold-based cartilage regeneration under interstitial perfusion in a bioreactor. *Biomechanics and Modeling in Mechanobiology*, *10*, 577–589. Cited on page(s) 39, 44, 47, 54, 71, 142.

Salter, E., Goh, B., Hung, B., Hutton, D., Ghone, N., & Grayson, W. L. (2012). Bone tissue engineering bioreactors: A role in the clinic? *Tissue Engineering Part B: Reviews*, *18*, 62–75. Cited on page(s) 19, 30.

Sandino, C., Planell, J., & Lacroix, D. (2008). A finite element study of mechanical stimuli in scaffolds for bone tissue engineering. *Journal of Biomechanics*, *41*, 1005–1014. Cited on page(s) 36, 37.

Scaglione, S., Wendt, D., Miggino, S., Papadimitropoulos, A., Fato, M., Quarto, R., & Martin, I. (2008). Effects of fluid flow and calcium phosphate coating on human bone marrow stromal cells cultured in a defined 2d model system. *Journal of Biomedical Materials Research Part A*, *86A*, 411–419. Cited on page(s) 49.

Schneider, C. A., Rasband, W. S., & Eliceiri, K. W. (2012). NIH image to ImageJ: 25 years of image analysis. *Nature Methods*, *9*, 671–675. Cited on page(s) 132.

Schwartz, Z., Simon, B. J., Duran, M. A., Barabino, G., Chaudhri, R., & Boyan, B. D. (2008). Pulsed electromagnetic fields enhance BMP-2 dependent osteoblastic differentiation of human mesenchymal stem cells. *Journal of Orthopaedic Research*, *26*, 1250–1255. Cited on page(s) 25.

Sengers, B. G., Van Donkelaar, C. C., Oomens, C. W. J., & Baaijens, F. P. T. (2005). Computational study of culture conditions and nutrient supply in cartilage tissue engineering. *Biotechnology Progress*, *21*, 1252–1261. Cited on page(s) 39.

Sikavitsas, V. I., Bancroft, G. N., Holtorf, H. L., Jansen, J. A., & Mikos, A. G. (2003). Mineralized matrix deposition by marrow stromal osteoblasts in 3d perfusion culture increases with increasing fluid shear forces. *Proceedings of the National Academy of Sciences*, *100*, 14683 –14688. Cited on page(s) 20.

Sikavitsas, V. I., Bancroft, G. N., & Mikos, A. G. (2002). Formation of three-dimensional cell/polymer constructs for bone tissue engineering in a spinner flask and a rotating wall vessel bioreactor. *Journal of Biomedical Materials Research*, *62*, 136–148. Cited on page(s) 21, 22.

Silva, J. C., & Rodrigues, A. E. (1996). Analysis of ZLC technique for diffusivity measurements in bidisperse porous adsorbent pellets. *Gas Separation & Purification*, *10*, 207–224. Cited on page(s) 163.

Singh, H., Teoh, S., Low, H., & Hutmacher, D. (2005). Flow modelling within a scaffold under the influence of uni-axial and bi-axial bioreactor rotation. *Journal of Biotechnology*, *119*, 181–196. Cited on page(s) 36.

Song, K., Liu, T., Cui, Z., Li, X., & Ma, X. (2008). Three-dimensional fabrication of engineered bone with human bio-derived bone scaffolds in a rotating wall vessel bioreactor. *Journal of Biomedical Materials Research Part A*, *86A*, 323–332. Cited on page(s) 22, 23.

Soulaine, C., Davit, Y., & Quintard, M. (2013). A two-pressure model for slightly compressible single phase flow in bi-structured porous media. *Chemical Engineering Science*, *96*, 55–70. Cited on page(s) 49, 96, 101, 102, 104, 106.

Sprio, S., Ruffini, A., Valentini, F., D'Alessandro, T., Sandri, M., Panseri, S., & Tampieri, A. (2011). Biomimesis and biomorphic transformations: New concepts applied to bone regeneration. *Journal of Biotechnology*, *156*, 347–355. Cited on page(s) 13, 14.

Stevens, M. M., Marini, R. P., Schaefer, D., Aronson, J., Langer, R., & Shastri, V. P. (2005). In vivo engineering of organs: The bone bioreactor. *Proceedings of the National Academy of Sciences of the United States of America*, *102*, 11450–11455. Cited on page(s) 25.

Steward Jr., R. L., Cheng, C.-M., Wang, D. L., & LeDuc, P. R. (2010). Probing cell structure responses through a shear and stretching mechanical stimulation technique. *Cell Biochemistry and Biophysics*, *56*, 115–124. Cited on page(s) 126.

Stops, A., Heraty, K., Browne, M., O'Brien, F., & McHugh, P. (2010). A prediction of cell differentiation and proliferation within a collagen–glycosaminoglycan scaffold subjected to mechanical strain and perfusive fluid flow. *Journal of Biomechanics*, *43*, 618–626. Cited on page(s) 37.

Sun, L.-Y., Hsieh, D.-K., Lin, P.-C., Chiu, H.-T., & Chiou, T.-W. (2010). Pulsed electromagnetic fields accelerate proliferation and osteogenic gene expression in human bone marrow mesenchymal stem cells during osteogenic differentiation. *Bioelectromagnetics*, *31*, 209–219. Cited on page(s) 25.

Swartz, M. A., & Fleury, M. E. (2007). Interstitial flow and its effects in soft tissues. *Annual Review of Biomedical Engineering*, *9*, 229–256. Cited on page(s) 57, 58, 67, 82, 83, 93, 95, 145.

Tarbell, J. M., & Shi, Z.-D. (2013). Effect of the glycocalyx layer on transmission of interstitial flow shear stress to embedded cells. *Biomechanics and Modeling in Mechanobiology*, *12*, 111–121. Cited on page(s) 53, 58, 95, 145.

Tardy, Y., Resnick, N., Nagel, T., Gimbrone, M. A., & Dewey, C. F. (1997). Shear stress gradients remodel endothelial monolayers in vitro via a cell proliferation-migration-loss cycle. *Arteriosclerosis, Thrombosis, and Vascular Biology*, *17*, 3102–3106. Cited on page(s) 57.

Thorens, B., & Mueckler, M. (2010). Glucose transporters in the 21st century. *American Journal of Physiology - Endocrinology and Metabolism*, *298*, E141–E145. Cited on page(s) 72, 73.

Topman, G., Sharabani-Yosef, O., & Gefen, A. (2012). A standardized objective method for continuously measuring the kinematics of cultures covering a mechanically damaged site. *Medical Engineering & Physics*, *34*, 225–232. Cited on page(s) 126.

Tsai, M.-T., Chang, W. H.-S., Chang, K., Hou, R.-J., & Wu, T.-W. (2007). Pulsed electromagnetic fields affect osteoblast proliferation and differentiation in bone tissue engineering. *Bioelectromagnetics*, *28*, 519–528. Cited on page(s) 25.

Vahedi Tafreshi, H., A Rahman, M. S., Jaganathan, S., Wang, Q., & Pourdeyhimi, B. (2009). Analytical expressions for predicting permeability of bimodal fibrous porous media. *Chemical Engineering Science*, *64*, 1154–1159. Cited on page(s) 163.

Valdés-Parada, F. J., Aguilar-Madera, C. G., Ochoa-Tapia, J. A., & Goyeau, B. (2013). Velocity and stress jump conditions between a porous medium and a fluid. *Advances in Water Resources*, . Cited on page(s) 49, 94, 169.

Valdés-Parada, F. J., Goyeau, B., & Alberto Ochoa-Tapia, J. (2006). Diffusive mass transfer between a microporous medium and an homogeneous fluid: Jump boundary conditions. *Chemical Engineering Science*, *61*, 1692–1704. Cited on page(s) 45.

Vance, J., Galley, S., Liu, D. F., & Donahue, S. W. (2005). Mechanical stimulation of MC3t3 osteoblastic cells in a bone tissue-engineering bioreactor enhances prostaglandin e2 release. *Tissue Engineering*, *11*, 1832–1839. Cited on page(s) 35.

VanGordon, S. B., Voronov, R. S., Blue, T. B., Shambaugh, R. L., Papavassiliou, D. V., & Sikavitsas, V. I. (2010). Effects of scaffold architecture on preosteoblastic cultures under continuous fluid shear. *Industrial & engineering chemistry research*, *50*, 620–629. Cited on page(s) 14, 38.

Voronov, R., VanGordon, S., Sikavitsas, V. I., & Papavassiliou, D. V. (2010a). Computational modeling of flow-induced shear stresses within 3d salt-leached porous scaffolds imaged via micro-CT. *Journal of Biomechanics*, *43*, 1279–1286. Cited on page(s) 35, 38.

Voronov, R. S., VanGordon, S. B., Shambaugh, R. L., Papavassiliou, D. V., & Sikavitsas, V. I. (2013). 3d tissue-engineered construct analysis via conventional high-resolution microcomputed tomography without x-ray contrast. *Tissue Engineering. Part C, Methods*, *19*, 327–335. Cited on page(s) 138.

Voronov, R. S., VanGordon, S. B., Sikavitsas, V. I., & Papavassiliou, D. V. (2010b). Distribution of flow-induced stresses in highly porous media. *Applied Physics Letters*, *97*, 024101. Cited on page(s) 35, 36, 38.

Vunjak-Novakovic, G., Obradovic, B., Martin, I., Bursac, P. M., Langer, R., & Freed, L. E. (1998). Dynamic cell seeding of polymer scaffolds for cartilage tissue engineering. *Biotechnology Progress*, *14*, 193–202. Cited on page(s) 17, 21.

Wang, D. M., & Tarbell, J. M. (1995). Modeling interstitial flow in an artery wall allows estimation of wall shear stress on smooth muscle cells. *Journal of Biomechanical Engineering*, *117*, 358–363. Cited on page(s) 35.

Wang, S., & Tarbell, J. M. (2000). Effect of fluid flow on smooth muscle cells in a 3-dimensional collagen gel model. *Arteriosclerosis, Thrombosis, and Vascular Biology*, *20*, 2220 –2225. Cited on page(s) 35.

Warnke, P., Springer, I., Wiltfang, J., Acil, Y., Eufinger, H., Wehmöller, M., Russo, P., Bolte, H., Sherry, E., Behrens, E., & Terheyden, H. (2004). Growth and transplantation of a custom vascularised bone graft in a man. *The Lancet*, *364*, 766–770. Cited on page(s) 25, 26, 29.

Warnke, P. H., Wiltfang, J., Springer, I., Acil, Y., Bolte, H., Kosmahl, M., Russo, P. A. J., Sherry, E., Lützen, U., Wolfart, S., & Terheyden, H. (2006). Man as living bioreactor: Fate of an exogenously prepared customized tissue-engineered mandible. *Biomaterials*, *27*, 3163–3167. Cited on page(s) 25.

Warren, P. B., & Stepanek, F. (2008). Wall shear rate distribution for flow in random sphere packings. *Physical Review Letters*, *100*, 084501. Cited on page(s) 35, 126.

Wartella, K. A., & Wayne, J. S. (2009). Bioreactor for biaxial mechanical stimulation to tissue engineered constructs. *Journal of Biomechanical Engineering*, *131*, 044501–044501. Cited on page(s) 24.

Whitaker, S. (1986a). Flow in porous media i: A theoretical derivation of darcy's law. *Transport in Porous Media*, *1*, 3–25. Cited on page(s) 61, 165.

Whitaker, S. (1986b). Flow in porous media II: The governing equations for immiscible, two-phase flow. *Transport in Porous Media*, *1*, 105–125. Cited on page(s) 94, 96, 101.

Whitaker, S. (1994). The closure problem for two-phase flow in homogeneous porous media. *Chemical Engineering Science*, *49*, 765–780. Cited on page(s) 104.

Whitaker, S. (1999). *The Method of Volume Averaging*. Theory and Applications of Transport in Porous Media. Dordrecht: Kluwer Academic Publishers. Cited on page(s) 60, 61, 62, 78, 85, 157, 160, 164, 165, 170.

Wood, B., Golfier, F., & Quintard, M. (2011). Dispersive transport in porous media with biofilms: local mass equilibrium in simple unit cells. *International Journal of Environment and Waste Management*, *7*, 24–48. Cited on page(s) 54, 94, 95, 111, 126.

Wood, B. D. (2009). The role of scaling laws in upscaling. *Advances in Water Resources*, *32*, 723–736. Cited on page(s) 111.

Wood, B. D., Quintard, M., & Whitaker, S. (2002). Calculation of effective diffusivities for biofilms and tissues. *Biotechnology and Bioengineering*, *77*, 495–516. Cited on page(s) 54, 72, 73.

Wood, B. D., Radakovich, K., & Golfier, F. (2007). Effective reaction at a fluid–solid interface: Applications to biotransformation in porous media. *Advances in Water Resources*, *30*, 1630–1647. Cited on page(s) 54, 72.

Wood, B. D., & Valdés-Parada, F. J. (2013). Volume averaging: Local and nonlocal closures using a green's function approach. *Advances in Water Resources*, *51*, 139–167. Cited on page(s) 111.

Wood, B. D., & Whitaker, S. (1998). Diffusion and reaction in biofilms. *Chemical Engineering Science*, *53*, 397–425. Cited on page(s) 54, 72, 82, 83, 84, 85, 95, 111.

Wood, B. D., & Whitaker, S. (1999). Cellular growth in biofilms. *Biotechnology and Bioengineering*, *64*, 656–670. Cited on page(s) 54, 59, 72.

Wood, B. D., & Whitaker, S. (2000). Multi-species diffusion and reaction in biofilms and cellular media. *Chemical Engineering Science*, *55*, 3397–3418. Cited on page(s) 54, 59, 72, 73, 83, 84, 85, 143.

Wu, Y.-y., Ban, Y., Geng, N., Wang, Y.-y., Liu, X.-g., Yu, T., & Gong, P. (2010). Evaluation of different culture techniques of osteoblasts on 3d scaffolds. *Central European Journal of Biology*, *5*, 456–465. Cited on page(s) 14, 23.

Yeatts, A. B., & Fisher, J. P. (2011). Bone tissue engineering bioreactors: Dynamic culture and the influence of shear stress. *Bone*, *48*, 171–181. Cited on page(s) 23.

Yoon, S.-H., Kim, Y. K., Han, E. D., Seo, Y.-H., Kim, B. H., & Mofrad, M. R. K. (2012). Passive control of cell locomotion using micropatterns: the effect of micropattern geometry on the migratory behavior of adherent cells. *Lab on a Chip*, *12*, 2391. Cited on page(s) 13.

Yu, P. (2012). Numerical simulation on oxygen transfer in a porous scaffold for animal cell culture. *International Journal of Heat and Mass Transfer*, *55*, 4043–4052. Cited on page(s) 39, 53, 94.

Zermatten, E., Vetsch, J. R., Ruffoni, D., Hofmann, S., Müller, R., & Steinfeld, A. (2014). Micro-computed tomography based computational fluid dynamics for the determination of shear stresses in scaffolds within a perfusion bioreactor. *Annals of Biomedical Engineering*, *42*, 1085–1094. Cited on page(s) 37.

Zhang, F., Tian, J., Wang, L., He, P., & Chen, Y. (2011). Correlation between cell growth rate and glucose consumption determined by electrochemical monitoring. *Sensors and Actuators B: Chemical*, *156*, 416–422. Cited on page(s) 126.

Zhao, F., Chella, R., & Ma, T. (2007). Effects of shear stress on 3-d human mesenchymal stem cell construct development in a perfusion bioreactor system: Experiments and hydrodynamic modeling. *Biotechnology and Bioengineering*, *96*, 584–595. Cited on page(s) 38, 39.

Zhao, F., Pathi, P., Grayson, W., Xing, Q., Locke, B. R., & Ma, T. (2005). Effects of oxygen transport on 3-d human mesenchymal stem cell metabolic activity in perfusion and static cultures: Experiments and mathematical model. *Biotechnology Progress*, *21*, 1269–1280. Cited on page(s) 39, 44, 71.

Zick, A. A., & Homsy, G. M. (1982). Stokes flow through periodic arrays of spheres. *Journal of Fluid Mechanics*, *115*, 13–26. Cited on page(s) 63, 126, 166.

Zygourakis, K., Bizios, R., & Markenscoff, P. (1991a). Proliferation of anchorage-dependent contact-inhibited cells. i: Development of theoretical models based on cellular automata. *Biotechnology and Bioengineering*, *38*, 459–470. Cited on page(s) 42.

Zygourakis, K., Markenscoff, P., & Bizios, R. (1991b). Proliferation of anchorage-dependent contact-inhibited cells. ii: Experimental results and validation of the theoretical models. *Biotechnology and Bioengineering*, *38*, 471–479. Cited on page(s) 42.